Nanoscale nuclear magnetic resonance with chemical structure resolution

Von der Fakultät 8 Mathematik und Physik der Universität Stuttgart zur Erlangung der Würde eines Doktors der Naturwissenschaften (Dr. rer. nat.) genehmigte Abhandlung

Vorgelegt von

Nabeel Ahmad Aslam

aus Bad Dürkheim

Hauptberichter:	Prof. Dr. Jörg Wrachtrup
1. Mitberichter:	Prof. Dr. Sebastian Loth
2. Mitberichter:	Prof. Dr. Fedor Jelezko

Tag der mündlichen Prüfung: 04.10.2018

3. Physikalisches Institut der Universität Stuttgart

2018

Contents

List of Figures

List of Tables

List of Abbreviations

A	mass number
Å	angstrom
AFM	atomic force microscopy
AOM	acousto-optic modulator
APD	single photon counting avalanche photodiode
AVC	atomic vapor cells
CASR	coherently averaged synchronized readout
CCD	charge-coupled device
cm	centimeter
CPW	coplanar waveguide
CVD	chemical vapor deposition
cw	continuous wave
DD	dynamical decoupling
DDNS	dynamical decoupling noise spectroscopy
DEER	double electron-electron resonance
DNP	dynamic nuclear polarization
EFG	electric field gradient
EPR	electron paramagnetic resonance
F	readout fidelity
fcc	face-centered cubic
FFT	fast Fourier transformed
FID	free induction decay
FIT	finite integration technique
FWHM	full width at half maximum
GHz	Gigahertz
GSD	ground state depletion (microscopy)
hBn	hexagonal boron nitride
HMM	Hidden Markov Model
HPHT	high pressure high temperature
ISC	intersystem crossing
kHz	kilohertz
LAC	level anti-crossing

lp	laser pulses
MHz	Megahertz
μm	micrometer
μs	microsecond
mm	millimeter
ms	millisecond
MRI	magnetic resonance imaging
MRFM	magnetic resonance force microscopy
MW	microwave
mT	millitesla
nm	nanometer
NMR	nuclear magnetic resonance
NOVEL	nuclear spin orientation via electron spin locking
NQR	nuclear quadrupole resonance
ns	nanosecond
NV	nitrogen-vacancy (center)
NV^-	negatively charged nitrogen-vacancy (center)
NV^0	neutrally charged nitrogen-vacancy (center)
NV^+	positively charged nitrogen-vacancy (center)
ODMR	optically detected magnetic resonance
PALM	photo-activated localization microscopy
PFPE	perfluoropolyether
PHIP	parahydrogen-induced polarization
ppm	parts per million
PSF	pointspread function
PVDF	polyvinylidene fluoride
Qdyne	quantum heterodyne
QEC	quantum error correction
QFT	quantum Fourier transform
QIP	quantum information processing
QND	quantum non-demolition
qubit	quantum bit
RF	radiofrequency
RT	room-temperature
SABRE	signal amplification by reversible excitation
SEOP	spin-exchange optical pumping
SNOM	scanning near-field optical microscopy

SNR	signal to noise ratio
SQUID	superconducting quantum interference device
SRIM	Stopping and Range of Ions in Matter
SSR	single-shot readout
STED	stimulated emission depletion (microscopy)
STM	scanning tunneling microscopy
STORM	stochastic optical reconstruction microscopy
T_1^{sensor}	longitudinal spin relaxation time of sensor spin
T_2^{sensor}	transverse spin relaxation time of sensor spin
T_1^{mem}	longitudinal spin relaxation time of memory spin
T_2^*	inverse inhomogeneous broadening; decay constant of FID
TE	transverse electric
TM	transverse magnetic
TMS	tetramethylsilane
TEM	transmission electron microscopy
TWT	traveling wave tube
ZFS	zerofield splitting
ZPL	zero-phonon line

Summary

NMR spectroscopy At the time Felix Bloch and Edward Purcell detected radio frequency signals, generated by nuclear spins, the huge impact of this observation was not foreseeable [1, 2]. These experiments laid the cornerstone for the field of nuclear magnetic resonance (NMR) and deservedly lead to the Nobel prize award in the year 1952. Outstanding properties of NMR are its non-invasiveness and its ability to detect unique fingerprints of sample molecules. The two major applications are magnetic resonance imaging (MRI) and NMR spectroscopy. MRI spatially resolves the nuclear spin density in a sample and is routinely used in hospitals to image e.g. the human brain in-vivo with a higher spatial resolution than any other imaging technique. NMR spectroscopy on the other hand is recording resonances arising from intra- and inter-molecular couplings. Observation of these frequency shifts based on e.g. the chemical shift effect or J-coupling allows molecule structure analysis and has lead to the identification of millions of organic molecules. In the case of ^{1}H spins the chemical shifts can vary over a range of 13 ppm [3]. J-coupling between ^{1}H spins is on the order of $\approx$ 10 Hz [3]. The applications of NMR are widespread with investigated objects including the brain, bones, proteins, drugs, metals, ceramics, superconductors or explosives [3]. The sensitivity of NMR is limited by the thermal polarization of the nuclear spins which increases with the applied magnetic field. For example ^{1}H spins at a field of 3 T and T = 300 K exhibit a degree of polarization on the order of 10^{-5}. As a result the spatial resolution of NMR spectroscopy via micro-coils has been limited to $(3\ \mu\text{m})^3$ [4, 5]. This prevents e.g. the detection of single proteins, where the titin protein, the largest known human protein, has a length of 1 μm [6]. Hence, due to the required large amount of molecules in the detection volume, conventional NMR spectroscopy yields an averaged signal and is not feasible to detect minor local modifications.

Different novel techniques have been employed with the goal to enhance NMR sensitivity. One approach is to hyperpolarize the nuclear spins. The most prominent of the hyperpolarization techniques is dynamic nuclear polarization (DNP) [7]. Here the higher thermal polarization of one spin species (due to its larger gyromagnetic ratio) is transferred to spins with a lower degree of polarization. DNP and other hyperpolarization methods are restricted to specific samples, require chemical reactions or low tempera-

tures, thus hindering a universal application.

On the other hand novel magnetometers have emerged which do not rely on magnetic field detection based on pick-up coils. Three examples of such magnetometers are atomic vapor cells (AVCs) [8, 9], superconducting quantum interference devices (SQUIDs) [10, 11] and magnetic resonance force microscopy (MRFM) [12]. While the magnetic field sensitivity of AVCs and SQUIDs can achieve values better than $\mathrm{fT}/\sqrt{\mathrm{Hz}}$, their spatial resolution is additionally limited by their distance to the nuclear spins. On the other hand the MRFM technique has demonstrated a detection volume on molecular length scales [13]. Here the signal is not based on the thermal polarization but on the statistical polarization which becomes significant on the nanoscale. The major drawback of MRFM is its requirement to operate at cryogenic temperatures and under vacuum conditions. Compared to ambient conditions the molecules' properties do change significantly. Under the mentioned conditions it is e.g. not possible to study living cells or dynamic processes like protein folding.

Quantum metrology with NV centers in diamond The nitrogen-vacancy (NV) center in diamond possesses an electron spin which can be optically readout and initialized at ambient conditions [14]. The NV center is the combination of a substitutional nitrogen atom and a neighboring vacancy in the diamond lattice. Its electron spin shows longitudinal relaxation times (T_1^{sensor}) reaching 6 ms [15]. The corresponding transversal relaxation time (T_2^{sensor}) [16] can be prolonged to the T_1^{sensor} time with a suitable dynamical decoupling sequence [17, 18, 19, 20]. The NV electron spin is capable of sensing its magnetic field environment due to its Zeeman and Hyperfine coupling terms. Applying a dynamical decoupling sequence increases the relaxation time on one hand, on the other hand the corresponding filter function can be tuned to resonate with nuclear spin transition frequencies. This has led to the detection of nearby single nuclear spins in the diamond lattice [21, 22, 23]. By placing a NV center a few nanometer away from the diamond surface, it is furthermore possible to detect external nuclear spins [24, 25]. The achieved detection volume is e.g. $(2\ \mathrm{nm})^3$ and depends on the depth of the NV center in the diamond [26]. The so far obtained NMR spectra only allow to distinguish between different nuclear spin species [27]. Individual peaks corresponding to chemical shift or J-coupling are covered by the 14 kHz broad (FWHM) NMR peak in the proof-of-principle experiment [24]. Therefore molecular identification has so far not been possible with NV center based NMR detection. The crucial parameter is the spectral resolution, which is mainly limited by three time scales. The first limitation comes from the relaxation time of the sensor spin (NV electron spin) itself. Once the sensor spin's state has decayed, it looses any correlation to the nuclear spins. Secondly the spatial diffusion of the nuclear spins in a liquid sets a limit. When the nuclear spins diffuse out of the nm-scale detec-

tion volume their signal becomes too weak to be detectable. These spins are replaced by other nuclear spins diffusing into the detection volume. However each set of statistically polarized nuclear spins varies in amplitude and phase and creates a different signal. The third limit comes from the T_2^* relaxation time of the nuclear spins. Stationary dipolar coupling among nuclear spins in solid-state systems leads to a broadening of the NMR peaks. Typically for organic molecules this results in a measured FWHM on the order of 15 kHz. However in liquid samples dipole-dipole interaction is averaged out due to molecular tumbling and diffusion. These three limitations have so far limited the spectral resolution to around 14 kHz and correspondingly to 12,000 ppm (at B = 0.02 T) [24]. In this work these limitations have been addressed with the goal of achieving a high spectral resolution, sufficient to resolve chemical shift effects.

Results and conclusion The application of high magnetic fields has two advantages for the goal of this work. First of all the frequency shift due to the chemical shift effect is linearly proportional to the applied magnetic field [3]. Therefore high magnetic fields facilitate the detection of chemical shifts. The second advantage is that high magnetic fields prolong the relaxation times of single nuclear spins in the vicinity of the NV center and thereby enable their use as memory spins. On the one hand the readout can be conducted via these memory spins in a single-shot, which significantly increases the sensitivity [28, 29]. And on the other hand novel schemes for sensing can be introduced, which store the phase information on the memory spin's long-lived population [30, 15].

In this work a magnetic field of 3 T is applied on a single NV center which translates to spin transition frequencies of around 86 GHz. Due to the high resistance occurring at these high microwave frequencies the commonly used coaxial cables and coplanar waveguide boards cannot be utilized. Instead, rectangular hollow waveguides made out of metal ensure low-loss transport of the microwaves. However this also means that the MW field is distributed over a length scale of millimeters in these waveguides, in contrast to the atomic length scale of the sensor. This cannot be compensated by higher MW power as the currently available MW sources and amplifiers in the corresponding frequency band provide less than 30 dBm. Consequently manipulating a single NV electron spin at a frequency of 86 GHz is not straightforward. It requires the design of MW resonators which are compatible with confocal microscopy. To this end two approaches have been followed in this work. A transition from waveguide to a $\lambda/2$ antenna has been simulated and the latter has been fabricated. The antenna has a resonance frequency and is additionally tapered in the center to increase the MW field locally. The achieved efficiency of microwave-power-to-NV-Rabi-frequency conversion is $C_{\mathrm{Rabi}} = 27\,\mathrm{MHz}/\sqrt{\mathrm{W}}$. The second approach is to couple to a cylindrical waveguide cavity. The produced cavity has a TM_{110} mode with a resonance frequency of around 75 GHz. It is possible to place the

diamond with the NV centers into the mode maximum. Here a microwave-power-to-NV-Rabi-frequency efficiency of $C_{\mathrm{Rabi}} = 0.75\,\mathrm{MHz}/\sqrt{\mathrm{W}}$ has been measured. Both approaches allow the control of a single NV electron spin up to a field of 3 T.

With the novel resonator structures the magnetic field dependence of the ^{14}N (NV center) nuclear spin's T_1 time can be investigated up to a field of 3 T. Under continuous readout, the T_1 time of the ^{14}N spin is primarily limited by hyperfine induced flip-flop processes in the electronic excited state. The probability for the occurrence of these events decreases quadratically with the applied magnetic field. Once the T_1 time of the ^{14}N spin is longer than the spin measurement time, single-shot readout (SSR) becomes possible. An approximate quadratic field dependence (up to 3 T) of the ^{14}N spin's T_1 under continuous readout has been verified in this work. Moreover, at 3 T the readout fidelity of SSR exceeds 99 % which is a crucial parameter for the application in quantum information processing and quantum metrology. At 2.77 T, the ^{14}N spin has a T_1 time under continuous readout of around 1 s and survives more than 330,000 readout laser pulses (of 300 ns length). In addition to this, the T_1 time of the ^{14}N spin has been investigated in the absence of laser excitation. Interestingly the ^{14}N spin shows two different decay mechanisms, depending on the charge state of the NV center: NV^0 and NV^-. In the case of the NV^0 charge state the T_1 time of the ^{14}N spin scales quadratically with the applied magnetic field and reaches 1.8 s at 2.77 T. The NV^- charge state has a weaker dissipating effect on the ^{14}N spin and therefore enables a T_1 time of 260 s at 1.5 T. Here the hyperfine coupling in the electronic ground state of NV^- is expected as the dominant relaxation mechanism resulting in a quadratic field dependence of the ^{14}N spin's T_1 time. A quadratic scaling is however only observed for lower magnetic fields. At higher magnetic fields the T_1 time saturates. The additional relaxation process might be related to the quadrupole coupling of the ^{14}N spin. Nevertheless the ^{14}N spin's population represents a suitable storage medium for quantum metrology purposes with its T_1^{mem} time of 260 s (at 1.5 T).

The main goal of this work is to achieve a high spectral resolution in NMR measurements. To this end a novel quantum metrology sequence based on entanglement between the sensor and the memory spin is introduced. Here, the NV electron spin as the sensor spin acquires a phase induced by the magnetic field signal. The phase information is stored on the nitrogen nuclear spin, the memory spin. Additionally the readout is performed efficiently via the memory spin in a single shot. The sequence forms a quantum metrology framework which allows implementation of arbitrary NMR sequences. The achievable spectral resolution is governed by the T_1^{mem} time of the ^{14}N spin which translates to a resolution of 1 mHz and 10^{-5} ppm (at 3 T). Moreover, the introduced quantum metrology sequence separates detection and nuclear spin manipulation and therefore minimizes the

relaxation induced by the sensor onto the sample spins.

For the detection of external nuclear spins the successful creation of shallow NV centers is necessary. Therefore $^{15}N^{+}$ ions are implanted into the diamond lattice with an energy of 5 keV. The created NV centers have a distance to the surface ranging from 23 nm to 48 nm. Their T_2^{sensor} coherence times are comparable to NV centers in bulk diamond. As a result, NMR detection of statistically polarized nuclear spins in liquid and solid samples, placed on top of the diamond, is demonstrated. In fact, the distance-dependence of the NMR signal allows a precise determination of the NV center depth. This relation also defines a volume, from where nuclear spins are contributing to 50 % of the NMR signal, the detection volume. In this work a detection volume down to $(18\ \text{nm})^3$ has been demonstrated. This corresponds to 6 zeptoliters and 330,000 nuclear spins (spin density of $58\ \text{nm}^{-3}$). This is 12 orders of magnitude smaller compared to conventional NMR.

The spatial diffusion of nuclear spins through the nanoscale detection volume is investigated for various liquid samples. For ^{1}H spins in highly viscous polybutadiene a diffusion time of $T_D = 5.4$ ms is measured, with a 34 nm deep NV center. Furthermore, based on the sensor-memory metrology probe, Ramsey experiments of ^{19}F and ^{1}H spins are performed. NMR spectra are obtained of ^{19}F spins in perfluoropolyether (PFPE) oil and of ^{1}H spins in polybutadiene oil. The FFT of the measurement results resolves the expected chemical shift splittings. The achieved spectral resolution of 1 ppm is mainly limited by diffusion and dipolar coupling. These results mark the first chemical shift resolved NMR spectroscopy on nanometer scale samples, at ambient conditions.

Solid-state samples are investigated on the nanoscale as well. Here, the corresponding nuclear spins are not spatially diffusing. However the spin magnetization within the nanoscale detection volume will still decay due to spin diffusion. For ^{1}H spins in solid ethyl-2-cyanoacrylate the corresponding decay time of 94 ms is measured, with a 44 nm deep sensor spin. Furthermore high resolution solid-state NMR is conducted by employing homonuclear decoupling sequences like WAHUHA and MREV-8. This counteracts the dipolar broadening and leads to a 17-fold enhancement in spectral resolution.

The demonstrated high spectral resolution, in conjunction with nanometer scale sample volumes, can be utilized for nanoscale NMR imaging. Imaging can be conducted by a scanning or a widefield approach. The advantage of the latter is its parallel operation on an ensemble of NV centers e.g. located in a $100 \times 100\ \mu\text{m}^2$ field of view. In this scenario however the spatial resolution will be limited by the diffraction limit of the optical microscope. For the wavelength range of NV^{-} fluorescence, this translates to a resolution limit of 267 nm. Two different approaches have been proposed and implemented in order to overcome the diffraction limit: Stimulated emission depletion (STED) [31]/ Ground state depletion (GSD) and Photo-activated localization microscopy (PALM)/Stochastic

optical reconstruction microscopy (STORM) [32, 33, 34]. The inventors of these methods, Stefan Hell, Eric Betzig and William Moerner, have been awarded with the Nobel prize for chemistry in the year 2014. STED exploits the non-linear optical response of the emitters and restricts the area where fluorescence can be emitted. It is a scanning technique and has already been implemented with NV centers in diamond [35]. On the other hand PALM/STORM microscopy is performed in a widefield setup and has so far not been applied to NV centers in diamond. This technique requires a stochastic switching of the emitters into an OFF state. This enables to localize the remaining emitters, in the ON state, with an accuracy better than the diffraction limit. Recently, profound knowledge about laser induced charge state switching of NV centers has been gained [36] and identified as a suitable stochastic mechanism for PALM/STORM. This charge state dynamics is exploited in this work for the first demonstration of STORM based super-resolution microscopy of NV centers in diamond. Widefield illumination combined with CCD imaging allows parallel detection of multiple NV centers in diamond. The achieved spatial resolution of 27 nm represents a ten-fold improvement compared to the diffraction limit. The resolution is mainly limited by the low photon collection efficiency and the sample drift during the measurement. Improving on both parameters would result in a resolution of around 10 nm. In contrast to STORM fluorophores, the NV centers possess an electron spin. Thus STORM microscopy can be combined with magnetic resonance techniques. Therefore the optical response of the NV center can be tagged with the individual spin transition frequency. This has on one hand the advantage of further improving the separation between individual NV centers. And on the other hand it enables widefield NV sensing of e.g. nuclear spins with a spatial resolution beyond the diffraction limit. Towards this goal, the STORM microscopy has been combined with ODMR in this work. This allows the assignment of individual ODMR signals to super-resolved NV electron spins with a magnetic field sensitivity of $\delta B \approx 190\,\mu\mathrm{T}/\sqrt{\mathrm{Hz}}$. Improvement in sensitivity can e.g. be achieved by increasing the photon collection efficiency and by using diamond samples with a longer T_2^* time. Due to the parallel signal acquisition, in a large field of view, the sensitivity of STORM-ODMR can potentially exceed the achievable sensitivity of scanning techniques.

Outlook In this work the control of a single NV electron spin has been extended to a magnetic field of 3 T, which has benefits for different applications. The main challenge in that regard has been the engineering of MW resonators capable of working up to 90 GHz. Applying a higher magnetic field increases the relaxation time of the nuclear spins coupled to the NV electron spin. In quantum information processing the NV electron spin qubit and nearby nuclear spins are envisioned to form a quantum register, which is more robust against bit and phase flip errors [37] than a single qubit. The higher field not only

increases the initialization fidelity of the nuclear spins in the quantum register, but also allows to include more ^{13}C spins to the register [38]. Moreover the thermal polarization of the nuclear spins increases with the applied magnetic field, which can be beneficial for NMR [39]. The same is true for signal coming from paramagnetic particles [40].

The detection of chemical shift peaks, stemming from nanometer scale sample volumes, increases the importance of NV based NMR spectroscopy enormously. However this work only shows proof-of-principle experiments, which need further improvements. For example the measurement time for acquiring a NMR spectrum is on the order of hours (see table A.3). Here, working with an ensemble of N electron spins, instead of a single spin, would improve the sensitivity by a factor of $\sqrt{N}$ and would significantly reduce the measurement time.

Another improvable parameter is the spectral resolution. It is limited by diffusion in liquid samples. This work has therefore been restricted to highly viscous samples. This limit can be overcome by trapping the nuclear spins in nano-dimples [41] and thereby restricting the diffusion within the detection volume. Another possibility would be to align the NMR detection to the homogeneously distributed thermal polarization [39]. Consequently diffusion would not be limiting the spectral resolution anymore. Additionally, the transfer of the high NV electron spin polarization (92 %) to the nuclear spins is in principle possible and would dramatically increase the NMR signal [42].

The samples investigated so far were of no particular interest for biologists or chemists. However the future interdisciplinary collaborations could enable the attachment of biological samples to the diamond surface. The sensor-memory probe system would then be able to image single molecules and yield their chemical composition. In general nanoscale NMR imaging [43, 44] combined with detecting the fingerprints of molecules would have a huge impact. The imaging method could be applied in a scanning modality or in a widefield setup [45]. Single molecule imaging could be facilitated by electron spin labels functioning as reporter spins [46]. Furthermore dynamic processes like protein folding could in future be investigated by NV spin based NMR.

In the demonstrated NMR measurements only one-dimensional NMR sequences have been applied. The quantum metrology sequence however is also compatible with more sophisticated NMR sequences. For example two-dimensional NMR would be able to analyze interactions between nuclear spins. Moreover, the integration of more nuclear spins, as memory spins, would allow the implementation of quantum algorithms resulting in multibit information in each measurement step [38, 47].

Outline of thesis The thesis begins with an introductory chapter 1 about NMR spectroscopy. The basic principles of NMR are described. Moreover, the interactions within the molecule and their effect on the NMR spectrum are explained. Finally the limitations

of conventional NMR are revealed and the NV center as a nanoscale sensor at ambient conditions is motivated. The chapter 2 introduces the NV center in diamond and describes its properties. Furthermore the experimental setup is explained in detail. Chapter 3 presents two approaches to conduct single electron spin manipulation up to a frequency of 90 GHz. Both methods are evaluated by the efficiency to convert the available MW power into Rabi oscillations of the NV electron spin. In chapter 4 the relaxation processes of the ^{14}N spin are investigated and analyzed. Specifically the magnetic field scaling of the T_1^{mem} time is measured up to a field of 3 T. Chapter 5 discusses nanoscale NMR spectroscopy. It includes an overview of other NV based NMR studies and motivates the need for improvement of the spectral resolution. Furthermore the quantum metrology sequence based on sensor-memory entangled states is introduced. As the main result NMR detection of nanoscale sample volumes in combination with chemical shift detection is demonstrated. Finally the method is compared to other techniques. The final chapter 6 shows results of STORM microscopy of NV centers in diamond. In addition to this STORM is combined with ODMR and its potential for magnetic field sensing with super-resolution is discussed.

Zusammenfassung

NMR Spektroskopie Zu der Zeit als Felix Bloch und Edward Purcell Radiowellen-Signale von Kernspins detektierten, ahnte man noch nicht, welche Auswirkungen diese Entdeckung für die Zukunft mit sich bringen würde [1, 2]. Diese Experimente legten den Grundstein für das Feld der Kernspinresonanz und führten verdientermaßen zu der Vergabe des Nobelpreises im Jahre 1952. Die herausragenden Eigenschaften der Kernspinresonanztechnik sind, dass diese nicht-invasiv und in der Lage ist, die einzigartigen magnetischen Fingerabdrücke von Molekülen zu detektieren. Die zwei Anwendungsfelder sind die Magnetresonanztomographie (MRT) und die Kernspinresonanzspektroskopie (NMR Spektroskopie). MRT ist in der Lage, die Spindichte innerhalb einer Probe räumlich aufzulösen und wird alltäglich in Krankenhäusern genutzt, um z.B. das menschliche Gehirn (in vivo) mit einer beispiellosen Auflösung abzubilden. Kernspinresonanzspektroskopie, auf der anderen Seite, misst die Resonanzfrequenzen, die von Wechselwirkungen innerhalb einzelner oder zwischen mehrerer Moleküle stammen. Die Beobachtung dieser Frequenzverschiebungen basiert z.B. auf dem Effekt der chemischen Verschiebung oder der J-Kopplung und erlaubt die Analyse der Molekülstruktur. Dies hat zur Identifikation von Millionen von organischer Moleküle geführt. Im Falle der chemischen Verschiebung von Protonen-Spins liegt die maximal mögliche Frequenzverschiebung bei etwa 13 ppm [3]. Auf der anderen Seite befindet sich die J-Kopplung zwischen Protonen-Spins auf der Größenordnung von etwa 10 Hz [3]. Die Anwendungen der Kernspinresonanz sind vielfältig. Zu den untersuchten Objekten gehören u.a. das Gehirn, Knochen, Proteine, Medikamente, Metalle, Keramik, Supraleiter und Sprengstoff [3]. Die Sensitivität der Kernspinresonanz ist durch die thermische Polarisierung der Kernspins limitiert, die mit dem angelegten Magnetfeld steigt. Protonen-Spins in einem Magnetfeld von 3 T und einer Temperatur von 300 K weisen beispielsweise einen Polarisationsgrad von 10^{-5} auf. Entsprechend ist die räumliche Auflösung der Kernspinresonanzspektroskopie (mithilfe von Mikrometer große Spulen) auf etwa $(3\ \mu\text{m})^3$ beschränkt [4, 5]. Dies verhindert zum Beispiel die Detektion von einzelnen Proteinen, da das größte bekannte menschliche Protein, das Titin Protein, eine Länge von etwa 1 μm hat [6]. Aufgrund der großen Anzahl an Molekülen im Detektionsvolumen, kann die konventionelle Kernspinresonanzspektroskopie nur ein gemitteltes Signal messen. Winzige lokale Änderungen der Probe bleiben

so verborgen.

Verschiedene neuartige Techniken sind mittlerweile mit dem Ziel in Erscheinung getreten, die NMR Sensitivität zu erhöhen. Eine Vorgehensweise ist es, die Kernspins zu hyperpolarisieren. Die berühmteste Hyperpolarisationsmethode ist die dynamische Kernpolarisierung (im Englischen: dynamic nulear polarization, DNP) [7]. Hier wird die höhere thermische Polarisierung einer Spin-Spezies (aufgrund eines höheren gyromagnetischen Verhältnis) auf Spins mit niedrigerem Polarisierungsgrad übertragen. DNP und andere Hyperpolarisationsmethoden funktionieren nur bei bestimmten Proben, benötigen chemische Reaktionen oder können nur bei tiefen Temperaturen angewendet werden. Dies verhindert eine universelle Anwendung.

Auf der anderen Seite wurden Magnetometer entwickelt, die nicht auf der Magnetfelddetektion durch Spulen angewiesen sind. Drei Beispiele solcher Magnetometer sind: eine mit Atomen gefüllte Dampfzelle (im Englischen: atomic vapor cells, AVCs) [8, 9], eine supraleitende Quanteninterferenzeinheit (im Englischen: superconducting quantum interference devices, SQUIDs) [10, 11] und das Magnetresonanz-Kraftmikroskop (im Englischen: magnetic resonance force microscopy, MRFM) [12]. Die Magnetfeld-Sensitivität von AVCs und SQUIDs kann zwar Werte von $\mathrm{fT}/\sqrt{\mathrm{Hz}}$ und besser vorweisen, die räumliche Auflösung wird jedoch zusätzlich von dem Abstand zu den Kernspins eingeschränkt. Die MRFM Methode hingegen hat ein Detektionsvolumen von molekularer Längenskala erreicht [13]. Hierbei basiert das Signal nicht auf der thermischen Polarisierung, sondern auf der statistischen, welche für die Nanometerskala bedeutsam ist. Der große Nachteil von MRFM ist jedoch, dass kryogene Temperaturen und Vakuumbedingungen zwingend erforderlich sind. Die molekularen Eigenschaften sind hierbei aber anders als unter Raumbedingungen. Desweiteren ist es unter den genannten Bedingungen nicht möglich, lebende Organismen oder Prozesse, wie die Proteinfaltung zu untersuchen.

Quanten Metrologie mit NV Zentren im Diamant Das Stickstoff-Fehlstellen Zent-rum (im Englischen: nitrogen-vacancy, NV-center) ist im Besitz eines Elektronenspins, welcher unter Raumbedingungen optisch ausgelesen und initialisiert werden kann [14]. Das NV Zentrum ist eine Kombination eines Stickstoff-Atoms und einer benachbarten Fehlstelle. Sein Elektronenspin zeigt longitudinale Relaxationszeiten (T_1^{sensor}) von bis zu 6 ms [15]. Die entsprechende transversale Relaxationszeit (T_2^{sensor}) [16] kann mithilfe einer geeigneten dynamischen Entkopplungssequenz (im Englischen: dynamical decoupling, DD) bis zu der T_1^{sensor} Zeit verlängert werden [17, 18, 19, 20]. Der NV Elektronenspin ist aufgrund seiner Zeeman und Hyperfine Kopplungsterme imstande, seine magnetische Umgebung zu messen. Eine dynamische Ent-kopplungssequenz erhöht nicht nur die Relaxationszeit, sondern hat auch eine entsprechende spektrale Filterfunktion, die mit den Kernspins in Resonanz gebracht werden kann. Dies hat zur Detektion von

im Diamant befindlichen Kernspins geführt [21, 22, 23]. Durch das Platzieren eines NV Zentrums einige Nanometer von der Diamant Oberfläche entfernt, ist es ferner möglich externe Kernspins zu detektieren [24, 25]. Das dabei erreichte Detektionsvolumen hat eine Größenordnung von Kubiknanometern und hängt von der Tiefe des NV Zentrums im Diamant ab [26]. Die bisher aufgenommenen NMR Spektren erlauben lediglich die Unterscheidung zwischen verschiedenen Kernspin Spezies [27]. Die in dem ersten NV basierten NMR Experiment erreichte Halbwertsbreite betrug 14 kHz [24] und verdeckte damit individuelle Peaks von Effekten, wie der chemischen Verschiebung oder der J-Kopplung. Deshalb war eine Identifizierung von Molekülen mit NV basierter NMR Detektion bisher nicht möglich. Der entscheidende Parameter ist dabei die spektrale Auflösung, die primär durch drei Zeitskalen eingeschränkt wird. Die erste Einschränkung kommt von der Relaxationszeit des Sensor Spins. Ist der Spinzustand des Sensors erst einmal zerfallen, so verliert er auch jegliche Korrelation zu den Kernspins. Zweitens setzt die räumliche Diffusion der Kernspins in Flüssigkeiten ein Limit, denn sobald die Kernspins aus dem wenige Nanometer großen Detektionsvolumen heraus diffundierend sind, wird deren Signal zu schwach, um es detektieren zu können. Diese Spins werden dann durch andere in das Detektionsvolumen diffundierende Kernspins ersetzt. Jedes Set an statistisch polarisierten Kernspins variiert jedoch in der Amplitude und in der Phase und erzeugt so ein voneinander abweichendes Signal. Die dritte Einschränkung kommt durch die T_2^* Relaxations-zeit der Kernspins. Stationäre dipolare Wechselwirkung unter Kernspins in Festkörpern sorgt für eine Verbreiterung der NMR Linien. Typischerweise erwartet man für organische Moleküle eine Halbwertsbreite von ungefähr 15 kHz. In Flüssigkeiten wird die Dipol-Dipol Wechselwirkung hingegen, aufgrund von Rotation und Diffusion von Molekülen, ausgemittelt. Diese drei Limitierungen haben die spektrale Auflösung bisher auf etwa 14 kHz und entsprechend auf 12.000 ppm (bei einem Feld von B = 0,02 T) begrenzt [24]. In dieser Arbeit wird gezeigt, wie diese Einschränkungen überwunden werden können. Dabei wird eine für die Beobachtung der chemischen Verschiebung, notwendige spektrale Auflösung erzielt.

Ergebnisse und Fazit Das Anlegen von hohen Magnetfeldern hat zwei Vorteile hinsichtlich des Ziels dieser Arbeit. Zum Einen steigt die Frequenzverschiebung, aufgrund der chemischen Verschiebung, linear mit dem angelegten magnetischen Feld an [3]. Deshalb wird die Detektion von chemischen Verschiebungen in Molekülen durch höhere Magnetfelder erleichtert. Zum Anderen steigen die Relaxationszeiten von Kernspins in der Umgebung von NV Zentren. Diese Kernspins können infolgedessen als Speichermedium genutzt werden. Daraus resultierend kann der Auslesevorgang des Kernspinzustands in einem einzigen Messschritt (im Englischen: single-shot readout, SSR) erfolgen, was die Mess-Sensitivität stark erhöht [28, 29]. Desweiteren ist es möglich, innerhalb von Mess-

Sequenzen die Phaseninformation auf den langlebigen Eigenzuständen des Kernspins zu speichern [30, 15].

Hierfür wird ein Magnetfeld von 3 T an einem einzelnen NV Zentrum angelegt. Das heißt, dass die Spin Übergangsfrequenz bei etwa 86 GHz liegt. Aufgrund des, bei diesen MW Frequenzen (<50 GHz), auftretenden hohen Widerstandes in den üblicherweise genutzten Koaxialkabel, müssen stattdessen Hohleiter verwendet werden, die für einen verlustarmen Transport von Mikrowellen sorgen. Das bedeutet wiederum, dass das Mikrowellen Feld, im Gegensatz zur atomaren Längenskala des Sensor Spins, über Millimeter verteilt ist und dadurch zu einer ineffizienten Anregung des Spins führt. Dies kann nicht durch höhere Mikrowellenleistung kompensiert werden, da zur Zeit erhältliche Mikrowellenquellen und Verstärker in dem entsprechenden Frequenzband eine Ausgangsleistung von weniger als 30 dBm vorweisen. Somit ist die Manipulation von einzelnen NV Elektronenspins bei einer Frequenz von 86 GHz nicht einfach. Die Entwicklung von Mikrowellen Resonatoren ist erforderlich, die mit der konfokalen Mikroskopie kompatibel sind. Zu diesem Zweck wurden zwei Ansätze in dieser Arbeit verfolgt. Zum Einen wurde ein Übergang von Hohleiter zu einer $\lambda/2$ Antenne simuliert und auch produziert. Die Antenne hat eine Resonanzfrequenz und ist zudem in der Mitte verjüngt, um das Mikrowellen Feld lokal zu erhöhen. Die erzielte Effizienz der Umwandlung von Mikrowellenleistung zu NV Rabi Frequenz ist $C_{\mathrm{Rabi}} = 27\,\mathrm{MHz}/\sqrt{\mathrm{W}}$. Der zweite Ansatz ist die Kopplung zu zylindrischen Hohlleiter Resonatoren. Der hergestellte Resonator besitzt eine TM_{110} Mode mit einer Resonanzfrequenz von etwa 75 GHz. Es ist möglich den Diamanten, mit den darin befindlichen NV Zentren, in den Bereich des Moden-Maximums zu bringen. Die dabei erzielte Effizienz von Mikrowellenleistung zu NV Rabi Frequenz beträgt $C_{\mathrm{Rabi}} = 0.75\,\mathrm{MHz}/\sqrt{\mathrm{W}}$. Beide Ansätze erlauben die Kontrolle eines einzelnen NV Elektronenspins bis zu einem Feld von 3 T.

Mit den neu entwickelten Resonatorstrukturen wurde die Magnetfeld Abhängigkeit der ^{14}N Kernspin- (vom NV Zentrum) T_1 Zeit bis zu einem Feld von 3 T untersucht. Bei kontinuierlichem Auslesen, ist die T_1 Zeit des ^{14}N Kernspins hauptsächlich durch die Flip-Flop Prozesse im angeregten elektronischen Zustand limitiert. Die Wahrscheinlichkeit für das Auftreten dieser Prozesse nimmt quadratisch mit dem angelegten Magnetfeld ab. Ist die T_1 Zeit des ^{14}N Spins länger als die Messdauer, ermöglicht dies ein Auslesen des Kernspinzustandes in einem einzigen Messschritt. Eine annähernd quadratische Abhängigkeit der ^{14}N Spin T_1 Zeit vom Magnetfeld, bei kontinuierlichem Auslesen, wurde in dieser Arbeit bis zu einem Feld von 3 T nachgewiesen. Darüberhinaus wurde eine Auslesegenauigkeit von mehr als 99 % erreicht, was für Anwendungen in der Quanteninformationsverarbeitung und der Quanten Metrologie von großer Bedeutung ist. Bei 2,77 T hat der ^{14}N Spin eine T_1 Zeit (unter kontinuierlichem Auslesen) von etwa 1 s und

überlebt mehr als 330.000 Laser Auslese Pulse (mit einer Länge von 300 ns). Zusätzlich wurde die T_1 Zeit des ^{14}N Spins in Abwesenheit von Laser Anregungen untersucht. Interessanterweise zeigt der ^{14}N Spin hier zwei verschiedene Zerfallsverhalten, die von dem jeweiligen Ladungszustand des NV Zentrums abhängen: NV^0 und NV^-. In dem Fall des NV^0 Ladungszustands, skaliert die T_1 Zeit des ^{14}N Spins quadratisch mit dem angelegten Magnetfeld und erreicht 1,8 s bei 2,77 T. Der NV^- Ladungszustand hat eine schwächer dissipierende Wirkung auf den ^{14}N Spin. Dadurch wird eine T_1 Zeit von 260 s bei 1,5 T im Falle von NV^- möglich. Die Hyperfein-Kopplung im elektronischen Grundzustand von NV^- wird hier als der dominante Relaxationsmechanismus erwartet und würde eine quadratische Skalierung der T_1 Zeit des ^{14}N Spin mit dem Magnetfeld mit sich bringen. Eine quadratische Abhängigkeit zeigt sich aber nur für niedrige Magnetfelder. Bei hohen Magnetfeldern sättigt die T_1 Zeit hingegen. Der zusätzlich auftretende Relaxationsprozess könnte womöglich mit der Quadrupol Wechselwirkung des ^{14}N Spin zusammenhängen. Nichtsdestotrotz stellen die Eigenzustände des ^{14}N Spins, mit der gemessenen T_1^{mem} Zeit von 260 s (bei 1,5 T), ein geeignetes Speichermedium für Quanten Metrologie Messungen dar.

Das Hauptziel dieser Arbeit ist es, eine hohe spektrale Auflösung in NMR Messungen zu erreichen. Zu diesem Zweck wird eine Quanten Metrologie Sequenz eingeführt, die auf Verschränkung zwischen dem Sensor Spin und dem Speicher Spin basiert. Der NV Elektronenspin fungiert als der Sensor Spin und sammelt eine Phase auf, die durch das Magnetfeld Signal erzeugt wird. Diese Phaseninformation wird auf dem Kernspin, dem Speicher Spin, ge-speichert. Außerdem erfolgt der Ausleseschritt des Zustands mittels dem Speicher Spin, effizient in einem einzigen Messschritt (SSR). Im Rahmen dieser Sequenz ist die Implementierung jeglicher NMR Sequenzen möglich. Die dabei erreichbare spektrale Auflösung ist durch die T_1^{mem} Zeit des ^{14}N Spins begrenzt und liegt damit bei etwa 1 mHz, bzw. 10^{-5} ppm (bei 3 T). Desweiteren separiert die Quanten Metrologie Sequenz den Detektionsteil von der Kernspin Manipulation und minimiert dadurch die Relaxationseffekte vom Sensor auf die Kernspins in der Probe.

Für die Detektion von externen Kernspins ist die erfolgreiche Bildung von NV Zentren nahe der Oberfläche unerlässlich. Dafür werden $^{15}N^+$ Ionen mit einer Energie von 5 keV in den Diamanten implantiert. Die so erzeugten NV Zentren haben einen Abstand zur Diamantoberfläche von 23 nm bis 48 nm. Die zugehörigen T_2^{sensor} Kohärenzzeiten sind vergleichbar mit denen von NV Zentren tief im Diamant. Damit kann das NMR Signal von statistisch polarisierten Kernspins von auf dem Diamant platzierten Flüssigkeiten und Festkörpern gemessen werden. Zudem kann die Abstandsabhängigkeit des NMR Signals für die präzise Bestimmung der NV Tiefe genutzt werden. Durch diese Abhängigkeit wird außerdem das sogenannte Detektions-volumen definiert, aus dem die Kernspins zu 50 %

des NMR Signals beitragen. In dieser Arbeit betrug das minimale Detektionsvolumen $(18\ \text{nm})^3$. Dies entspricht sechs Zeptolitern, mit ins-gesamt 330.000 Kernspins (bei einer Spindichte von $58\ \text{nm}^{-3}$). Das ist zirka 12 Größenordnungen geringer als bei der konventionellen NMR notwendig.

Die Diffusion der Kernspins durch das Nanometer große Detektionsvolumen wird für verschiedene Flüssigkeiten untersucht. Für ^{1}H Spins im hoch viskosen Polybutadiene wird mithilfe eines 34 nm tiefen NV Zentrum eine Diffusionszeit T_D von 5.4 ms gemessen. Desweiteren werden, basierend auf der Sensor-Speicher Metrologie Sequenz, Ramsey Experimente von ^{19}F und ^{1}H Spins durchgeführt. NMR Spektren wurden von ^{19}F Spins in Perfluoropolyether (PFPE) Öl und von ^{1}H Spins in Polybutadiene Öl aufgenommen. Die Fourier Transformation (FT) der Messresultate zeigt klar die jeweils erwartete Frequenzaufspaltung aufgrund der chemischen Verschiebung. Die dabei erzielte spektrale Auflösung von 1 ppm ist hauptsächlich durch Diffusion und dipolare Wechselwirkung begrenzt. Diese Resultate bedeuten die erstmalige Demonstration von Raumtemperatur NMR Spektroskopie von Nanometer großen Proben, bei gleichzeitiger Auflösung der chemischen Verschiebung.

Festkörper wurden ebenfalls auf der Nanometer Skala untersucht. Dabei diffundieren die entsprechenden Kernspins nicht räumlich. Es gibt jedoch die Spin Diffusion, die für einen Zerfall der Spin Magnetisierung im Nanometer großen Detektionsvolumen sorgt. Für ^{1}H Spins im festen Ethyl-2-Cyanoacrylat beträgt die entsprechende Zerfallsdauer 94 ms, gemessen mit einem 44 nm tiefen Sensor Spin. Zudem wurden, zwecks hochauflösender NMR Spektroskopie von Festkörpern, Homonukleare Entkopplungssequenzen, wie WAHUHA und MREV-8 angewandt. Diese wirken der dipolaren Verbreiterung entgegen und führen zu einer 17-fachen Verbesserung der spektralen Auflösung.

Die demonstrierte hohe spektrale Auflösung in Nanometer großen Proben, kann für die NMR Bildgebung auf Nanoskala genutzt werden. Bildgebung wird üblicherweise entweder durch einen Scan- oder durch ein Weitfeldmikroskop implementiert. Der Vorteil des Weitfeldmikroskops ist die parallele Adressierung eines Ensembles von NV Zentren z.B. in einem $100 \times 100\ \mu\text{m}^2$ großen Sichtfeld. In diesem Szenario ist die räumliche Auflösung aber durch das Beugungslimit von optischen Mikroskopen limitiert. Für den Wellenlängenbereich der NV^- Fluoreszenz bedeutet das ein Auflösungslimit von 267 nm. Zwei Ansätze zum Überwinden des Beugungslimits wurden vorgeschlagen und implementiert: STED (Stimulated emission depletion) Mikroskopie [31]/GSD (ground state depletion) Mikroskopie und PALM (im Englischen: Photo-activated localization) Mikroskopie /STORM (im Englischen: Stochastic optical reconstruction) Mikroskopie [32, 33, 34]. Die Erfinder dieser Methoden, Stefan Hell, Eric Betzig und William Moerner, wurden im Jahre 2014 mit dem Chemie-Nobelpreis ausgezeichnet. STED nutzt die nicht-lineare

optische Antwort der Emitter aus und schränkt den Bereich ein, aus der Fluoreszenz emittiert werden kann. Es ist eine Scan-Technik, die bereits an NV Zentren im Diamant demonstriert wurde [35]. PALM/STORM Mikroskopie, auf der anderen Seite, nutzt ein Weitfeldmikroskop und konnte bisher nicht auf NV Zentren angewandt werden. Diese Technik benötigt einen Prozess zum stochastischen Ausschalten der abzubildenden Emitter. Die restlichen Emitter, im angeschalteten Zustand, können dann mit einer Genauigkeit weit unterhalb des Beugungslimits lokalisiert werden. Vor Kurzem konnte tiefer gehende Kenntnis über laser-induzierte Ladungszustands Dynamik von NV Zentren erlangt [36], und als geeigneter stochastischer Prozess für PALM/STORM ausgemacht werden. Diese Ladungszustands Dynamik wird in dieser Arbeit verwendet, um zum ersten Mal STORM basierte hochaufgelöste Mikroskopie von NV Zentren im Diamant zu zeigen. Weitfeld Beleuchtung kombiniert mit CCD Bildgebung erlaubt die parallele Detektion von mehreren NV Zentren im Diamant. Die dabei erzielte räumliche Auflösung beträgt 27 nm und ist damit eine zehn-fache Verbesserung im Vergleich zum Beugungslimit. Die Auflösung ist hauptsächlich durch niedrige Photonen Detektions-effizienz und dem, während der Messung, driftenden Diamanten, begrenzt. Eine Optimierung beider Parameter würde eine Auflösung von etwa 10 nm ermöglichen. Im Gegensatz zu STORM Fluorophoren, besitzen die NV Zentren zudem einen Elektronenspin. Deshalb kann die STORM Mikroskopie mit Magnet Resonanz Techniken kombiniert werden. Die optische Antwort des NV Zentrums kann hierbei durch die individuellen Spin Übergangsfrequenzen markiert werden. Ein Vorteil ist, dass die räumliche Unterscheidbarkeit zwischen individuellen NV Zentren steigt. Der andere Vorteil ergibt sich in NV basierten Bildgebungs-Experimenten, wo z.B. die Kernspins mit einer räumlichen Auflösung besser als das Beugungslimit detektiert werden könnten. In der Hinsicht wird in dieser Arbeit STORM Mikroskopie mit ODMR verknüpft. Das erlaubt die Zuordnung von individuellen ODMR Signalen zu hochaufgelösten NV Elektronenspins mit einer Magnetfeld Sensitivität von $\delta B \approx 190\,\mu\mathrm{T}/\sqrt{\mathrm{Hz}}$. Eine Verbesserung der Sensitivität kann z.B. durch eine höhere Photonen Detektionseffizienz und durch Nutzung von Diamanten mit langer T_2^* Zeit erreicht werden. Aufgrund der simultanen Signalerfassung in einem großen Sichtfeld, kann die Sensitivität von STORM-ODMR potentiell, die von Scan-Techniken erzielten Werte, übertreffen.

Ausblick Durch diese Arbeit wird die Kontrolle über den NV Elektronenspin bis zu einem angelegten Magnetfeld von 3 T erweitert. Dies hat Vorteile für verschiedene Anwendungen. Die zentrale Herausforderung, in dieser Hinsicht, war das Entwickeln von Mikrowellen Resonatoren, die im Stande sind, bei bis zu 90 GHz zu arbeiten. Das Anlegen eines höheren Magnetfeldes erhöht die Relaxationszeit von Kernspins, die an den NV Elektronenspin gekoppelt sind. In der Quanteninformationsverarbeitung können das

NV Elektronenspin Qubit und benachbarte Kernspins ein Quantenregister bilden, welches robuster gegenüber dem Auftreten von Bit und Phasen Flip Fehlern ist [37]. Das höhere Magnetfeld erhöht nicht nur die Initialisierungsgenauigkeit der Kernspins im Quantenregister, sondern ermöglicht zudem, das Register um weitere ^{13}C Spins zu erweitern [38]. Desweiteren nimmt die thermische Polarisierung der Kernspins mit dem angelegten Magnetfeld zu, was für NMR Anwendungen interessant sein kann [39]. Dasselbe gilt für das Signal von Paramagnetischen Teilchen [40].

Die Detektion der chemischen Verschiebung in Nanometer großen Proben erhöht die Wichtigkeit der NV basierten NMR Spektroskopie enorm. Die hier gezeigten Experimente zeigen zunächst einmal nur die Machbarkeit, bedürfen nun aber weitere Verbesserungen. Zum Beispiel ist die Messzeit, um ein NMR Spektrum aufzunehmen, auf der Größenordnung von Stunden (siehe Tabelle A.3). Dabei würde das Miteinbeziehen von N Elektronenspins, im Vergleich zu einem einzelnen Spin, die Sensitivität, um einen Faktor $\sqrt{N}$ verbessern und die Messzeit damit deutlich reduzieren.

Ein weiterer verbesserungsfähiger Parameter ist die spektrale Auflösung. Diese wird durch die in Flüssigkeiten auftretende Diffusion begrenzt. Deshalb mussten die Proben in dieser Arbeit zwingend eine hohe Viskosität aufweisen. Diese Einschränkung kann überwunden werden, indem die Kernspins in Nanometer großen Vertiefungen gefangen [41] und damit die Diffusion innerhalb des Detektionsvolumen begrenzt wird. Außerdem gibt es die Möglichkeit die NMR Detektion auf die in der Probe homogen verteilte thermische Polarisation der Kernspins auszurichten [39]. Dabei würde die Diffusion die spektrale Auflösung nicht mehr begrenzen. Zusätzlich ist es möglich die hohe NV Elektronenspin Polarisation (92 %) auf die Kernspins zu übertragen und damit das NMR Signal drastisch zu erhöhen [42].

Die bisher untersuchten Proben waren nicht von besonderem Interesse für Biologen oder Chemiker. In Zukunft könnten interdisziplinäre Kollaborationen z.B. das Binden von Molekülen an die Diamantoberfläche ermöglichen. Das Sensor-Speicher Spin System würde es dann erlauben einzelne Moleküle abzubilden und deren chemische Zusammensetzung zu ermitteln. Im Allgemeinen wird die Kombination von NMR Bildgebung auf Nanoskala [43, 44] zusammen mit der Detektion von Molekül-spezifischen Fingerabdrücken eine große Bedeutung haben. Das bildgebende Verfahren könnte dabei in einem Scan- oder einem Weitfeld-Experiment [45] durchgeführt werden. Die Abbildung von einzelnen Molekülen könnte durch Elektronenspin Marker erleichtert werden, die als Reporter Spins fungieren würden [46]. Außerdem könnte die NV Spin basierte NMR Technik in Zukunft dynamische Prozesse wie Proteinfaltung untersuchen.

In den dargelegten NMR Messungen wurden lediglich ein-dimensionale NMR Sequenzen eingesetzt. Die Quanten Metrology Sequenz ist aber auch kompatibel mit fortge-

schrittenen NMR Sequenzen. Zwei-dimensionale NMR würde zum Beispiel in der Lage sein, Wechselwirkungen zwischen den Kernspins zu untersuchen. Darüberhinaus kann die Einbindung von weiteren Kernspins als Speicher Spins, die Implementierung von Quanten Algorithmen ermöglichen. Daraus resultierend würde man mit jedem Messschritt eine Multibit Information gewinnen [38, 47].

Gliederung der Arbeit Die Arbeit beginnt mit einem einführenden Kapitel 1 über NMR Spektroskopie. Die grundlegenden Prinzipien von NMR werden hier beschrieben. Außerdem werden Wechselwirkungen innerhalb des Moleküls und deren Auswirkungen auf das NMR Spektrum thematisiert. Zuletzt werden in dem Kapitel die Einschränkungen der konventionellen NMR aufgezeigt und das NV Zentrum, als ein bei Raumtemperatur funktionierender Nano Sensor motiviert. Das Kapitel 2 stellt das NV Zentrum im Diamant vor und beschreibt dessen Eigenschaften. Außerdem wird der experimentelle Aufbau im Detail erklärt. Kapitel 3 stellt zwei Ansätze vor, mit denen eine Manipulation von einzelnen Elektronenspins bis zu einer Frequenz von 90 GHz möglich ist. Beide Methoden werden anhand der Effizienz, die verfügbare Mikrowellenleistung in Rabi Oszillationen umzuwandeln, ausgewertet. In Kapitel 4 werden die Relaxationsprozesse des ^{14}N Spins erforscht und analysiert. Insbesondere wird die Magnetfeld Skalierung der zugehörigen T_1^{mem} Zeit bis zu einem Feld von 3 T gemessen. Kapitel 5 behandelt die NMR Spektroskopie auf der Nanoskala. Dies beinhaltet eine Übersicht anderer NV basierter NMR Studien. Das Kapitel regt zudem die Notwendigkeit der verbesserten spektralen Auflösung an. Weiterhin wird die Quanten Metrologie Sequenz vorgestellt, die auf verschränkte Zustände zwischen dem Sensor und dem Speicher Spin basiert. Das Hauptresultat ist die NMR Detektion von Proben auf Nanoskala in Kombination mit der Detektion der entsprechenden chemischen Verschiebung. Zum Ende des Kapitels wird die Methode mit anderen Ansätzen verglichen. Das finale Kapitel 6 zeigt die Ergebnisse der STORM Mikroskopie von NV Zentren im Diamant. Außerdem wird STORM mit ODMR kombiniert und die Sensitivität der Magnetfeld Messung, mit hoher räumlicher Auflösung, besprochen.

List of publications

1. *Multi-spin-assisted optical pumping of bulk 13C nuclear spin polarization in diamond*, D. Pagliero, K. R. K. Rao, P. R. Zangara, S. Dhomkar, H. H. Wong, A. Abril, N. Aslam, A. Parker, J. King, C. E. Avalos, A. Ajoy, J. Wrachtrup, A. Pines and C. A. Meriles, Phys. Rev. B 97, 024422 (2018).

2. *Nonvolatile nuclear spin memory enables sensor-unlimited nanoscale spectroscopy of small spin clusters*, M. Pfender, N. Aslam, H. Sumiya, S. Onoda, P. Neumann, J. Isoya, C. A. Meriles and J. Wrachtrup, Nature Communications 8, 834 (2017).

3. *Protecting a Diamond Quantum Memory by Charge State Control*, M. Pfender, N. Aslam, P. Simon, D. Antonov, G.O. Thiering, S. Burk, F. Favaro De Oliveira, A. Denisenko, H. Fedder, J. Meijer, J.A. Garrido, A. Gali, T. Teraji, J. Isoya, M.W. Doherty, A. Alkauskas, A. Gallo, A. Grüneis, P. Neumann and J. Wrachtrup, Nano Letters 17(10), 5931-5937 (2017).

4. *Nanoscale nuclear magnetic resonance with chemical resolution*, N. Aslam, M. Pfender, P. Neumann, R. Reuter, A. Zappe, F. Favaro de Oliveira, A. Denisenko, H. Sumiya, S. Onoda, J. Isoya and J. Wrachtrup, Science 357, 67 (2017).

5. *Proposal of room-temperature diamond maser*, L. Jin, M. Pfender, N. Aslam, P. Neumann, S. Yang, J. Wrachtrup, and R.-B. Liu, Nature Communications 6, 8251 (2015).

6. *Single Spin Optically Detected Magnetic Resonance with E-Band Microwave Resonators*, N. Aslam, M. Pfender, R. Stoehr, P. Neumann, M. Scheffler, H. Sumiya, H. Abe, S. Onoda, T. Ohshima, J. Isoya, and J. Wrachtrup, Review of Scientific Instruments 86, 064704 (2015).

7. *Addressing Single Nitrogen-Vacancy Centers in Diamond with Transparent in-Plane Gate Structures*, M. V. Hauf, P. Simon, N. Aslam, M. Pfender, P. Neumann, S. Pezzagna, J. Meijer, J. Wrachtrup, M. Stutzmann, F. Reinhard, and J. A. Garrido, Nano Letters

14, 2359-2364 (2014).

8. *Single spin stochastic optical reconstruction microscopy*, M. Pfender*, N. Aslam*, G. Waldherr, P. Neumann, and J. Wrachtrup, Proceedings of the National Academy of Sciences 111, 14669 (2014). *equally contributed

9. *Photo induced ionization dynamics of the nitrogen vacancy defect in diamond investigated by single shot charge state detection*, N. Aslam, G. Waldherr, P. Neumann, F. Jelezko, and J. Wrachtrup, New Journal of Physics 15, 013064 (2013).

1. Nuclear magnetic resonance spectroscopy

Atoms are consisting of electrons and nuclei which are bound together by electrostatic coupling. Furthermore multiple atoms can be connected to each other by chemical bonds and form a molecule. Understanding the exact molecular structure is important for various fields like medicine, chemistry or biology. Here the spin of the nucleus provides a possibility to non-invasively probe the chemical composition. This is enabled by its coupling to magnetic fields generated externally and within the molecule. The field of research is called nuclear magnetic resonance (NMR) and is the main focus of this work.

In the first section 1.1 the reader is introduced to the basic principles of NMR. The next section 1.2 explains the concept of relaxation and how it can affect the NMR measurements. The experimental apparatus of conventional NMR spectroscopy is described in section 1.3. Moreover the section includes an overview of the possible spin couplings within a molecule and how they influence the measurement outcome. The limitations of conventional NMR spectroscopy are described in section 1.4. Finally novel techniques of pursuing NMR detection with a higher sensitivity are presented in 1.5.

1.1. Principles of NMR

Relativistic quantum mechanics derives a particle's property called: the spin. It is the intrinsic angular momentum of the particle. The spin vector is quantized along the z-direction (according to the conventions). It also has a quantized magnitude which is described by the nuclear spin quantum number I. Accordingly there is a nuclear spin angular momentum operator $\underline{I}$. In order to completely describe the state of a nuclear spin, two observables need to be measured: The square of the angular momentum I^2 and the projection of the operator I along the z-direction I_z. The eigenvalues of I^2 are [I(I+1)]. The square root of the eigenvalue yields the quantized magnitude of the spin: $\sqrt{[I(I+1)]}$. On the other hand the eigenvalues of I_z are the nuclear magnetic quantum number m_i: m_i = I, I-1, ..., -I with (2I+1) possible values.

Not every nuclei exhibits a spin. While a single proton and a single neutron each have

nuclear spin	I	γ [MHz/T]	natural abundance
^{1}H	1/2	42.576	99.985 %
^{19}F	1/2	40.078	100 %
^{13}C	1/2	10.71	1.1 %
^{2}H	1	6.536	0.015 %
^{15}N	1/2	-4.314	0.37 %
^{14}N	1	3.08	99.63 %

Table 1.1.: The gyromagnetic ratio γ, the nuclear spin quantum number I and the natural abundance of exemplary nuclear spin species.

a spin of $\frac{1}{2}$, the net spin of the nuclei will depend on the number of protons and neutrons within the nuclei. An even number of protons and neutrons leads to no net spin in total. Consequently either the number of protons or the number of neutrons or both need to be odd in order to have a nuclear spin. In addition to this an odd mass number A (sum of number of protons and of neutrons) leads to a half integer spin while for an even A the spin is an integer. Isotopes of a chemical element have a different number of neutrons and can therefore possess a differing spin. E.g. ^{14}N has a spin of I = 1, while ^{15}N has a spin of I = $\frac{1}{2}$.

Each spin is associated with a magnetic moment which makes it susceptible to magnetic fields. The magnetic moment operator $\underline{\mu}$ and the corresponding nuclear spin angular momentum operator $\underline{I}$ are related to each other:

$$\underline{\mu} = \gamma \cdot \underline{I} \tag{1.1}$$

with γ as the gyromagnetic ratio of the nuclear spin. The gyromagnetic ratio differs from nuclei to nuclei. Some examples can be found in table 1.1.

The magnetic moment of a nuclear spin interacts with magnetic fields, which results in the nuclear Zeeman shift. Its corresponding Hamiltonian is:

$$H_{Zeeman} = -\underline{\mu} \cdot \underline{B_0} \tag{1.2}$$

with the applied magnetic field B_0. The quantization axis of the nuclear spins is typically defined by the applied magnetic field B_0 which points along the z-direction.

$$H_{Zeeman} = -\gamma \cdot I_z \cdot B_0. \tag{1.3}$$

Taking the nuclear magnetic quantum number m_i into account leads to (2 I + 1) possible energy levels in the presence of a magnetic field B_0. The $m_i = 0$ state is not sensitive to an applied magnetic field and will therefore not shift with B_0. The energy differences

between different m_i levels depend on the gyromagnetic ratio γ of the nuclear spin. A nuclear spin with $I \geq 1$ shows a splitting even in the absence of a magnetic field due to the quadrupole splitting. However for the presented study only nuclear spin species with $I = \frac{1}{2}$ are of interest.

The magnetic moment $\langle \underline{\mu} \rangle$ is the expectation value of the magnetic moment operator $\underline{\mu}$. An applied magnetic field B_0 causes a precession of the nuclear spins magnetic moment $\langle \underline{\mu} \rangle$ with the larmor frequency ω_L:

$$\omega_L = -\gamma \cdot B_0. \tag{1.4}$$

The magnetic moment $\langle \underline{\mu} \rangle$ rotates around $\underline{B_0}$ on a cone with an opening angle. This angle depends on the intial angle between $\underline{\mu}$ and $\underline{B_0}$.

Nuclear magnetic resonance (NMR) is based upon the ability to create a resonance between different Zeeman sublevels. This can be achieved by the application of an oscillating magnetic field $B_1(t)$. These microwaves (MW) are linearly polarized and are weak regarding their field strength. Hence it is sufficient to only consider the x-component (transverse to B_0) of $B_1(t)$. This leads to the time-dependent Hamiltonian:

$$H_1 = -\gamma \cdot B_{1x} \cdot cos(\omega t) \cdot I_x. \tag{1.5}$$

The selection rules only allow transitions with $\Delta m_i = \pm 1$. Consequently the energy difference between two Zeeman sublevels is:

$$\Delta E = \gamma \cdot B_0. \tag{1.6}$$

This matches the absolute value of the Larmor frequency ω_L. Therefore resonance can occur when the frequency of $B_1(t)$ is equal to ω_L.

The magnetic moment operator $\underline{\mu}$ of the spin does not only interact with external magnetic fields but also with the magnetic field created by neighboring spins. Each nuclear spin creates a dipole field $B_{dipole}(\underline{r})$:

$$B_{dipole}(\underline{r}) = \frac{\mu_0}{4\pi}\gamma \frac{3\ \underline{e}_r(\underline{I}\ \underline{e}_r) - \underline{I}\ \underline{e}_r^2}{r^3} \tag{1.7}$$

with the magnetic moment μ_0 and the unit vector $\underline{e}_r$ of the spins relative position $\underline{r}$. If e.g. a second nuclear spin is in the vicinity it can interact with $B_{dipole}(\underline{r})$ of the first nuclear spin. This interaction will result in the dipole-dipole Hamiltonian:

$$H_{dd} = -\frac{\mu_0}{4\pi}\gamma_1\gamma_2 \frac{3\ (\underline{I}_1\ \underline{e}_r)(\underline{e}_r\ \underline{I}_2) - \underline{I}_1\ \underline{I}_2}{r^3} \tag{1.8}$$

with the gyromagnetic ratios $\gamma_{1,2}$ of the nuclear spins $I_{1,2}$. Furthermore the vector $\underline{r}$ is connecting the nuclear spins. The dipole-dipole Hamiltonian has a homogeneous and an

inhomogeneous part. The inhomogeneous part leads to an additional splitting of the levels on the order of the dipole interaction. On the other hand the homogeneous part results in spin flip-flop processes between spins which lead to a broadening of lines. Typically in a sample many nuclear spins are interacting with each other via their dipole field. Each nuclear spin has a random orientation and therefore the generated dipole field will be inhomogeneously spread over the sample. Consequently the resonance of the nuclear spins is up- and down-shifted from the bare Larmor frequency. In a NMR measurement of an ensemble of nuclear spins this will lead to the observation of dipolar broadened lines. For samples with a higher spin density the obtained spectral linewidth will be broader than for a lower spin density. The dipolar broadened NMR spectrum can therefore be analyzed to extract information about the involved nuclear spins and their composition.

The discussed dipole-dipole coupling also causes an effect called spin diffusion. It involves spin flip-flop processes between neighboring spins which can propagate over the whole sample. Spin diffusion constants can be measured and contain information e.g. about the spin-spin distances. E.g. in polymers spin diffusion lengths of 1 $\mathrm{nm^2ms^{-1}}$ have been measured [48].

In liquid samples the nuclear spins experience translational and rotational diffusion relative to each other. Depending on the viscosity of the liquid these diffusion processes occur slower or faster. The diffusion leads to an effect of averaging out the dipolar coupling. This is called motional narrowing. Liquid state NMR therefore yields narrower spectral lines than in the case of solid state samples.

It is important to understand the time-dependent behavior of $\langle \underline{\mu} \rangle$. Therefore the Bloch equation is derived from a semi-classical model:

$$\frac{d\langle \underline{\mu} \rangle}{dt} = \gamma \left(\langle \underline{\mu} \rangle \ \times \ \underline{B} \right). \tag{1.9}$$

The discussion is limited to a spin system with two states but can be extended to more levels. In equation 1.9 the previously discussed oscillating magnetic field 1.5 can be added. Furthermore it is assumed that $\underline{B}$ points into the z-direction. This leads to the three spatial components:

$$\frac{d\langle \underline{\mu} \rangle_x}{dt} = \gamma \left(\langle \underline{\mu} \rangle_y \ B_0 - \langle \underline{\mu} \rangle_z \ B_1 \sin \omega t \right) \tag{1.10}$$

$$\frac{d\langle \underline{\mu} \rangle_y}{dt} = \gamma \left(\langle \underline{\mu} \rangle_z \ B_1 \cos \omega t - \langle \underline{\mu} \rangle_x \ B_0 \right) \tag{1.11}$$

$$\frac{d\langle \underline{\mu} \rangle_z}{dt} = \gamma \left(\langle \underline{\mu} \rangle_x \ B_1 \sin \omega t - \langle \underline{\mu} \rangle_y \ B_1 \cos \omega t \right) \tag{1.12}$$

For a better visualization of the spin dynamics these equations are usually transformed into the rotating frame. This means that the reference frame rotates around the z-direction

with a frequency ω. In this case the oscillating magnetic field becomes static and the Bloch equation changes to:

$$\frac{\partial\langle\underline{\mu}\rangle}{\partial t} = \langle\underline{\mu}\rangle \times [(\omega + \gamma B_0)\underline{e}_z + \gamma B_1 \underline{e}_x]. \tag{1.13}$$

The dynamics of $\langle\underline{\mu}\rangle$ can be visualized by the Bloch sphere. The magnetic moment can e.g. point exactly into the direction of B_0 or into the opposite direction. These two orientations correspond to the two eigenstates of I_z: $|\uparrow\rangle$ and $|\downarrow\rangle$. The radius of the Bloch sphere is the magnitude of $\langle\underline{\mu}\rangle$. Superposition states between $|\uparrow\rangle$ and $|\downarrow\rangle$ can be populated as well. These states can be described by the two angles θ and ϕ. While θ is the angle between $\langle\underline{\mu}\rangle$ and the z-direction, ϕ is the angle from the x-axis in the xy plane.

In the case of resonant MW application, a magnetic moment $\langle\underline{\mu}\rangle$ starting in the $|\uparrow\rangle$ state rotates around the x-axis. At some point it reaches the xy-plane. The corresponding pulse is named a $\pi/2$ pulse (because of $\theta = \pi/2$). A longer pulse can switch the state to the $|\downarrow\rangle$ state. Here the pulse is called a π pulse. In fact, in a measurement the pulse length can be varied and the corresponding result can be measured. Continuous driving leads to oscillations between the $|\uparrow\rangle$ and $|\downarrow\rangle$ states, which are called Rabi oscillations.

1.2. Relaxation

NMR experiments are based on the detection of an ensemble of polarized nuclear spins. The sum of the magnetic moment operators of all nuclear spins forms the total magnetic moment operator. Its expectation value is called magnetization $\underline{M}$ and it can be treated analogous to a single spin. In the presence of a magnetic field B_0 the nuclear spins will tend to align their orientation along B_0 to reach the minimum of energy. However the thermal energy counteracts this effect, especially at room-temperature. The thermal energy is expressed by:

$$E_{thermal} = k_B T \tag{1.14}$$

with the Boltzmann constant k_B and temperature T in K. Typically the Zeeman energy is much smaller than the thermal energy resulting in a small number of polarized spins. The ratio of spins in the $|\uparrow\rangle$ ($N_{|\uparrow\rangle}$) and $|\downarrow\rangle$ ($N_{|\downarrow\rangle}$) states is described by:

$$\frac{N_{|\uparrow\rangle}}{N_{|\downarrow\rangle}} = e^{-\frac{\gamma B_0}{k_B T}}. \tag{1.15}$$

For a magnetic field of 3 T at room-temperature the ratio yields a value of ≈ 1 - 10^{-5}. Hence a large number of nuclear spins is required to produce a detectable signal.

In the previous section 1.1 the dynamics of the magnetic moment $\langle\underline{\mu}\rangle$ was discussed with the help of Bloch equations. What has been ignored so far, but is observed experimentally

in NMR experiments, are relaxation effects. For this purpose two relaxation times T_1 and T_2 can be introduced into the Bloch equation 1.9:

$$\frac{d\langle\underline{\mu}\rangle_x}{dt} = \gamma\left(\langle\underline{\mu}\rangle \times \underline{B}\right)_x - \frac{\langle\underline{\mu}\rangle_x}{T_2} \tag{1.16}$$

$$\frac{d\langle\underline{\mu}\rangle_y}{dt} = \gamma\left(\langle\underline{\mu}\rangle \times \underline{B}\right)_y - \frac{\langle\underline{\mu}\rangle_y}{T_2} \tag{1.17}$$

$$\frac{d\langle\underline{\mu}\rangle_z}{dt} = \gamma\left(\langle\underline{\mu}\rangle \times \underline{B}\right)_z - \frac{\langle\underline{\mu}\rangle_0 - \langle\underline{\mu}\rangle_z}{T_1} \tag{1.18}$$

with $\langle\underline{\mu}\rangle_0$ being the value of $\langle\underline{\mu}\rangle_z$ which is reached after the T_1 time.

Introducing the T_1 and T_2 times has the purpose to distinguish between longitudinal and transversal relaxation. By longitudinal relaxation the decay of the z-component of the magnetic moment is meant. After MW application the state of the magnetic moment can be brought away from the thermal equilibrium. The system however will decay back into the thermal equilibrium by energy exchange with the environment. This happens exponentially with the characteristic decay time of T_1. It can be measured by preparing the spin in the $|\downarrow\rangle$ state and probe its decay in time.

Transversal relaxation on the other hand is the exponential decay of the x- and y-components of $\langle\underline{\mu}\rangle$ and its timescale is described by the T_2 time in the Bloch equations 1.16 and 1.17. Measuring the T_2 time is possible by creating a superposition state between $|\downarrow\rangle$ state and the $|\uparrow\rangle$ state: $\frac{1}{\sqrt{2}}$ $(|\downarrow\rangle + |\uparrow\rangle)$. Hence the magnetization $\underline{M}$ along the z component is transferred into a magnetization along the transversal direction $\underline{M}_{xy}$. This is called coherence and the process of $\underline{M}_{xy}$ decay is named decoherence. The interaction between spins leads to different resonance frequencies of the nuclear spins. As a result the precession of the magnetic moment in the xy plane occurs fast for some nuclear spins and slower for others. Because of this, after some time the nuclear spins precession will not be synchronized to each other and the coherence will be lost. This causes a homogeneous broadening in the NMR spectrum.

There is a second effect called inhomogeneous broadening which leads to decoherence. The single nuclear spins all decay with the T_2 time but with slightly different frequency. The measurement is however performed on a large number of nuclear spins. Consequently the differing frequencies will cause a destructive interference which leads to the T_2^* time.

The T_2^* time can be measured by the so called free induction decay (FID) or Ramsey measurement. It begins with the initialization into one of the eigenstates. Afterwards a $\pi/2$ pulse brings the magnetization into the xy plane. After a varied evolution time τ a second $\pi/2$ pulse maps the state back to the eigenstate and is finally measured. The resulting signal can oscillate due to the presence of nearby nuclear spins and decays with the T_2^* time.

It is possible to counteract the destructive interference effect with nuclear spins by applying a π pulse in the center of the evolution time. This refocuses the evolution of the spins and leads to a decay time of T_2. The corresponding measurement is called Hahn echo measurement [49]. Depending on the spin environment it can be necessary to apply more π pulses within the evolution time. Many different sequences called dynamical decoupling have therefore been introduced which further increase the T_2 time [17, 18, 19, 20]. However the ultimate limit is set by the T_1 time.

In principle the discussed spin properties and measurement sequences can be applied to electron spins as well.

1.3. Conventional NMR spectroscopy

Conventionally NMR detection is performed by Faraday pick-up coils analogue to the experiment by Felix Bloch [1]. In a NMR spectroscopy experiment a sample typically with $(\mathrm{mm})^3$ of volume is placed in a magnetic field in order to achieve thermal polarization. The magnetization $\underline{M}$ of the nuclear spins precesses around the direction of the magnetic field B_0. $\underline{M}$ and B_0 are however oriented parallel to each other. Despite the rotation, $\underline{M}$ appears stationary. Therefore no voltage can be induced in a pick-up coil. The solution is to create a transverse magnetization by applying a $\pi/2$ pulse on the nuclear spins. The resonant pulse can be generated by the coil itself. Precession of the transversal magnetization generates an oscillating magnetic field. This induces an oscillating voltage signal within the pick-up coil which can be detected. The signal decays with the T_2^* time. The oscillating signal is fast Fourier transformed (FFT) which yields the desired NMR spectrum. The width of the observed peaks is $1/(\pi T_2^*)$. For liquid state NMR the T_2^* times can be on the order of seconds. Hence the corresponding linewidths are sub-Hz.

However the more prominent technique based on NMR is magnetic resonance imaging (MRI). MRI is used in medicine e.g. to image human bodies. Compared to NMR spectroscopy MRI is an imaging method which applies gradient magnetic fields. The magnetic field locally encodes information which can be read out voxel (the smallest detectable volume) by voxel. E.g. the spin density can be different over the sample. In addition to this it is possible to weigh the detection with T_1, T_2 and T_2^* measurements. In this study however the focus will be on NMR spectroscopy.

The goal of NMR spectroscopy is to non-invasively extract information about the chemical composition of the sample. This is done by achieving a high spectral resolution in the corresponding NMR spectrum. Each nuclear spin species exhibits a different gyromagnetic ratio (see table 1.1). The first obtainable information in a NMR spectrum is therefore about the nuclear spin species. Furthermore solid state NMR exhibits a broad

linewidth due to the stationary dipole-dipole coupling between the nuclear spins. Hence the linewidth contains information about the spin-spin interaction. Moreover, spin diffusion can be examined which yields information about the distance between the spins. Liquid state NMR on the other hand shows smaller linewidths due to motional averaging. Consequently it is easy to differentiate between a solid and a liquid sample. This can be interesting when investigating bulk to surface interfaces [50].

NMR spectroscopy is capable of more sophisticated analysis of the chemical structure of the sample. The resonance frequencies of the nuclear spins within the molecules are additionally shifted by the local chemical environment. The most significant effects are: chemical shift, quadrupole coupling, direct dipole-dipole coupling and J-coupling.

The chemical shift effect is the indirect coupling of the nuclear spins with the magnetic field generated by the electrons. First a current is induced within the cloud of valence and the bonding electrons by the external magnetic field. This current flow then generates an additional magnetic field itself. This field usually shields the external magnetic field resulting in a reduction of the nuclear spins resonance frequency. But it can also lead to an increase of the resonance frequency. Since the electron density in a molecule is inhomogeneously distributed each nuclear spin can have a different chemical shift. The detection of these chemical shifts therefore yields information about the chemical structure of the molecule. E.g. the ^{13}C spins in ethanol (CH_3CH_2OH) exhibit two different chemical shifts (see figure 1.2). Furthermore the chemical shift is (in good approximation) linearly dependent on the applied magnetic field.

The description by quantum-mechanics of the electrons yields two parts which play a role in inducing the current flow [3]. The first is the diamagnetic term which refers to circulating electrons in the electronic ground state induced by the external field. The second term refers to circulating electrons in the excited state and is called paramagnetic. Both have similar absolute values but differ in their sign. Therefore it is difficult to quantitatively predict and understand the observed chemical shift [3]. The chemical shift further depends on the angle between the orientation of the molecule and the applied magnetic field [3]. It mostly occurs within a molecule, but it can also have a small effect due to intermolecular interactions e.g. in different solvents. Additionally there might be a deviation between the liquid and solid form of molecules.

The magnetic field of the used NMR spectrometer can be quite different. Therefore it makes sense to define the chemical shift value field-independent:

$$\delta = \frac{\omega - \omega_{\mathrm{ref}}}{\omega_{\mathrm{ref}}} \tag{1.19}$$

with the Larmor frequency ω of the nuclear spins in the sample and of a reference compound ω_{ref}. The chemical shift δ is a field-independent parameter and is typically given

in parts per million (ppm $\equiv 10^{-6}$). The chemical shift of the reference compound is set to zero. Tetramethylsilane (TMS) is often used as the reference molecule for ^{1}H, ^{13}C and ^{29}Si NMR. The advantages of using TMS are its weak chemical reactivity and its from other molecules detuned resonance frequency. A small fraction of TMS within the sample is sufficient to get a reference signal and to scale the chemical shift axis accordingly.

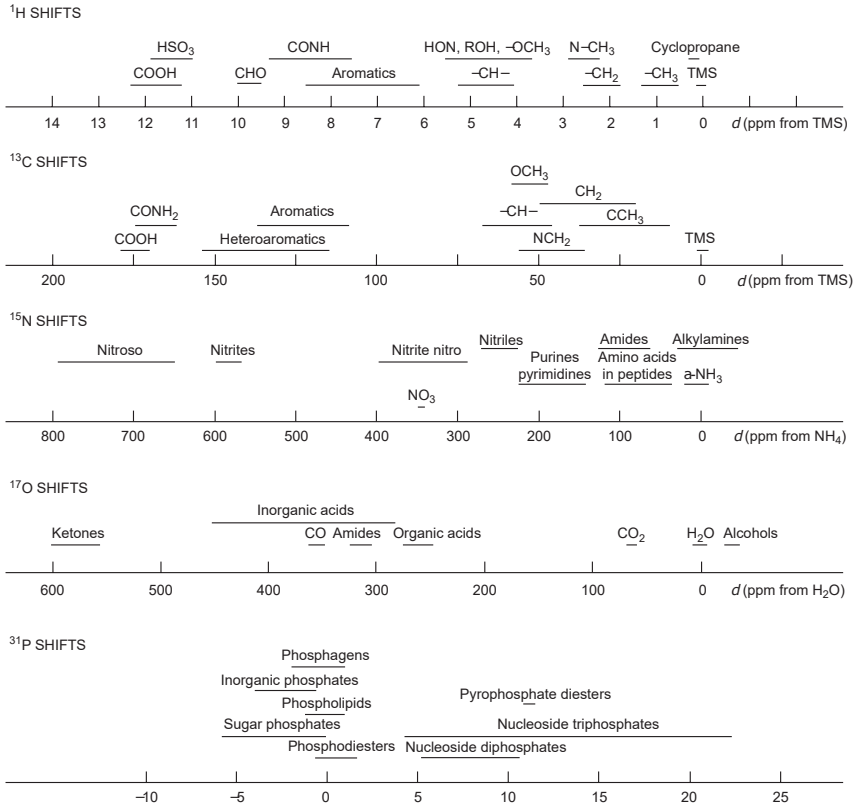

Figure 1.1.: Chemical shift ranges in organic molecules. The range of ^{1}H, ^{13}C , ^{15}N , ^{17}O and ^{31}P chemical shifts in organic molecules is given. The graphic is taken from [3] and the data is from [51].

The chemical shift strength varies between different nuclear spin species and different molecular sub-groups (see figure 1.1). The chemical shift range for the nuclear spin species are (ordered downwards): ^{15}N with $\approx$ 800 ppm, ^{17}O with $\approx$ 600 ppm, ^{13}C with $\approx$ 175 ppm, ^{31}P with $\approx$ 27 ppm and ^{1}H with $\approx$ 13 ppm. These different chemical shift values can be explained i.a. by the following relations. Generally speaking the higher the electron density is, the better the external magnetic field is shielded. Consequently the electro-negativity of the atom plays an important role. Atoms with a higher electro-negativity decrease the electron density at the position of the neighboring nuclear spin. This leads to a smaller shielding effect. Furthermore low-lying excited states increase the chemical shift effect. Atoms with a larger atomic mass usually have more low-lying excited states and

therefore tend to show larger ranges of chemical shift. E.g. ^{209}Pb can have a chemical shift of up to thousand ppm. It is difficult to precisely calculate the chemical shift of nuclear spins within a molecule. However there exist rules for specific molecule groups such as Shoolery's rule for methylene groups which can be used to estimate the chemical shift [3].

The quadrupole coupling occurs only for nuclear spins with $I \geq 1$ and leads to a splitting of levels even without any magnetic field. It is the coupling between the electric quadrupole moment of the nuclear spin and the electric field gradient (EFG) at its position. The latter depends on the symmetry of electron distribution and is large for a highly antisymmetric distribution as can be the case e.g. in covalent bonds. Analogue to NMR, nuclear quadrupole resonance spectroscopy (NQR) can be performed which yields information about the EFG and consequently about the electron density distribution within the molecule. In a liquid the quadrupole coupling averages out due to the traceless tensor of the electric field gradient. However it still has an effect on the relaxation of the corresponding nuclear spin.

Direct dipole-dipole couplings are as the name suggests direct interactions between the nuclear spins. The equation describing the interaction has been introduced (see equation 1.8). This term can average out for nuclear spins in liquids due to motional averaging but is relevant for nuclear spins in solids.

J-coupling on the other hand are indirect magnetic interactions between nuclear spins mediated through bonding electrons. A nuclear spin interacts via hyperfine coupling with the electrons of the chemical bond. This affects other nuclear spins which are connected to the bonds as well and leads to a splitting of their energy levels. The effect can occur for nuclear spins connected via a single bond but also on a long range with multiple bonds involved. The magnitude of the J-coupling however typically decreases with the number of involved bonds. J-coupling only occurs intramolecular. Besides the distance the shift also depends on the bond and the torsional angle. Usually it is valid to say that for larger bond angles the magnitude of the J-coupling is larger. The sign of the J-coupling can vary as well. For a connection via a single bond the J-coupling is positive for nuclear spins with the same sign of gyromagnetic ratio γ and negative for the opposite case. If more than one chemical bond are involved then the sign will depend on the angle and other parameters as well. The number of involved chemical bonds creating the J-coupling is given as a superscript, e.g. in ^{1}J.

The observation of J-coupling not only includes a simple shift in frequency but also the occurrence of multiplets. For each nuclear spin the lines will split according to the number of neighboring nonequivalent nuclear spins. For example in ethanol (CH_3CH_2OH) the ^{13}C spin of the CH_2 group will interact via J-coupling with the two ^{1}H spins in the

same group. The interaction between the ^{13}C spin and one of the ^{1}H spins first results in a splitting upwards and downwards. The shift in both directions is half of the J-coupling magnitude. These two lines then again split because of the interaction of the ^{13}C spin with the second ^{1}H spin (see figure 1.2). Because of the same shift in frequency the inner line will have double the intensity. The three peaks form a triplet and their ratio in intensities is 1:2:1. For a number n of interacting nuclear spins with $I = \frac{1}{2}$ the number of observable peaks will be (n + 1). Accordingly the interaction between the ^{13}C spin and the three ^{1}H spins of the CH_3 group leads to four peaks (quartet). In this case the ratio of the peak intensity is 1:3:3:1.

The values of J-coupling are independent of the magnetic field. In the case of ethanol the value for coupling between the ^{13}C and the ^{1}H spins in the CH_2 group is $^{1}J_{CH}$ = 140.4 Hz. And for coupling between the ^{13}C and the ^{1}H spins in the CH_3 group is $^{1}J_{CH}$ = 124.9 Hz. The longer range interaction between the ^{13}C spin of the CH_2 group and the three ^{1}H spins of the CH_3 is $^{2}J_{CH}$ = - 4.6 Hz. Typically values for the J-coupling are: $^{1}J_{CH} \approx 135$ Hz, $^{1}J_{CC} \approx 50$ Hz and $^{3}J_{HH} \approx 7$ Hz. In contrast to the direct dipole-dipole coupling, the J-coupling does not average out in liquid state NMR. It represents a spectral fingerprint for obtaining information about the chemical bond of the molecule: its angle and distances. Liquid state NMR spectroscopy becomes very powerful when J-coupling and chemical shifts are both detected and in consequence allows the reconstruction of the whole chemical structure of the sample molecule. Typically this is possible because of the high spectral resolution of NMR spectrometers reaching sub Hz.

1.4. Limitations

The NMR technique has gone through enormous developments since its invention. While many properties could be further improved e.g. the spectral resolution, scientists have failed to significantly improve the spatial resolution of the inductive based NMR (in the last decades). It would e.g. be very interesting to achieve the NMR detection of a single molecule or of a single nuclear spin, as this would allow new insights into various fields of research. The effective molecular radius of glucose is 0.33 nm [52]. However conventional NMR requires a large number of molecules within a sample in order to detect the NMR signal. Conventional NMR spectroscopy typically uses sample volumes of $(mm)^3$.

The reasons for the poor sensitivity are many fold. First of all the coils are large compared to the aimed molecular scale. Consequently a smaller sample comes with a larger distance to the coil. On the other hand an oscillating magnetic field produced by the nuclear spins decreases with r^{-3} (distance r). Miniaturizing the coils is a solution but has its limitations. For sub-mm coil diameters the self-resistance of the Faraday

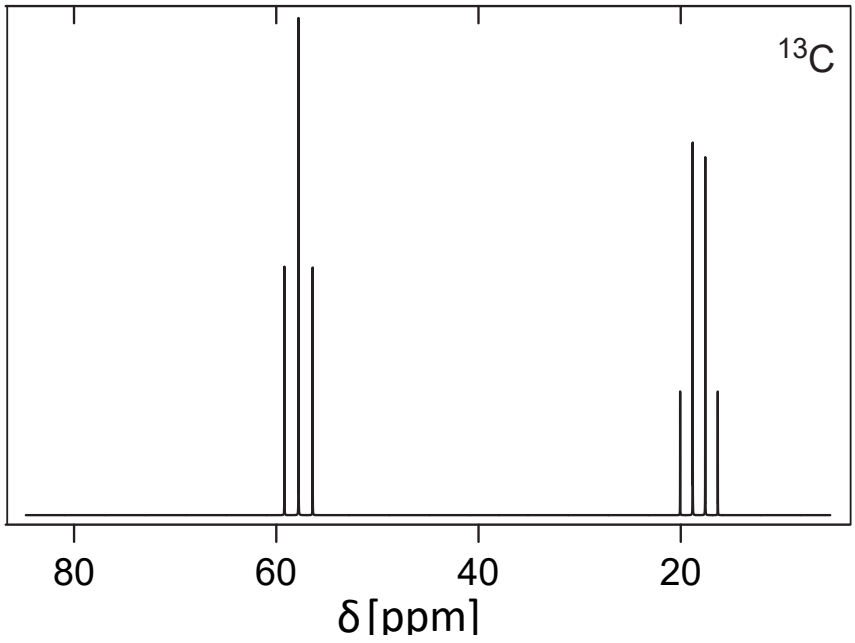

Figure 1.2.: ^{13}C NMR spectrum of ethanol at a magnetic field of 4.7 T. The graph is from [3].

coils becomes larger than the signal itself [53]. Using superconducting material would be a solution but it prevents room-temperature (RT) operation. The sample and the superconducting coil can be isolated from each other but this would significantly increase the distance between them. So far the best achieved resolution with miniaturized coils is $(3\ \mu\text{m})^3$ [4, 5].

It has been pointed out that NMR detection relies on the thermal polarization. Hence the polarization degree of 10^{-5} (B = 3 T and RT) sets a limit to the minimum number of nuclear spins within a sample. On the other hand the statistical polarization is the variance of the longitudinal magnetization which becomes relevant for a smaller number of nuclear spins. At some critical point the statistical polarization can dominate over the thermal polarization. Consequently it becomes very difficult to detect the signal based on thermally polarized spins. Higher magnetic field strengths or lower temperatures increase the thermal polarization. The currently most powerful superconducting magnet can create a field of 32 T [54]. The low temperature operation on the other hand has the disadvantage that it alters the properties of the sample.

1.5. Novel techniques in NMR

There are two approaches of increasing the sensitivity in NMR. The first approach is to increase the signal coming from the nuclear spins by hyperpolarizing them. The second

approach is to use a completely different sensor system apart from the detection based on a pick-up coil.

Hyperpolarization methods allow to extend the signal strength beyond the thermal polarization. Consequently low or zero field NMR spectroscopy becomes possible. Several methods are used nowadays: Dynamic nuclear polarization (DNP) [7], spin-exchange optical pumping (SEOP) [55] and parahydrogen-induced polarization (PHIP) [56, 57]. The most prominent method is DNP. DNP means the transfer of polarization from a spin species with a higher gyromagnetic ratio γ to spins with a smaller γ [7]. Typically the polarization transfer occurs from electron to nuclear spins. Because of the larger γ the electron spins thermal polarization is e.g. 660 times larger than that of ^{1}H spins. In addition to this there are methods to further increase the degree of polarization of electron spins e.g. by chemical reactions [58], spin injection [59] or optical pumping [60]. The polarization can be transferred by spontaneous cross relaxation via the hyperfine interaction [61, 62] or by mixing of electron and nuclear spin states.

SEOP is used to polarize nuclear spins in noble gases like ^{3}He or ^{129}Xe which enhances the imaging of human lungs [63]. Circularly polarized photons first interact with the electrons of alkali-metal atoms and thereby polarize their spins. Subsequently inter-atom collisions between alkali-metal electrons and the noble gases lead to transfer of polarization.

Molecular hydrogen can occur in ortho or para configuration. In orthohydrogen (o - H_2) the two proton spins are aligned parallel to each other. For parahydrogen (p - H_2) on the other hand they form an anti-parallel orientation. The ratio between the two so-called spin isomers increases dramatically in favor of parahydrogen when cooled below 30 K. The spin state of parahydrogen is the singlet state (I = 0) $\frac{1}{\sqrt{2}}$ ($|\uparrow\downarrow\rangle$ - $|\downarrow\uparrow\rangle$) which as such does not generate a NMR signal. However there are two ways of transferring this spin order of parahydrogen into measurable hyperpolarized nuclear spins. The first approach is to use parahydrogen in hydrogenation reactions which adds hyperpolarized nuclear spins to the target molecule [64]. The target molecule needs to be unsaturated before the reaction. The second way is called Signal Amplification by Reversible Excitation (SABRE) [65]. Here the spin order of parahydrogen is transferred indirectly by J-couplings of the molecule.

The introduced hyperpolarization methods are successfully used for specific samples but cannot be applied universally.

Novel magnetometers have emerged which show a high sensitivity. Among them three can be pointed out: atomic vapor cells (AVC) [8, 9], superconducting quantum interference devices (SQUID) [10, 11] and magnetic resonance force microscopy (MRFM) [66].

In the AVC technique a vapor of alkali atoms is trapped in a cell. In a first step the atoms inside the vapor are polarized. This is done with circularly polarized photons. Once

a magnetic field is applied the magnetic moments of the atoms begin to precess around it. As the next step linearly polarized photons can be applied to the alkali atoms for NMR detection. Here the readout parameter is the tilt angle of the photons polarization. It changes due to the precessing alkali atoms which is called Faraday rotation. The effect is proportional to the magnetic field. The reached sensitivities of AVCs are $\mathrm{aT}/\sqrt{\mathrm{Hz}}$. AVCs have been used in the context of measuring NMR signals [8, 9, 67]. However the typical size of AVCs of cm^3 hinders their application as a nm-scale sensor.

The DC SQUID is based on a superconducting loop which is divided by two Josephson junctions. The Josephson junction is a thin insulating barrier where electrons can tunnel through due to the Josephson effect. Once the incoming current exceeds the critical current of the junction, a measurable voltage occurs across the junction. In the DC SQUID version a DC current is applied constantly. Furthermore an external magnetic field B_0 applied through the loop induces a screening current in the loop which compensates B_0. Quantum interference restricts the magnetic flux Φ through the superconducting ring to be a multiple of the magnetic flux quantum: $\Phi_0 = \mathrm{h}/2\mathrm{e}$ with the Planck constant h and the elemental charge e. The induced current therefore adjusts the flux Φ to the next multiple of Φ_0. DC SQUID magnetometers have measured fields of aT strength [68] and a noise floor of $\mathrm{fT}/\sqrt{\mathrm{Hz}}$ [69]. Imaging with SQUID magnetometers have been performed with a spatial resolution of 120 nm [70]. The disadvantage of SQUID magnetometers is the requirement of low temperatures.

MRFM is a technique which combines the principles of atomic force microscopy (AFM) with MRI [12]. A ferromagnetic tip is used on a cantilever. Its displacement is measured by laser interferometry. The spins within the sample are experiencing the magnetic field of the tip and an additional static field B_0. The spins are manipulated by an oscillating magnetic field with RF frequency. When the magnetic tip is brought close to the spins a resonance can be generated by the RF frequencies which causes a force on the tip. Consequently the oscillation frequency of the cantilever is shifted which can be detected. It is important to reduce the Brownian motion of the tip as this leads to noise. This is achieved by operating the MRFM setup at cryogenic temperatures (sub-K) and under vacuum conditions. Due to the high sensitivity of the MRFM, detection volumes in the nm^3 scale are reached [13]. Furthermore MRI with nm resolution has been achieved [71] and even detection of single electron spins has been accomplished [66]. It is however not possible to implement this technique at ambient conditions which is necessary for application in biology.

None of the presented novel techniques allow the nanoscale detection of NMR signal at ambient conditions. Recently a defect in diamond called nitrogen-vacancy (NV) center has gained attention as a nanoscale sensor at ambient conditions. It shows a high sensitivity

while operating at ambient conditions. Its measurement apparatus is a combination of ESR/NMR techniques and confocal microscopy. In the next chapter the NV center in diamond and its properties will be discussed in detail.

2. Nitrogen vacancy center in diamond - the sensor spin

The nitrogen-vacancy center in diamond is exceptional in many ways. Its electron spin can be optically initialized and readout and shows long coherence times at ambient conditions. This has triggered many applications, e.g. in quantum information processing [72, 73, 74, 38], quantum communication [75, 76], quantum sensing [77, 78, 79, 80, 81] and as a room-temperature maser [82].

In this chapter the properties of the NV center in diamond and the experimental setup are described. Section 2.1 discusses the properties of the host material, diamond. Next the NV center is introduced and the different ways of creating NV centers in diamond are explained (see section 2.2). Afterwards the electronic and optical properties of NV centers are discussed in section 2.3. The spin properties are described in the following section 2.4. Moreover the different charge states and their interplay is discussed in section 2.5. The different components of the experimental setup are described in section 2.6. Furthermore the mechanism of spin readout (section 2.7) and spin relaxation (section 2.8) are explained. Finally the applications of the NV centers are discussed (section 2.9).

2.1. Diamond

Diamond is composed of carbon atoms that are covalently bonded in a lattice structure. Each atom is connected to four other carbon atoms and has a distance of 1.54 Å. The atomic orbitals of these carbon atoms are sp^3 hybridized. The angle between the four resulting orbitals is 109.5° which effectively forms a tetrahedron. This results in a zincblende structure with the difference that the diamond is consisting of solely one atom species (except the impurities). The structure can be described by two face centered cubic (fcc) structures shifted against each other by one fourth. The lattice constant is 3.57 Å. Consequently the density in diamond is 3.52 $\frac{g}{cm^2}$.

The strong covalent bonds lead to the unprecedented hardness of diamond. Therefore the Debye temperature is very high: 1860 K [83]. The hardness is 10 given in mohs and 140000 in rosiwal, which makes the diamond the hardest mineral known. This is why dia-

mond finds application in grinding and polishing. Another application of diamond is as a heat sink because of its high thermal conductivity. Furthermore diamond is an insulator and optically transparent in a wide range of wavelengths (visible). This comes from the fact, that saturation of the valence electrons, translates to a large bandgap of 5.48 eV. In addition to this diamond has a high refractive index of 2.42 (wavelength dependent) and a high dispersion. Impurities can be found in the diamond lattice, e.g. boron and nitrogen. Their concentration serves as an important parameter for the classification of diamonds.

The phase diagram of carbon shows the conditions for the creation of diamond. Diamonds naturally occur in the mantle of the earth where they find optimal conditions of high pressure and high temperature. Diamonds can for example be brought to the earth's surface by erupting volcanoes. They have also been found in meteorites. It is also possible to create diamonds synthetically. One possibility is by application of high pressure and high temperature (HPHT) and adding catalysts. And the second approach is chemical vapor deposition (CVD). The CVD process is homoepitaxial which means that a diamond is required as a seed layer. It works in a plasma chamber where temperature and pressure can be adjusted. Filling the chamber constantly with hydrogen and methane gas and radiating it with a high power MW field creates a plasma. Highly reactive hydrogen is created in the plasma which breaks the bonds at the diamond surface. The so generated dangling bonds of the carbon atoms can bind the carbon atoms of the methane. Thereby the diamond grows. Controlling the ratio between ^{13}C and ^{12}C is possible by the gas mixture which is introduced into the chamber. The orientation of the diamond's surface depends on the seed diamond. In this study HPHT and CVD diamonds of different orientations have been used. For some applications it is beneficial to create diamond particles with a size of less than 100 nm, the so-called nanodiamonds. The most prominent way of nanodiamond creation is by milling a diamond crystal.

Besides carbon, other atoms find their way into the diamond lattice as well. They can form defects, which can be optically addressed and a few of them possess a spin. The defect used in this work is the NV center in diamond which is introduced in the next section.

2.2. NV center and its creation

The NV center in diamond consists of a substitutional nitrogen atom and a vacancy next to it. Identification of this defect has been accomplished decades ago. A characteristic fluorescence emission spectrum has been measured with a wide vibronic band and a zero phonon line at 637 nm (1.945 eV) [84]. In addition to this it has been found out, that NV

centers have a trigonal symmetry. The electronic level structure with E and A_1 levels has been revealed. Through EPR studies it is furthermore known that NV centers have a spin triplet with a zero field splitting of 2.87 GHz. The NV center has singlet states (partly metastable) and a triplet ground and excited state [85]. The symmetry of the NV center is c_{3v}. The NV axis can be oriented along the four possible axes of the crystal lattice.

For the generation of NV centers, nitrogen impurities and vacancies are needed. Nitrogen impurities are quite abundant in nature. Therefore it is possible that they do enter into the diamond lattice naturally. Vacancies on the other hand are mobile at high temperatures and can move to the nitrogen impurities to form a stable NV center in diamond. NV centers can be artificially formed by different methods, which will be explained in the following.

For sensing applications it is important to generate NV centers close to the diamond surface. In general three approaches have been established for the creation of shallow NV centers: vacancy creation in doped diamond, nitrogen ion implantation and δ doping. The diamond sample can be doped with nitrogen impurities during growth [86]. The remaining substitute for the formation of NV centers are the vacancies. There can be created by irradiating the diamond with neutrons, electrons or He-ions [86, 87, 88]. Depending on the nitrogen concentration in the diamond and the dose of irradiation, the concentration of NV centers can be controlled. Ensembles of NV centers with concentrations reaching 16 ppm have been generated with this method [89]. On the other hand control over the depth is difficult since the vacancies are created along the beam path through the diamond. However the energy of the beam sets the upper limit in depth.

The second approach is the implantation of $^{15}N^+$ into the diamond lattice [90, 91]. This creates not only vacancies within the lattice but also places ^{15}N into the diamond, both being the ingredients of the NV center. The dose of the implanted nitrogen ions can be set according to the desired NV density. The depth of the NV centers is controlled by the implantation energy and can be simulated by SRIM [92]. An implantation energy of 7 keV translates to an average NV depth of 10 nm [91]. The nitrogen ions can create lattice damages which can have a deteriorating effect on the relaxation properties of the NV center [93, 94]. These lattice damages are less pronounced in the case of implanting with lighter particles as electrons.

When using the δ doping method the creation of shallow NV centers is incorporated in the CVD growth process. During the final stage of the growth process nitrogen gas is introduced into the CVD chamber, leading to the incorporation of nitrogen atoms into the diamond lattice [95]. Afterwards vacancies can be created with the methods described earlier. In all three cases annealing of the diamond is necessary. The annealing makes the vacancies mobile leading to two different, relevant scenarios. When a vacancy is trapped

by a substitutional nitrogen atom, they together form an NV center. However, when a vacancy first finds another vacancy, the resulting defect is a so called di-vacancy, which itself is stable and can exist in various charge states. Di-vacancies are mostly a source of noise and can be analyzed via EPR measurements [96]. During annealing these vacancy related defects can diffuse to the surface where they get trapped.

2.3. Electronic and optical properties

The NV center occurs in different charge states. The most prominent charge state of the NV center is the negatively charged state NV^-, which is discussed in this section. Whenever the NV center is mentioned throughout the thesis it refers to the negatively charged state. Other charge states and the dynamics between them are discussed in section 2.5.

The total number of electrons in the dangling bonds of the NV center is 6. Different theoretical models [97, 98, 99] along with group theory [100] have led to the electron configuration shown in figure 2.1 [101]. The lowest state is located in the valence band and has an a_1 symmetry. There is an upper state located in the bandgap with a_1 symmetry as well. On top two degenerate states with e symmetry (e_x and e_y) can be found. In the ground state both a_1 states are fully occupied. The two remaining electrons fill each of the two e states and build an antisymmetric orbital. They form an electron spin as a triplet S=1 system. The excited state can be populated by transferring one electron from the $a_1(2)$ state into one of the e states. The transition dipoles in both cases are perpendicular to the NV axis. Therefore laser excitation along the NV axis is optimum. The energy difference between the ground and the excited state is 1.945 eV [102].

There are three major contributions which govern the energy level scheme of the ground and the excited state. The first term is the spin-orbit coupling. In the ground state spin-orbit coupling does not apply. However in the excited state spin-orbit interaction is significant and leads to the occurrence of two additional levels: one up and one down-shifted level [103]. It has been shown that at room-temperature this spin-orbit coupling of the excited state is averaged out and it is sufficient to consider the remaining couplings [104]. The second contribution to the Hamiltonian is spin-spin interaction which is significant in both, the ground and the excited state. For the demonstrated application of the NV center as a sensor spin, this spin-spin term is crucial. It is composed of the zero-field splitting, coupling to other spins and the Zeeman term. Because of its significance it will be separately discussed in the next section 2.4. The third and last term is the interaction with strain or electric fields. It leads to an additional splitting. In ensemble of NV centers GHz broad optical linewidths have been observed [105]. The optical linewidth of a single NV in a bulk diamond is in the range of only MHz. Broadening comes from the fact that

the strain is locally different from NV to NV. By applying an electric field to a NV center, its optical linewidths can be tuned and brought into resonance with other NV centers [106].

At low-temperature (e.g. T = 4 K) the optical linewidth is narrower than the mentioned energy shifts. Therefore ground to excited state optical transitions can be induced selective to orbital and spin states [105]. Furthermore a lambda-type excitation is feasible by interaction of two ground state sub-levels with one excited state level [107, 108].

The distribution of the spin density plays an important role in understanding the spin properties of the NV center and has been simulated by theorists [109, 110]. According to these calculations the spin density in the ground state is mostly confined near the carbon atoms in the first shell. At the position of the nitrogen atom the spin density is negligible [111]. This changes for the excited state where a part of the spin is indeed located at the nitrogen atom. It has also been shown that upon excitation the location of neighboring carbon and nitrogen atoms change relative to the vacancy [109, 110].

Due to the solid-state environment of the diamond it is necessary to understand the coupling to phonons. Phonons can couple to vibration modes of the NV center and can thereby induce a change of the electrons wavefunction. Additionally as mentioned above excitation and relaxation of the NV center changes the distance between the atoms which induces vibrations as well [112, 113]. The latter is the reason for the large phonon sideband of the ground and the excited state. This translates into a large range of possible excitation wavelengths [36]. Commonly 532 nm is used as the excitation wavelength due to the availability of the laser. After excitation into the phonon sideband the system relaxes non-radiatively into the lowest excited state. From there relaxation into the phonon sideband of the ground state results in a broad emission spectrum. Actually only 4 % of the photons emit at the ZPL of 637 nm [114] (see figure 2.2). The corresponding Debye-Waller-factor is 0.04 which is typical for vacancy related defects. Other defects with a higher atomic mass exhibit a much higher ZPL to phonon sideband ratio [115, 116]. The ZPL of the emitter is considerably broadened at room-temperature (NV center: width of a few nm).

At room-temperature and in the case of a single NV center the level scheme can be simplified (figure 2.3). Spin-orbit coupling is averaged out in the excited state [104]. Strain is also negligible in the used diamonds. This leaves the triplet ground and excited state only affected by spin-spin coupling. In addition to the triplet states there are singlet states as well (figure 2.3). They can be populated by intersystem crossing (ISC). ISC can occur from the excited state due to spin-orbit coupling. It is unclear how many singlet states exist and how they are ordered. According to Rogers et al and Acosta et al there is a ^{1}E excited state in the singlet [117, 118]. The lifetime of the ^{1}E excited state is less than 1

ns [118]. From there relaxation is possible radiatively or non-radiatively to the $^1A_1$ state. The emitted photons are in the infrared range [117]. From the $^1A_1$ state the system can relax directly or via the third singlet state of ^1E symmetry into the triplet ground state. Here the important point is that these ISC rates are spin-dependent [119, 120, 121]. The electron spin has three states: $m_s = 0,\pm1$. For $m_s = 0$ the probability of ISC is almost zero and the system decays, with its spin conserved, into the ground state by emitting a photon. The corresponding lifetime of the excited state (in $m_s = 0$) is 12 ns. In the case of $m_s = \pm 1$, a decay via ISC is approximately as probable as the radiative decay into the triplet ground state. The lifetime in the excited state (in $m_s = \pm 1$) is 7.8 ns [122]. For the decay via the singlet states a decay time of 250 ns has been measured [123]. This indicates that one of the singlet ground states is metastable. Surprisingly the relaxation from the singlet states into the triplet ground state is spin-dependent as well. However in this reverse ISC scenario $m_s = 0$ is populated preferentially. This not only allows optical spin polarization but also spin readout which will be explained in the section 2.7.

Please note that in most NV based applications the triplet system is utilized. Recently there has been work on exploiting the radiative decay channel of the singlet state for magnetometry purposes [124].

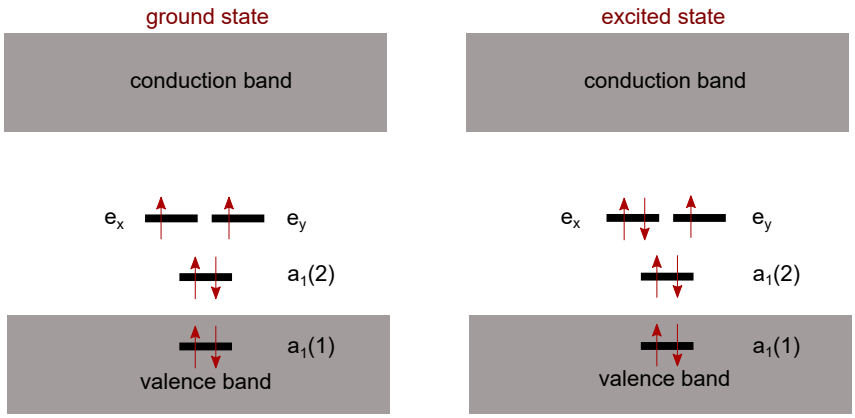

Figure 2.1.: Electron configuration of NV^-. The electronic states are shown for the ground state and the excited state [125, 109]. Six electrons are occupying four levels with a_1 and e symmetry.

2.4. Spin properties

In this section the NV electron spin's properties in the electronic ground state are evaluated. For the here presented measurements the spin states are mostly utilized in the ground state. Coupling to the intrinsic (^{14}N or ^{15}N) or other nearby nuclear spins is left out in the discussion. This will be discussed in chapter 4.

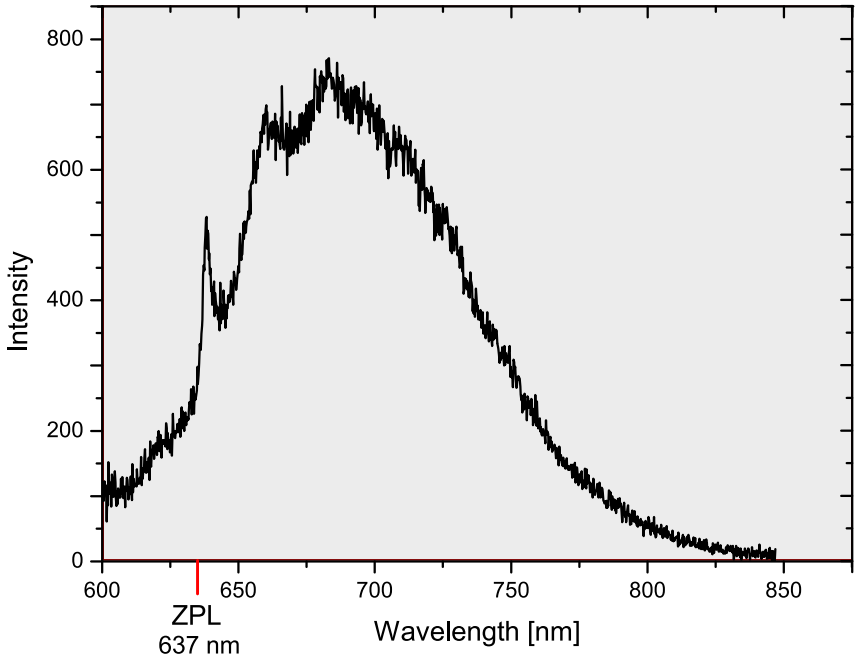

Figure 2.2.: Fluorescence spectrum of NV^-. A single NV center in bulk diamond is illuminated with a 532 nm laser light at saturation power. Acquisition of a spectrum is conducted with a spectrometer.

The Hamiltonian of the NV electron spin is [119, 126]:

$$H = H_{ZFS} + H_{zeeman} \tag{2.1}$$

with H_{ZFS} as the zero field splitting and H_{zeeman} the Zeeman term. The existence of the ZFS can be explained by the coupling of the magnetic dipoles of the two unpaired electrons [127]. The resulting coupled spin system has a total spin S=1 with three distinct magnetic field projections onto the axis connecting nitrogen and vacancy $m_s = 0,\pm 1$. This axis will be referred to as z-axis. The spin density of the NV center is not spherical but mainly deviates along the NV axis. It builds a disk-like shape. Therefore the z-component of the ZFS D_z is not equal to D_x and D_y. The ZFS term can be described by the formula:

$$D = \frac{3}{2} D_z \tag{2.2}$$

$$E = \frac{D_x - D_y}{2} \tag{2.3}$$

D_x and D_y only differ from each other in the case of a distorted c_{3v} symmetry. The measured values are: D = 2870 GHz [128] $\gg$ E $\sim$ MHz. Thus, in the present work E can be safely ignored without loss of generality.

When a magnetic field is applied, the electron spin levels experience a Zeeman shift

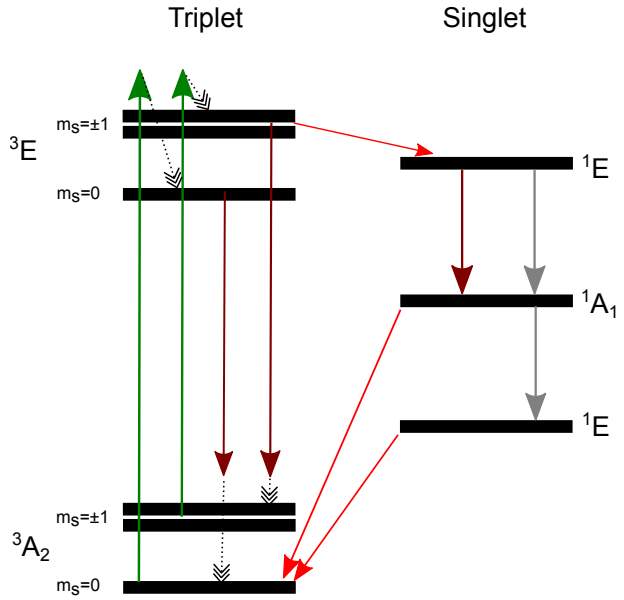

Figure 2.3.: Level scheme of NV$^-$. Triplet and singlet ground and excited states are forming the level scheme of the NV center. Laser illumination (green arrows) induces excitation from the triplet ground state to the triplet excited state. Subsequently relaxation from the phonon modes to the lowest excited state occurs, which is depicted by dotted arrows. Spin dependent ISC from the triplet to the singlet and back is shown by red arrows. Dark red arrows illustrate the radiative decay in the triplet and in the singlet states. Non-radiative decay in the singlet states is depicted by grey arrows.

according to the formula 2.5. Usually only a magnetic field along the NV axis is applied, since a transverse field results in mixing of the m_s states and reduces the effectiveness of the used spin readout and polarization mechanism. An applied magnetic field shifts the $m_s = \pm 1$ levels but does not affect the $m_s = 0$ state (see figure 2.4). This means that a magnetic field compensating the ZFS, results in a crossing of $m_s = 0$ and $m_s = -1$ levels. With these considerations the Hamiltonian terms can be further specified to:

$$H = DS_z^2 + \gamma_{es} B_z S_z. \tag{2.4}$$

Here γ_{es} is the gyromagnetic ratio of the electron spin (divided by 2π) and can be expressed by:

$$\gamma_{es} = \frac{g_e \mu_B}{h} \tag{2.5}$$

with the g-factor of the NV electron spin $g_e = 2.0028$ [126], the Bohr magneton μ_B and the Planck constant h.

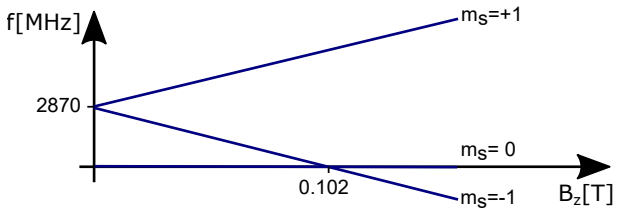

Figure 2.4.: Ground state electron spin m_s states in a magnetic field. The frequency of the electron spin is defined by the ZFS and the Zeeman shift (see equation 2.4). The ZFS is compensated by the Zeeman shift at 102 mT, for the case of the ground state. The excited state case would be analogue to the ground state but with the compensating point at 50 mT.

2.5. Charge state properties

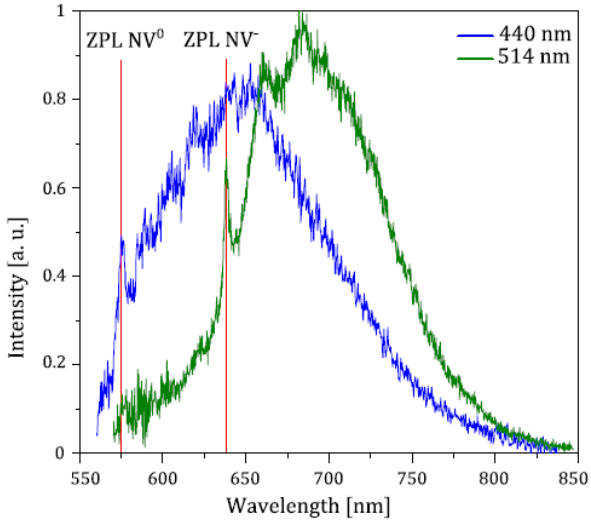

Figure 2.5.: Fluorescence spectrum of NV$^-$and NV^0. Two fluorescence emission spectra with different excitation wavelengths are obtained with a spectrometer. Green spectrum refers to the excitation wavelength of 514 nm exhibiting a NV$^-$ fluorescence spectrum. Blue data points are coming from the excitation with 440 nm and shows a typical NV^0 spectrum. The ZPL of NV$^-$ and NV^0 are marked in the graph [36].

Depending on the Fermi level at the NV center location, its charge state can vary. The known charge states are NV$^-$ (6 electrons), NV^0 (5 electrons) and NV$^+$ (4 electrons). The properties of NV$^-$ have been described in the previous sections. NV^0 is an optically active defect with a distinct fluorescence emission spectrum showing a ZPL at 575 nm (2.156 eV). Due to a difference in the emission wavelengths, NV$^-$ and NV^0 can be spectrally separated (figure 2.5). Therefore an optical filter selective to NV$^-$ fluorescence is used. The NV^0 charge state has an electron spin of S=$\frac{1}{2}$. Its electronic configuration has been

proposed in a paper by Adam Gali and co-workers [129]. So far it has not been able to directly readout the spin state of NV^0. The ground state of NV^0 is assumed to experience the dynamic Jahn teller effect [130].

Applying a laser with a wavelength of 638 nm transfers the NV^- center into a long-lived dark state [131]. NMR studies of the NV center's intrinsic nitrogen nuclear spin have shown that this observed dark state is actually the NV^0 charge state [132, 36]. Hence it is possible to change the charge state by laser illumination. Through these NMR studies the T_1 time of the NV^0 electron spin could be estimated to approximately 13 μs [132, 15]. Changing the excitation wavelength also changes the ratio between NV^- and NV^0. Illumination with green laser light (532 nm) yields a ratio of 70 % (NV^-) to 30 % (NV^0) [132]. With orange laser light (594 nm) however the ratio is roughly 10 % (NV^-) to 90 % (NV^0) [36].

The mentioned NMR studies showed a quadratic power dependence of the ionization and recombination rates [132]. This meant that for both processes two photons are required (see figure 2.6). It is suggested that the first photon excites the NV^- state into the excited state. The system would normally relax into the ground state by emitting a photon. But there is a probability that a second process occurs. It is possible that while in the exited state a photon ionizes the electron into the conduction band. Due to the missing electron, the charge state ends up in NV^0. This two-photon ionization depends on the applied laser intensity and the wavelength. Recombination works accordingly. After excitation of the NV^0 state, a second photon can levitate an electron from the valence band to the ground state of NV^0, which ultimately changes the charge state to NV^-. With green (532 nm) laser illumination, this ionization and recombination charge dynamics is continuously occurring. However no jumps of NV^- fluorescence are observable in the timetrace.

For low laser intensities the fluorescence counts scale linearly proportional to the laser intensity. On the other hand the two-photon-ionization and recombination rates of the charge state increase quadratically with the laser intensity. The photons emitted while in the NV^- state and without ionization are called photons per burst. This number is the product of the fluorescence count rate and the charge state lifetime (the inverse of the ionization rate). Forming the product shows that the number of photons per burst must increase for decreasing laser intensities. Moreover, the absorption of NV^- and NV^0 both depends on the excitation wavelength [36, 133, 134, 135]. This also has an effect on the number of photons per burst. It has been shown that 594 nm yields the maximum number of photons per burst. Using 592 nm as the excitation wavelength and setting a low laser intensity of 1 μW (measured in front of the objective), enables the observation of fluorescence jumps (figure 2.7). These jumps correspond to charge state switching be-

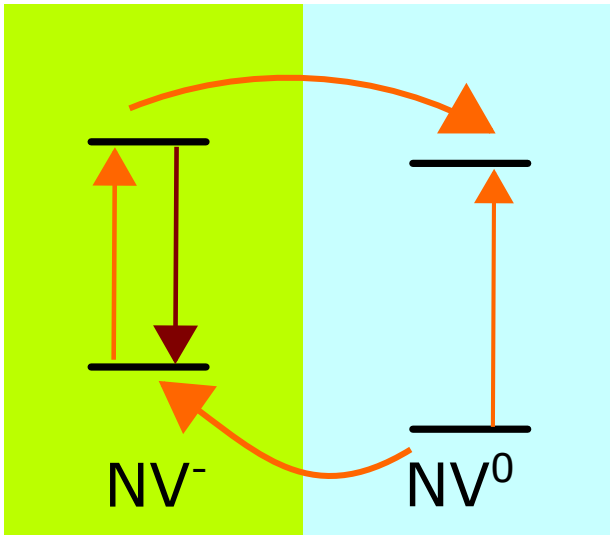

Figure 2.6.: Scheme of charge state energy levels of NV center in diamond. The two charge states of NV center are the negatively (NV^-) and the neutrally charged state (NV^0). Both are represented by their energy levels. Orange arrows are depicting the transition into other states induced by the laser.

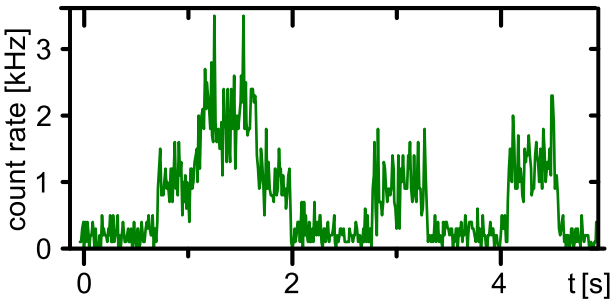

Figure 2.7.: Charge state switching trace. Laser at a wavelength of 594 nm is continuously applied. The fluorescence trace is recorded by an APD. An optical filter prevents the detection of NV^0 fluorescence and ensures the distinguishability between NV^0 and NV^-. The level of fluorescence determines whether one, two or no NV centers are in the NV^- charge state. The average number of photons per burst is 290.

tween NV^- and NV^0 and occur on a timescale of seconds. Forming a photon histogram of the timetrace and setting a photon threshold, allows to separate NV^0 from NV^- cases [36]. The charge state readout is non-destructive, if the readout time is selected much shorter than the charge state lifetime. Then it represents a single-shot readout of the charge state. Hence short orange (592 nm) charge state readout pulses can be included in different measurement protocols in order to distinguish between NV^- and NV^0 cases. It is also possible to ionize or recombine the NV^- charge state by only one photon. For

this purpose the excitation wavelength needs to be smaller than 470 nm [36].

So far a laser-induced stochastic way of charge state switching has been described. However there can also be a deterministic approach. The idea is to temporally change the Fermi level at the position of the NV center. Plane gate structures with alternating hydrogen and oxygen terminated diamond surface are employed for this purpose [136, 137, 138]. By applying a voltage through two hydrogen terminated surfaces, which are separated by a oxygen terminated surface, a potential difference is created. This shifts the Fermi level and can change e.g. a NV^- state to a NV^0 state. This technique enabled the detection of a dark state which has been assumed to be a third charge state [138]. For its investigation, NMR studies of the intrinsic ^{14}N and ^{15}N nuclear spins have been conducted (analogue to [132]). This has lead to the identification of this dark state being the spinless NV^+ charge state [139].

2.6. Experimental setup

The experimental setup is a combination of a confocal microscope and a ESR/NMR setup. For the most part of this work a superconducting vector magnet has been used. In the last chapter of this thesis presenting high resolution microscopy (chapter 6), a widefield setup has been employed in addition to a confocal microscope. The different components of the setup will be discussed in the following sections.

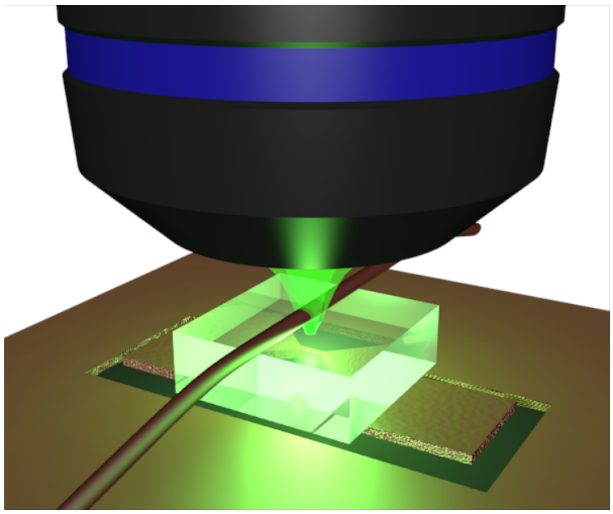

Figure 2.8.: Zoom in view of the experimental setup. Laser light with a wavelength of 532 nm excites single NV centers in the diamond membrane. The light is focused by a high NA oil objective. A tapered CPW $\lambda/2$ antenna delivers MW frequencies up to 90 GHz for electron spin manipulation. Nuclear spins are controlled by a RF wire which is spanned over the diamond. Liquid and solid samples are placed on top of the diamond.

2.6.1. Superconducting vector magnet

The superconducting vector magnet has a room-temperature bore of 10 cm diameter (see figure 2.9 A). The coils are made out of niobium. An arrangement of coils, located in a vessel filled with liquid helium (4 K), allows the application of magnetic field in all three directions. The vessel can hold approximately 100 l of liquid helium. Isolation from the environment is drastically improved by introducing a layer of high vacuum between the vessel and the environment. The resulting loss rate of liquid helium is approximately 14 l per day. Hence twice a week it is necessary to fill the vessel with liquid helium. Moreover the helium vessel is connected to a recovery line which collects the evaporated helium gas.

In x-direction (along the optical path) a solenoid generates a tunable field strength of up to 3 T (figure 2.9 B). The deflection Helmholtz coils enable the application of 0.2 T in y- and z-direction. These coils can be employed for aligning the field along the NV axis. The specified magnetic field persistence of the main coil is less than 0.65 ppm/hr. There is a pick-up coil wounded in the central part of the main coil, which further stabilizes the magnetic field. The specified field persistence for the y- and z- coil is 4.9 ppm/hr and 4.3 ppm/hr, respectively. In the NMR experiments the main coil's field strength ($\sim$3 T) dominates over the field generated by the deflection coils ($\sim$ 10 mT). Consequently the persistence of the main coil matters for the experienced field by the NV electron spin. In the NMR experiments shown in chapter 5 a spectral resolution of 1 ppm is targeted and the measurement times are on the order of a few hours. In conjunction with the pick-up coil, the persistence in the x-axis is expected to be much lower than 0.65 ppm/hr. Moreover the magnetic field can be precisely tracked by the NV center. As a result, the magnet field stability does not limit the achieved spectral resolution in the NMR measurements.

In conventional NMR, the samples typically have a size on the order of millimeters and therefore the magnetic field homogeneity is important. In this work, on the other hand, the sensor and the sample spins are confined to a nm scale volume. This significantly lowers the restrictions on the homogeneity of the magnetic field. The field homogeneity (over 10 mm diameter spherical volume) of the magnet is specified to be 0.05 % for the main coil and 1 % for the deflection coils.

Ramping up the field is enabled by heating locally at a contact point to the coils and thereby exceeding the critical temperature of the superconductor. The material at this point becomes normally conductive and allows to transfer current into the coil. This enables to increase the current in the coils with the specified ramp rates. The field ramp rates are 0.17 T/min (x-coil), 0.056 T/min (y-coil) and 0.062 T/min (z-coil). For example a total time of 18 min is needed for ramping the field from 0 to 3 T. At 3 T the coil can be disconnected from the external circuit by switching off the heater. Filling the vessel

with liquid helium is possible with the magnet operating at 3 T. Hence the field can be on for as long as the measurement requires. However it has been observed that immediately after the filling of liquid helium, the magnetic field becomes unstable for a few hours. Thereafter it settles down to the specified values.

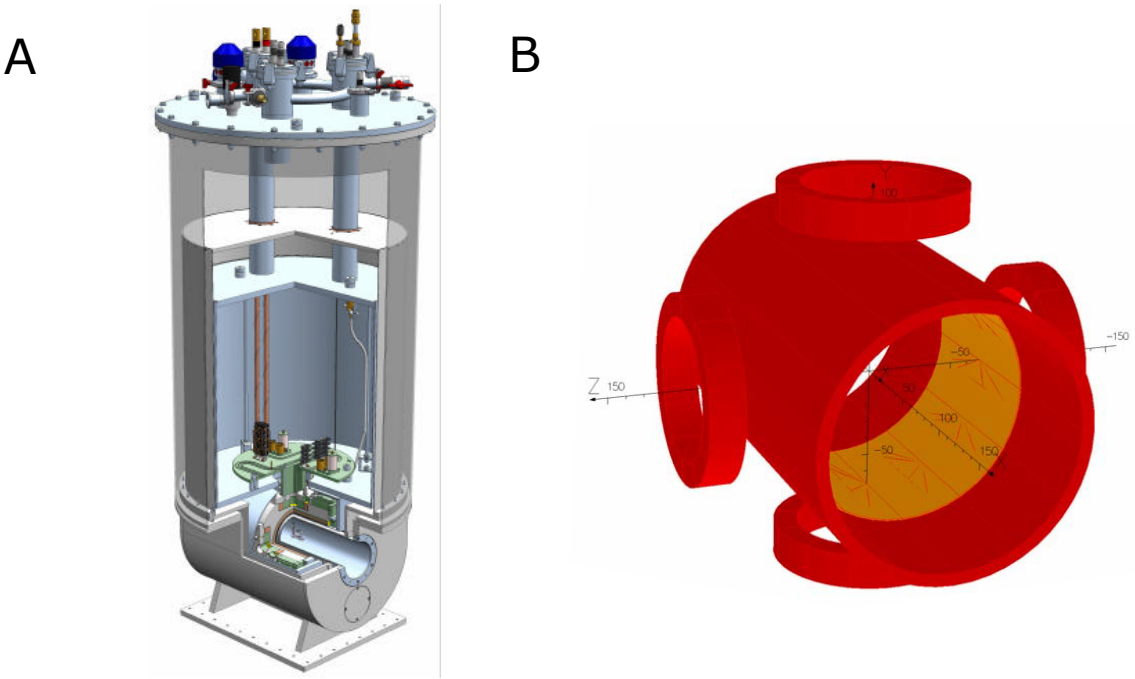

Figure 2.9.: Superconducting vector magnet with a room-temperature bore. A shows the cut view of the vector magnet. It has a height of 160 cm and a diameter of 70 cm (in the upper part). Its weight is 285 kg. The magnet consists of a vacuum vessel as an outer layer and a helium vessel. The vacuum vessel is necessary in order to isolate the helium vessel from the environment and hence reduce helium leakage. Due to the large helium vessel long helium hold times are possible. The superconducting coils are located in the helium vessel. A bore of 10 cm diameter allows room-temperature access. B shows the coil configuration. A solenoid in x-direction generates a magnetic field of up to 3 T. Two pairs of Helmholtz coils allow the application of 0.2 T in y- and z-direction. In the center of the solenoid an external influence coil is additionally wound, in order to reduce the magnetic field decay. Graphs are taken from the manual provided by Scientific Magnetics.

2.6.2. Optical microscope

The measurements rely on optically addressing single NV centers and collecting their fluorescence response. For this purpose a confocal microscope [14] is built. Lasers with a wavelength of 532 nm are utilized for excitation. If the laser cannot be triggered itself, it can be guided through an acousto-optical modulator (AOM). This enables the generation of laser pulses. The mode of the laser light might deviate from a perfect gaussian mode.

Therefore the laser pulses are coupled in and out of a single-mode fiber. Focusing of the light into the diamond is done via an oil-immersion objective with a NA of 1.35. The objective is mounted on a piezo scanner in order to scan the laser beam. The piezo-scanner is capable of scanning an area of 100 × 100 μm^2 in x- and y-direction and 25 μm in z-direction. The fluorescence is collected through the same objective and guided through a beam sampler with an anti-reflection coating, matching the emission spectrum of NV^-. Restriction to a confocal volume is achieved by focusing the light through a pinhole with 50 μm diameter. Spectral isolation from the excitation laser or from the fluorescence of other defects (e.g. NV^0) is achieved by using a suitable optical filter. Detection of the photons is performed by a single photon-counting avalanche photodiode (APD).

The main challenge of this setup is to place the diamond sample, the objective and the piezo scanner into a bore with only 10 cm of diameter. An additional constraint is to only use non-magnetic material within the bore of the magnet. To meet these requirements the following steps are taken. A steel based assembly with three rods is manufactured by the machine shop (see figure 2.10). The whole assembly is matched to the bore's dimensions and can be pushed into the bore. Once completely located inside the bore, the metal plate on one end can be attached to the magnet. The box on the other end functions as a holder of the non-magnetic piezo scanner. The attached objective had a metallic (magnetic) spring which in our case needed to be taken out by the manufacturer. Due of the limited range of the piezo-scanner, the diamond sample needs to be positioned as well. Remote 3d positioning is enabled by three non-magnetic translational stages (by Smaract). The translational stages each have a scanning range of 26 mm. Their scan resolution is approximately 100 nm.

For the high resolution microscopy experiments (see chapter 6) it is necessary to apply a widefield illumination and image with a CCD camera. The setup is extended such that confocal and widefield microscopy is possible on demand. In the case of widefield illumination the objective is not scanned. Additional lenses are flipped into the excitation path which focus the laser light onto the back focal plane of the oil objective. Depending on the focal length of the lenses this results in an increased illumination spot compared to the confocal case. Instead of an APD an electron multiplying CCD camera (iXon Ultra 897, Andor Technology) is used for the detection of photons. One pixel in the CCD image is set to correspond to 100 nm in the focal plane.

2.6.3. ESR and NMR excitation

Electron spin manipulation at 3 Tesla is conducted by MW fields with frequencies of $\approx 87\,\mathrm{GHz}$. For the first time such high frequencies are applied in order to manipulate a single electron spin. This is not a trivial task and requires careful understanding and use

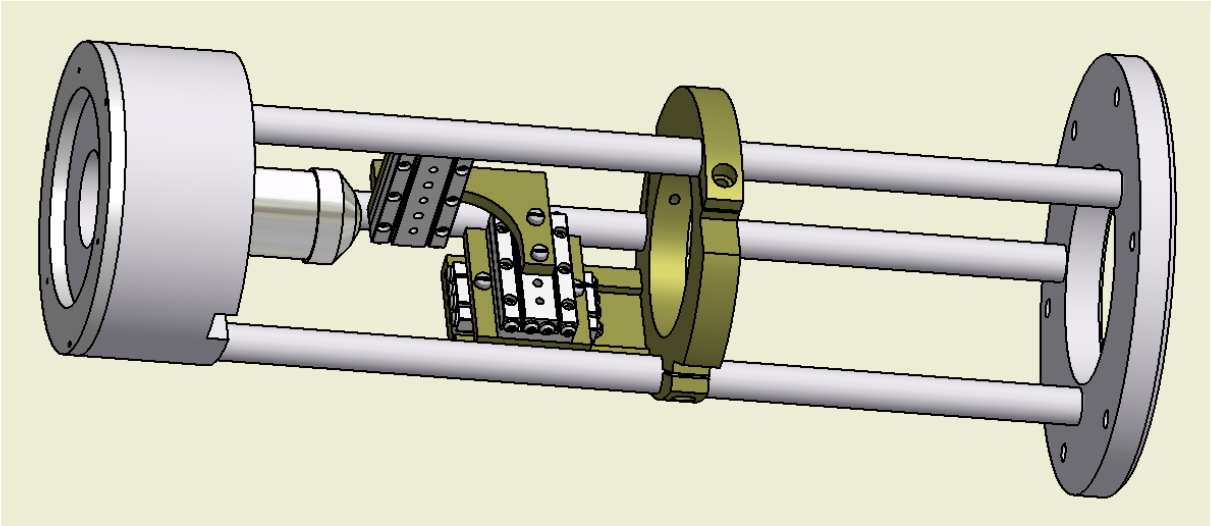

Figure 2.10.: Experimental setup within the magnet. A steel assembly consisting of three rods and a circular box is used to place the sample in the room-temperature bore of the magnet. The piezo scanner is located in the box and scans the mounted oil objective. The sample is attached to translational stages which enable remote 3d positioning.

of MW engineering. Chapter 3 is dealing with these aspects. For fields up to 10 GHz ($\approx$ 0.35 T), the used microwave equipment is different, which will be explained in this chapter.

The necessary devices for MW manipulation are first introduced. In this work both electron and nuclear spins have been manipulated by MW and RF fields, respectively. The basic device for the generation of MW/RF is a signal generator. Here the used signal generator is an Anritsu MG3697C with a frequency range between 2 GHz and 67 GHz. Its maximum output power of 10 dBm (between 2 GHz and 20 GHz) is usually not sufficient to drive the NV electron spin fast enough. Therefore it is necessary to increase the power by MW amplifiers (Gigatronics 1050 A). The MW are guided through a coplanar waveguide (CPW) board. In the vicinity of the NV center, the conducting line of the CPW board is either narrowed or it is replaced by a thin (e.g. 50 μm diameter) copper wire in order to locally increase the field.

For the high field (3 T) and consequently high frequency case ($\approx$ 87 GHz) the situation is different. First of all the MW coming from the signal generator are frequency multiplied by a factor of 6 (OML S12MS W12). The generated MW frequencies lie in the E-band range (see table 3.1) and serve as the MW carrier of a bias balanced mixer (Semic RF SFB-12-E2). In addition to it, an Arbitrary Waveform Generator (Keysight M8190A AWG) generates pulses with the desired frequency, amplitude and phase and is mixed to the carrier signal. The output signal of the mixer is amplified (Millitech AMP-12-02540).

The MW are guided via hollow waveguides and coupled to an antenna or to a waveguide cavity. Further details will be given in chapter 3.

Depending on the measurement protocol nuclear spins need to be manipulated by RF. Their resonance frequency is below 130 MHz. The RF can be generated by the second output of the AWG and amplified. In the low field case, the MW frequencies for electron and nuclear spin manipulation can be combined and guided through the same MW structure e.g. a CPW board. In the case of a high field (3 T) a separate wire can be placed above the diamond in order to independently apply RF for nuclear spin control (see chapter 3).

2.7. Spin readout

Two properties of the NV electron spin are of great importance all NV related applications. The first property is the ability to polarize the spin and the second is the possibility to readout the spin state. Both properties are valid for low and room temperature operation.

In section 2.3 it has been explained that the ISC is spin-dependent. Excitation into the triplet excited state in the case of $m_s = 0$ will be followed by a radiative decay. However in the case of $m_s = \pm 1$ it is equally possible that relaxation occurs via an ISC to the singlet excited state (see figure 2.3). The decay via the singlet is almost non-radiative, takes 250 ns and populates the $m_s = 0$ state in the triplet ground state with a high probability. The exact ISC rates for the different m_s states are not clearly known. There have been studies which suggest differing ISC rates [140]. Electron-vibration interaction is most probable the reason for the spin-dependent ISC [141, 142, 143].

In the readout step the fluorescence counts of the ZPL and of the phonon sidebands are detected. Due to the mentioned spin-dependent ISC rates green (532 nm) laser illumination of at least 300 ns length is sufficient to initialize the spin state into the m_s=0 state. Laser induced polarization of the electron spin is independent of the initial spin state. The counts detected during a 300 ns laser pulse are however depending on the initial state. Beginning with $m_s = 0$ yields 30 % more counts compared to $m_s = \pm 1$ (see figure 2.11).

The spin-dependent fluorescence emission enables optically detected magnetic resonance (ODMR). The measurement protocol starts with an initializing laser pulse of 300 ns length. It is followed by a coherent MW manipulation of the electron spin. The frequency of the latter pulse is typically swept over a range of 15 MHz. And finally the spin state is readout with a 300 ns laser pulse. Depending on the applied magnetic field a resonance can be observed in the form of a dip in fluorescence. This means that the

electron spin state has successfully been transferred to one of the $m_s = \pm 1$ states. Furthermore it is possible to do Rabi measurements on the electron spin. For this purpose the pulse length is varied. The resulting oscillations can be fitted by a cosine function in order to yield the Rabi frequency Ω. The detected fluorescence counts are on the order of 300 kHz. Hence a single laser pulse yields 0.09 photons for the $m_s = 0$ state and 0.06 for the $m_s = \pm 1$ state. Moreover the presence of photon shot noise decreases the signal to noise ratio (SNR). An accumulation of many laser pulses is therefore required for signal detection. Each time the whole sequence including the MW operation has to be repeated which leads to long measurement times.

An alternative way is to include the nuclear spin into the readout process. In chapter 4 it will be shown that single shot readout (SSR) of a nuclear spin is possible and significantly enhances the SNR. At low temperature, SSR of the electron spin is enabled by spin state selective optical transitions.

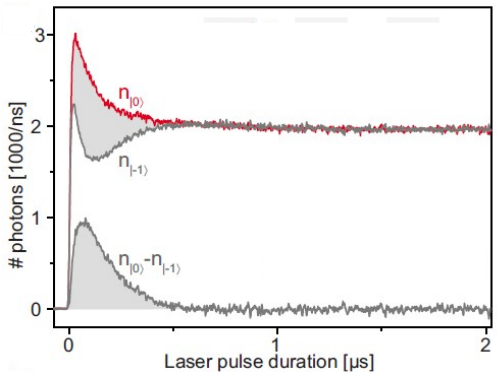

Figure 2.11.: Spin-dependent fluorescence emission. Red curve corresponds to the $m_S = 0$ state and upper gray curve to m_S = - 1. The lower gray graph is the difference between the two curves (figure from [144]).

2.8. Spin relaxation

The methods known in ESR and NMR can be applied to the electron spin of the NV center in order to measure the relevant relaxation times. In chapter 1.2 the concept of longitudinal and transversal relaxation has been introduced. Longitudinal relaxation (T_1 time) is occurring by exchange of energy with the environment. In the triplet ground state of the NV center, the spin-orbit coupling is very weak. Moreover the singlet ground state is energetically detuned and therefore prevents coupling to each other. Furthermore vibrations of the diamond lattice occur far detuned from the resonance frequencies ($\sim$

GHz). These considerations result in the expectation of a long T_1 time.

The T_1 time is measured by first initializing the spin. This is followed by a varying evolution time and finally a readout of the spin state. The measured T_1 time is around 5 ms for a single NV center at ambient conditions. For a solid-state system and ambient conditions this is a remarkably long decay time.

The T_2^* time can be deduced from a Ramsey measurement. In the case of the NV center it will strongly depend on the ^{13}C environment. This bath of ^{13}C spins leads to inhomogeneous broadening which can be refocused by dynamical decoupling methods. The simplest form of dynamical decoupling is a Hahn echo sequence. Hahn echo measurements on the NV center have obtained a T_2 time of 2 ms [16]. Higher order dynamical decoupling sequences, e.g. CPMG or XY-8 can further lengthen the decay time up to the T_1 time [17, 18, 19, 20].

2.9. Applications

The long transversal and longitudinal relaxation times at ambient conditions [16] makes the electron spin of the NV center interesting for quantum information processing (QIP). With its S=1 spin system it can form a qutrit or a qubit by restricting the quantum gates to two spin states. Coupling to other qubits is possible via dipole-dipole coupling. Indeed coupling and entanglement between two NV centers have been demonstrated [72, 74]. QIP requires the qubit to be noise resistant. For this purpose the qubit can be combined with more qubits in order to form a logical qubit. The additional qubits assist in protocols like quantum error correction (QEC) which protects the main qubit from errors. In the case of the NV center the intrinsic ^{14}N and nearby ^{13}C spins act as assisting qubits. These nuclear spins can be readout in a Quantum non demolition (QND) fashion and build together a quantum register [145, 146] (chapter 4). It has been shown that initialization, projective readout and application of local and non-local gates is possible on this quantum register [147]. Furthermore first QEC protocols has been applied in order to decrease the phase flip error rate of a single qubit [147, 148]. In this work the performance of the so-called memory spins is further improved by operating in a high magnetic field regime (chapter 4). One main requirement of QIP is to have a scalable system. In this regard the NV center based qubits fall short. Measurable dipole-dipole coupling between the qubits requires a distance of less than 20 nm, at ambient conditions [72, 74]. Creating NV centers in a deterministic way and with nm resolution have been proposed [149], but never experimentally implemented. The reason is the difficult interplay of placing a nitrogen atom into the diamond lattice and having a vacancy next to it. Statistically two or three NV centers with sufficient coupling strengths can be found in reasonable amount of

time [150] but larger numbers are difficult to achieve. An alternative to the dipole-dipole coupling approach is to couple distant NV center spins via their spin state-selective fluorescence photons at beamsplitters [151]. This requires low temperature operation and photonic structure engineering in order to enhance the success rate [152]. The approach via photons is especially interesting for quantum communication as fibers allow low-loss transmission over long distances [153].

This work focuses on the second important application of the NV center which is quantum metrology. The electron spin of the NV center is sensitive to magnetic fields [78, 77], electric fields [154] and temperature [80, 81]. The susceptibility to magnetic fields is sufficient to detect electron and nuclear spins external to the diamond [155, 24, 25]. This high sensitivity to different parameters combined with the sub-nm scale of the NV center makes imaging with nm resolution possible [45, 156, 43, 44].

3. Sensor spin manipulation at 3 T

3.1. Challenges at high MW frequencies

Magnetic resonance of nuclear and electron spins is performed in numerous techniques. While in conventional NMR or ESR a large number of spins is located inside the sample, detection of single electron spins and nuclear spins is possible as well. This has been demonstrated in single molecules [157, 158], defects in the solid-state [159, 160, 161] and in rare earth ions [162]. The readout is done optically or electrically. What is common for these applications is that the manipulation of the nuclear and electron spins is performed with MW fields. The corresponding frequencies are mainly set by the applied magnetic field and are typically below 10 GHz. In this frequency range it is suitable to first guide the MW field via coaxial cables then transform it onto a coplanar waveguide (CPW) structure [163, 161]. And finally in the vicinity of the spin the central conductor line can be narrowed down to the μm-scale in order to increase the MW field density.

The so-far mentioned experiments have been limited to MW frequencies less than 10 GHz. However it can be beneficial to apply a high magnetic field (B $>$ 1 T). One benefit is a higher degree of decoupling of the nuclear spins from the electron spins in the vicinity [29, 164, 38, 28]. This enables long T_1 times of the nuclear spins. In NMR a high magnetic field is preferred because of the following reasons. One reason is the higher thermal polarization which increases the signal strength [39]. The other reason is the increased chemical shift splitting which linearly increases with the external magnetic field (see chapter 1.3). A larger frequency shift facilitates the chemical structure analysis. In conventional NMR the nuclear spins are detected directly at elevated magnetic fields. If the NMR detection however is conducted via electron spins then frequencies larger than 60 GHz have to be applied. This is the case in NV center based NMR where the NV electron spins plays the role of the sensor (see chapter 5).

The application of MW with a frequency larger than 60 GHz comes along with some challenges. The transmission through coaxial cables becomes very lossy. This can be explained by the skin depth which decreases with $\propto 1/\sqrt{f}$, where f is the MW frequency. Consequently the current flows through a reduced area which means a higher resistivity. One solution would be to increase the diameter of the conductor line. However this re-

Table 3.1.: Waveguide frequency bands.

X band	8.2 GHz to 12.4 GHz
K_u band	12.4 GHz to 18.0 GHz
K band	18.0 GHz to 26.5 GHz
K_a band	26.5 GHz to 40.0 GHz
Q band	33 GHz to 50 GHz
V band	40 GHz to 75 GHz
E band	60 GHz to 90 GHz
W band	75 GHz to 110 GHz
F band	90 GHz to 140 GHz
D band	110 GHz to 170 GHz

duces the possible mode frequencies. Transport of high MW frequencies (for f>60 GHz) is therefore conducted in so-called waveguides. Waveguides are hollow rectangular pipes made out of conducting material. They restrict the MW propagation spatially and guarantee low transmission loss. Different modes can be generated within the waveguide which depend on the wavelength of the MW and the dimensions of the waveguide. The frequency range of MW frequencies is divided into different bands (see table 3.1). In this study the frequencies lie in the E-band ranging from 60 GHz to 90 GHz. The dimension of the corresponding rectangular waveguide is 3.10 mm x 1.55 mm. The fundamental MW mode of the waveguide is TE_{10}. Hence the field intensity is distributed over a mm scale in contrast to the μm-scale case when working with CPWs. This could eventually be compensated by a higher MW intensity. However the semiconductor-based MW sources and amplifiers in the E-band regime only output a power of less than 30 dBm. Consequently the challenge at high MW frequencies is to achieve a high microwave-power-to-magnetic-field conversion efficiency $C_{\mathrm{mag}} = B_1/\sqrt{P_{\mathrm{MW}}}$ (respectively microwave-power-to-Rabi-frequency conversion efficiency $C_{\mathrm{Rabi}} = \Omega/\sqrt{P_{\mathrm{MW}}}$). Please note that very high power microwave sources like gyrotrons do exist. However their use in the context of single electron spin detection would lead to serious heating issues.

In this chapter novel MW structure designs are introduced which extend the ODMR measurement of single electron spins up to a 90 GHz MW frequency (correspondingly 3 T). In this case the electron spin is associated with the NV center [14]. However the shown techniques can be applied to other systems as well like phosphorous in silicon (Si:P) [161, 165] and rare-earth ions [162, 166, 167, 168].

The high field setup introduced in section 2.6.1 is used for the here described measurements. The MW devices used for high frequency generation have been discussed in

section 2.6.3. MW guiding is performed with hollow waveguides. For the final part of spin manipulation near the diamond two approaches have been used and investigated. The first is a waveguide to coplanar resonator transition (see section 3.2) and the second is the TM_{110} waveguide cavity (see section 3.3). The here presented results are published in [169].

3.2. Waveguide to CPW resonator transition

3.2.1. Design and simulations

The transport of MW is performed via rectangular waveguides (E-band) which are guided into the room-temperature bore of the superconducting magnet. The end of the rectangular waveguide within the magnet is connected to a dielectric plate (see figure 3.1A). As will be explained later the dielectric material can for example be sapphire or a material used in MW boards (e.g. Rogers Ultralam 3850). The plate has a patch antenna made

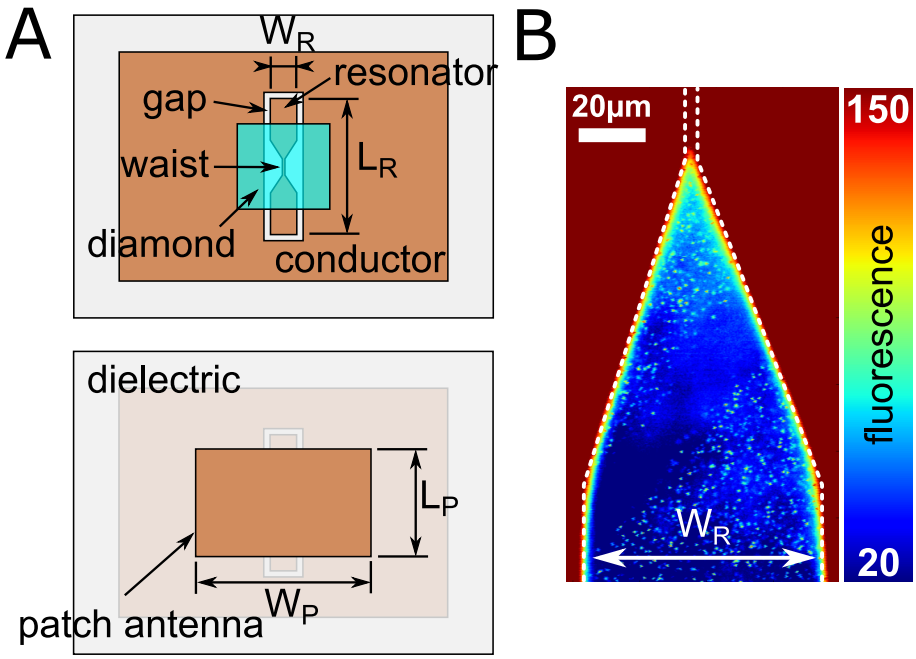

Figure 3.1.: The waveguide to CPW resonator transition. A Both sides of the assembly are shown. On one side of the dielectric material there is the the patch antenna (below) facing the waveguide and on the other side there is the $\lambda/2$ resonator (top). The diamond membrane is placed on top of the $\lambda/2$ resonator. B A confocal scan of the diamond with the structure of CPW resonator underneath is shown. Here the used dielectric material is the Rogers Ultralam 3850 which exhibits a high background fluorescence. Nevertheless single NV centers are visible near the waist of the resonator.

out of copper on one side (facing the waveguide). On its opposite side it has a CPW $\lambda/2$ copper antenna. The TE_{10} mode of the waveguide is capacitively coupled to the antenna structure. The $\lambda/2$ antenna has a resonance frequency which depends on the dimensions of the antenna. Additionally the antenna is narrowed down in the center to a width of ≈ 20 μm. This spatial confinement locally increases the MW intensity. Through the capacitive coupling the $\lambda/2$ antenna gets excited and induces mirror charges on the patch antenna which focus the MW field. In the ground plane of the $\lambda/2$ antenna oscillating current densities are induced as well. This leads to a reduction of radiation loss and to an additional concentration of the B_1 field near the $\lambda/2$ resonator. Right below and above the $\lambda/2$ antenna the B_1 field is orientated perpendicular to the external magnetic field which is favorable for NV centers with a certain orientation. Moreover the concentration of the field is higher within the dielectric material. Replacing it with diamond would therefore be favorable. For this purpose first of all a diamond with a suitable size would be required and the optical access to the NV centers would not be straightforward. In this study the diamond is placed above the $\lambda/2$ antenna. The spin of NV centers close to the tapered region of the antenna can then be manipulated by the antenna. The sapphire plate has a thickness of 170 μm. In principle a thinner dielectric plate favors the coupling to the waveguide mode. However other factors like mechanical stability of the whole assembly and the availability also need to be considered. The goal is to reach critical coupling and this depends on all geometric parameters of the assembly and not solely on the thickness of the dielectric. Instead of sapphire, a thin Rogers Ultralam 3850 PCB board has been used as well as the dielectric material in the experiments. The requirements for the dielectric are a high optical transparency and a high dielectric constant ε. The parameters of the used dielectric, the patch antenna and the $\lambda/2$ resonator are measured by optical microscopy and are listed in the table 3.2.

Before manufacturing the waveguide to CPW resonator transition, simulations are run with the software CST microwave studios in order to optimize the geometric parameters (see table 3.2). CST microwave studio provides a visualization of numerical simulations based on the finite integration technique (FIT). Here, the maxwell equations are solved and mapped onto a mesh. The rectangular waveguide and the dielectric with the antennas can be designed in this software. The input waveguide port defines the propagation direction. By setting local probes, parameters like the current density (or the B_1 field) can be simulated for varying MW frequencies. It is also possible to get the B_1 field distribution in 2d or in 3d. The geometric parameters e.g. the width or the length of the CPW resonator (figure 3.1A) are varied in the simulation in order to maximize the B_1 field.

A result of the simulation is shown in figure 3.2. Here the field $H_{1,x}$ (in A/m) is simulated with the application of a MW frequency resonant to the antenna. The tapering in

Table 3.2.: Summary of geometric parameters of CPW resonators.

Waveguide to CPW resonator	#1	#2
patch antenna length L_P	729 µm	667 µm
patch antenna width W_P	1531 µm	1476 µm
resonator length L_R	1085 µm	1014 µm
resonator width W_R	165 µm	85 µm
relative dielectric constant ϵ	2.9	
dielectric thickness	100 µm	
conductor thickness	10 µm	30 µm
gap CPW	42 µm	121 µm
width of waist	85 µm	3 µm
length of waist	88 µm	80 µm
conductor material	copper	
dielectric material	Rogers Ultralam 3850	

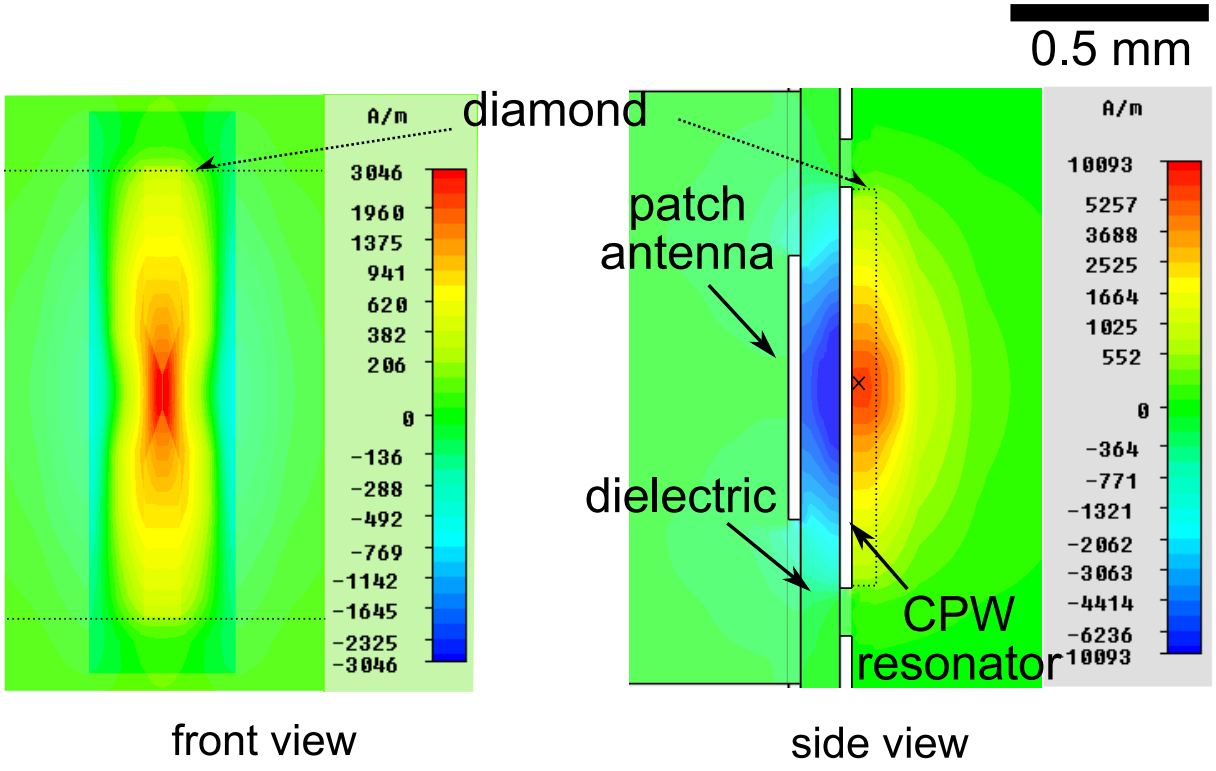

Figure 3.2.: 2d CST simulation of CPW resonator. The simulated $H_{1,x}$ field (in A/m) is shown from the front (left) and from the side (right). The diamond, the dielectric material and the antennas are labeled.

the center of the resonator locally increases $H_{1,x}$. For the resonator #2 with a waist of 3 µm width, the $H_{1,x}$ field is probed 20 µm above the resonator (marked with a cross). The simulation yields a MW efficiency of $C_{\mathrm{mag}} = 5.3\,\mathrm{mT}/\sqrt{\mathrm{W}}$, which given in Rabi frequency is $C_{\mathrm{Rabi}} = 105.0\,\mathrm{MHz}/\sqrt{\mathrm{W}}$.

The simulations show that dielectric materials on top of the resonator result in a reduced MW intensity due to dielectric losses. More importantly they lead to a significant frequency shift of the resonance (see figure 3.4). This is true for diamond and immersion oil which are usually both part of the experiments. Consequently the simulated CPW resonators have a resonance frequency varying between 60 and 80 GHz (see figure 3.4). Besides the dielectric losses, the radiative and conductive losses are important in estimating the achievable quality factor. Radiative losses have been reduced by the ground plane of the CPW resonator. Conductive losses on the other hand can come from metal surfaces with a higher surface roughness. The quality factor of the resonator #2 have been simulated to be $Q_{2,\mathrm{sim}} = 89$. Here the conductive, dielectric and radiative losses contribute with 192, 891 and 204, respectively.

Additional resonances can occur in the transition elements which disturb the desired resonance of the CPW resonator. E.g. the patch antenna itself can have a resonance frequency which should not match the resonance of the CPW resonator. The patch antenna does have the advantage of concentrating the MW field within the dielectric but its presence is not required. In fact CPW resonators on sapphire plates without patch antennas have been produced which show similar performance and are simpler to produce. In addition to the electron spins, driving the nuclear spins is possible by applying RF via an additional wire or a coil. The waveguide to CPW resonator transition design has been inspired by microstrip to waveguide transitions used in automotive radar systems [170].

For the production of the CPW resonators optical lithography with subsequent wet chemical etching has been used.

3.2.2. Results

The produced CPW resonators are evaluated by ODMR measurements at the corresponding MW frequencies. The interesting parameter here is the Rabi frequency Ω which is linearly increasing with the B_1 field. First an ODMR measurement is performed. The sequence (see section 2.7 for details) is composed of a readout and initialization laser pulse and a subsequent spin manipulation by a MW pulse. The frequency of the MW pulse is swept over a large range. A resonant pulse transfers the spin state from $m_s = 0$ to $m_s = -1$. This leads to a decrease in the detected fluorescence. In figure 3.1B the confocal scan of the diamond is shown which is located right above the CPW resonator. NV centers near the waist have a higher B_1 field. Indeed an ODMR signal can be observed

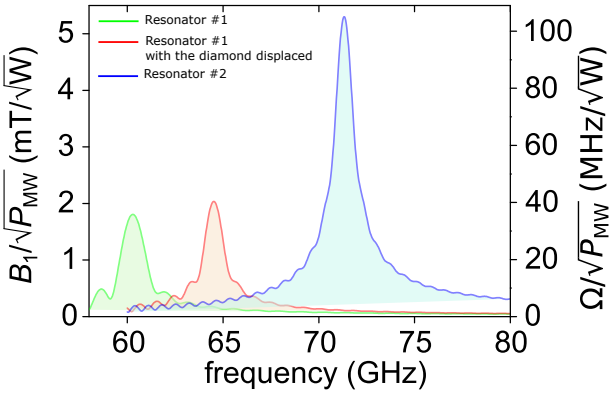

Figure 3.3.: 1d CST simulation of CPW resonator. The $H_{1,x}$ field is simulated 20 µm above the resonator. The red and green curves belong to resonator #1. The blue curve corresponds to resonator #2. In the green and blue case, the diamond is covering the whole resonator. In the red case, however, the diamond is displaced relative to the resonator, leaving a part of the resonator uncovered.

(analogue to figure 3.8A) at an applied magnetic field of 2.78 T. The hyperfine coupling to the ^{14}N nuclear spin can be resolved as well. Furthermore Rabi oscillations between the spin states $m_s = 0$ to $m_s = -1$ can be measured by varying the MW pulse length (analogue to figure 3.8B). The Rabi frequency Ω can be extracted by fitting the data with a sine function.

Measurements are performed on two different CPW resonators (see table 3.2). The main difference between them is the width of the waist. While it is 85 µm for the resonator #1, it is only 3 µm for the resonator #2. The generated B_1 field of resonator #2 should therefore be much larger near the tapered region. The crucial parameter, here, is C_{Rabi} in dependence of the MW frequency. Using a superconducting vector magnet enables the application of arbitrary magnetic fields and hence to tune the NV center spin transition to any MW frequency. The measurement protocol is as follows. For each resonator a NV center with roughly 20 μm distance to the resonator (in z-direction) is selected. The magnetic field is swept to the starting point of the measurement range. Next an ODMR is measured which yields the resonance frequency. Finally a measurement of the Rabi oscillations gives the Rabi frequency. And then the measurement protocol is repeated at the next magnetic field point.

Figure 3.4 shows the MW frequency dependent Rabi frequencies measured for three different configurations. The green and the red measurement correspond to resonator #1. They differ in the relative position of the diamond to the resonator. The green curve belongs to the case where the 1 mm x 1 mm sized diamond completely covers the CPW resonator. While for the red curve the diamond is only covering half of the CPW resonator.

As predicted by the simulations (see figure 3.3) the displacement to each other leads to a frequency shift. In this case it is a large shift of 2.66 GHz which can be explained by the large dielectric constant of the diamond. The NV centers do not have the exact same distance to the waist of the resonator. This explains the different amplitudes. For the resonator #1 the maximum MW efficiency is $C_{\mathrm{Rabi}} = 10.6\,\mathrm{MHz}/\sqrt{\mathrm{W}}$ (green resonance).

The results of CPW resonator #2 are shown in the blue curve. Here the diamond is fully covering the resonator. The resonance frequency differs from the resonator #1 due to the different geometric parameters (see table 3.2). The maximum MW efficiency of resonator #2 is $C_{\mathrm{Rabi}} = 27\,\mathrm{MHz}/\sqrt{\mathrm{W}}$ which is larger than compared to resonator #1. Here the investigated NV center for the resonator #2 has a larger distance from the waist. This was necessary due to the large background fluorescence coming from the dielectric material (Rogers Ultralam 3850) which makes it difficult to address NV centers right above the waist. Therefore the selected single spin has a position where the resonators width amounts to 20 µm. The use of sapphire prevents this problem as it reduces the background fluorescence dramatically. It can be concluded that the tapering of the CPW resonator leads to an enhanced B_1 field. The measured quality factors of the resonators #1 and #2 are $Q = 39$ and $Q = 48$ respectively.

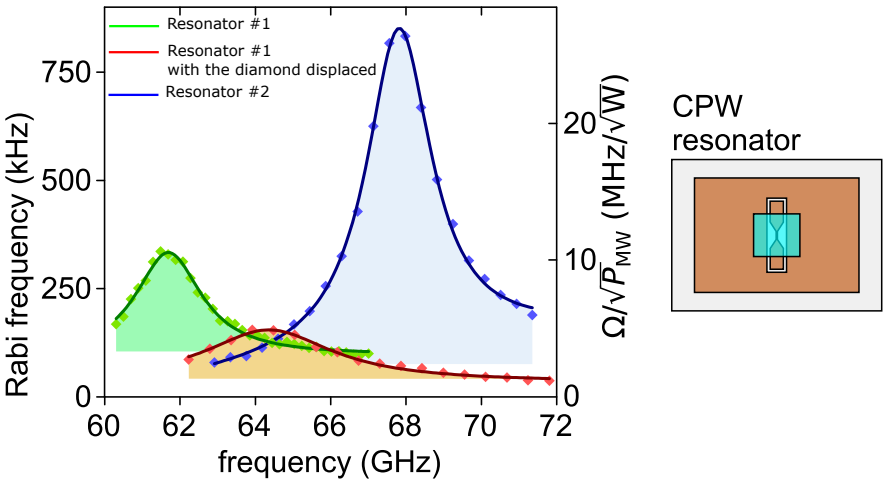

Figure 3.4.: Resonance curves of the CPW Resonator. The resonance of CPW resonator #1 and #2 is evaluated by measuring the MW frequency dependent Rabi frequencies with single NV spins. The green and red curve belong to the resonator #1 and the blue curve to the resonator #2. In the green and blue case the diamond is placed in the center of the CPW resonator effectively covering it. In the red case however the diamond is only covering half of the resonator. The used NV spins do not have the same relative position to the waist which explains the different amplitudes.

3.3. TM_{110} waveguide cavity

3.3.1. Design and simulations

An alternative way to do spin manipulation at 3 T is to use cavity resonators which e.g. find application in microwave ovens, in radar systems or in particle accelerators [171]. The MW waveguide cavities allow spectral confinement and show increased B_1 field concentration at certain points. They can be rectangular or cylindrical and are characterized by their mode. The mode can be transverse electric (TE) or transverse magnetic (TM) [171]. Furthermore three suffix numbers (mnp) specify the shape of the mode: TE_{mnp} or TM_{mnp}. Here m, n and p represent the number of half waves along the x- (width), y- (height) and z-direction (along the axis of the cylinder). The occurrence of a mode depends on the applied MW frequency, the length and the radius of the cavity. Inductive coupling is e.g. achieved by a hole in the cavity side facing the rectangular waveguide. The efficiency of coupling increases when the B_1 field in the waveguide is parallel to the B_1 field in the cavity at the position of the hole.

The cavity mode has to be chosen wisely as the experimental setup does set some constraints. For example the direction of the magnetic field generated by the main coil and the optical axis are important factors. Typically MW cylindrical cavities with the TE_{011} mode [82] are used. However for optical readout of single spins it is necessary to have an optical access near the concentrated B_1 field in the cavity. This limitation stems from the short working distance of the oil objective of $\approx 0.3\,\mathrm{mm}$. The TE_{011} mode profile however is revealing a B_1 field concentrated in the center. For a resonance frequency of 75 GHz the TE_{011} cavity would have a radius of 2.4 mm and a length of 4.8 mm. [171]. Therefore the diamond placed in the center of the cavity would have a distance beyond the working distance of the objective.

The requirements set for the cavity mode lead to the selection of the TM_{110} mode. Its B_1 field is concentrated in the center of the cavity and when mounted suitably within the bore it points perpendicular to the external magnetic field. Accordingly it is perpendicular to the used NV orientation (NV axis is perpendicular to the $\langle 111 \rangle$ surface of the diamond) which is ideal for spin manipulation. Figure 3.5 shows the design of the cavity. The cavities surface facing the waveguide has a hole in the center which results in inductive coupling of the mode of the waveguide to the cavity. As required both the incoming B_1 field and the B_1 field in the center of the cavity are orientated parallel to each other (see figure 3.6). Furthermore along the axis of the cylinder there is no node of the B_1 field (see right side of figure 3.6) Therefore a hole on the opposite side of the cavity allows optical access to the maximum of the B_1 field (see right side of figure 3.5). Here the diamond can be placed which results in a B_1 field enhancement due to the higher refractive index of

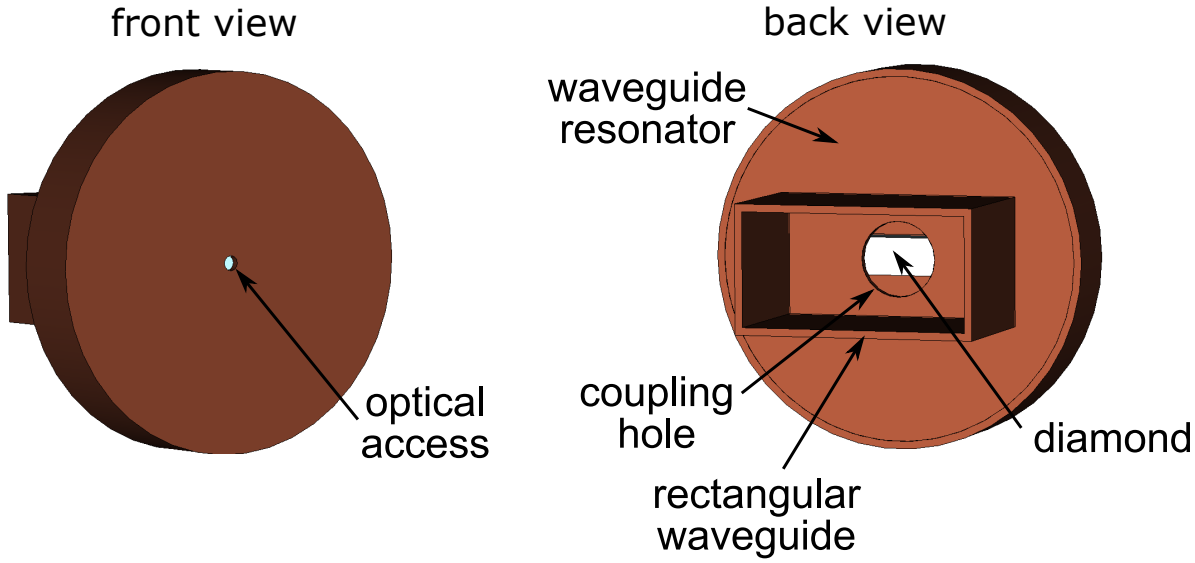

Figure 3.5.: TM_{110} cylindrical MW cavity design. The cylindrical MW cavity with the TM_{110} mode is shown. On one side the rectangular waveguide is attached to the cavity (right). There is a centered hole on the cavity which allows inductive coupling. The diamond is positioned within the cavity and is optically accessible by a hole on the back side of the cavity (left).

diamond compared to air. The resonance frequency of the cavity depends on its radius a but not on the cavity length d. However reducing the cavity length d increases the ratio of quality factor Q and cavity volume V [171] and consequently the B_1 field strength. The Q/V ratio is doubled for $2a/d = 5$ in comparison to $2a/d = 1$.

The coupling efficiency can be controlled by the hole diameter which can result in an undercoupled, a critically coupled or an overcoupled cavity. The B_1 field is maximized by critically coupling. CST simulations of the cavity (see figures 3.6,3.7) for varying the hole diameter are performed in order to yield the optimum diameter of the coupling hole. The simulation gives an estimated cavity quality factor of $Q_{\mathrm{sim}} = 643$. Furthermore in the simulations the MW efficiency is probed 20 µm away from the optical access which yields a value of: $C_{\mathrm{mag}} = 0.87\,\mathrm{mT}/\sqrt{\mathrm{W}}$ and $C_{\mathrm{Rabi}} = 17.6\,\mathrm{MHz}/\sqrt{\mathrm{W}}$.

The fabrication of the TM_{110} cavity out of a single metal piece with a cylindrical hollow space inside and small holes on both ends (for optical access and MW coupling) was not feasible with the available resources. This would have been ideal as the current flows over the edges of the cavity and any interruption leads to conductive losses. Consequently the TM_{110} is made out of three parts. The first part is the metal plate with a bore of 2.4 mm radius and a length of 1 mm (see table 3.3). The choice of metal is copper due to its high electric conductivity. Next a copper film with 8 µm thickness is attached to the copper plate. The film has a hole of 400 µm radius which has the purpose of coupling

the MW to the cavity. The third and final part builds a glass slide covered with a thin copper layer of 20 µm thickness and is attached to the other side of the copper plate. With lithography techniques a hole of 525 µm diameter is introduced into the copper layer. The hole enables optical access to the cavity. The geometric parameters of the TM_{110} cavity are summarized in table 3.3.

The relevant loss mechanism can be categorized in conductive and radiative losses. The conductive losses come mainly from interruptions in the contact between the three parts. Specifically for the TM_{110} mode current needs to flow across the cylindrical part and the surfaces. Surface roughness also plays a role which can be reduced by polishing the copper surfaces. Radiative losses are significant in this case since there are holes on both sides. While the coupling hole is necessary for exciting the cavity, the hole for the optical access should be kept as small as possible in order to avoid high radiative losses and distortion of the cavities mode (see left part of figure 3.6). Additionally the current density at the centered position (which is the position of the hole) is expected to be maximum. The simulation without the optical access yields a significant increase of the MW efficiency: $C_{\mathrm{mag}} = 1.68\,\mathrm{mT}/\sqrt{\mathrm{W}}$ and $C_{\mathrm{Rabi}} = 33.3\,\mathrm{MHz}/\sqrt{\mathrm{W}}$. This underlines the use of an optical access with a diameter as small as possible.

The TM_{110} mode is not the only suitable cavity mode. E.g. the TM_{010} has in principle a suitable field profile. Its B_1 field is maximized at the edges of the cylindrical MW cavity [171]. Consequently the coupling hole and the hole for optical access would need to be positioned on the edges. It is also possible to laser cut the diamond and shape it in a cylindrical way with the corresponding length and radius. The diamond would then need to be covered with a metal and would function as a MW cavity itself. The mode volume would be reduced due to the large dielectric constant of the diamond. Furthermore the conductive losses would be decreased due to an improved metallic contact across the edges. CST simulations have been performed in order to yield the necessary parameters (results not shown).

3.3.2. Results

The circular TM_{110} waveguide cavity is evaluated analogue to the CPW resonator. ODMR measurements are successfully performed with the cavity and one example is shown in figure 3.8. The diamond is placed completely within the TM_{110} cavity. The single NV electron spin used for ODMR and the other measurements is located $\approx 20\,\mu\mathrm{m}$ deep in the diamond and in the center of the hole. The Rabi frequencies Ω are measured at different magnetic field strengths and accordingly different MW frequencies (see figure 3.7). The maximum Rabi frequency is $\Omega = 300\,\mathrm{kHz}$ which corresponds to a MW efficiency of $C_{\mathrm{Rabi}} = 0.75\,\mathrm{MHz}/\sqrt{\mathrm{W}}$. The corresponding quality factor is estimated to be $Q = 56$. These values

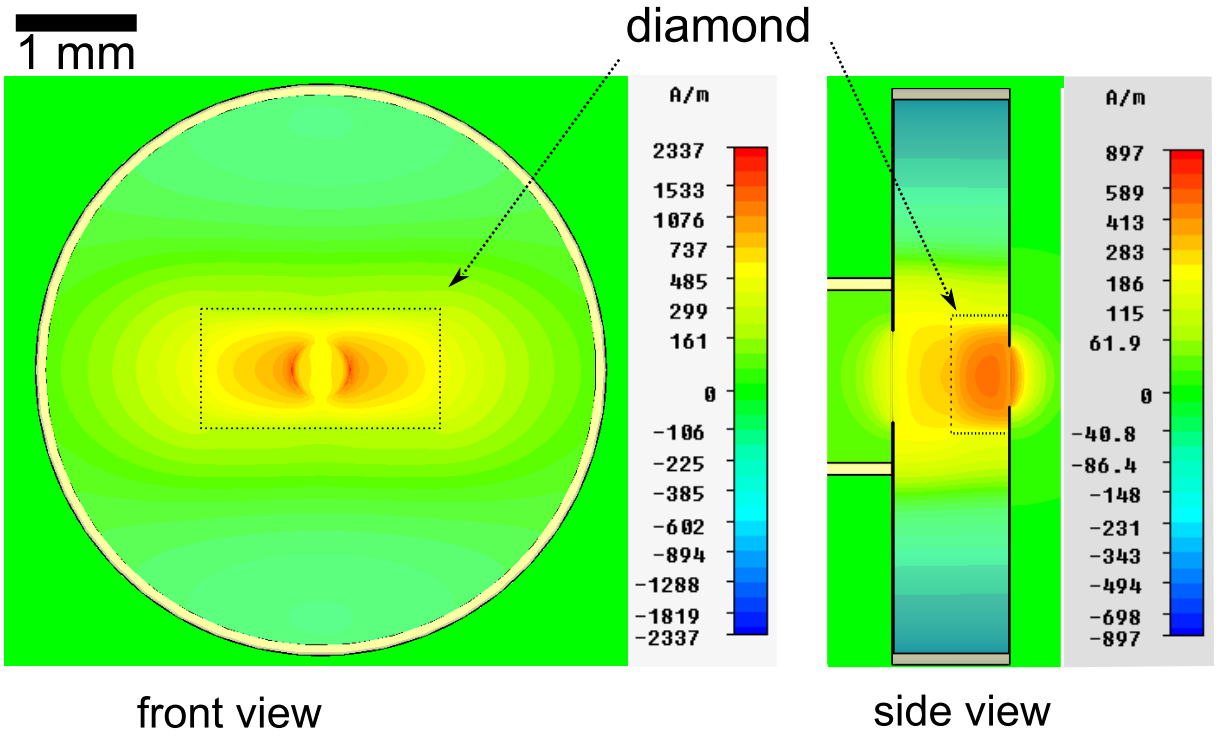

Figure 3.6.: 2d CST simulation of cylindrical MW cavity. The $H_{1,x}$ field distribution is simulated in the resonant case for a cylindrical MW cavity with a TM_{110} mode. The diamond is located inside the cavity. The 2d field map in the xy plane ($20\,\mu m$ apart from the optical access) is shown on the left. The right side shows the cross section of the field profile (at the center of the xy plane).

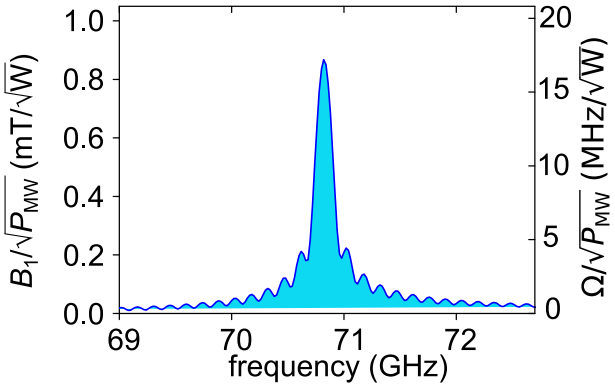

Figure 3.7.: 1d CST simulation of cylindrical MW cavity. The MW efficiency around the resonance peak is simulated at a distance of $20\,\mu m$ from the optical access (z-direction) and at the center of the xy plane. The cavity has the TM_{110} mode (see figure 3.5).

deviate from the simulations. This is attributed to the non-ideal contact between the three parts. An improved fabrication and better polishing would increase the quality factor Q

and hence the MW efficiency. Both are also expected to be enhanced by decreasing the diameter of the optical access.

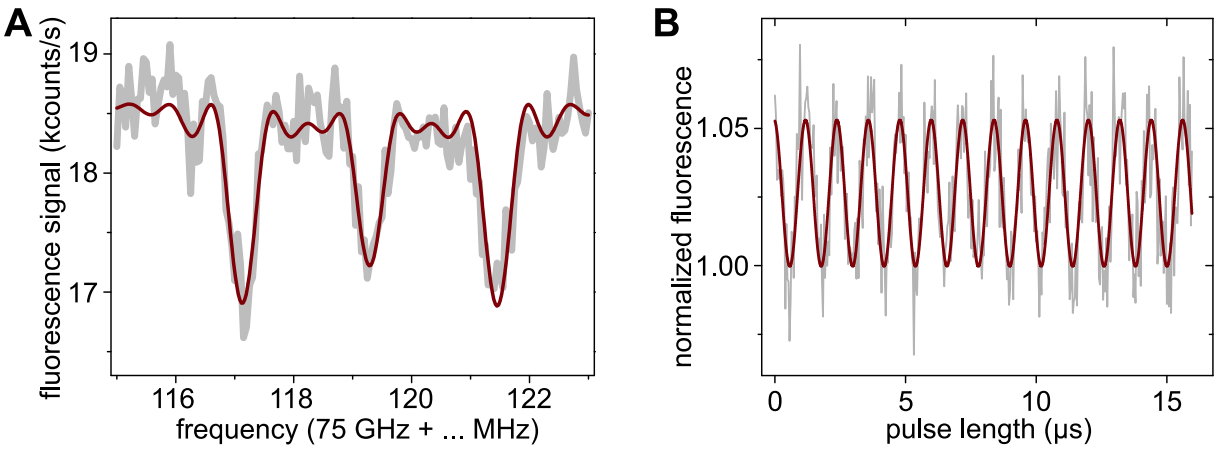

Figure 3.8.: ODMR and Rabi measurement with the TM_{110} MW cavity at $\approx$ 3 T. A is showing the result of an ODMR measurement of a single NV electron spin. The transition occurs between the states $m_s = 0$ and $m_s = -1$. The magnetic field is $2.78\,\mathrm{T}$. Hyperfine coupling to the intrinsic ^{14}N nuclear spin is observable. B The measured Rabi oscillations between the NV electron spin states $m_s = 0$ and $m_s = -1$. The corresponding Rabi frequency Ω is $832\,\mathrm{kHz}$.

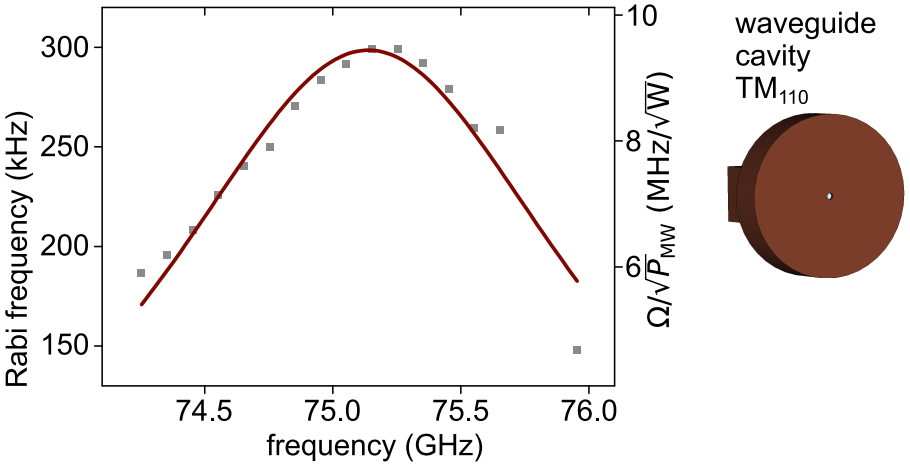

Figure 3.9.: Resonance curves of the TM_{110} MW cavity. The resonance of the TM_{110} MW cavity is determined by measuring the MW frequency dependent Rabi frequencies of a single NV electron spin. For that purpose the magnetic field and thereby the transition frequency is tuned over a range.

Table 3.3.: Summary of geometric parameters of the waveguide cavity.

TM_{110} cavity	
diameter	4.8 mm
length	1.0 mm
diameter of optical access	525 µm
diameter of MW coupling hole	800 µm
thickness of metal face with optical access	8 µm
thickness of metal face with MW coupling hole	20 µm
material	copper

3.4. Summary

Both the CPW resonator and the cylindrical waveguide cavity have proven to work for spin control at high frequencies. Multiple improvements in the fabrication process are suggested in the text which would enhance the quality factors significantly. A comparison of both approaches leads to the conclusion that the CPW resonator achieves a higher MW efficiency. This is mainly due to the spatial confinement coming from tapering the antenna.

4. The memory spin - Magnetic field scaling

The NV center in diamond with its electron spin has been introduced as a nanoscale sensor [77, 78] and a system to implement quantum information processing (QIP) [72, 73, 74, 38] and quantum communication [75, 76]. However, a major drawback is the optical readout of the sensor yielding low photon count rates and hence large photon shot noise. For sensing applications this translates into long measurement times, and for QIP it prevents the implementation of building blocks like quantum Fourier transform (QFT) or quantum error correction (QEC) steps. Required is the possibility of a single-shot readout (SSR) or of a quantum non-demolition (QND) measurement which results in a projection of the system as well as certain knowledge about its state in a single measurement run. The state of the qubit is projected onto an eigenstate. Besides the readout it allows the initialization of the qubits which is necessary for efficiently working quantum algorithms. The latter aspect becomes especially important for large quantum systems. In the case of the NV electron spin the laser readout pulse yields only 0.03 signal photons before it is initialized into the $m_s = 0$ state and any information about its previous state is lost. Therefore SSR of the electron spin is not possible at room-temperature. It is only possible at low temperatures where narrow optical lines allow spin state selective readout and therefore more signal photons [105].

Nuclear spins, on the other hand, don't have the optical initialization behavior as the NV electron spin. It is not possible to read them out directly, but hyperfine coupling to the NV electron spin enables access. A strongly coupled single nuclear spin can be utilized for SSR at room-temperature [29, 38, 146]. For this purpose ^{14}N , ^{15}N or ^{13}C spins within the diamond lattice can be considered. The readout is carried out via the sensor spin. Nuclear spin state selective pulses (CNOT gates) allow to swap the information from the electron to the nuclear spin. It is necessary for a non-demolition measurement that the spin has a longer relaxation time than the required readout time. Due to a much weaker interaction strength with the environment, the nuclear spins can potentially have long relaxation times. It will be shown in the following sections that the relaxation time of the nuclear spin increases quadratically with the applied magnetic field. Therefore they can

also be exploited as memory qubits and be combined with the NV electron spin, which works as the sensor qubit. Together they form a logical qubit which can be more robust to the occurrence of errors [38]. Mapping the sensor spin state to the memory spin is possible with a suitable CNOT gate. The resulting readout of the memory spin in a single-shot opens new avenues in the field of metrology and quantum information processing as it yields the maximum possible information of a quantum measurement.

So far a field of 0.65 T [38] has been applied to the NV center for the implementation of nuclear spin SSR. At this field the ^{14}N memory spin has shown readout fidelities of 95 % and a lifetime under continuous readout of 40.000 laser pulses. In this study a magnetic field of up to 3 T is applied which allows a lifetime of the memory spin of more than 330.000 laser pulses and fidelities reaching 99 %. In addition to the benefits of an enhanced readout, the memory spin can be incorporated in a sensing protocol to enhance the spectral resolution [30, 15]. Here the crucial parameter is the longitudinal relaxation time T_1^{mem} of the memory spin. The T_1^{mem} of a single ^{14}N spin has been measured in this study to be 260 ± 20 s at 1.5 T (at room-temperature). In this chapter the T_1^{mem} measurement and the limiting factors for T_1^{mem} will be described.

In principle other coupled single nuclear spins (e.g. ^{13}C) can act as memory spins as well [38, 146]. However here the focus lies on the intrinsic ^{14}N (or ^{15}N) nuclear spin as it is available on each NV center. The chapter first discusses the Hamiltonian of the system (section 4.1). Thereafter the spin dynamics at the LAC of the electronic excited state is explained (see section 4.2). Next the single-shot readout of nuclear spins will be described in the section 4.3. Here the magnetic field scaling under continuous SSR will be presented as well. Finally in section 4.4 T_1^{mem} measurements of the ^{14}N spin will be shown and discussed. The measurement results have been published in [15].

4.1. Hamiltonian

In this section the systems Hamiltonian is extended by coupling of the ^{14}N (or ^{15}N) memory spin. While the quantum gates are conducted in the electronic ground state, each laser pulse can lead to the electronic excited state which induces a different coupling to the memory spin. Therefore the discussion considers both the ground and the excited states of the NV center. Furthermore spin-orbit coupling can be neglected in both cases: In the ground state spin-orbit coupling does not occur and in the excited state it is averaged out [104]. As a result the Hamiltonian can be written as the sum of four parts [29].

$$H = H_{\text{sensor}} + H_{\text{memory}} + H_{\text{interaction}} + H_{\text{mw}} \tag{4.1}$$

$$H_{\text{sensor}} = DS_z^2 + \gamma_{\text{sensor}} B_z S_z \tag{4.2}$$

The sensor spin is first of all characterized by the zero-field splitting D which differs between the ground (2870 MHz, given in the units of frequency) and the excited state (1420 MHz). The Zeeman term depends on the applied magnetic field and reaches 84 GHz at B = 3 T.

$$H_{\text{memory}} = QS_z^2 + \gamma_{\text{memory}} B_z I_z^{\text{memory}} \tag{4.3}$$

If the memory spin is a ^{14}N spin then a quadrupole splitting Q needs to be considered. In the ground state the quadrupole coupling Q is -4.945 MHz. For the case of ^{15}N and ^{13}C this term drops out. The second part is the Zeeman term which is 13 MHz for the ^{14}N spin and at B = 3 T, according to the table 1.1.

$$H_{\text{interaction}} = \underline{S} \cdot A \cdot \underline{I} \tag{4.4}$$

The hyperfine coupling is represented by the hyperfine tensor A. It consists of the isotropic Fermi contact coupling H_{Fermi} and the anisotropic dipole coupling between the electron and the nuclear spin H_{DD}.

$$H_{\text{interaction}} = H_{\text{Fermi}} + H_{\text{DD}} \tag{4.5}$$

$$H_{\text{Fermi}} = a_{\text{iso}} \underline{S} \cdot \underline{I} \tag{4.6}$$

where a_{iso} is proportional to the electron spin density at the location of the nucleus $|\Psi_e|^2$. In the case of the ground state the spin density is concentrated at the dangling bonds to the carbon atoms. At the position of the nitrogen atom the electron spin density is very small. Consequently the isotropic part of the hyperfine interaction of the nitrogen nuclear spin is small in the ground state. However in the electronic excited state the spin density increases at the nitrogen location.

$$H_{\text{DD}} = \frac{\mu_0}{4\pi} \gamma_{\text{sensor}} g_n \mu_n \frac{\underline{S} \cdot \underline{I} - 3(\underline{S} \cdot \underline{e}_r)(\underline{e}_r \cdot \underline{I})}{r^3} \tag{4.7}$$

The dipole-dipole interaction also affects nuclear spins that are farer away, with a $1/r^3$ distance dependence. As mentioned the hyperfine terms can be summarized in the hyperfine tensor A (see equation 4.4) which has the form: A = diag($A_\perp$,$A_\perp$,$A_\parallel$) with $A_\parallel$ = a_{iso} + 2b, $A_\perp$ = a_{iso} - b and b = ($A_\parallel$ - $A_\perp$) / 3. As a result, the hyperfine interaction Hamiltonian can be written as:

$$H_{\text{interaction}} = (S_+ I_-^{\text{memory}} + S_- I_+^{\text{memory}}) A_\perp^{\text{memory}}/2 + S_z A_{||}^{\text{memory}} I_z^{\text{memory}} \tag{4.8}$$

where $S_\pm = S_x \pm iS_y$.

The hyperfine Hamiltonian can be separated into perpendicular and parallel terms to B_z. The parallel part $A_{||}^{\text{memory}}$ sets the gate time between the sensor and the memory. For the ^{14}N spin, $A_{||}^{\text{memory}}$ = 2.17 MHz has been measured in the ground state. Due to a larger spin density at the nitrogen position the hyperfine interaction increases to 40

MHz in the excited state [172, 173]. In the case of the ^{15}N spin the corresponding values are: $A_{||}^{\text{memory}}$ = 3.03 MHz in the ground state and $A_{||}^{\text{memory}}$ = - 60 MHz in the excited state [172, 173]. The perpendicular term $A_{\perp}^{\text{memory}}$ on the other hand is responsible for spin mixing (flip flop events). In the ^{14}N ground state $A_{\perp}^{\text{memory}}$ is 4 MHz. An isotropic case of $A_{||}^{\text{memory}} \approx A_{\perp}^{\text{memory}}$ is assumed for the excited state for the ^{14}N spin. For ^{15}N a significantly differing value is measured in the excited state: $A_{\perp}^{\text{memory}}$ = - 40 MHz [172].

Typically the zero-field splitting and the Zeeman interaction of the electron spins (both in z-direction) are on the order of GHz while the hyperfine coupling is in the MHz range. As a result the nuclear spins have a relatively small effect on the states of the electron spin. Therefore the secular approximation can be applied to the Hamiltonian [174]. As a consequence the quantization axis of the electron spin does not change due to interaction with the nuclear spins. Only its energy levels can be affected by them. On the contrary, the quantization axis of the nuclear spin is set by the Zeeman coupling, as well as the hyperfine interaction. The latter is switched off in the $m_s = 0$ electron spin state. The quantization axis for $m_s = \pm 1$ can therefore have a different angle due to the created hyperfine field. This strongly depends on the position of the nuclear spin relative to the NV center. For example the intrinsic ^{14}N (or ^{15}N) is located on the NV axis. Thus the quantization axes of the nuclear spin for the $m_s = 0$ and $m_s = \pm 1$ are parallel. Non-parallel orientation on the other hand enables so-called forbidden transitions, where electron spin transitions also induce a change of the nuclear spin state [174].

$$H_{\text{mw}} = \Omega \exp(i\omega t) S_x \otimes |-1\rangle_n \langle -1|_n \tag{4.9}$$

The main component of the SSR is the nuclear spin state selective MW pulse, the CNOT gate. It is applied conditioned on e.g. the nuclear spin state $|-1\rangle_n$, with Ω as the Rabi frequency.

In the Hamiltonian the coupling between nuclear spins is neglected, since the used diamond samples have a diluted nuclear spin bath. Furthermore effects caused by non-secular terms like hyperfine enhancement have not been discussed [175]. The latter becomes e.g. observable in the form of faster nuclear Rabi oscillations. Here the electron spin mixes into the nuclear spin dynamics which leads to a higher effective gyromagnetic ratio of the nuclear spin. The strength of this effect weakens when electron and nuclear resonance frequencies are detuned from each other.

4.2. Spin dynamics at the LAC

Typically the splittings of electron and the nuclear spin energy levels differ by many orders of magnitude. Therefore spin flip-flop processes (see perpendicular part in the

Hamiltonian 4.8) are suppressed. Application of a magnetic field can lead to a LAC point in the electronic ground and excited state (see figure 2.4). Here the transition frequencies of the nuclear and the electron spin become similar and hence induce strong interactions between them. The spin dynamics at the LAC of the ground state is similar to the one of the excited state.

A nuclear spin with I = $\frac{1}{2}$ is assumed (e.g. ^{15}N). The discussion can also be transformed to a I = 1 nuclear spin. On the side of the electron spin only the two states m_s = 0, -1 are relevant. As a result four eigenstates ($|m_s, m_I\rangle$) can be formed, away from the LAC: $|0, -\frac{1}{2}\rangle$, $|0, \frac{1}{2}\rangle$, $|-1, -\frac{1}{2}\rangle$, $|-1, \frac{1}{2}\rangle$. The states $|0, \frac{1}{2}\rangle$ and $|-1, -\frac{1}{2}\rangle$ do cross the LAC [176]. On the other hand $|0, -\frac{1}{2}\rangle$ and $|-1, \frac{1}{2}\rangle$ are mixed at the LAC creating new eigenstates:

$$|+\rangle = \alpha\,|0, -\frac{1}{2}\rangle + \beta\,|-1, \frac{1}{2}\rangle \tag{4.10}$$

$$|-\rangle = \beta\,|0, -\frac{1}{2}\rangle - \alpha\,|-1, \frac{1}{2}\rangle \tag{4.11}$$

with

$$\alpha = \sqrt{\frac{1}{2} + \frac{\Delta}{2\Omega_{LAC}}} \tag{4.12}$$

$$\beta = \frac{A_\perp}{\Omega\sqrt{1 + \frac{\Delta}{4\Omega_{LAC}}}} \tag{4.13}$$

$$\Omega_{LAC} = \sqrt{2A_\perp^2 + \Delta^2} \tag{4.14}$$

$\Delta(B_z)$ represents the distance to the LAC point and is the difference between the z-terms of the electron and the nuclear spin Hamiltonian. Ω_{LAC} is the spin mixing rate. In the case of the excited state the LAC occurs at a magnetic field of 50 mT. Constant illumination with a 532 nm laser will first of all pump the electron spin into the $m_s = 0$ state. Accordingly the state $|0, \frac{1}{2}\rangle$ will not be affected by the LAC dynamics. However in the case of $|0, -\frac{1}{2}\rangle$ the excited state LAC will induce a mixing with the $|-1, \frac{1}{2}\rangle$ state. The population of the latter state depends on the magnetic field and is maximum at the LAC [176]:

$$p(B_z) = 4\alpha^2\beta^2 = \frac{A_\perp^2}{A_\perp^2 + \Delta(B_z)^2/2} \tag{4.15}$$

In fact this can be exploited to achieve nuclear spin polarization of the ^{15}N spin (or ^{14}N) [176]. The spin mixing at the LAC occurs on a time scale (depends on Ω_{LAC}) similar to the decay rate of the excited state. This leads to a higher probability for ISC to the metastable state. From there the electron spin state decays to the $m_s = 0$ ground state. Consequently independent from the initial spin states the system relaxes into the $|0, \frac{1}{2}\rangle$ state upon illumination. This polarization process is dominant at the LAC and decreases when the magnetic field is detuned from the LAC. Other nuclear spins like proximal ^{13}C

spins can be polarized as well. However the polarization efficiency depends on the spin position relative to the NV axis and is maximum for spins laying on the NV axis [176]. Furthermore the careful initialization of the spin states at the LAC has been used for a $\sqrt{3}$ fold improvement in SNR of the electron spin readout [144].

In the previous discussion a perfectly aligned magnetic field along the NV axis has been assumed. In an experiment this is difficult to achieve. A misaligned magnetic field at the excited state LAC not only results in lower nuclear spin polarization but also reduces the detected fluorescence counts. The aforementioned states that do cross at the LAC start anti-crossing in the presence of a transverse field. This leads to spin-mixing. A decrease in fluorescence counts is the consequence as the ISC probability increases.

Aligning the field is generally crucial in maintaining the favorable coherence properties of the NV electron spin. Therefore the spin dynamics at the LAC can be exploited for alignment of the magnetic field along the NV center axis. The first step is to apply a magnetic field of approximately 50 mT along the NV axis. Next the deflection coils are swept one by one while continuously monitoring the fluorescence response. Magnetic field alignment is achieved at the point where the fluorescence is maximum (see figure 4.1). Analogue to this, magnetic field alignment can be achieved at the ground state LAC (102 mT) as well.

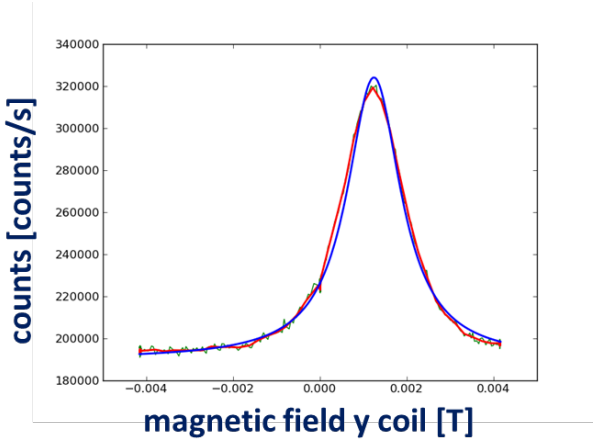

Figure 4.1.: Magnetic field alignment at the excited state LAC. A single NV center oriented perpendicular to the ⟨111⟩ diamond surface is constantly illuminated with a 532 nm laser (with saturation intensity). The x-coil generates a magnetic field of 50 mT corresponding to the excited state LAC. The fluorescence response is monitored while one of the deflection coils is swept from -4 mT to +4 mT.

4.3. Single-shot readout

The interaction between electron and nuclear spins via flip-flop events at the LAC has been explained in the previous section. On the other hand nuclear spins have been motivated as memory spins enabling SSR. A requirement for SSR of the ^{14}N (or ^{15}N) nuclear spin is that it does not flip during the measurement. Hence in this section it will be discussed how the nuclear spin's population can be protected from the electron spin dynamics.

The lifetime of the nuclear spin under laser excitation is important for the implementation of SSR. The relaxation of the nuclear spin is dominated by flip-flop events with the NV electron spin and is maximum at the LAC. In section 4.1 the system's Hamiltonian has been introduced. The $A_\perp$ term is identified as responsible for the flip-flop events. $A_\perp$ differs depending on whether the NV center is in the ground or in the excited state. In the ground state $A_\perp$ is 2.17 MHz. In the excited state however $A_\perp$ is $\sim$ 40 MHz [172, 144]. Hence laser excitation increases the probability for a flip-flop event to occur. At the LAC of the excited state (50 mT) the Zeeman term is canceled by the zero-field term of the excited state. The parallel (z-component) terms in the Hamiltonian are at a minimum and the $A_\perp$ part is pronounced. Consequently at the LAC flip-flop events are dominant and reduce the relaxation time of the nitrogen nuclear spin to a minimum. By applying a higher magnetic field along the NV axis, the Zeeman term in the Hamiltonian becomes more dominant over the $A_\perp$ term. This allows a decoupling of the electron and nuclear spin dynamics [28, 177]. In analogy to the equation 4.15 the relaxation time of the nuclear spin increases quadratically with increasing detuning from the LAC [29, 146]:

$$T_1^{mem\ under\ excitation} \sim \frac{A_\perp^2/2 + (\omega - 1.42\ \mathrm{GHz})^2}{A_\perp^2/2} \tag{4.16}$$

with ω being the electron spin transition frequency. SSR is achievable once the T_1^{mem} time under continuous readout is longer than the time it takes to distinguish between the spin states. For the known $A_\perp^{\mathrm{memory}}$, the frequency ω corresponding to 1.5 Tesla and an electron spin excitation rate Γ_{flip} of 1 MHz, the expected T_1^{mem} is approx. 1 s.

In the following the principle of SSR is explained. In a pulsed ODMR measurement the hyperfine coupling between the NV center and single nuclear spins in the vicinity can be resolved as long as the coupling is stronger than $\frac{1}{\pi T_2^*}$ (see figure 4.2). The achievable total ODMR contrast is approximately 30 %. These hyperfine resolved ODMR spectra allow an access to the nuclear spin. The nuclear spin's population can be mapped onto the NV electron spin. This is accomplished by a nuclear spin state selective electron π-pulse followed by an electron spin readout [29] (see figure 4.3). The aforementioned π-pulse represents a C_nNOT_e-gate. It transfers the state $|-1_n\rangle|0_e\rangle$ to $|-1_n\rangle|-1_e\rangle$. But

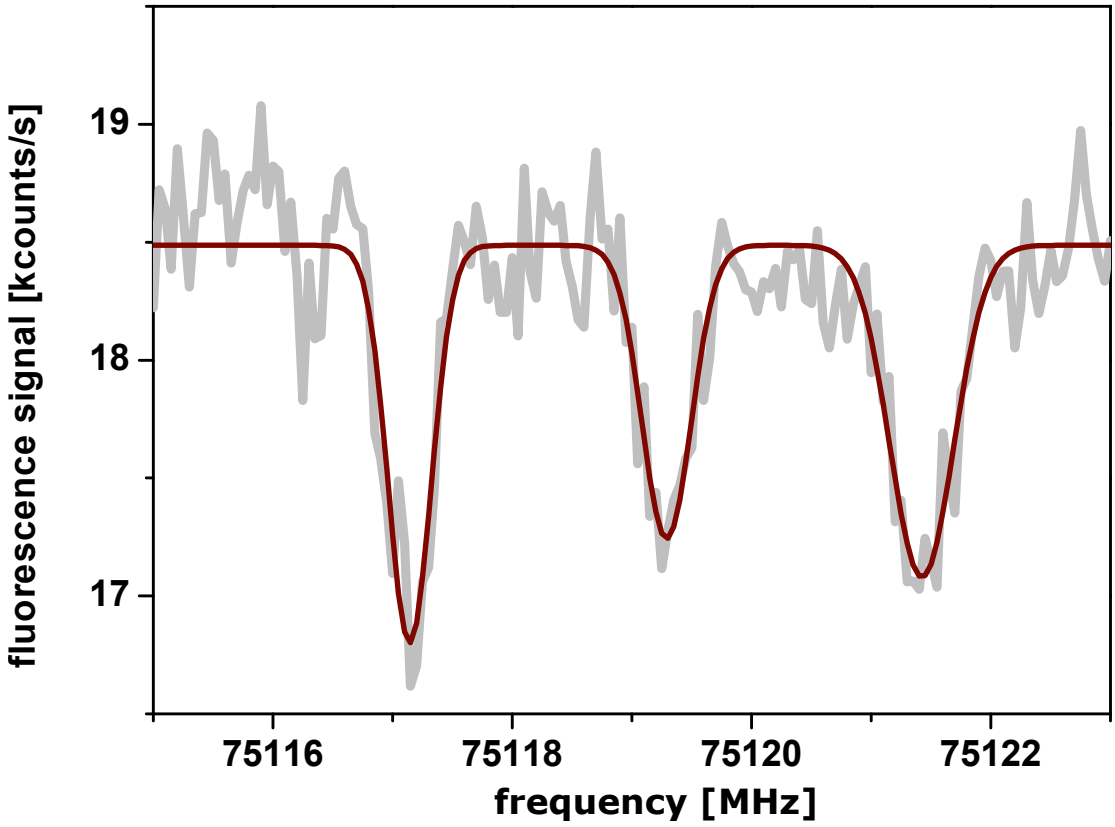

Figure 4.2.: Hyperfine-resolved ODMR spectrum. The figure shows an ODMR spectrum of the $m_S = 0$ to $m_S = -1$ transition at a magnetic field of 2.78 T. The 2.16 MHz hyperfine splitting caused by the host ^{14}N nuclear spin is clearly resolved.

leaves the state $|0_n\rangle|0_e\rangle$ unchanged. The π pulse is required to only affect one resonance line in the ODMR spectrum. Therefore fast pulses are not allowed. Typically a π pulse of 1300 ns length is sufficient to drive the transition without affecting neighboring lines. Next a readout laser pulse of 300 ns duration is applied which simultaneously serves as an initialization pulse for the next repetition. A subsequent waiting time of $\approx$ 1000 ns length ensures that the NV center has relaxed via the metastable state into the ground state before the sequence can be repeated again. A single laser pulse (with 532 nm and an intensity corresponding to the optical saturation of the NV center) typically only gives 0.09 photons for m_s=0 and 0.06 photons for m_s=$\pm$1. Therefore repetitions of the whole sequence on the order of 1000 are required for a single-shot measurement (total length of $\sim$ ms). Otherwise the signal is dominated by photon shot noise.

A single shot measurement trace of the ^{14}N nuclear spin state is recorded and shown in figure 4.4. Clearly quantum jumps between two fluorescence levels can be observed (marked by a blue line). The upper fluorescence level corresponds to the m_i= 0,+1 states and the lower level represents the m_i= -1 state. A photon histogram is constructed with

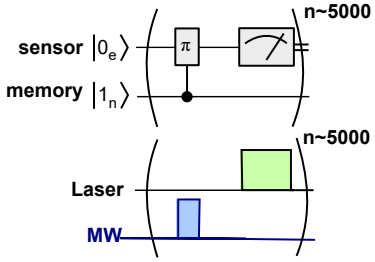

Figure 4.3.: SSR sequence of memory spin. On top, a wire diagram depicts the principle of SSR. The pulse sequence (shown below) includes a short laser pulse (300 ns) for readout and initialization. Moreover a nuclear spin state ($m_i = +1$ state) selective MW pulse on the electron spin $m_s = 0$ to $m_s = -1$ transition is applied. The pulse sequence is repeated 5000 times and all detected fluorescence photons are binned together.

the fluorescence timetrace and shown on the right side of figure 4.4. Two poissonian distributions can be separated. The fit of a superposition of two poissonians is marked with a red line. The width of each poissonian distribution is the square-root of the detected photons. Derived from the fit, a photon threshold can be set. Single shot readout and initialization of the nuclear spin is possible by simply observing whether the photon counts are above or below the threshold. The readout fidelity is determined by how well the two poissonian distributions are separable. This depends on the ODMR contrast, the fluorescence counts and the number of repetitions in the measurement. Here the achieved readout fidelity [29] is 99 %. In addition to this, the longitudinal relaxation of the ^{14}N nuclear spin under continuous readout is on the order of seconds (see figure 4.4) at 2.78 T. The timetrace shows that the lifetime of the ^{14}N nuclear spin is much longer than the duration of a single measurement step. Thus the SSR measurement does not destroy the state. This means that a projective quantum non-demolition (QND) measurement is indeed possible [178].

The precise analysis of the fluorescence timetraces of the ^{14}N nuclear spin can yield information about its longitudinal relaxation time. The analysis is not straightforward because of the stochastic nature of the quantum jumps. Therefore a hidden Markov model (HMM) can be made use of. It is mimicking the nuclear spins behavior. There are two unknown states which the system can reside in and in between them a stochastic switching can occur. The transition probability however stays constant over time and can be determined by the HMM analysis [179, 29].

A series of SSR timetraces has been recorded at different magnetic field points in order to check the field scaling of the lifetime. At each point the ^{14}N nuclear spin lifetime is evaluated in units of time and number of laser pulses. Longer longitudinal relaxation times allow more repetitions and thus a higher number of photons. This significantly increases

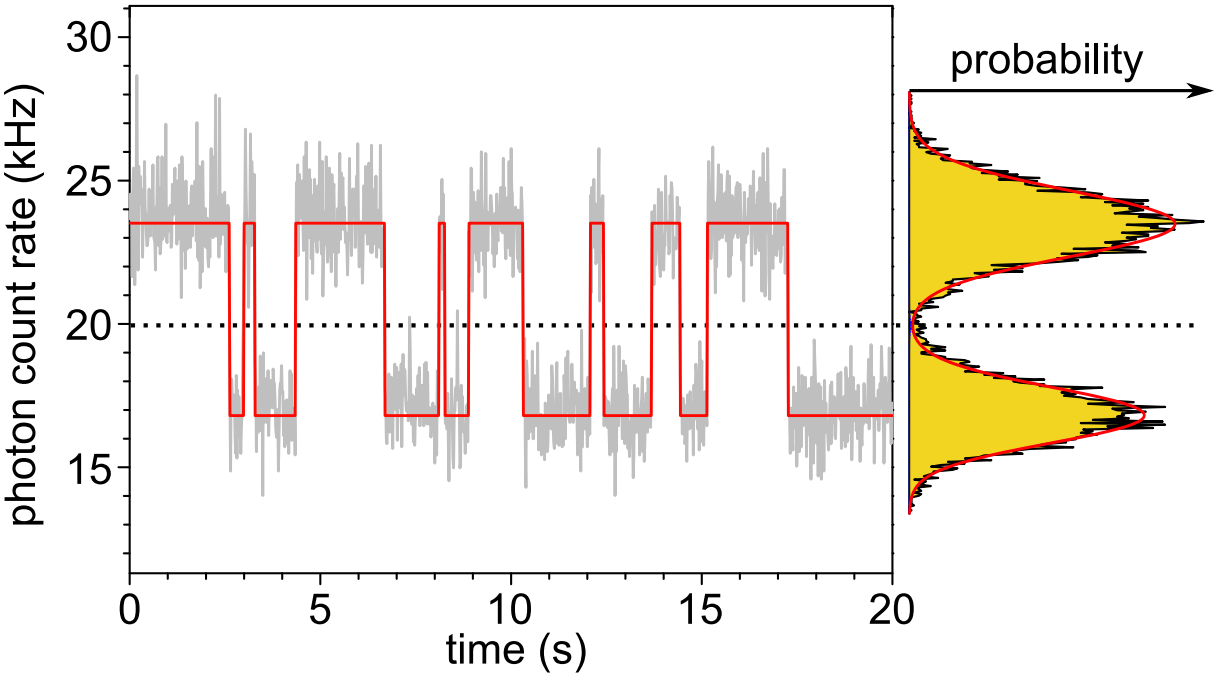

Figure 4.4.: Single-shot readout of a single nitrogen nuclear spin. Continuous readout of the nitrogen nuclear spin reveals quantum jumps. The high fluorescence level corresponds to the $m_I = -1, 0$ nuclear spin states, the low fluorescence level to $m_I = +1$. The red line is the result of a two-state Hidden-Markov-Model analysis of the fluorescence timetrace [29].

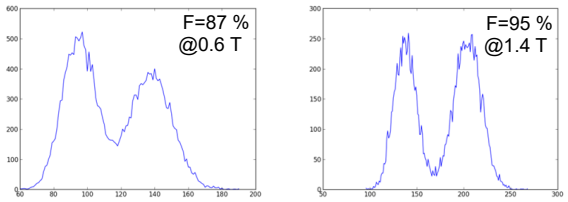

Figure 4.5.: Photon histogram of SSR. SSR traces are taken at two different magnetic fields: 0.6 T and 1.4 T. The SSR fidelity is increased substantially at higher magnetic field.

the separability of the different nuclear spin states in the photon histograms (see figure 4.5). Figure 4.6 is showing the results for the ^{14}N lifetime. The measurement results can be fitted and yield: T_1^{mem}= 0.155(2) s · [(B-0.05) T^{-1}]$^{1.68(1)}$ with the magnetic field B given in T. The expected T_1^{mem} time of 1 s at 1.5 T (equation 4.16) agrees approximately with the measured T_1^{mem}. Accordingly the lifetime can be given in number of laser pulses (lp): T_1^{mem}[lp] = 61,833 lp · [(B-0.05) T^{-1}]$^{1.68}$. The deviation from a pure quadratic dependence can be explained by the fact that there is also a 30 % chance [36] that the NV center resides in the NV^0 charge state. In that case the much shorter NV^0 electron spin T_1 time

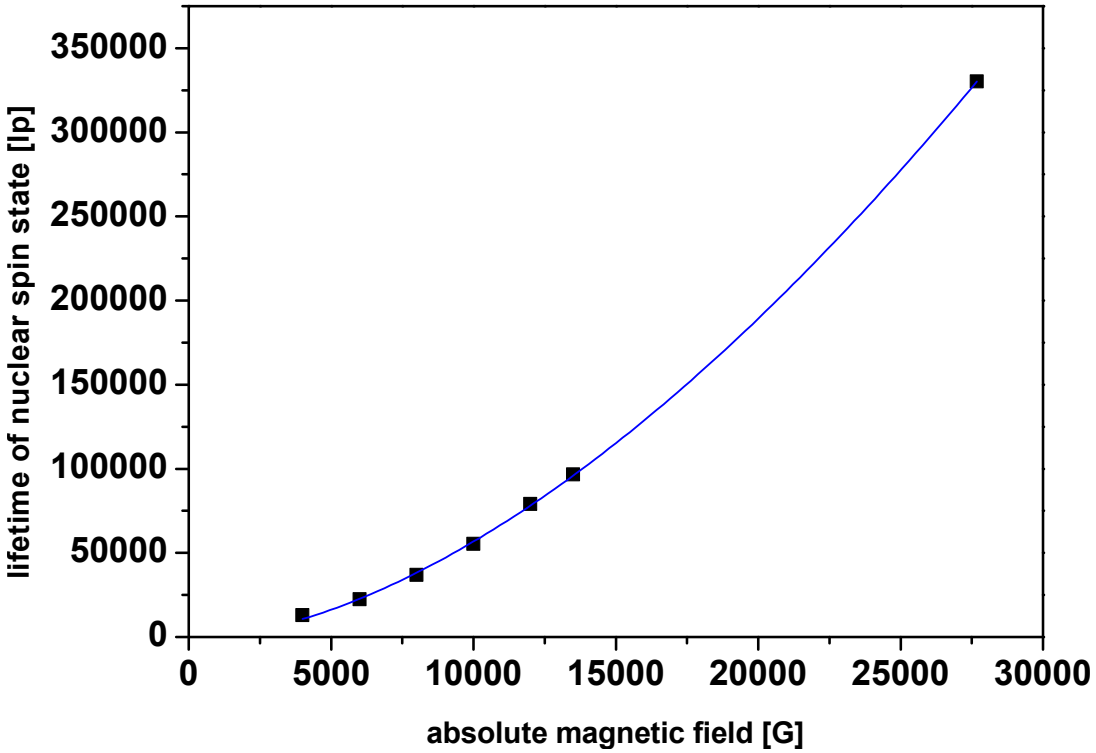

Figure 4.6.: Magnetic field scaling of ^{14}N lifetime during continuous memory readout. The lifetime of continuous SSR is measured in number of laser pulses (length of 300 ns) at varying magnetic field points. It has a minimum at the LAC of the excited state (50 mT) and increases approximately quadratic with the magnetic field. The fit yields: T_1^{mem}[lp] = 61,833 lp · [(B-0.05) T^{-1}]$^{1.68}$ and T_1^{mem}= 0.155(2) s · [(B-0.05) T^{-1}]$^{1.68(1)}$ (for B given in T).

leads to faster relaxation of the ^{14}N nuclear spin [132, 15].

The single shot readout can be used for efficient NMR measurements of the ^{14}N nuclear spin or any other memory spin. After the initialization of the ^{14}N nuclear spin (by SSR), it is manipulated by RF pulses delivered by a wire (see figure 4.7A,B). Subsequently the nuclear spin is readout in a single shot. The probability of flipping the spin is then the measurement result. A NMR spectrum is constructed by sweeping the RF frequency (see figure 4.7C). Furthermore Rabi oscillations on the ^{14}N nuclear spin have been achieved (see figure 4.7D). Please note that the total range of the measurement results in figure 4.7C and D is not symmetric. First of all the readout fidelity F limits the dynamic range between F and (1-F). Moreover, there is the (30 % probability) presence of the NV^0 charge state where the applied RF manipulation is not resonant anymore [132].

The high fidelities of the SSR achieved here facilitate the implementation of quantum error correction (QEC) [38] and quantum Fourier transformation (QFT) [47]. Furthermore in the case of nanoscale sensing the more efficient readout reduces the measurement time

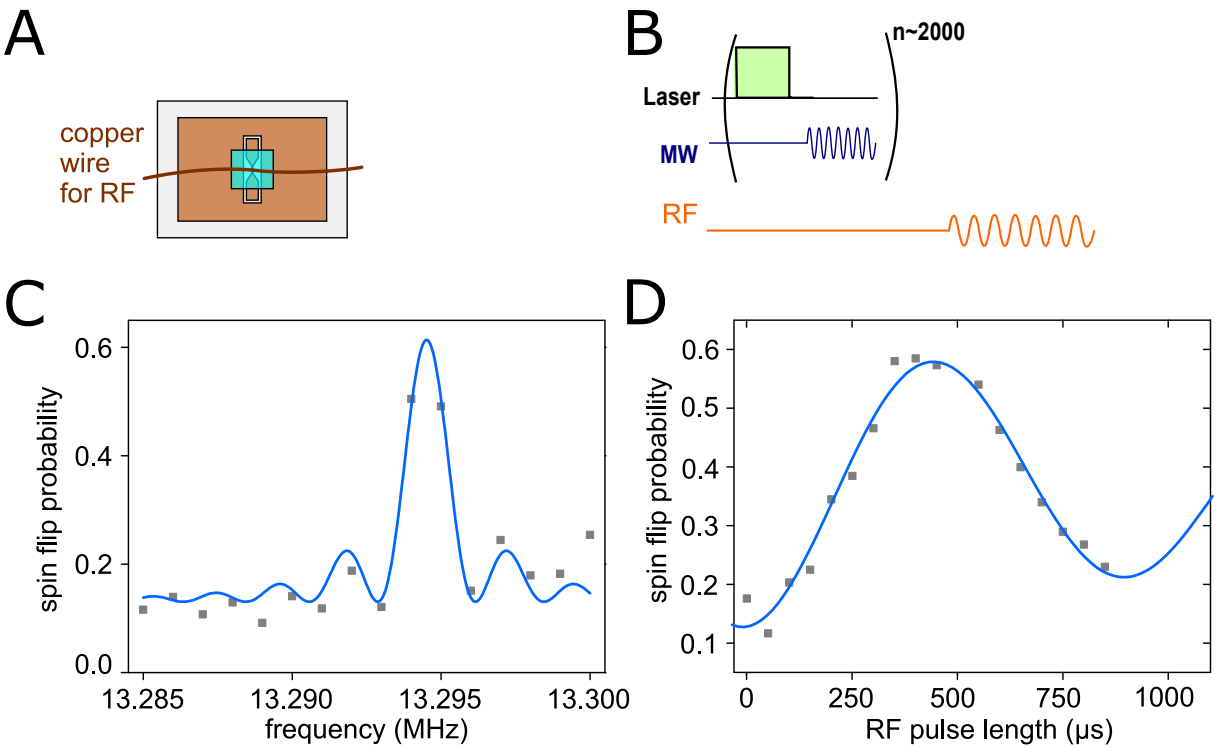

Figure 4.7.: ^{14}N NMR via Single-shot readout. A Nuclear spin manipulation is achieved by delivering RF through a wire on top of the diamond. On the bottom side of the diamond a CPW resonator provides MW control for the electron spin. B Pulse sequence of NMR conducted via SSR of ^{14}N nuclear spin. C ^{14}N NMR spectrum obtained by measuring the spin flip probability depending on the RF frequency. D Rabi measurement of the ^{14}N nuclear spin via SSR.

required to detect the signal [180]. Conventional readout would require the sequence to be applied each time before a single readout laser pulse. Especially for measurements involving long evolution times the actual sequence time can be much longer than the readout itself. Hence it becomes important to have an efficient readout step.

At high magnetic field the alignment can be conducted via the longitudinal relaxation time of the nitrogen nuclear spin. This T_1^{mem} time is sensitive to any misalignment of the magnetic field [29]. Under continuous SSR the T_1^{mem} time can be measured in dependence of the misaligned field (see figure 4.8). A longer T_1^{mem} time corresponds to a higher degree of field alignment.

4.4. Longitudinal relaxation

So far the lifetime of the ^{14}N nuclear spin has been investigated under continuous readout. In this section the T_1^{mem} time of the ^{14}N nuclear spin will be measured without optical excitation. The ^{14}N nuclear spin has been motivated as a memory spin in combination

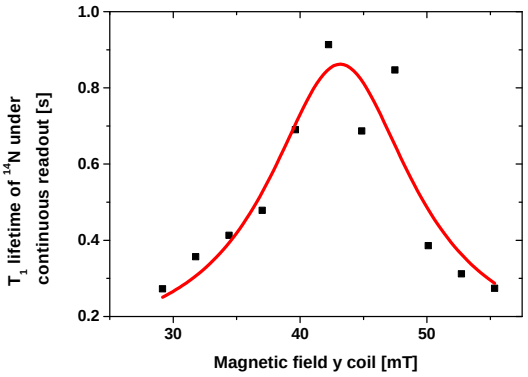

Figure 4.8.: Magnetic field alignment with SSR. The main coil (x-direction) generates a field of 1.5 T and the z-coil a field of 4 mT. Both are fixed while the y-coil is swept from 30 mT to 55 mT. At each point a fluorescence time trace with SSR of the ^{14}N is recorded. The corresponding T_1^{mem} time is determined and plotted. A Lorentzian fit function yields 43 $\pm$ 1 mT as the y-field of the maximum and a width of 14 $\pm$ 5 mT.

with the NV electron spin as the sensor spin [30]. Therefore it is crucial to find out for how long information can be stored on the ^{14}N memory spin's population.

Regarding the relaxation mechanisms of the nuclear spin, one can discuss homonuclear and electron-to-nuclear coupling. The concentration of ^{14}N spins in the studied samples is only 11 ppb. In addition to this, the quadrupole splitting of the ^{14}N for NV centers is different from the one of P1 centers. Therefore ^{14}N to ^{14}N coupling can be neglected for the considered time scales. Analogue to the case discussed in the previous section the perpendicular hyperfine interaction limits the T_1^{mem}. In absence of laser excitation, the coupling in the ground state is relevant, which is 20 times smaller than in the excited state. At the LAC of the ground state (at 102 mT) the spin flip-flop events are most dominant and set the minimum of T_1^{mem}. The T_1^{mem} time is therefore expected to show a magnetic field scaling of:

$$T_1^{\text{mem}} \sim \frac{A_\perp^2/2 + (\omega - 2.87\ \text{GHz})^2}{A_\perp^2/2} \tag{4.17}$$

with $A_\perp$=2.17 MHz. Γ_{flip} is the inverse of the T_1^{sensor} time ($\approx$ 5 ms). Hence the expected T_1^{mem} time would be on the order of 10^6 s at 1.5 T.

The T_1^{mem} time of the ^{14}N nuclear spin is measured by performing two consecutive SSR steps and increasing the waiting time in between them (figure 4.9 A). The probability not to flip the nuclear spin can be plotted in dependence of the waiting time. In order to prevent any effect induced by laser light leaking through the AOM a flip mirror blocks the excitation path for waiting times larger than 5 s. For a magnetic field of 1.35 T the T_1^{mem}

measurement has been recorded (see figure 4.9 B). The expected decay of the signal is not mono- but bi-exponential. Ultimately this can be explained by the photo-ionization induced by laser excitation. Illumination with a 532 nm laser leaves the charge state in 70 % cases in NV^- and in 30 % cases in NV^0. This means that whenever the last laser pulse is applied in the SSR there is a 30 % probability that the charge state will reside in NV^0 afterwards. The hyperfine coupling bet-ween the nuclear and the electron spin is different for the NV^0 case compared to NV^-. The main difference, however, is that the T_1 time of the electron spin in NV^0 is only approx. 13 μs [132, 15]. This is two orders of magnitude shorter than in the NV^- case. Consequently the decay related to NV^0 is expected to occur on a shorter timescale and with an amplitude of 30 % of the total range. And indeed this is what is observed in figure 4.9 B. The fit function is a bi-exponential decay function:

$$y = A_1 \cdot \exp(-x_1/t) + A_2 \cdot \exp(-x_2/t) + y_0 \tag{4.18}$$

The two timescales are $x_1 = 0.5$ s and $x_2 = 180$ s, corresponding to NV^0 and NV^-, respectively. The fidelity at time t = 0 s is 94 % which is reduced to a value of 35 % on very long timescales. The latter can be explained by the presence of three different nuclear spin states. Hence in the thermal equilibrium the probability will get reduced to one third. The two observed decay timescales have different amplitudes. The shorter lived decay shows an amplitude of 0.13 and the decay with the longer timescale shows an amplitude of 0.46. These values translate to a 23 % to 77 % ratio which approximately matches the expected 30:70 charge state ratio between NV^0 and NV^- [36]. It indicates that the bi-exponential behavior originates from the photo-ionization but does not confirm it. For this purpose additional measurements are necessary.

In the pulse sequence (figure 4.9 A) two charge state readout steps are added [132, 36] (details about charge state readout can be found in chapter 2.5). The first readout step measures the charge state in the beginning of the waiting time and the second one at the end. The second charge state SSR has the purpose of ensuring that the charge state has not changed under dark conditions. It is observed that the charge state is not altered during the waiting time, independent of the initial charge state. Now with this additional information it is possible to distinguish between the cases of NV^0 and NV^-. Indeed selecting only NV^0 cases yields a mono exponential decay with a decay time of 0.5 s (figure 4.9 C). The expected offset of the decay would be again 33 %·(1-F) with F being the readout fidelity. However the fitted offset is 50 %. This can be explained by the limited fidelity of the charge state readout. NV^- cases can falsely pass the NV^0 selection which alters the result to a higher offset. The deviation can be explained by 30 % wrong assignment of the charge readout.

For NV^- the charge state postselection of the results has been done as well. It yields

a mono-exponential decay curve (figure 4.9 D) as in the case of NV^0. The two charge state selective measurements prove that the origin of the bi-exponential behavior indeed comes from the photo-ionization. The fitted decay time in the NV^- case is 260 ± 20 s. This is the longest T_1^{mem} time of a single nuclear spin measured in a solid-state system at room-temperature. However the measured T_1^{mem} times for the NV^- case are three orders of magnitude smaller than the expected T_1^{mem} times (equation 4.17). For the calculation of the NV^0 case a Γ_{flip} of 0.1 MHz can be assumed. This leads to an expected T_1^{mem} time on the order of $\sim$ 1000 s (at 1.5 T) which deviates by three orders of magnitude from the measured value as well. The reason for this huge deviation will be discussed at the end of the section.

The T_1^{mem} time is measured for varying magnetic field both for the NV^0 and the NV^- case. In figure 4.10 the magnetic field scaling of the ^{14}N nuclear spins T_1^{mem} time is plotted. In the case of figure 4.10 A the charge state is NV^- during the dark interval and for figure 4.10 B it is NV^0. For NV^0 we can deduce a quadratic dependence from the fit:

$$T_1^{\text{mem}}{}_{NV^0} = 0.239(3)\frac{s}{T^2} \cdot B^2 \tag{4.19}$$

This quadratic dependence is expected analogue to the case of continuous readout discussed in the previous section. There is however no LAC involved and therefore we expect the minimum at zero magnetic field. The hyperfine coupling between the NV^0 and ^{14}N nuclear spin is 3.03 MHz. It is assumed that the perpendicular hyperfine constant $A_\perp$ is on the same order. This does not differ much from the NV^- value for $A_\perp$ (2.17 MHz). However due to large spin-orbit interaction the T_1 time of the NV^0 electron spin is more than 2 orders of magnitude shorter than of NV^- [132]. According to the simulation in [15] T_1 of NV^0 should be around 13 μs. This represents a fast fluctuating noise source for the ^{14}N nuclear spin and leads to a substantially shorter $T_1^{\text{mem}}{}_{NV^0}$ time.

Indeed the values for $T_1^{\text{mem}}{}_{NV^-}$ are longer (see figure 4.10 A). However the magnetic field scaling is not solely following a quadratic relation. While for small magnetic fields we observe a quadratic behavior, T_1^{mem} seems to saturate for high magnetic fields. The results can be fitted by the sum of a magnetic field dependent term and a constant term:

$$T_1^{\text{mem}}{}_{NV^-} = \left[[1.7(1.2) \cdot 10^3 \frac{s}{T^2} \cdot (B - 0.1\ T)^2]^{-1} + [260(40)s]^{-1}\right]^{-1}. \tag{4.20}$$

The quadratic magnetic field dependence is expected from the hyperfine part. The origin of the constant term on the other hand is unclear and further measurements are necessary. Furthermore the measured T_1^{mem} times are three orders of magnitude smaller than the expectation. Interaction with phonons via the spin-orbit coupling could be one limiting possibility. However the latter is negligible for the ground state. One explanation could be that the here used ^{14}N nuclear spin exhibits a quadrupole interaction. The electric

quadrupole moment might experience a different electric field upon vibration at the position of the nucleus. This would open a channel for interaction between phonons and the nuclear spin which is usually not observed. Nevertheless with a measured T_1^{mem} of 260 s the ^{14}N memory spin shows its potential as a storage medium for example in high resolution NMR experiments [30].

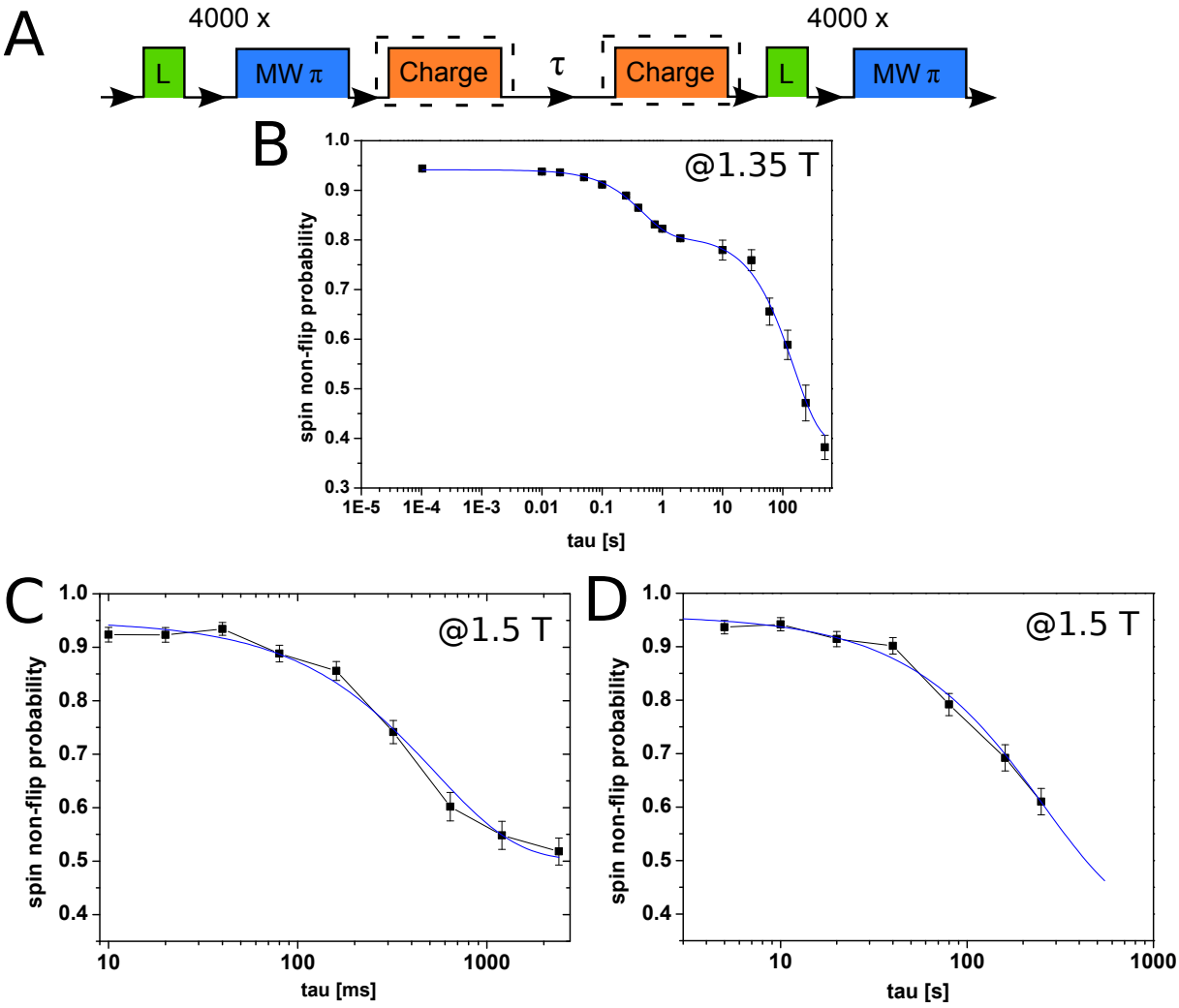

Figure 4.9.: T_1^{mem} **measurement of** ^{14}**N** . A Pulse sequence of the ^{14}N T_1 measurement is shown. Subsequent SSR steps of the nuclear spin with 4000 repetitions are interrupted with a varying waiting time τ. In addition to the SSR, charge state SSR (see [36]) can be added in order to post-select the different charge state cases. For charge state SSR a 594 nm laser with a intensity of 1 μW is applied for 20 ms. B The graph shows the T_1^{mem} lifetime at 1.35 T. The data shows two different decay constants, 0.5 s and 180 s. The fast decay corresponds to those measurement runs, during which the NV center resides in the NV^0 charge state, the slow decay corresponds to the NV^- case. By using charge state readout and data post selection, one can isolate pure NV^0 and NV^- measurements. C The measurement for the NV^0 charge state and D for NV^- is performed at a B-field of 1.5 T.

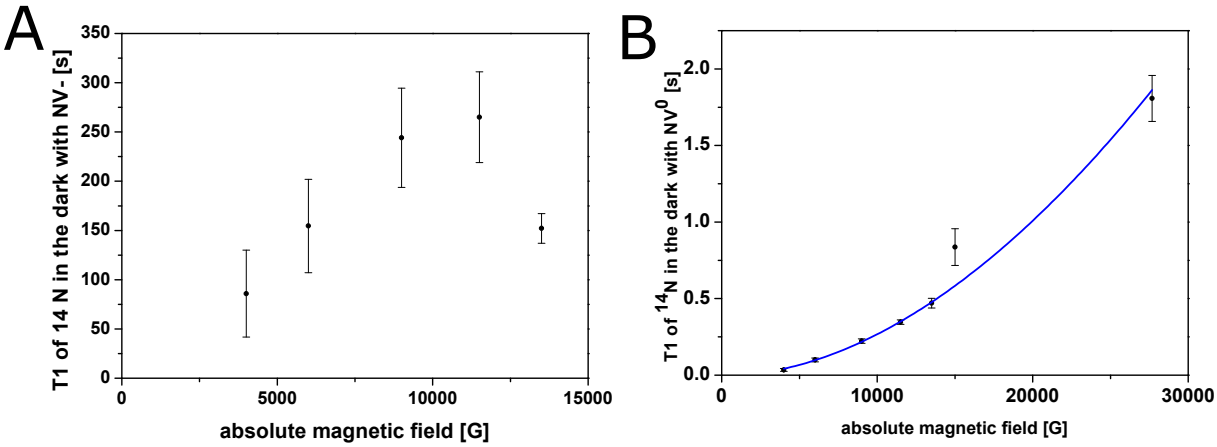

Figure 4.10.: Magnetic field scaling of ^{14}N lifetime. The T_1^{mem} measurements are performed at various magnetic field points. A shows the magnetic field scaling of T_1^{mem} time of ^{14}N in the case when the NV center resides in the NV^- charge state during the waiting period. B shows the corresponding case of NV^0.

5. Nanoscale NMR spectroscopy based on sensor-memory entanglement

5.1. The nanoscale regime

The quest for a technique that is capable of detecting NMR signal of nanometer scale sample volume lasted for decades. It was motivated by the poor sensitivity of conventional NMR requiring millimeter scale samples, far greater than the size of single molecules. The signal in conventional NMR is based on the weak thermal polarization degree and therefore limits its sensitivity. Thermal polarization depends on the applied magnetic field and temperature (see equation 1.15). At room-temperature (T = 300 K) and at an applied magnetic field of B = 3 T the thermal polarization of ^{1}H yields a value of 10^{-5}. Micro-coils increase the sensitivity and as a result the detection volume is reduced to the range of $(3\ \mu\text{m})^3$ [4, 5]. The nanoscale molecular regime was reached for the first time by the MRFM technique [12, 66, 13, 181, 71] (see chapter 1.5). This technique provides unprecedented sensitivity of NMR detection but requires low temperatures and vacuum conditions. The latter requirements restrict its application to a limited number of samples.

The NV center in diamond, on the other hand, possesses an electron spin, capable of sensing its environment at ambient conditions. It can be optically readout and combined with the known methods of EPR and NMR. And indeed single shallow NV centers have demonstrated the detection of nuclear spins out of a $\sim (10\ \text{nm})^3$ sample volume, located on top of the diamond surface [24, 25]. One of the main differences between conventional NMR and nanoscale NMR is that the latter is based on detection of statistically polarized nuclear spins rather than thermally polarized [182]. Statistical polarization becomes significant for small number of nuclear spins. Here the randomly orientated nuclear spins build up a net magnetization which is not averaged out. This magnetization fluctuates on the timescale of T_1 and changes in amplitude over time. The number of statistically polarized spins is $\sqrt{N}$ with N being the total number of spins. The statistical polariza-

tion can be seen as the variance of the Boltzmann distribution 1.15. While the degree of thermal polarization is independent from N the number of nuclear spins, the average statistical polarization increases with the inverse of the square-root of N spins.

$$SP = \sqrt{\frac{I+1}{3I}\frac{1}{N}} \tag{5.1}$$

[183]. In conventional NMR the statistical polarization is negligible. However by decreasing the number of spins in the detection volume, the statistical polarization can at some point start dominating over the thermal polarization. This critical number of spins marks the cross-point between the thermal and the statistical polarization:

$$N_C = \frac{3}{I(I+1)}\left(\frac{k_B T}{\hbar\gamma B}\right)^2 \tag{5.2}$$

For T = 300 K and B = 3 T the critical number of ^{1}H nuclear spins is $2 \cdot 10^9$. A solution with organic molecules typically has a ^{1}H spin density of 50 nm^{-3}. For a detection volume of e.g. (10 nm)^3 the number of ^{1}H nuclear spins is $5 \cdot 10^4$ and thus orders of magnitude below the critical number. The detection volume contains the number of spins that contribute to 50 % of the signal.

In the case of NV based NMR detection, nearby (typically in a distance of 10 nm) statistically polarized nuclear spins are inducing a phase accumulation on the NV electron spin. With the nanoscale NMR detection at ambient conditions the NV center in diamond offers new possibilities for NMR.

NMR spectroscopy requires high spectral resolution which is not straightforward to achieve in nanoscale NMR. Chapter 1.3 has described in detail how the interpretation of high resolution NMR spectra can be used to identify molecules within a sample. The main effects governing the shape of the NMR spectrum for example of liquids are chemical shift and J-coupling. Chemical shift is the shielding or anti-shielding effect of the applied magnetic field at the nuclear spin position through the local electron density. The effect increases with the applied magnetic field. This has lead to the definition of a relative spectral resolution in ppm which is independent of the magnetic field: $\delta = \frac{\omega - \omega_{\mathrm{ref}}}{\omega_{\mathrm{ref}}}$ (see also equation 1.19). As introduced in chapter 1.3 the values of chemical shift depend i.a. on the electron negativity of the atom and can be in the range of $\sim$ 100 ppm for ^{19}F and $\sim$ 13 ppm for ^{1}H (see figure 1.1). Hence for ^{1}H NMR spectroscopy a relative spectral resolution of at least $\sim$ 1 ppm is required for molecule identification. Generally the spectral resolution depends on the maximum achievable phase accumulation time T:

$$\delta\nu = \frac{1}{\pi T}. \tag{5.3}$$

In this definition the magnetic field does not occur. However increasing the applied magnetic field facilitates the observation of NMR peaks originating from chemical shift

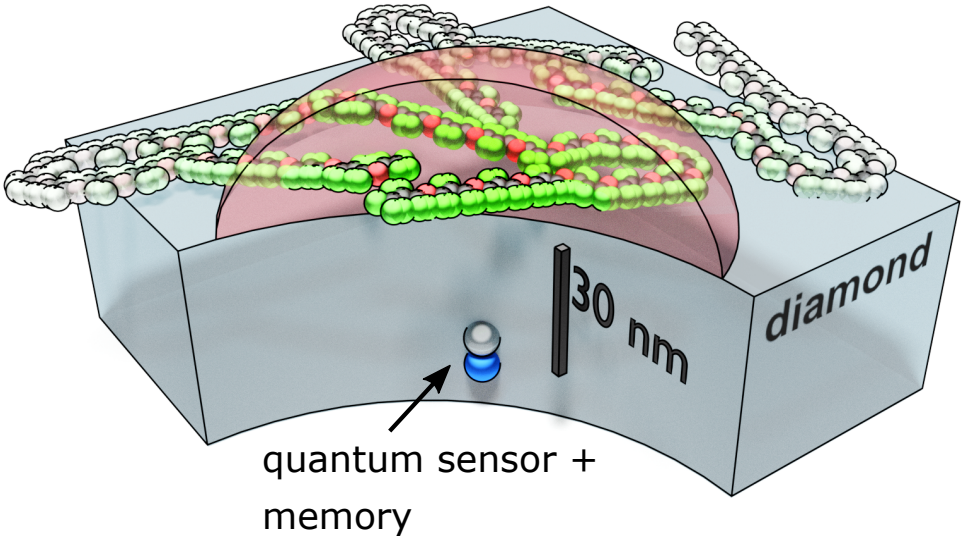

Figure 5.1.: Sketch of NV nanoscale NMR. The NV center electron spin (quantum sensor) and its associated nuclear spin (quantum memory) are located approximately 30 nm deep in the diamond lattice. The sample of interest contains molecules and is placed above the diamond surface. The molecule indicated is perfluoropolyether (PFPE). The nuclear spins of the molecules generate a signal which is detected by the quantum sensor. The coupling strength between the sensor and the sample spins is depending on the distance. Therefore a volume can be defined from where more than 50 % of the signal is originating. This so-called detection volume is indicated by a red coloured hemisphere. (designed by Ingmar Jakobi).

effects. At 0.03 T the ^{1}H chemical shift of 1 ppm translates into a shift of 1.3 Hz in absolute frequency units. Increasing the field to 3 T corresponds to a shift of 127.7 Hz. The magnetic field B can be included in equation 5.3 which leads to the definition of a relative spectral resolution:

$$\Delta\delta = \frac{2}{\gamma \cdot B} \cdot \frac{1}{T}. \tag{5.4}$$

The dependence of this parameter (in ppm) to the applied field B and the phase acquisition time T is plotted in figure 5.2. In addition to this a line shows the maximum observed ^{1}H chemical shift range and indicates which magnetic field B and time T is required to resolve chemical shift peaks. It becomes clear that it is beneficial to apply a high magnetic field. This is one of the reasons why most of the NV nanoscale NMR experiments of this study are carried out at 3 T. Contrary to the chemical shift, the J-coupling is independent from B but depends on T. Therefore the (typically observed) frequency shifts for ^{13}C -^{1}H and ^{1}H-^{1}H J-couplings are plotted with vertical dashed lines in the 2d plot. The main question is what is limiting the maximum achievable phase accumulation time T.

First of all the sensor itself sets a constraint to the available time. Depending on the used pulse sequence this limit can be the coherence time T_2^{sensor} or the longitudinal

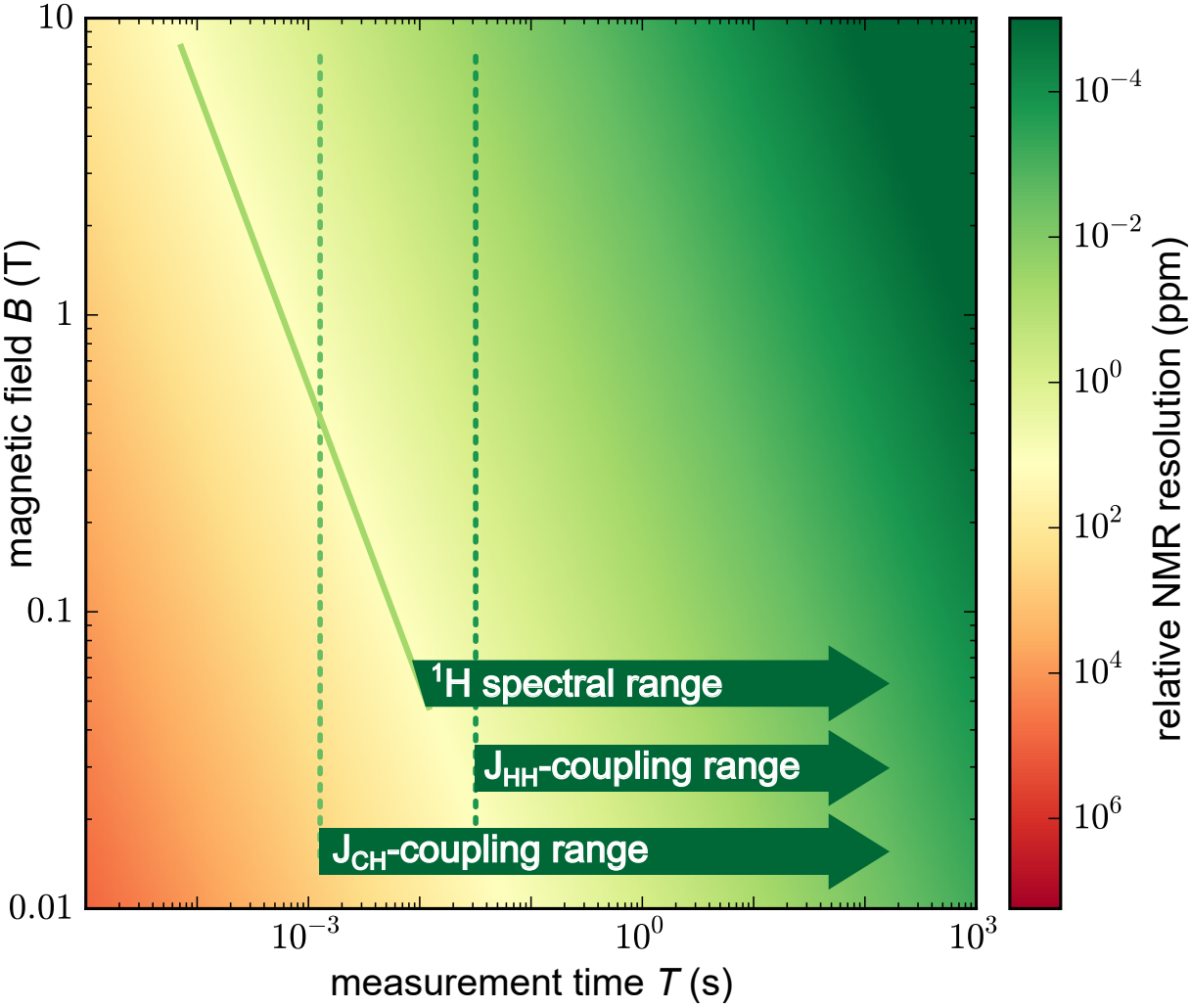

Figure 5.2.: Relative spectral resolution in ppm and required parameters for molecular structure analysis with ^{1}H NMR spectroscopy. A 2-dimensional plot for the relative spectral resolution [ppm] defined in formula 5.4 is shown. On the y-axis the applied magnetic field B is varied and on the x-axis the measurement time T. The dashed vertical lines mark the required parameter regime for resolving proton-proton and proton-carbon J-couplings (J_{HH} and J_{CH}). Solid green line refers to the maximum observed ^{1}H chemical shift in known molecules ($\Delta\delta < 13$ ppm).

relaxation time T_1^{sensor}. The second limitation is the T_2^* of the sample spins. As explained in chapter 1.1, for solid state samples the T_2^* of the nuclear spins is short due to dipolar interaction among the spins. For liquid state samples on the other hand the situation is different. Due to the motional averaging effect the dipolar interaction is canceled out and this results in a long T_2^* time. For liquid state samples a third limitation has to be pointed out, which is the diffusion time T_D. The spins closer to the sensor are contributing stronger to the NMR signal than the one farer away. The diffusing spins in the liquid can at some point have a very large distance to the sensor spin and become uncorrelated

to them. Hence they will not contribute to the NMR signal anymore. This time scale can be described by the diffusion time T_D. Due to the randomly changing magnetic field amplitude B_{rms} generated by the statistically polarized spins, the field is inhomogeneously distributed over the sample. Consequently the spins that replace the previously correlated spins would generate a different signal. As a result the diffusion time T_D sets another limitation to the spectral resolution. Therefore three time scales limit the relative spectral resolution:

$$\Delta\delta = \frac{2}{\gamma \cdot B} \cdot \underbrace{\left(\frac{1}{T_2^{\text{sensor}}} + \frac{1}{T_2^*} + \frac{1}{T_D} \right)}_{T^{-1}}. \tag{5.5}$$

In this chapter it will be explained in detail how it is possible to increase the relative spectral resolution 5.5 by a factor of 10,000 compared to previous studies in order to record chemical shift resolved NMR spectra. Figure 5.3 shows a schematic representation of the NV nanoscale NMR sensor. As introduced in chapter 2.6 the sensor spin in diamond is placed in a room-temperature bore of a superconducting vector magnet. The magnet delivers a field strength of up to 3 T (main coil). The fluorescence response of the sensor is readout optically by a confocal microscope. The nuclear spins are manipulated by a RF wire and the electron spin by a MW waveguide to antenna structure. The sample of interest is placed right on top of the diamond surface and the sensor is capable of detecting the NMR signal of the sample.

In the following the structure of the chapter will be described. The title of each part is italicized. In the second section *Sensing of AC signals with NV centers* the previous and ongoing work in the field will be reviewed and the measurements of this study will be set in context. The next part is devoted to the *Characterization of shallow NV centers*, which is the first step towards NV nanoscale NMR. The *NMR with spin locking* part shows the first successful attempt of this work to detect external (^{1}H) spins. The following section describes the *Hamiltonian of sensor, memory and sample spins*. The interplay between the sensor, memory and sample spins which is underlying the high resolution NV nanoscale NMR experiments is explained in the *Quantum metrology framework* section. The *Sample signal* part explains how the signal is generated. After that the dependence of the signal to the NV depth is further discussed for *Depth determination*. In the next part the *Spatial diffusion on the nanoscale in liquids* is investigated. With all the necessary ingredients at hand high resolution *Liquid state NMR spectroscopy* experiments are described. This section first starts with Ramsey measurements of liquids containing ^{19}F spins and ends with measurements on ^{1}H spins. Afterwards *Spin diffusion on the nanoscale in solids* is examined. Along the same lines the *Solid state NMR spectroscopy* part deals with Ramsey and homonuclear decoupling experiments on solid-state samples with the goal

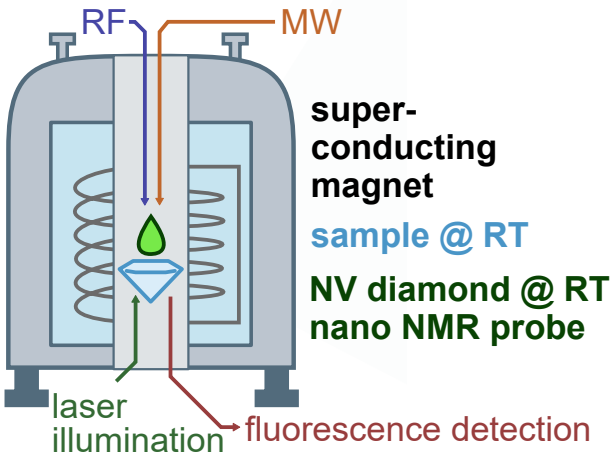

Figure 5.3.: Schematic representation of the NV nano NMR sensor. The diamond containing the shallow NV centers is situated in the room-temperature bore of a superconducting vector magnet. In its main direction it can produce a magnetic field of 3 T and 0.2 T in the two other directions. The sample is either in a liquid or a solid form and is placed on top of the diamond surface. Excitation of single NV centers is conducted by illumination of a 532 nm laser through a high-NA oil objective. The fluorescence response is collected by the same objective and recorded by an APD. Electron spin manipulation is conducted with microwaves in the frequency range of 60 GHz to 90 GHz. Hollow waveguides are used to guide the microwaves to the diamond lattice. The memory spin and the sample spins are manipulated by RF excitation through a wire.

of achieving high spectral resolution. The nanoscale NMR measurements on liquids and solids can be combined to perform *Multilayer NMR* spectroscopy. For future applications it is important to analyze the *Sensitivity of the technique*, which is discussed in a section. The NMR method of this study is compared to other methods in the section with the title *Comparison to other NMR methods*. The chapter ends with an *Outlook* which describes how NV nano NMR spectroscopy could be developed further and have a larger impact. The work presented in this chapter has been published in [184] and [15].

5.2. Quantum metrology with NV centers

In all NV NMR applications the electron spin of the NV center in diamond serves as the sensor spin. The sensor spin needs to be in close proximity of the sample spins as the B_{rms} field drops by $1/d^{3/2}$ with d being the sensor depth. For the detection of spins outside of the diamond it is therefore necessary to create shallow NV centers close to the

surface. In addition to this the challenge is to reach sufficiently long T_2^{sensor} and T_1^{sensor} times of the NV electron spin. In chapter 2.2 the different methods for the creation of NV centers are described. There is an on-going effort to increase the yield of NV center creation and improve the coherence properties of the shallow NV centers [185, 186]. Recently the investigation of low energy nitrogen ion implantation has lead to interesting findings [187]. The di-vacancy (V_2) defect has been identified as a dominant source of spin relaxation. Its formation during the annealing process can be suppressed by charging the implantation induced vacancies. The latter is achieved by implanting the nitrogen ions through a boron doped diamond layer which represents a charge layer of free carriers. This approach not only increases the spin coherence times by a factor of ten but also doubles the NV center yield. Furthermore diamond samples with a diluted nuclear spin bath (^{12}C concentration exceeding 99.995 %) also lead to an improvement in coherence times. In these samples bulk NV centers can yield T_2^{sensor} times reaching the ms scale [15]. Indeed shallow NV centers benefit from the diluted spin bath as well. The presence of noise sources on the diamond surface or in its vicinity limit the T_2^{sensor} times of shallow sensor spins [188, 189, 190]. Therefore T_2^{sensor} times are typically shorter for NV centers closer to the diamond surface.

Statistically polarized ^{1}H spins in a volume of $(5\text{ nm})^3$ can generate a net magnetic field of 390 nT at the position of a 7 nm distant sensor spin [24]. The detection of this tiny NMR signal requires a minimal coherence time as will be discussed in the following. For the measurement of its magnetic field environment, the Ramsey sequence can be applied on the sensor spin (as discussed for nuclear spins in chapter 1.2). After the initial $\pi/2$ pulse the sensor spin becomes sensitive to the magnetic field environment. The latter results in an accumulation of phase which can be mapped onto the sensor spin population with a second $\pi/2$ pulse and finally readout. The phase can be acquired for a time period limited by the decay time of the sensor spin, which is T_2^*. However application of dynamical decoupling (DD) sequences allows to exploit the longer T_2^{sensor} time (see chapter 1.2). These sequences are refocusing the sensor spin by filtering out noise frequencies (e.g. created by the ^{13}C nuclear spin bath) that are slower than the refocusing frequency [17, 18, 19, 20]. The most basic form of dynamical decoupling is the Hahn echo pulse sequence which adds a single π pulse in the center of the phase accumulation time of a Ramsey experiment [49]. It can be extended by more π pulses with different phase cycles e.g. XY-4 and KDD-XY. These sequences not only filter out spin noise but also counteract detunings and imperfect π pulse lengths. This leads to coherence times T_2^{sensor} reaching T_1^{sensor} and has been shown for the NV center [19, 191]. By applying DD sequences, phase accumulation can be achieved for time scales sufficient for the detection of the NMR signal. However as pointed out the DD sequences also filter out the spin

noise, coming from the sample. Therefore it is important to make the sequences selective to the resonance frequencies of the nuclear spins. Two approaches have been followed in that regard which lead to the detection of nanoscale NMR.

The first demonstration of NV nano NMR has been achieved independently in two labs (University of Stuttgart and IBM Research). Mamin et. al at IBM Research has used comparatively deep sensor spins (10 - 50 nm) which are less sensitive to spin noise on the surface [25]. Applying a Hahn echo sequence is therefore sufficient to achieve a few hundred μs in coherence time. A PMMA layer containing ^{1}H spins has been placed on top of the layer. Selectivity to these ^{1}H spins has been achieved by flipping the magnetization of ^{1}H spins. For this purpose resonant RF π pulses are applied on the ^{1}H spins in both phase accumulation periods. On the other hand the sensor spins in the work by Staudacher et. al (University of Stuttgart) have a depth of only 7 nm. Since their proximity to the diamond surface shortens their coherence time significantly, a higher order dynamical decoupling sequence (XY8-112) needs to be applied [24]. Each dynamical decoupling is associated with a filter function in the frequency domain. Depending on the rate of the π pulse application, the filter function is moving in frequency. Hence it can be brought in resonance with the transition frequencies of the nuclear spins. At this frequency point the sensor spin experiences decoherence which can be measured. With this so-called Dynamical Decoupling Noise Spectroscopy (DDNS) method ^{1}H spins in liquid and solid samples have been detected.

The two approaches differ in the active or passive detection of nuclear spins. In both cases the sample volume that accounts for more than half of the signal is coming from a half-sphere on the diamond surface with a diameter on the order of the NV depth. The minimal achieved detection volume of $(5\text{ nm})^3$ is 12 orders of magnitude smaller than required in conventional NMR.

Next the nanometer detection volume can be exploited for imaging purposes. There are mainly two possibilities for its implementation. The first one is the combination with scanning probe microscopy and the second one is widefield imaging. Both have been realized with the NV center in diamond. An AFM tip containing the sample has been scanned over the NV center in diamond [43]. During scanning the filter function of the DDNS sequence is on resonance to the sample spins. Once the sample spins are located within the detection volume of the sensor spin, the NMR signal is detected. A resolution of ≈ 10 nm has been achieved by this technique. It is limited by the distance between the sample spins and the sensor spin. In one work a structure containing ^{19}F and ^{1}H spins was imaged with chemical contrast by exploiting their different gyromagnetic ratio [43]. In a parallel work the imaging of a PMMA sample attached to a quartz tuning fork is demonstrated [44]. It is also possible to scan the sensor spin and have the sample station-

ary. For example integration of the sensor spin into the AFM tip is possible [192]. The widefield approach on the other hand uses an ensemble of sensor spins to detect nuclear spins with a resolution limited by optical diffraction[1] [27, 193]. Here a sample with ^{1}H and ^{19}F enriched areas has been imaged [27].

One of the aims in NV nanoscale research is to achieve a sensitivity of detecting single nuclear spins outside of the diamond. For this purpose the distance of the sensor spins to the diamond surface has to be reduced while maintaining the coherence properties. Detection of NMR based on a shallow NV center with a depth of only 1.9 nm has been shown [26]. Furthermore the sensor spins sensitivity has been increased to the point where detecting single nuclear spins becomes possible [194]. Multiple single nuclear spins located in a silica layer (placed on top of the diamond) have been detected and their positions relative to the sensor determined [194]. The first detection of single proton spins has been accomplished by exploiting optically inactive electron spins on the diamond surface as reporter spins [46]. Due to their higher gyromagnetic ratio the dipole-dipole coupling to these so-called dark spins is stronger compared to nuclear spins. Hence shorter phase accumulation times in the used DEER sequence are sufficient to detect the signal of the nuclear spins. The much smaller distance of the dark spins to the nuclear spins facilitates their detection. For this purpose the DEER sequence is modified in order to detect single proton spins next to the dark spins [46]. The detection of single nuclear spins paves the way to the yet to achieve imaging of single molecules. In fact the relative position of the nuclear spins is encoded in the hyperfine couplings [46]. A magnetic field gradient can further increase the spectral shift between the nuclear spins in the obtained NMR spectrum. Hence it facilitates the localization of each single nuclear spin. In the case of the NV center, magnetic write heads have been characterized as a source of a magnetic field gradient and a gradient of 10 mT/nm has been achieved [195].

While in the proof-of-principle NMR experiments the samples were not interesting for biology or chemistry the recently detected samples might get more attention for the prospected applications. For example single protein NMR detection via shallow NV centers in diamond has been demonstrated [196]. Furthermore Nuclear quadrupole resonance (NQR) spectroscopy of hexagonal boron nitride (hBn) samples has been shown [197]. The increased sensitivity and proper sample preparation even allowed the detection of a monolayer of hBn [197]. This opens the route to a quantum simulator based on an array of nuclear spins in a 2d material [198].

For all NMR experiments discussed so far achieving a high spectral resolution has not been the focus. For example in the first NMR detection paper by Staudacher et al the

[1] More information on the limit set by optical diffraction and methods to overcome it can be found in chapter 6.

linewidth of the NMR peak is 14 kHz. This corresponds to a relative spectral resolution of $\sim$ 16000 ppm (see eq. 5.5) at a magnetic field of B = 0.02 T. However for molecular structure analysis it is important to resolve the chemical shift and J-coupling splittings in the NMR spectrum (see chapter 1.3). The typical ^{13}C -^{1}H J-couplings are in the range of $\sim$ 135 Hz and ^{1}H-^{1}H J-couplings are even smaller: $\sim$ 7 Hz. The chemical shift of ^{19}F spins can vary in a range of 100 ppm and ^{1}H spins show a range of 13 ppm (see figure 1.1 and 5.2). It becomes clear that molecule identification is not possible with the previously achieved spectral resolution.

Three time scales are governing the achievable resolution as indicated in equation 5.5. The first limitation comes from the sensor spin itself [24]. The DD sequence in DDNS decays and looses all its correlation to the nuclear spins on a timescale of T_2^{sensor}. One route to overcome this is to perform correlation spectroscopy [50, 199]. Here the phase accumulation or sensing time is separated into two parts. In the center the phase information is stored on the electron spin population. A correlation between the two sensing parts then yields the NMR signal. The maximal possible length of the central storage part limits the spectral resolution. The corresponding decay time scales is the T_1^{sensor} time. Consequently T_2^{sensor} can be replaced in equation 5.5 by the longer T_1^{sensor}:

$$\Delta\delta = \frac{2}{\gamma \cdot B} \cdot \underbrace{\left(\frac{1}{T_1^{\text{sensor}}} + \frac{1}{T_2^{*}} + \frac{1}{T_D} \right)}_{T^{-1}}. \tag{5.6}$$

The T_1^{sensor} time for bulk NV centers is $\sim$ 5 ms, which would correspond to a spectral resolution of $\sim$ 64 Hz (equation 5.3). This would represent a large improvement compared to previous studies. It would however still hinder e.g. the detection of ^{1}H-^{1}H J-couplings. Furthermore the T_1^{sensor} times of shallow NV centers are typically much shorter than of bulk NV centers [188, 189, 190].

Recently a novel quantum metrology method has been proposed and realized by three different groups (Jelezko, Degen and Walsworth) which claim to achieve a sensor independent spectral resolution [200, 201, 39]. It is named Qdyne (by the Jelezko group) and combines conventional heterodyne detection with sensing via a quantum probe (NV electron spin). The idea is based on the coherent nature of a signal during the course of a long measurement. The signal can e.g. be an oscillating magnetic field generated by a signal generator. In this case the sensing result of the sensor spin will depend on the signal's initial phase relative to the beginning of the measurement. Typically this signal phase is averaged out when multiple measurements are conducted. However with the help of an external clock of high precision this initial signal phase can be tracked by subsequent sensing steps. Consequently a correlation between the multiple measurement results in a reconstruction of the sample signal. The best achievable spectral resolution of a test

signal of 0.6 mHz is independent of the sensor relaxation time. It is only limited by the stability of the external clock. Moreover the precision in frequency estimation scales with $1/\mathrm{T}_{total}^{3/2}$ instead of $1/\mathrm{T}_{total}^{1/2}$ which is the case in correlation spectroscopy, with T_{total} the total measurement [200]. In comparison Qdyne continuously acquires the sample phase. In contrast to that in correlation spectroscopy the sensor spin is not accumulating any phase during the storage time.

Despite these advantages the cited work failed to detect high resolution NMR spectra of nanoscale samples obtained with a single sensor spin. With the Qdyne method high spectral resolution has only been achieved with an ensemble of $5 \cdot 10^8$ sensor spins detecting a volume of $(10\ \mu\mathrm{m})^3$ containing nuclear spins. The detection is based on thermal polarization and makes the μm scale on the sensor and the sample spins side necessary. The signal generated by thermally polarized spins does not alter spatially and hence is not lost by diffusion. The other reason for the failing attempt to combine high spectral resolution and nanoscale NMR detection is measurement back-action. For a single nuclear spin or a nanoscale ensemble the continuous projection of the sensor leads to back-action on the nuclear spin which limits its coherence lifetime and broadens the NMR peak. In fact all previously obtained NV spin based NMR spectra are broadened by measurement back-action [15]. However for μm scale distances to the sample spins like in the mentioned work the back-action effect decreases in accordance to the hyperfine interaction.

This work presents solutions to overcome the obstacles of nanoscale NMR and achieves nanoscale NMR detection along with high spectral resolution. A novel method is introduced which exploits a quantum memory based on the host nitrogen nuclear spin. In chapter 5.13 the quantum memory approach will be compared to the other NMR methods including Qdyne.

5.3. Characterization of shallow NV centers

The NV nanoscale NMR work is highly depending on the successful formation of NV centers close to the diamond surface. Moreover long T_2^{sensor} times are required for the detection of nanoscale NMR signal. Hence it is necessary to characterize the shallow NV centers thoroughly before the actual NMR measurement.

The experimental setup does set constraints onto the diamond sample that can be used. The main coil with a field strength of 3 T is much stronger than the alignment coils with 0.2 T. Hence it is necessary to match the main coil's orientation with one of the crystal axes in the diamond lattice. Since the main coil is pointing along the optical path, the NV axis is required to be perpendicular to the surface. Diamond crystals with $\langle 111 \rangle$ surface orientation do have this crystal axis and can therefore be used. Furthermore spin control

of the shallow NV centers is performed by the CPW resonator located on the other side of the diamond. Simulations and experiments show that with the available MW power the distance between the sensor spin and the MW antenna should not exceed 100 μm (see chapter 3). Otherwise the Rabi frequency is too small to achieve the full sensor spin resonance contrast ($\approx$ 30 %). Consequently the diamond's thickness needs to be less than 100 μm. It is very challenging to get a suitable $\langle 111 \rangle$ diamond membrane since $\langle 111 \rangle$ diamond surfaces are the hardest to polish.

The $\langle 111 \rangle$ diamond used for the NV nanoscale NMR is provided by Prof. Isoya from the University of Tsukuba in Japan. It is laser-cut from a low strain, (100) high pressure and high temperature (HPHT) diamond. Its surfaces are polished and its dimensions are 2 mm x 2 mm x 0.088 mm. The concentration of P1 centers is 11 ppb. Its ^{12}C abundance is 99.995 %.

The $\langle 111 \rangle$ diamond membrane with its diluted nuclear and electron spin provides a good basis for the creation of shallow NV centers. The facilities in Stuttgart provide the possibility of $^{15}N^+$ and He^+ implantation with energies up to 10 keV and a variable implantation dose. In contrast to previous studies [194, 46] the goal of this work is not to detect single nuclear spins. Hence it is not necessary to place the sensor spin as close as possible to the diamond surface. The single NV electron spins can be located deeper in the diamond as long as they are capable of detecting a nanoscale ensemble of nuclear spins. In the discussion of section 5.8 it will be shown that for example a 30 nm deep NV center requires a sensing time of 100 μs for achieving 50 % NMR contrast (for a typical spin density). At this large distance to the surface compared to previous studies [24] the implantation induced noise should play a minor role and the time scale of 100 μs should be within the realms of possibility.

The focus in this work is to achieve the best possible spectral resolution. Equation 5.6 shows that the diffusion time T_D plays a crucial role for the achievable spectral resolution. The diffusion time T_D is ultimately related to the detection volume and increases proportionally to it. On the other hand the detection volume scales by $\sim$ d with the sensor spin depth d (see chapter 5.8). As a result T_D increases linearly with the NV depth d as well.

Previous NV NMR studies have used an energy of 2.5 keV for the implantation of $^{15}N^+$ and achieved a NV depth of $\sim$ 7 nm [24]. In this work an implantation energy of 5 keV is selected to achieve larger depths of the NV centers. This comes along with the ion channeling effects in $\langle 111 \rangle$ diamond which are expected to be more pronounced than in the $\langle 100 \rangle$ case. As a result larger depths are expected compared to other studies. The $^{15}N^+$ are implanted with a dose of $5 \cdot 10^9$ cm^{-2} in order to get single NV centers in a diffraction limited spot. After the implantation, the diamond is annealed at 950 °C for 2

hours. The latter leads to diffusion of vacancies to the surface and enables the formation of stable NV centers.

Various steps have to be taken before a NV center can be found, which is suitable for NMR application. After mounting the diamond sample into the setup, the magnetic field is aligned along the NV axis. The alignment is conducted at the LAC of the excited state (at 0.05 mT) as described in chapter 4.2. Here the fluorescence response is very sensitive to misaligned fields. Once the magnetic field is aligned at 0.05 mT and the alignment angle is known, the absolute magnetic field along the NV center axis can be increased to 3 Tesla. The sweep to 3 Tesla does change the angle slightly as the coils are not perfectly perpendicular to each other and there are hysteresis effects. However the so introduced mismatch between the NV axis and the field direction does not significantly affect the sensor or memory spin properties. If required, magnetic field alignment at 3 Tesla is possible by measuring the T_1^{mem} time of the nitrogen nuclear spin for different field angles (see chapter 4.3).

The fluorescence level is the first indicator for a suitable single NV center and excludes three out of four NV centers as they are misaligned. The achieved spin contrast in a pulsed ODMR measurement is the second indicator and should ideally reach 30 %. It might be reduced due to local background fluorescence coming from the surface or due to charge state instability. Finally the T_2^{sensor} time needs to be longer than 100 μs for the expected depths of more than 30 nm. The sequence used for high resolution NMR is a Hahn echo type measurement and will be described in section 5.6. Hence the crucial parameter is the T_2^{sensor} time measured by a Hahn echo sequence. The latter has been measured by exploiting the ^{15}N nuclear spin as a memory spin for SSR. Figure 5.4 shows the result of a Hahn echo measurement yielding a T_2^{sensor} time of 539 $\pm$ 23 μs. The measured T_2^{sensor} times range from 1 μs to 550 μs. Approximately 3 % of the NV centers with the correct crystal orientation yield a T_2^{sensor} time of more than 100 μs. The reason is that due to the high implantation energy and ion channeling effects the ions are scattered in a wider area. Especially the shallower NV centers (d $<$ 10 nm) are sensitive to the spin noise coming from the vacancy related defects and from noise coming from the surface. In addition to this the diamond sample contains an inhomogeneous concentration of boron impurities which act as electron acceptors and can alter the charge state. In section 5.8 the depth of the NV centers is determined. It can be noticed that the sensor spins with T_2^{sensor} times exceeding 300 μs also have a depth d of more than 30 nm. This underlines the dependence of T_2^{sensor} times and the distance to the diamond surface. Various sensor spins are found which show a T_2^{sensor} time sufficiently long for NMR detection and can be applied for the latter.

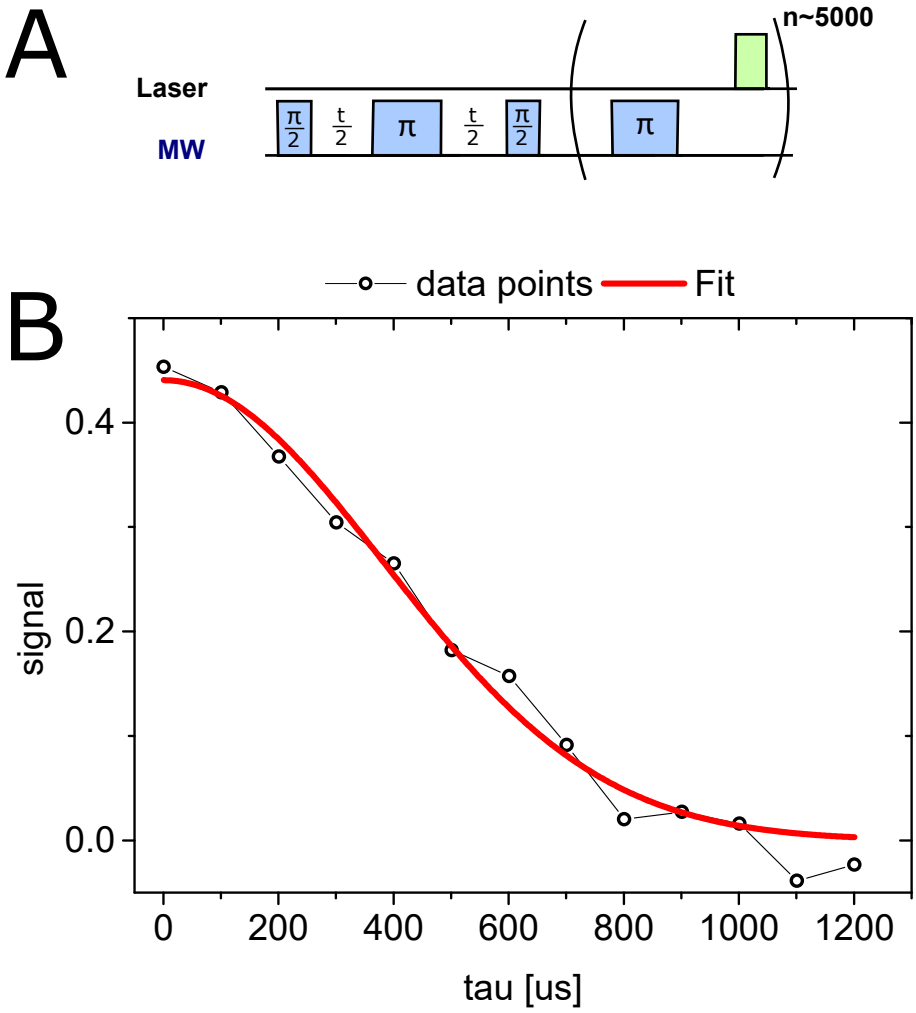

Figure 5.4.: Hahn echo measurement of sensor spin A shows the pulse sequence of the Hahn echo experiment performed via SSR of ^{15}N. B shows the result of the Hahn echo measurement of a sensor spin with a depth of 49.2 ± 0.3 nm. The results are fitted by an exponential function of the form A · exp(-(t/T_2^{sensor})^p) with T_2^{sensor}= 539 ± 23 μs, p = 2.0 ± 0.2 and A = 0.44 ± 0.02.

5.4. NMR with spin locking

Different methods have been applied for the detection of nuclear spins via the NV center in diamond and discussed in section 5.2. Another approach is the NMR detection based on spin-locking which is described in this section. Although the high spectral resolution in NMR is obtained with another method based on a memory spin (see section 5.6), the spin-locking method is exploited for a first test of the created shallow NV centers. In comparison to the DDNS method it sets less demands to the resources required for its implementation as will become clear in the course of the section. Spin-locking is especially useful for spin polarization transfer from one spin species to another. For example in

DNP the thermal polarization of electron spins can be transferred to nuclear spins via spin-locking [7]. Here a modified version of spin-locking is employed for the detection of nuclear spins via shallow NV centers.

In general polarization can be transferred by flip-flop processes between the spins. The rate depends on the energy mismatch between the corresponding spin states and is maximum for degenerate spin states. For spins with a differing gyromagnetic ratio, like in the case of the electron and nuclear spins, flip-flop events are suppressed. One possibility to bring the spin states in resonance to each other is by simultaneously driving transitions of both spin species and fulfilling the so-called Hartmann-Hahn condition [202]:

$$\Omega_1 = \Omega_2 \tag{5.7}$$

$$\gamma_1 B_1 = \gamma_2 B_2 \tag{5.8}$$

with Ω_i being the Rabi frequency, γ_i the gyromagnetic ratio, B_i the amplitude of the resonant alternating magnetic field and index i=1,2 for the two spin species. In this case a double resonance in the rotating frame is created. It has been observed in the experiment that simultaneous driving of both nuclear and electron species induces decoherence on each other. Furthermore the small gyromagnetic ratio of the nuclear spins makes it difficult to achieve the Rabi frequency of the electron spins.

Alternatively it is also possible to transfer the polarization by only controlling the electron spin by an alternating magnetic field. This method is called Nuclear spin orientation via electron spin locking (NOVEL) and its sequence is shown in figure 5.5. $|0\rangle$ and $|1\rangle$ are in the case of the NV center the spin states associated with m_s=0 and m_s=-1. Here the m_s=+1 state is ignored in the consideration but it is in principle possible to replace the m_s=-1 state by the m_s=+1 or even to implement a double quantum transition between the m_s=-1 and m_s=+1 [203, 204]. The electron spin is first initialized in one of the two eigenstates. In the case of the NV center a laser pulse is sufficient for an initialization of more than 92 %. A $\pi/2$ pulse along the x-axis flips the electron spin into the xy plane of the Bloch sphere. Immediately afterwards a continuous MW field along the y-axis locks the electron spin. This so-called spin-locking pulse creates MW dressed states:

$$|+\rangle = \frac{1}{\sqrt{2}}(|0\rangle + |1\rangle) \tag{5.9}$$

$$|-\rangle = \frac{1}{\sqrt{2}}(|0\rangle - |1\rangle) \tag{5.10}$$

The separation between them is given by Ω, the Rabi frequency of the spin-locking pulse. Afterwards a second $\pi/2$ pulse along the x-axis maps the phase information onto the electron spin's population. The sequence concludes with a readout laser pulse. The dynamic range of the signal can be obtained by introducing a reference measurement. This

is achieved by alternating the phase of the second $\pi/2$ pulse by π. The reference measurement also counteracts background fluorescence effects. In the absence of a resonant interaction with nuclear spins, the signal of the spin-locking pulse will decay with $T_{1\rho}$. The $T_{1\rho}$ time can be as long as the T_1 time of the electron spin and strongly depends on the amplitude stability of the MW field. This is closely related to the power stability of the used MW source.

The condition for polarization transfer is satisfied when Ω matches the Larmor frequency of the nuclear spins:

$$\gamma_e B_{1e} = \gamma_n B_0 \tag{5.11}$$

with γ_e and γ_n the gyromagnetic ratio of electron and nuclear spin, B_{1e} the amplitude of the alternating magnetic field acting on the electron spin and B_0 the applied magnetic field.

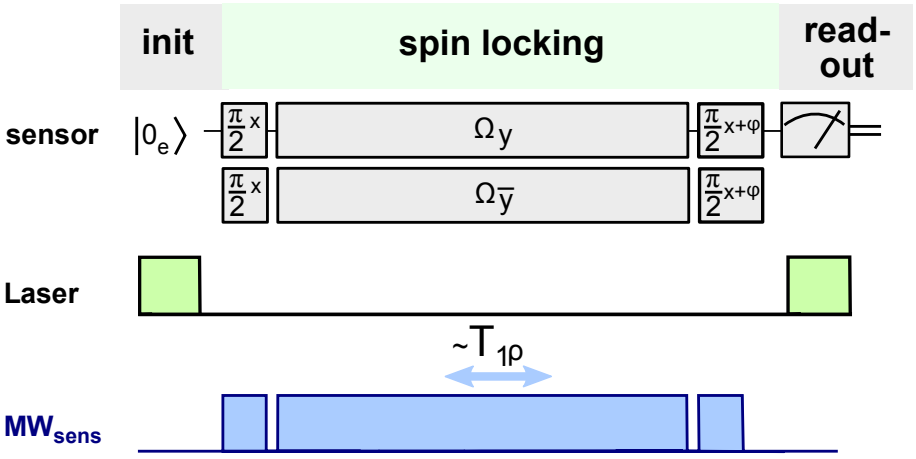

Figure 5.5.: Pulse sequence NMR detection via NOVEL The sequence has three parts: the initialization, the spin locking part and the readout. The upper part shows the quantum gates that are applied on the sensor spin. On the bottom the corresponding laser and MW pulses are depicted. The spin locking time is limited by the $T_{1\rho}$ time. The spin locking sequence is primarily used to polarize the sample spins and needs to be extended for the detection of sample spins (see text). For this purpose the phase of the spin locking pulse needs to be alternated by 180° after each run. In addition to this the phase of the final $\pi/2$ pulse is alternated between $\phi = 0°$ and $\phi = 180°$ to get the full dynamic range of the signal.

For the detection of the nuclear spin bath the NOVEL sequence needs to be modified. In general the idea is that the NV electron spin is transferring its polarization to hyperfine coupled nuclear spins. As a result the NV electron spin becomes unpolarized which can be detected. However this polarization leakage is only observable for an unpolarized spin bath. Once the nuclear spin bath is polarized to 100 %, flip-flop processes between the

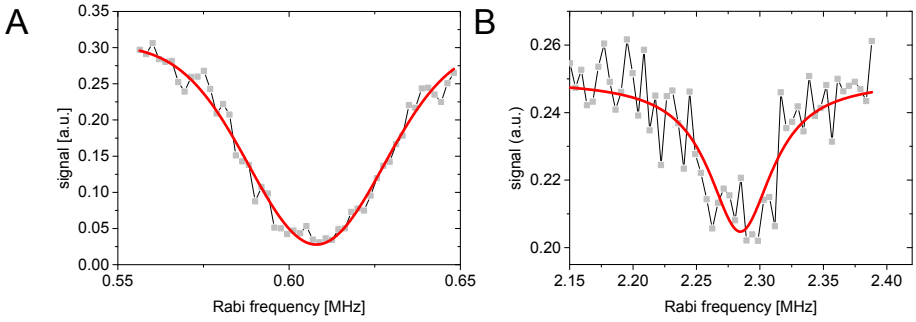

Figure 5.6.: Results NMR spin locking detection of ^{1}H and ^{13}C spins A NMR spectra of ^{13}C spins in the diamond lattice at B=0.057 T. Spin locking time is set to 100 μs. B NMR detection of ^{1}H spins in polybutadiene (immersion oil) at B=0.054 T. Spin locking time is 100 μs.

electron and nuclear spins cannot occur anymore. Consequently no effect of polarization leakage will be observable on the electron spin. The solution is to alternate the direction along which the spin locking is performed (see figure 5.5). This alternates the direction of the induced nuclear spin orientation and leaves for the subsequent spin locking repetition the right orientation.

The detection of nuclear spins by the NOVEL technique is demonstrated for ^{13}C spins in diamond and for ^{1}H spins in immersion oil (polybutadiene). For this purpose the length of the spin-locking pulse is fixed and its Rabi frequency is swept. The latter is achieved by varying the amplitude of the MW field. This can be implemented by mixing an adjustable signal generated by the AWG to a local oscillator signal. Hence it is necessary to calibrate the amplitude of the MW signal with the Rabi frequency. Afterwards the NOVEL sequence described in figure 5.5 can be applied for the sensing of nuclear spins. Besides the required π phase shift of the spin locking pulse after each run, there is an additional reference measurement as well. This results into four sequences, each yielding a measurement result which can be subtracted from each other. The applied magnetic field of $B_0 \approx 50$ mT represents the LAC of the excited state and leads to the polarization of ^{15}N nitrogen nuclear spin. Consequently the MW application on the sensor spins only needs to be resonant to one of the three hyperfine induced lines. This prevents effects caused by the detuning of the MW pulse.

The main parameter governing the magnetic field sensitivity is the maximum achievable $T_{1\rho}$ time (analogue to the T_2^{sensor} time in DDNS). Spin-locking represents a form of continuous dynamical decoupling. Therefore long $T_{1\rho}$ times reaching the T_1^{sensor} time can be expected. These time scales are typically shorter for shallow NV centers. However as explained in the previous section 5.3 the here used shallow NV centers have a rather large depth of more than 30 nm which should protect them from surface noise [188, 189, 190].

Additionally the importance of the MW power stability for $T_{1\rho}$ has been underlined. Therefore a power-stable traveling wave tube (TWT) is used as an amplifier. As a result a spin-locking pulse length of 100 μs shows an approximate 1/e decay (the non-resonant amplitude in figure 5.6) which indicates a $T_{1\rho}$ time on the same order.

In figure 5.6A the Rabi frequency of the spin locking pulse is swept through the range of the ^{13}C Larmor frequency. At the point of resonance the spin state of the single NV center is depopulated from the $m_s = 0$ state which can be observed as a drop in fluorescence. For the ^{13}C spins in the diamond lattice a peak at 607.9 $\pm$ 0.3 kHz is measured, which is consistent with the expected frequency at this magnetic field. Furthermore a FWHM of 46 kHz is observed. Based on the spin locking time of 100 μs a linewidth of 3 kHz would have been expected. The much larger width can be explained by the large distribution in hyperfine interactions. This is expected for a diamond sample with a natural abundance of ^{13}C . The NMR contrast amounts to 91 % and can be explained by the 100 μs long spin locking pulse, which allows to polarize almost the whole ^{13}C nuclear spin bath.

Next the frequency range is extended to the resonance of the ^{1}H spins which are located on top of the diamond surface. The ^{1}H spin containing sample is immersion oil which serves as a test sample. A nanometer scale volume of statistically polarized ^{1}H spins generates a peak at a frequency of 2.285 $\pm$ 0.002 MHz, which matches well with the expected resonance frequency of ^{1}H spins. The Lorentzian fit yields a linewidth (FWHM) of 68 kHz. This large value in width can be explained by the diffusion of sample spins (see section 5.9). The obtained NMR contrast of 18 % for a phase accumulation time of 100 μs indicates a depth of the shallow NV center of 43 nm (for a detailed description of depth determination see section 5.8).

The spin locking method can be compared with the DDNS method. One important aspect is the required Rabi frequency. In the case of spin locking the required Rabi frequency has to exactly match the Larmor frequency of the sample spins. On the other hand for DDNS the filter function is tuned to the resonance frequency of the nuclear spins. The π pulses in the sequence are required to ideally act instantaneously, which cannot be realized in an experiment. However they should be much faster than the Larmor period. Otherwise during the π pulse, the spin will start evolving and acquiring a phase. Therefore the required Rabi frequency for DDNS has to be larger than the Larmor frequency of the sample spins. This can be a problem when MW equipment with high power is not available which is especially the case for frequencies higher than 10 GHz. Besides this lower condition to the required Rabi frequency another advantage of the spin locking method is its unambiguous NMR detection. In DDNS on the other hand, higher order resonances can make an unambiguous identification of the spin species difficult. For example the fourth order resonance peak of ^{13}C spins has a similar frequency than the ^{1}H

frequency and has lead to false assignment to the latter. In general implementation of the spin locking sequence is less complex since only three MW pulses are involved compared to many hundreds in DDNS [24]. If a power stable MW source is available a $T_{1\rho}$ time reaching the T_1^{sensor} time can be achieved.

For future applications it will be interesting to combine the polarization transfer from NV centers to nuclear spins with subsequent high spectral resolution nanoscale NMR. First studies have been conducted into this direction [204, 205, 206].

5.5. Hamiltonian of sensor, memory and sample spins

In this section the individual components of the NV nanoscale NMR system and their interactions among each other will be described by the spin Hamiltonian H. Partly the Hamiltonian terms have already been discussed in chapter 2.4 and chapter 4.1. However here in addition to the sensor spin and the memory spin, sample nuclear spins have been included.

A single NV center in diamond is the sensor spin. Its intrinsic ^{14}N or ^{15}N nitrogen nuclear spin have the role of the memory spin. As shown by Waldherr et. al single ^{13}C spins in diamond can also act as memory spins [38]. The sample spins can be of any nuclear spin species. In this study as an example ^{13}C , ^{1}H and ^{19}F NMR spectroscopy has been demonstrated. In principle electron spins can be investigated as well since their frequency is detuned from the sensor spin (due to the ZFS).

Each of the components can be expressed by its Hamiltonian. Additionally an interaction Hamiltonian can be defined.

$$H = H_{sensor} + H_{memory} + H_{sample} + H_{interaction} \tag{5.12}$$

In the following each Hamiltonian term is described. The first term is the Hamiltonian corresponding to the sensor spin. It consists of the zero field splitting (ZFS) and the Zeeman term. The ZFS originates from the dipole interaction between the two unpaired electron spins and has the magnitude D = 2.87 GHz. On the other hand the Zeeman term of the sensor can reach 87 GHz in the experiment at a magnetic field of 3 T.

$$H_{sensor} = DS_z^2 + \gamma_{sensor} B_z S_z \tag{5.13}$$

The second term deals with the memory spin. Analogue to the sensor spin it has a Zeeman term as well. For the ^{15}N it is around 9 MHz at 3 T. In the case of a ^{14}N spin an additional term comprising the quadrupole coupling would appear in the Hamiltonian (see equation 4.3).

$$H_{memory} = \gamma_{memory} B_z I_z^{memory} \tag{5.14}$$

The sample spins interact with an applied magnetic field by Zeeman coupling. Depending on the homogeneity of the magnetic field B_z, the field experienced by the sensor spin can be different from the one exerted to the sample spins. However the detection volume in this work is on the scale of $\sim$ (30 nm)^3 and the distance to the sensor is $\sim$ 30 nm. The inhomogeneity of the magnetic field is on the order of 10^{-12} ppm per nm in all directions. Hence the same B_z can be applied to both the sensor and the sample spins. For ^{1}H, ^{19}F and ^{13}C spins the Zeeman term is 126 MHz, 118 MHz and 32 MHz, respectively, at 3 T.

$$H_{sample} = \gamma_{sample} B_z \sum_{sample} I_z^{sample} \tag{5.15}$$

Finally the coupling of the spins to each other is summarized in the interaction term. The sensor to memory coupling is the strongest with 3.03 MHz for ^{15}N and 2.17 MHz for ^{14}N . This allows gate times to be on the μs scale. For the interaction between sensor and sample spins the $S_{x,y} I_{x,y,z}^{sample}$ terms can be neglected due to the secular approximation. The remaining terms are of the form of $S_z I_z^{sample}$ on one side and $S_z I_{x,y}^{sample}$ on the other side. The DDNS based detection of sample spins is based on the latter terms. Contrary to that the here used memory spin approach relies on the $S_z I_z^{sample}$ terms. Both terms are weak compared to the nuclear Zeeman term. For example ^{1}H spins 17 nm apart from the sensor spin generate a (zz-type) hyperfine coupling of $A_{||} \approx 35$ Hz. A long sensing time and a large ensemble of nuclear spins ensure the observation of the signal. The memory to sample interaction can be neglected due to the low gyromagnetic ratio of the nuclear spins.

$$H_{interaction} = S_z A_{||}^{memory} I_z^{memory} + S_z \sum_{sample} A_{||}^{sample} I_z^{sample} + S_z \sum_{sample} A_{\perp}^{sample} I_{x,y}^{sample} \tag{5.16}$$

5.6. Quantum metrology framework

In the following NV nano NMR experiments a novel quantum metrology pulse sequence is applied. It involves the interplay between the sensor and the memory spin and creates a framework, enabling the implementation of an arbitrary NMR sequence. The basic principle is a correlation of two phase accumulation parts of the sensor spin. They are interrupted by an intermediate storage part where the phase information is stored on the memory spin. In this central part the sample spins are manipulated according to the desired NMR sequence. The readout at the end is executed by a QND measurement of the memory spin (see chapter 4.3). The final memory state is compared with the initial memory state, yielding the flip probability. The latter contains the phase information. In the protocol controlled NOT gates guarantee the entanglement between the sensor and the memory spin. Zaiser et al introduced the method for the first time and used it for

sensing of ^{13}C spins (located in the diamond lattice) with a spectral resolution of 210 Hz (FWHM) [30]. The sequence is extended by Pfender et al [15] to a more noise-resistant method. The latter sequence is chosen for the NMR experiments of this work. In the following the basic sequence will first be explained [30] and subsequently the extended version [15] will be discussed.

Figure 5.7 depicts the pulse sequence containing the gate operations and pulses that are applied. The implanted nitrogen ions are $^{15}N^{+}$. Hence in further considerations only the case of ^{15}N spin with two states: $m_i = \pm \frac{1}{2}$ is discussed. These states are corresponding to the qubit states $|0\rangle_n$ and $|1\rangle_n$, respectively. The sensor spin can reside in three states: $m_s = -1, 0, +1$. The $m_s = -1, 0$ states are defined as $|1\rangle_e$ and $|0\rangle_e$ and only the transition between them is utilized. The electron spin is polarized with around 92 % probability to the $\Psi_e = |0\rangle_e$ state. The memory spin state is initialized through the QND measurement into one of its states Ψ_n. The initialization probability is given by the SSR readout fidelity which is more than 99 % at the applied B field of 3 T. The sample spins are in a thermally mixed state.

We can divide the basic sequence in four parts: ***first sensing step***, ***storage and NMR application time interval***, ***second sensing step*** and finally the ***readout***. A RF $\pi/2$ pulse is applied on the memory spin generating the state: $\Psi_n = \frac{1}{\sqrt{2}} (|0\rangle_n + |1\rangle_n)$. Due to the small gyromagnetic ratio the memory spin is not accumulating any phase from the sample spins. The sensor is in its eigenstate and therefore also not acquiring any phase originating from the sample. This changes when a nuclear spin-controlled NOT gate is applied on the electron spin (C_nNOT_e). The sensor and memory get fully entangled and the resulting state is:

$$\Psi_e \otimes \Psi_n = C \cdot (|0\rangle_n + |1\rangle_n) \otimes (|0\rangle_e + |1\rangle_e) \tag{5.17}$$

For a time τ the sensor spin is sensitive to the magnetic field environment and can accumulate a phase ϕ induced by the statistically polarized sample spins: $\phi_1 = \gamma_{sample} B_z \tau$. The maximum possible phase accumulation time is limited by the T_2^{sensor}. This ***first sensing step*** is terminated by a second C_nNOT_e gate leaving the phase information stored on the memory spin.

$$\Psi_e \otimes \Psi_n = C \cdot (|0\rangle_n + e^{i\phi_1} |1\rangle_n) \otimes (|0\rangle_e) \tag{5.18}$$

The second C_nNOT_e gate does not need to be identical with the first one. It can also be chosen such that the sensor spin ends in the $|1\rangle_e$ state. This can be of benefit if a selectivity of sample spins by their hyperfine interaction is desired [30], [15]. In the NMR measurements shown here the hyperfine interaction between the ^1H and ^{19}F spins is weak with less than 12 Hz (for d = 34 nm). The sensor spin state after the second C_nNOT_e gate

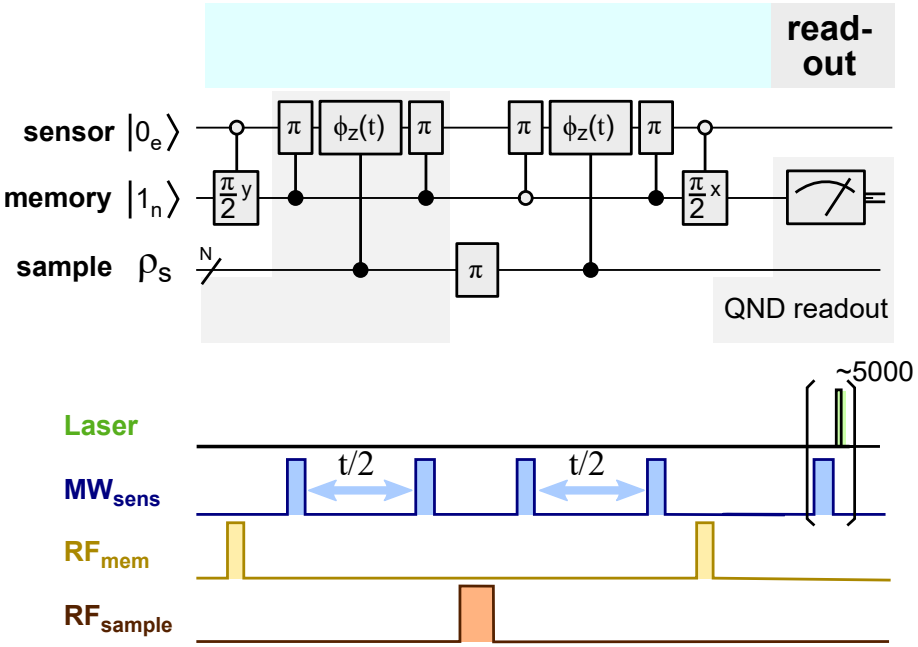

Figure 5.7.: Pulse sequence of the encoding step.. **Top** A wire diagram with the gates between the three components (sensor, memory and sample spins) is depicted. **Bottom** The corresponding pulses of laser, MW and RF excitation are shown. The sensor and memory start in initialized states whereas the sample spins are in a mixed state. Of central importance are the C_nROT_e gates between sensor and memory which control the sensor to sample interaction. Open or filled circles indicate on which qubit state the gate is conditional on. Two sensing periods are interrupted with a π flip of the sample spins, thereby representing a correlation measurement. In the end the memory is readout with a projective QND measurement. This short version of the complete sequence allows detection of sample spins and an estimation of sensor depth. Detailed description of the sequence and its application can be found in the text.

therefore does not play a major role in the considerations. In the ***storage and NMR application time interval T*** the orientation of the sample spins can be flipped by a π pulse. Afterwards the two C_nNOT_e gates are repeated in order to yield the ***second phase accumulation*** time. The final state is given by:

$$\Psi_e \otimes \Psi_n = C \cdot (|0\rangle_n + e^{i\Delta\phi}|1\rangle_n) \otimes (|0\rangle_e) \tag{5.19}$$

with $\Delta\phi = \phi_1 - \phi_2$. If there is no change of the magnetic field environment in T, the phases ϕ_1 and ϕ_2 will be the same and will cancel each other. If however the sample spin's orientation has been flipped by a π pulse then the accumulated phase in the second sensing step will add to the first one and a signal will appear. Please note that instead of a simple π pulse a Ramsey sequence can be applied to the sample spins as well. Finally a $\pi/2$ pulse on the memory spin maps the phase information on the population of the

memory spin which is then ***readout*** by a QND measurement.

The so far described sequence can alone be used for NMR detection [30]. On one

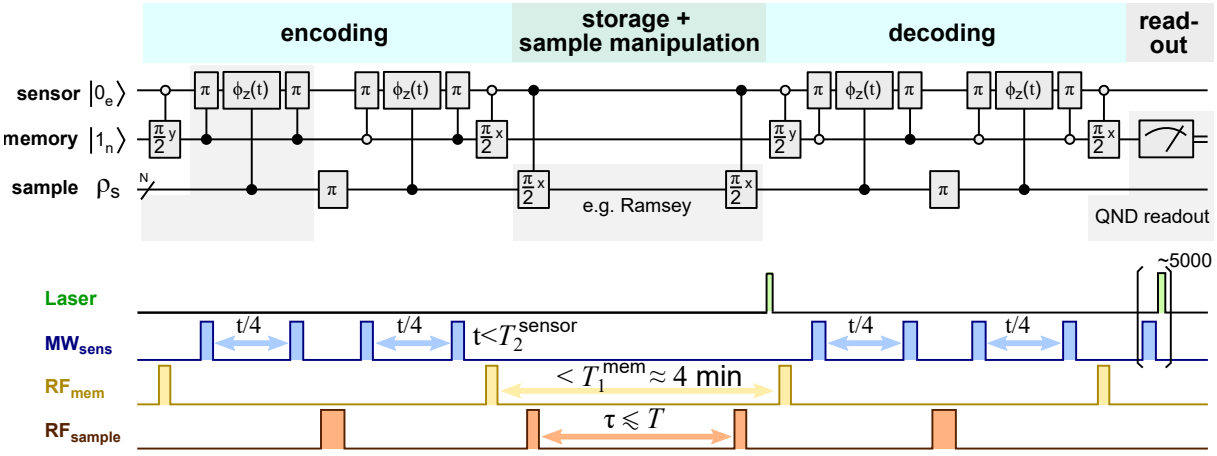

Figure 5.8.: Pulse sequence of memory based high resolution NMR protocol. The extended sequence is subdivided into four steps: 1. Encoding, 2. Storage and Sample manipulation, 3. Decoding and 4. Readout. The encoding step is identical to the sequence in figure 5.7. In the decoding the gates are analogue to the encoding part except the phase of the memory pulses. In addition to it the state the C_nROT_e gates are conditional on, differs as well. During encoding and decoding the sensor accumulates a phase for a time t which is limited by the T_2^{sensor}. Between the two parts the sample signal is stored on the memory population, which decays on the order of $T_1^{\text{mem}} \approx$ 4 min. In the meantime the sample spins can be manipulated e.g. to perform a Ramsey measurement. The measurement time τ determines the achievable spectral resolution in the NMR spectrum. The readout is conducted as a QND measurement of the memory state.

side a long phase accumulation time τ is required in order to reach a high magnetic field sensitivity. The time τ decays approximately with the T_2^{sensor} time [30]. On the other side the intermediate time T limits the spectral resolution and is therefore required to be long, as well. For very short τ the intermediate time T decays according to the T_2^{mem} time which is approximately 3/2 times the T_1^{sensor} time. However when τ is increased the decay time of the intermediate part will decay on a significantly shorter timescale [30].

Therefore an extended version has to be applied which allows both long T and long τ (see figure 5.8). In that case the previously described sequence builds only the first **encoding** step. The second part is the **storage and sample manipulation part**. It is followed by the **decoding** step which repeats the gates of the **encoding** step. The sequence ends with the QND **readout** of the memory spin. Here the phase accumulation is separated into four instead of two parts. Both the encoding and the decoding are selective to the sample spins due to the resonant π pulses. This represents a form of decoupling from other noise sources and increases the selectivity of the sequence to the

sample spins [15].

In the **storage** part the phase information is stored in the superposition state of the memory spin. This state will decay on a time scale given by the T_2^{mem} ($\approx 3/2\ T_1^{\text{sensor}}$). The phase information can be stored on the population of memory spin as well. The population of the memory spin decays on a longer time scale governed by the T_1^{mem} time. In chapter 4.4 the magnetic field scaling of the T_1^{mem} time has been investigated. At 1.5 T the T_1^{mem} measurement yields a decay time of 260 s (see figure 4.9). Hence in the equation 5.6 defined for the spectral resolution, the T_1^{sensor} time can be replaced by the much longer T_1^{mem}. The other two time scales T_D and T_2^* of the equation 5.6 are shorter than the T_1^{mem} time. Consequently it can be noted that the spectral resolution in the measured NMR spectra is primarily not limited by the sensor-memory probe itself, but the sample spins.

For the storage on the memory spin's population an additional $\pi/2$ pulse on the memory spin has to be applied in the beginning of the **storage** part. At the end of the storage time a second $\pi/2$ pulse on the memory spin prepares the necessary superposition state for the following **decoding** step. While the phase information gained in the **encoding** step is stored, the sample spins can be manipulated according to a Ramsey measurement. This can be achieved by two $\pi/2$ pulses applied to the sample spins and separated by a time τ.

The **decoding** includes all the steps of the encoding and probes any changes induced on the sample spins in the storage period. Finally a $\pi/2$ pulse is applied to the memory spin and its state is **readout** by a QND measurement.

The memory spin population represents a classical memory. In the case of using its superposition state as the storage medium, it represents a quantum memory. The storage of the phase information on a classical memory, instead of the quantum memory comes at the cost of loosing contrast. Mapping to the eigenstate of the memory spin represents a classical memory, which leads to the loss of coherence on the memory and results into half of the maximum possible NMR contrast. This is in contrast to the case of the superposition state as the medium of storage, where the whole information of $e^{i\phi}$ can be stored.

Depending on the nature of the sample spin's polarization the phase of the memory spin pulses needs to be adjusted. If the sample spins are statistically polarized then both the initial and the final $\pi/2$ pulses on the memory spin are required to have the same phase. However if the spins are aligned in a specific direction (as is the case for thermal polarization) then it is necessary to have a 90° phase shift between the aforementioned $\pi/2$ [30]. In this work the sample spins are statistically polarized.

Obtaining reference measurements has the advantage of getting the whole dynamic range of the signal and to counteract effects like background signal. Therefore the phase

of the last $\pi/2$ pulse (on the memory spin) prior to the QND readout is shifted by 180° after each sequence. The actual signal is then the subtraction of two subsequent results.

The time scales for the sensing and the storage part can be evaluated. These parameters are varied and the resulting signal on the memory spin is measured. First in the basic sequence (fig. 5.7A) the phase accumulation time is swept from 0 to 1.4 ms and the decay of the signal is measured (see figure 5.9). The intermediate time T is set to 10 μs with no pulse applied to the sample spins. The measured decay time is 377 $\pm$ 17 μs which is comparable to typically expected T_2^{sensor}.

Next, the time interval T is varied with a fixed sensing time of $\tau = 300$ μs (see figure 5.9B). An oscillation of the memory signal can be observed. The reason for its occurrence is a detuning in the pulses on the memory spin. The oscillation vanishes once the detuning is set to zero. The resulting decay time of 8 ms is approximately the expected $3/2 \cdot T_1^{\text{sensor}}$ time. The decay of the storage period is limited by the T_1^{sensor} time as long as the storage medium is the superposition of the memory spin. This changes once the population of the memory spin is used as the storage medium. The decay time in this case is limited by the T_1^{mem} which is more than 260 s for an applied magnetic field of 1.5 T (see chapter 4.4).

5.7. Sample signal

The sample spins can be ^{13}C spins in diamond or ^{1}H and ^{19}F spins on top of the diamond surface. However the main focus of this work is the detection of external nuclear spins. The solid or liquid samples are placed on the surface of the diamond and are covering the whole diamond. The interaction of the sensor to sample spins restricts the detection to a volume depending on the depth of the sensor spin. An exemplary detection volume of (30 nm)^3 with a spin density of 50 nm^{-3} contains $1.35 \cdot 10^6$ nuclear spins. As noted before, the thermal polarization of the ^{1}H spins is only 10^{-5} (at B = 3 T and T = 300 K). The number of polarized spins is too small to be detectable by the NV nano NMR technique. The statistical polarization which is the variance of the magnetic field created by the sample spins is however large enough to be detected. In the aforementioned example $\approx$ 1200 nuclear spins are statistically polarized. Each of these nuclear spins has a dipole-dipole interaction with the sensor spin (see also equation 1.8):

$$B_{DD} = \frac{\mu_0 \hbar \gamma_{sample} \gamma_{sensor}}{8\pi^2} \frac{1 - 3\cos^2\theta_{12}}{r_{12}^3} \tag{5.20}$$

with the distance r between the sensor and the sample spin. Since the sample spins are statistically polarized the sum of their dipole field's square has to be formed (see chapter

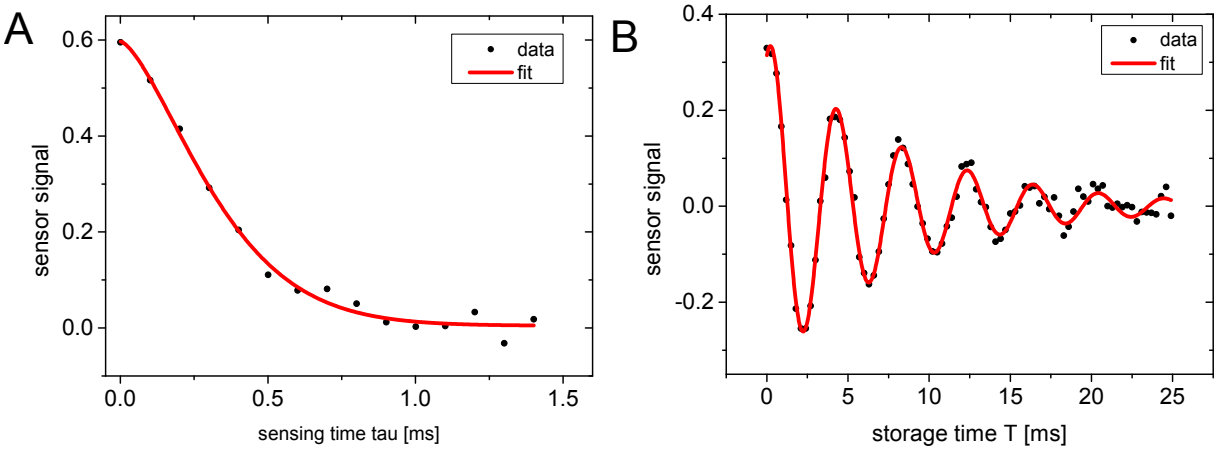

Figure 5.9.: Characterization of NMR protocol. **A** Sensor signal in dependence of the sensing time t, measured with the short version of the NMR protocol 5.7. No RF pulse is applied to the sample spins. Data is fitted with function: $y = A \cdot e^{-(x/t_0)^p} + y_0$. The fit yields a decay time of t_0 = 0.377 ± 0.017 ms and p = 1.5 (for a fixed intermediate time T = 10 μs). **B** Variation of storage time T in the extended NMR protocol 5.8. Instead of the memory population the storage medium is the superposition state of the memory. This can be achieved by omitting the RF pulses affecting the memory in the storage time. Again no RF pulse is applied to the sample spins. Fit function is: $y = A \cdot e^{-x/T_0} \cdot sin(\pi \cdot (x - xc)/w) + y_0$. The fitting parameter are: Decay time T_0 = 8.0 ± 0.3 ms and an oscillation frequency of 250 Hz (for a fixed sensing time t = 0.3 ms). The oscillation stems from the pulses which are detuned due to a difference between the employed and actual hyperfine shift.

5.1).

$$B_{rms}^2 = \sum_i^N B_{DD}^2 \tag{5.21}$$

In section *Depth determination* 5.8 the expression for B_{rms} will be derived. Because of its $r^{-3/2}$ dependence, sample spins closer to the sensor spin will contribute more to the signal than others. Hence a detection volume can be defined that contains sample spins contributing to half of the signal. The presence of B_{rms} leads to the phase Φ accumulated by the sensor spin. For an ensemble of N sample spins the phase Φ is:

$$\Phi = \prod_i^N \otimes \left(e^{-i\pi B_{DD} t \sigma_z/2} \right) \tag{5.22}$$

with the Pauli operators σ_i (i = x,y,z).

In the following the sample signal is theoretically described by a density matrix formulation. Here only the sensor spin is sensitive enough to acquire the phase Φ, but not the memory spin. However since Φ is mapped to the memory spin states and readout, it is sufficient to only consider the memory and the sample spins. In the beginning of the

sequence the memory is initialized and N sample spins are in a mixed state.

$$\begin{aligned}\rho_{init} &= \rho_{memory}^{init} \otimes \rho_{sample}^{init} \\ &= (I + \sigma_z)/2 \otimes I^{\otimes N}/2^N\end{aligned} \tag{5.23}$$

In the **encoding** part the sensor spin accumulates the phase Φ by the interaction with the sample spins. The RF pulse in the encoding is assumed to flip all the sample spins by exactly π. As described in the previous section the phase Φ will be stored on the superposition state of the memory:

$$\rho = \frac{I^{\otimes(N+1)} - \sigma_y \otimes Im(\Phi) + \sigma_x \otimes Re(\Phi)}{2^{N+1}} \tag{5.24}$$

After the encoding, it is possible to readout the memory subsequent to a $\pi/2_y$ pulse. This basic sequence [30] allows the simple detection of sample spins and is also suitable for an estimation of the sensor depth (see section 5.8). After applying the aforementioned $\pi/2_y$ pulse, the new density matrix is:

$$\rho = \frac{I^{\otimes(N+1)} - \sigma_y \otimes Im(\Phi) + \sigma_z \otimes Re(\Phi)}{2^{N+1}}. \tag{5.25}$$

Only the σ_z term of the memory is readout. The signal generated by the sample spins can be determined by forming the trace.

$$\begin{aligned}S_1(t) &= 1 - Tr(Re(\Phi))/2^N \\ &= 1 - \prod_i^N cos(\pi B_{DD} t)\end{aligned} \tag{5.26}$$

Assuming $B_{DD}t \ll 1$ the expression can be written as:

$$S_1(t) = 1 - e^{-\sum_i^N (\pi B_{DD} t)^2/2} \tag{5.27}$$

This expression for the signal describes the difference between the two cases of flipping the sample spins by a π pulse (in the center of the encoding) and not altering the sample spins. With this basic sequence different measurements can be conducted. For example by sweeping the frequency of the π pulse acting on the sample spins a NMR spectrum can be reconstructed (see figure 5.10A). Results of NMR detection of samples containing ^{13}C , ^{1}H and ^{19}F spins are shown in figure 5.10A. The difference in the gyromagnetic ratio for ^{13}C with $\gamma/2\pi$ = 10.705 MHz/T, ^{1}H with $\gamma/2\pi$ = 42.576 MHz/T and ^{19}F with $\gamma/2\pi$ = 40.059 MHz/T enables the spectral distinction with respect to each other. The signal is normalized in the spectra. The ^{13}C sample spins are located in the diamond lattice. Due to coherent interaction of the sensor spin with a few strongly coupled ^{13}C spins the

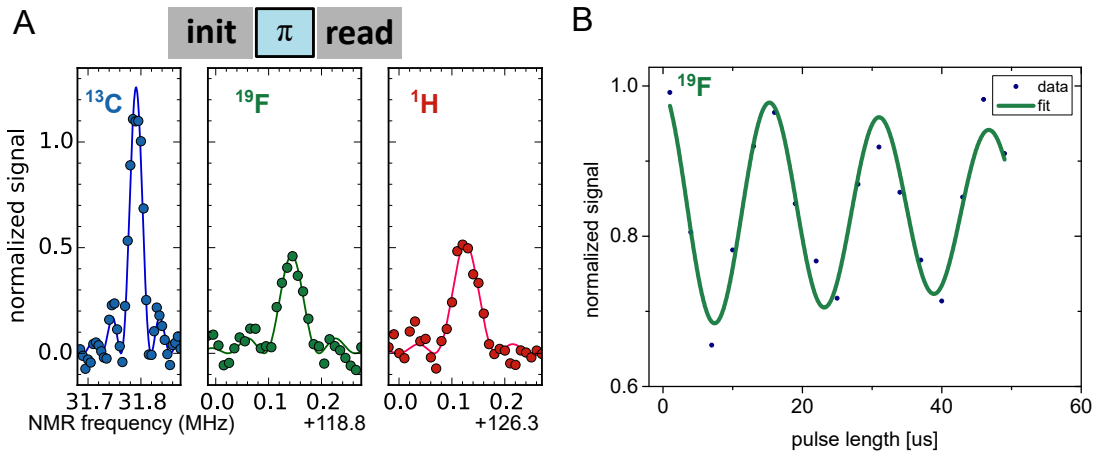

Figure 5.10.: Nanoscale NMR detection of ^{13}C , ^{19}F and ^{1}H spins. **A** The short sequence of the NMR protocol is employed for the detection of nuclear spins. A π pulse is applied on the sample spins. By sweeping the frequency of the pulse a NMR spectrum can be reconstructed. The resonance frequency of the sample spins depends on their gyromagnetic ratio. The left graph displays the resonance of ^{13}C spins, located in the diamond lattice. In the center and right graphs ^{19}F and ^{1}H spins in polyvinylidene fluoride (PVDF) are detected. The sensing time t in all measurements is 100 μs. The depth of the NV used for ^{19}F and ^{1}H detection is 23 nm (procedure for depth determination is explained in section 5.8). The resonance peaks are fitted by a sinc function. In the ^{13}C case coherent interaction between the sensor and single ^{13}C spins in the close proximity occurs which leads to a normalized signal larger than 1. On the other hand the interaction with ^{19}F and ^{1}H spin ensemble is incoherent and restricts the signal to 1. **B** A Rabi measurement of ^{19}F spins in perfluoropolyether (PFPE) oil is shown. The frequency of the RF pulse is set on resonance to the ^{19}F spins and the pulse length is varied. At the same time the intermediate time T is fixed to the longest pulse length. The data is fitted with a sine damped function: $y_0 + A \cdot e^{-x/t_0} \cdot sin(\pi \cdot (x - x_c)/w)$. The obtained Rabi frequency is 64 kHz. The distance of the sensor to the sample spins is $\approx$ 95 nm. In all graphs the signal is normalized.

signal can be larger than 1. The ^{1}H and ^{19}F signal on the other hand stems from incoherent interaction with spins in polyvinylidene fluoride (PVDF). Its chemical structure is -$(C_2H_2F_2)_n$-. Hence the spin density of ^{1}H and ^{19}F spins is the same. The sensor spin is 23 nm apart from the surface of the diamond. This distance sets the required sensing time t (see figure 5.12). In the measurement a sensing time of 100 μs is chosen and results in approx. 50 % of NMR contrast.

Furthermore a Rabi measurement on the sample spins can be achieved by varying the RF pulse length. Figure 5.10B shows a Rabi measurement of ^{19}F spins in perfluoropolyether (PFPE) oil with a Rabi frequency of 64 kHz. The basic sequence [30] is also suitable for the estimation of sensor depth, which is discussed in section 5.8.

If the purpose of the measurement is to achieve a high-resolution in the NMR spectrum, then the sample spin information is not readout right after the encoding. Instead a $\pi/2_x$ pulse is applied on the memory spin in order to store the phase information on the memory spin's population.

$$\rho = \frac{I^{\otimes(N+1)} - \sigma_z \otimes Im(\Phi) + \sigma_x \otimes Re(\Phi)}{2^{N+1}} \tag{5.28}$$

The term $\sigma_z \otimes$ Im (Φ) now stores the information about the sample spins magnetization and decays on a time scale set by the T_1^{mem} time (see chapter 4.4). Afterwards the sample spins can be manipulated according to the desired NMR sequence. For a Ramsey sequence for example two $\pi/2$ RF pulses are applied on the sample spins. Effects like chemical shift let the sample spins evolve faster or slower. This can be considered by a change of the angle α_i between the sample spin alignment and the z-axis. The memory loses any coherence in the storage part by either relaxation of the sensor or by the repolarizing laser pulse applied on the sensor. Subsequently in the decoding the gates of the encoding are repeated. The difference between the acquired phase of the encoding and that of the decoding part is the signal. Tracing out the sample spins results in:

$$\begin{aligned} &Tr(\rho) = (I + C\sigma_y)/2 \\ &\text{with } C = \left(\prod_i^N (1 - 2\,\sin^2(\pi B_{DD} t/2)\,\cos^2(\frac{\alpha_i}{2})) - \prod_i^N (1 - 2\,\sin^2(\pi B_{DD} t/2)\,\sin^2(\frac{\alpha_i}{2}))\right)/2 \end{aligned} \tag{5.29}$$

For a sensor depth of larger than 35nm, $B_{DD}t \ll 1$ is valid and the expression can be simplified to:

$$\approx -\sinh\left(\sum_i^N \frac{(\pi B_{DD} t)^2}{4}\cos(\alpha_i)\right) e^{-\sum_i^N (\pi B_{DD} t)^2/4} \tag{5.30}$$

In the case of flipping all sample spins with the same angle $\alpha_i = \alpha$, the difference between a π flip and no flip is:

$$S_2(t) = 2\,\sinh\left(\sum_i^N \frac{(\pi B_{DD} t)^2}{4}\right) e^{-\sum_i^N (\pi B_{DD} t)^2/4} \tag{5.31}$$

The signal $S_2(t)$ ranges from 0 to 1. 1 means full decoherence due to the interaction with the sample spins. The total sensing time of the encoding and decoding is t, while for the encoding, solely, it is t/2.

In this theoretical formulation, consideration of any type of relaxation of the sensor or of the sample spins is missing. Accounting for dephasing of the sensor is straightforward by adding the term $e^{-(t/T_2^{\text{sensor}})^n}$ to the term in 5.27. In the previous section this dependence has been measured (figure 5.9 A). The sample spins dynamics can affect the signal as well.

Diffusion (out of the detection volume) of the sample spins in liquids or spin diffusion leads to an exponential decay of the $\cos(\alpha_i)$ term in 5.30 (discussed in section 5.9). Moreover transversal relaxation of the sample spins will also have an effect on the aforementioned term. For all measurements a corresponding reference measurement is performed by adding a phase shift of 180° to the last memory $\pi/2$ pulse. The subtraction with the reference measurement shows the full visibility of the signal. Here the visibility is 0.65. Its deviation from 1.0 comes from the finite single-shot readout fidelity ($\approx$ 95 %) and the fact that the sensor resides for 30 % of time in the neutrally charged state [36]. The presented results e.g. in figure 5.10 are normalized.

5.8. Depth determination

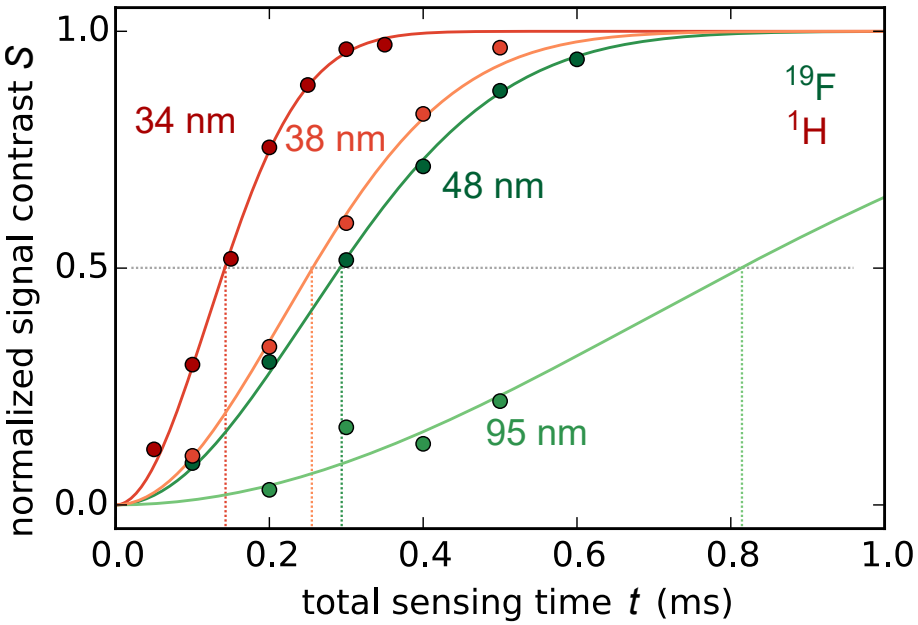

Figure 5.11.: Depth determination of the sensor spin. The sample signal depends on the sensing time t, the spin density ρ and the distance to the sensor d. Samples with known spin density ρ can be used to determine the depth d. For that purpose the sensing time t is varied and the measured data is fitted with equation 5.32 in order to extract the sensor depth. Samples used for determining the depth of different NV centers are: polybutadiene oil (^{1}H, dark red, $\rho \approx 58$ nm^{-3}), ethyl-2-cyanoacrylate solid glue (^{1}H, dark red, $\rho \approx 43$ nm^{-3}) and PFPE oil (^{19}F, light and dark green, $\rho \approx 47$ nm^{-3}). Dashed lines indicate the sensing time needed for achieving 50 % signal contrast. Note: In the case of the light green curve an additional proton containing layer is added between the sample and the diamond surface.

The determination of the sensor spin depth d is crucial for NV nano NMR. The depth

defines the detection volume of the sensor [24, 25]. On the other hand, the diffusion time T_D for statistically polarized spins in a liquid is related to the detection volume.

The technique for depth determination is relying on the distance dependent interaction between the sensor and the sample spins introduced in equation 5.20. First it is important to derive the B_{rms} field expression. The arrangement of the sensor and sample spins is as following. A single sensor is located in the diamond lattice and its orientation is perpendicular to the $\langle 111 \rangle$-oriented diamond surface. An ensemble of sample spins is homogeneously distributed on the surface of the diamond. Each sample spin has a distance dependent interaction with the sensor spin (5.20). In order to get the total interaction strength a sum over all sample spins can be formed. The sum can be transformed into an integration over a half-sphere above the sensor spin. The integration leads to an analytical solution for B_{rms}:

$$B_{rms}^2 = \frac{\pi^3 \rho c^2}{4\gamma^2 d^3} \tag{5.32}$$

where ρ is the spin density and c is the dipole-dipole coupling parameter (see table A.2).

As explained in section 5.7 the sample spin's statistical polarization leads to decoherence on the sensor spin. The signal increases with the sensing time t and has a Gaussian shape due to the weakly coupled ensemble of sample spins. The expression for the B_{rms} field 5.32 can be inserted into the equation for the signal 5.27. Hence the exact shape of the curve depends on the depth of the sensor. NV centers with a larger depth d will reach full decoherence at a shorter sensing time t. This signal dependence can be measured with the encoding sequence by varying the sensing time t. In addition to it, a reference measurement is performed which is insensitive to the sample spins (no flip of the sample spins). With the results of the reference measurement the signal can be normalized in order to filter out the T_2^{sensor} decay. The normalized signal is then fitted to equation 5.32 and 5.27. If the spin density ρ is known, then the unknown parameter of sensor depth d can be extracted from the fit.

In these considerations it is assumed that the π pulse within the encoding step perfectly flips all of the sample spins. Additionally the decay of the sample spin's magnetization is assumed to occur on a time scale much longer than required for the depth measurement (which is limited by the T_2^{sensor} time). This assumption holds true as the spin diffusion time is measured in section 5.9 to be 5 ms for a liquid sample and in section 5.10 to be even 94 ms for a solid. Hence the decay of the magnetization is negligible on these time scales.

With this method the depth of various NV centers is determined and the results are plotted in figure 5.11. Different samples are used for the depth determination: polybutadiene oil, ethyl-2-cyanoacrylate and PFPE oil. The used oils are highly viscous and therefore ensure that spatial diffusion does not change significantly the spin magnetiza-

tion during the measurement. The signal is recorded for various sensing times t and fitted with equation 5.32 (see figure 5.11). The estimated depths range from 34.6 nm to 47.8 nm. Here, the $^{15}N^{+}$ ions have been implanted with an energy of 5 keV. Similar work with $\langle 100 \rangle$ oriented diamonds resulted in a much smaller depth [91]. This deviation can be explained by ion straggling and channeling during the implantation process [187] which is more pronounced in the case of $\langle 111 \rangle$ oriented diamonds.

Depending on the field strength of the statistically polarized spins a minimal sensing time is required to detect the NMR signal. The achievable sensing time is limited by the T_2^{sensor} time. On one hand it has been observed that the T_2^{sensor} times increase with the depth d of the sensor spin due to the presence of surface noise. On the other hand the B_{rms} field generated by the sample spins decreases by $1/d^{3/2}$. Therefore it makes sense to quantify the required sensing time for each depth and compare it with the measured T_2^{sensor} times. The required T_2^{sensor} scales as following with the depth d:

$$\text{required } T_2^{\text{sensor}} \sim \sqrt{\frac{d^3}{\rho}} \tag{5.33}$$

where ρ is the spin density. In figure 5.12 the required T_2^{sensor} for the detection of different ^{1}H spin densities (with a NMR contrast of 50 %) is plotted in dependence of the sensor depth d: For the ^{1}H spin density of water, we find that the required sensing time is ≈ 14 μs for a 10 nm deep NV and ~ 71 μs for a 30 nm deep NV. Achieving these coherence properties requires a suitable host material and low implantation-induced damages. In figure 5.12 the T_2^{sensor} times of three shallow NV centers are plotted in dependence of the depth d. It can be seen that the three shallow NV centers are capable of detecting 10 M of proton spins.

Increasing the depth d also means that more nuclear spins need to contribute to the signal. Consequently the detection volume increases. The sample spins that contribute to half of the B_{rms} signal originate from a detection volume of $\approx 0.49 \cdot \text{d}^3$. In figure 5.14 the corresponding detection volume have been plotted.

For a depth of 35 nm (figure 5.11 dark red curve) and a ^{1}H spin density of $\rho \approx 58$ nm^{-3} (polybutadiene) the statistical magnetization is $B_{rms} \approx 46$ nT. In the detection volume there are $1{\cdot}10^6$ nuclear spins in total. Out of them 550 are statistically polarized. On the other hand thermal polarization would only amount to 12 polarized spins, a factor 1/46 smaller. The largest distance observed between the sensor and the sample spins is 95 nm (figure 5.11 light green curve). In this scenario the total number of nuclear spins is $2{\cdot}10^7$ (^{19}F spins with a density of $\rho \approx 47$ nm^{-3} in PFPE oil). The 2200 statistically polarized spins create a magnetization of $B_{rms} \approx 9$ nT. The number of thermally polarized spins is 200. An even larger detection volume would enable the detection of sample spins based on the thermal instead of the statistical polarization. This would require a modification

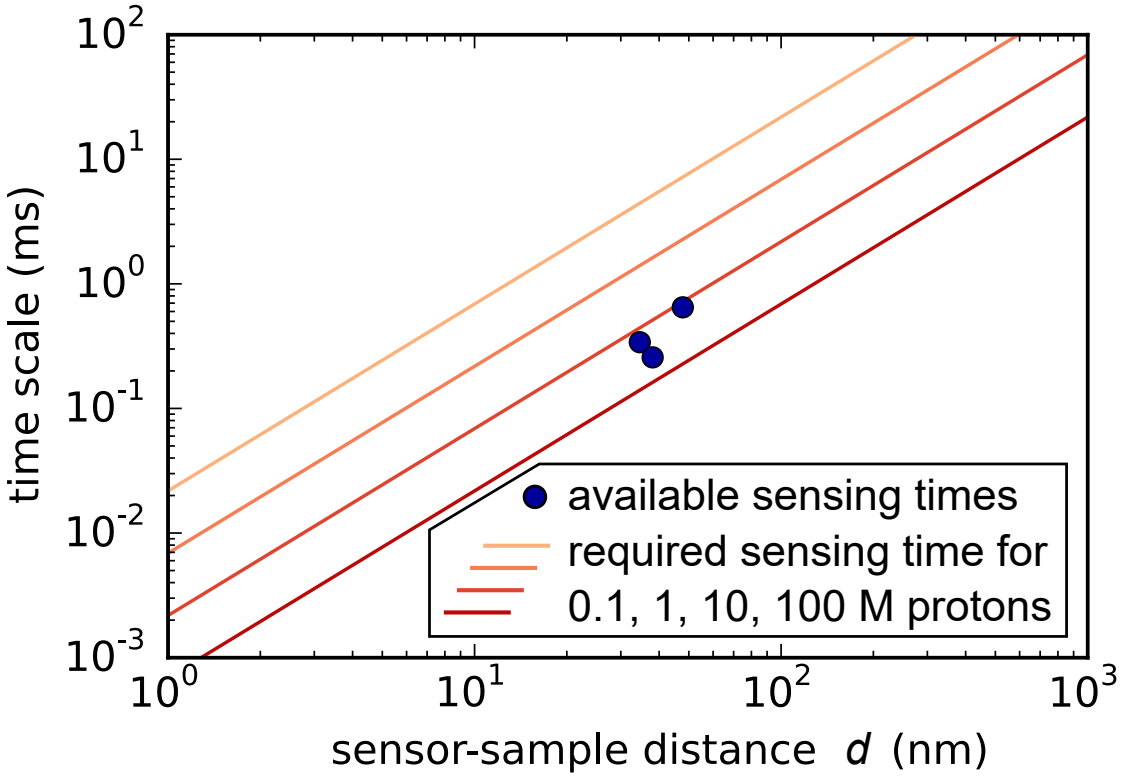

Figure 5.12.: Required sensing time for achieving 50 % NMR contrast in dependence of the sensor to sample distance Lines correspond to different proton spin molar concentrations given in Mol. For comparison: the ^{1}H spin density in water is 111 Mol or 67 per nm^3. The required sensing time scales with $\propto \rho^{-1/2} d^{3/2}$ (ρ: spin density and d: sensor to sample distance). Available sensing times are indicated as red dots and correspond to measured T_2^{sensor} times of various NV centers. In addition to this the depth of these NV centers is determined.

of the sequence as discussed in section 5.6.

5.9. Liquid state nano NMR spectroscopy

Liquid state NMR spectroscopy is a well established technique in chemistry. Its impact is based on the ability to detect the individual fingerprints of the molecules. In the stationary case the dipole-dipole coupling would overlap these fingerprints. The motion of the molecules, translational and rotational, however averages out the coupling. Nanoscale liquid-state NMR based on the statistical polarization has one great disadvantage. This is the fact that sample spins can diffuse out of the detection volume. The sample spins that do replace them have a different net magnetization and hence will not be correlated in the measurement. Therefore it is important to investigate the diffusion dynamics of the sample spins since it is one of the main limiting factors to obtain a high spectral

resolution (equation 5.6).

5.9.1. Spatial diffusion in liquids on the nanoscale

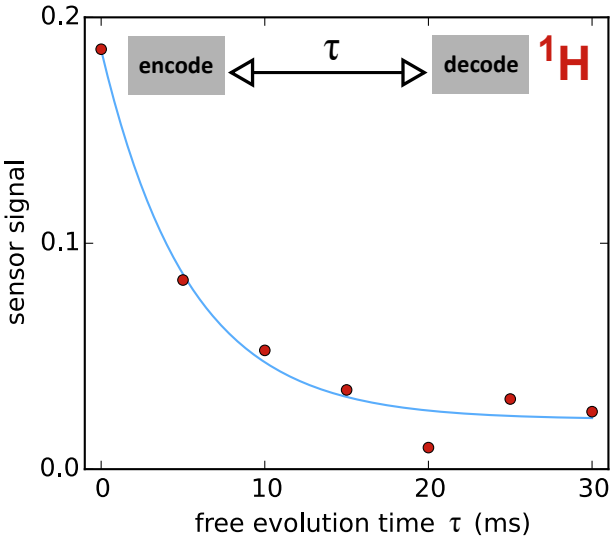

Figure 5.13.: Investigation of spatial diffusion on the nanoscale. Magnetization decay of ^{1}H spins in liquid polybutadiene measured by a 34.4 nm deep sensor. During the sample manipulation part of the NMR protocol (5.8) a RF π pulse is applied off- and on-resonant on the sample spins. The subtraction of both measurements then gives the decay of the sample spin magnetization. It is fitted with an exponential decay function which yields a diffusion time T_D of 5.4 $\pm$ 0.9 ms. The origin of the decay is the diffusion of the sample spins out of the detection volume.

The sensor-memory based NMR technique allows the measurement of the spin magnetization decay. During the storage and sample manipulation part a π pulse flips the sample spins magnetization. Its decay can now be measured by introducing a varying waiting time. A reference measurement with no flip rules out any other decay mechanisms and leads to the observation of solely the spin magnetization decay. The decay can be characterized by an exponential function $e^{-\tau/T_D}$, with a correlation time T_D [199, 207, 208, 209]. After a sufficiently long time the measured B_{rms} signal in the encoding and the decoding becomes completely uncorrelated. Hence the spin magnetization signal has to decay to an offset level of zero.

The sample spins move on average by the root-mean-squared displacement $\sqrt{\langle x^2 \rangle}$. This value depends among others on the viscosity η of the liquid. The diffusion coefficient D comprises all the medium dependent parameters. The root-mean-squared displacement then can be described as:

$$\sqrt{\langle x^2 \rangle} = \sqrt{2DT_D} \tag{5.34}$$

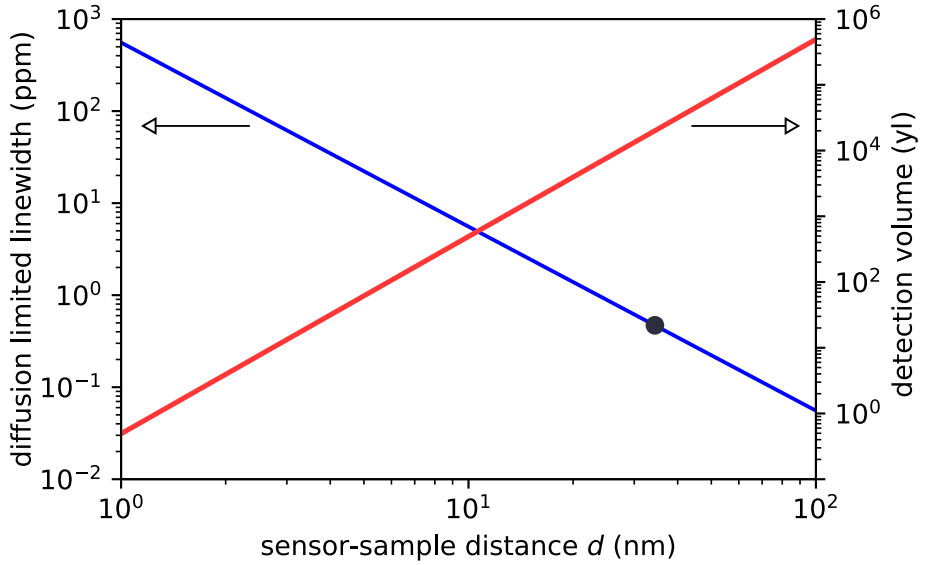

Figure 5.14.: Diffusion limited linewidth [ppm] and detection volume in dependence of the sensor to sample distance. The spectral resolution of nanoscale NMR of liquid samples is restricted by diffusion. For a specific sensor depth the diffusion time T_D is measured of ^{1}H spins in polybutadiene. The corresponding NMR linewidth (left axis) is marked as a circle in the plot ($\frac{2}{\gamma B T_D}$). This result can be extended by extrapolation to various sensor depths d ($\propto d^{-2}$, blue line). Moreover, the detection volume (right axis) depends on the sensor-to-sample distance d ($\approx 0.49 \cdot d^3$) as well. The detection volume is the volume containing the sample spins that contribute to half of the B^2_{rms} signal. Red line shows the depth scaling.

A displacement larger than the range of the detection volume results in an uncorrelated signal. The detection volume has been formulated in dependence of the NV depth d as $0.49 \cdot \mathrm{d}^3$. The depth d can therefore be directly related to the diffusion dynamics:

$$d = \sqrt{2cDT_D} \tag{5.35}$$

with c as a constant.

Through equation 5.35 it becomes clear that the diffusion time T_D is proportional to d^2. Since T_D is limiting the spectral resolution $\Delta\delta$ (eq. 5.6) a larger depth d would in principle increase $\Delta\delta$. The depths determined in this work are larger than the reported in the previous NV nano NMR papers [24, 27, 210]. In addition a large viscosity of the medium is of benefit. In fact the selected molecules for nano liquid state NMR are polymers with a high molecular mass.

The spin magnetization is measured for ^{1}H spins in polybutadiene and the results are shown in figure 5.13. The exponential fit yields a correlation time T_D of 5.4 ± 0.9 ms. The sensors depth is determined in a separate measurement by the method described in section 5.8 to be 34.4 nm (results not shown). With the known parameters c·D is determined to

be 110 nm^2 ms^{-1}. Please note that unexpectedly the fit of the magnetization signal does not yield an offset of zero. This can be explained by the tendency of the polybutadiene to become solid after some time. A probably thin solid layer on the diamond surface would then lead to a second decay occurring on a much larger time scale. This would additionally lead to broadening of the NMR line but with a smaller amplitude.

With the known depth d and the measured diffusion time T_D the relation 5.35 can be used to extrapolate T_D to various depths. In figure 5.14 the resulting diffusion limited linewidth $\Delta\delta$ is plotted in dependence of the depth d. For example for d = 34.4 nm and T_D = 5.4 ms, the diffusion limited linewidth $\Delta\delta$ is 0.46 ppm (at 3 T). The typically required linewidth for distinguishing between ^{1}H chemical shift peaks is 1 ppm. This can be achieved for the liquid polybutadiene with a sensor depth of $\approx$ 25 nm. The corresponding detection volume in yoctoliter is plotted on the right axis of figure 5.14. A depth of 25 nm corresponds to a detection volume of $8{\cdot}10^3$ yl, while d = 100 nm correspond to $5{\cdot}10^5$ yl. These dimensions are 11 and 9 orders of magnitude smaller than in the conventional NMR [4, 5].

The diffusion limitation can be overcome by trapping the sample in nano-pores or nano-dimples [41]. In this case the detection volume would match the sample volume and the sample spins would remain correlated during the measurement sequence. Another approach is to base the detection on the thermal magnetization. The sample spins magnetization would be homogeneous over the whole sample and would all lead to the same phase accumulation no matter how fast they would diffuse. This would require a larger detection volume to increase the ratio between thermal to statistical polarization. Hyperpolarization would increase the ratio as well [204, 205, 206].

5.9.2. Ramsey experiments on nuclear spins in liquids

Figure 5.13 reveals that NMR linewidths sufficient for chemical shift detection are in reach for the sensor depth range measured in this work. The next step is to implement a NMR experiment of sample spins in a liquid. For this purpose a Ramsey experiment has to be performed with a subsequent FFT of the data. The quantum metrology framework (section 5.6) provides the possibility to manipulate the sample spins in the storage part. For a Ramsey experiment the sample spins are flipped by a RF $\pi/2$ pulse and the subsequent waiting time until the final $\pi/2$ pulse is varied. The length of the storage part is fixed in order to filter out spin magnetization decay effects. It can be chosen to be up to T_D. A longer period would reduce the signal amplitude significantly.

In the measurement phase modulation for generating an artificial oscillation is introduced. The phase of the final RF $\pi/2$ pulse is modulated with a frequency ν: $\phi = 2\pi\nu\tau$. The advantages of phase modulation are first of all that the resonance peaks can be shifted

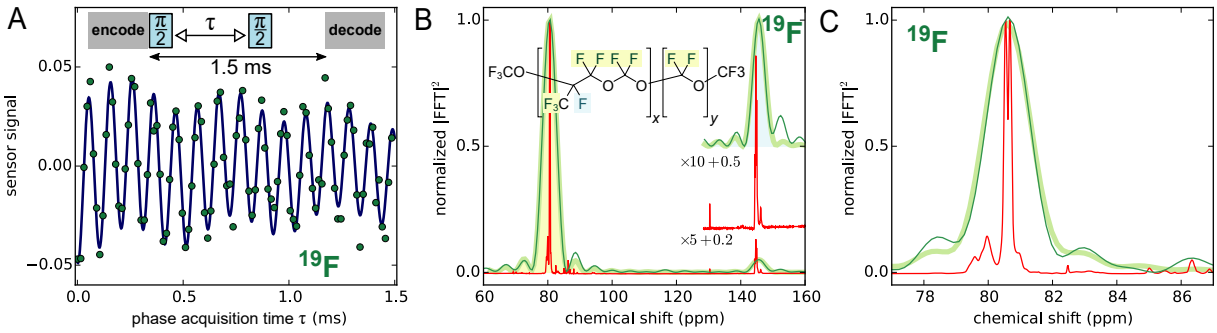

Figure 5.15.: ^{19}F **High-resolution NMR spectroscopy**. **A** Ramsey measurement of ^{19}F spins in PFPE oil. The time length T of the sample manipulation part is fixed to 1.5 ms to ensure the same diffusion effect for all phase acquisition times τ. The data is fitted with two cosine functions with an exponential decay. The oscillation frequencies are 2.1 kHz and 9.8 kHz. **B** Comparison between conventional NMR and sensor-memory based nanoscale NMR. The FFT power spectra of the Ramsey measurement from A is plotted in green and its corresponding fit as a bold light green line. Measurement results obtained with a 400 MHz NMR spectrometer of PFPE are plotted as a red line. The chemical structure of PFPE is depicted in the graph. ^{19}F atoms within the molecule and with different chemical shift are highlighted in pale green and blue. They are assigned to the NMR spectrum by color coding the area under the peaks. The peak with a lower intensity is enhanced by a factor of 5 and 10, for better visibility. Zero padding is added to the data before applying the FFT. **C** Zoom-in view of the high intensity NMR peak (around 80 ppm). The phase acquisition time τ is increased to the diffusion limit of 5 ms and yields a FWHM of 1.3 ppm (decay time 2.5 ms). In contrast to it the FWHM in the conventional NMR measurement is an order of magnitude smaller.

away from zero in the FFT and thereby away from the noise generated due to e.g. the decay of the signal. Furthermore multiple resonance frequencies (e.g. due to chemical shift) with a similar absolute detuning but a different sign would normally overlap in the FFT spectrum. Phase modulation however prevents this. For a better visualization of the peaks zero-padding is added to the data.

The chemical shift range for ^{19}F spins is with ≈ 100 ppm much larger compared to the case of the protons. Hence observing distinct chemical shift peaks is less challenging for ^{19}F spins. The first experiments are therefore performed with ^{19}F spins. The sample of choice is perfluoropolyether (PFPE) oil with the molecular formula: $CF_3O[-CF(CF_3)CF_2O-]_x(-CF_2O-)_yCF_3$ with about $x = 140$ and $y = 13$ subunits per polymer strand. The results of the Ramsey experiments are shown in figure 5.15. A modulation of the signal hints to a second oscillating term. The two signals correspond to two different chemicals shift groups of the polymer. The inset of figure 5.15 B depicts the chemical structure with the two color coded chemical shift groups. In the same figure the FFT power spectra is shown with the two corresponding peaks. Here two measurements

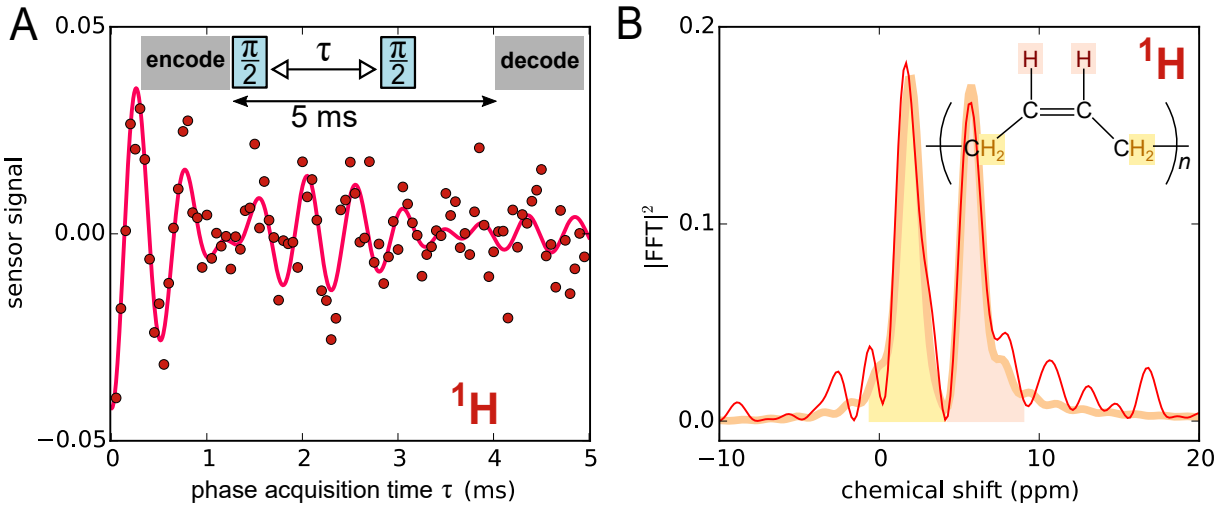

Figure 5.16.: ^{1}H **High-resolution NMR spectroscopy**. **A** Ramsey measurement of ^{1}H spins in liquid polybutadiene. Two exponentially decaying cosine functions are fitted to the results, obtaining a frequency of 1.7 kHz and 2.2 kHz. The time T is fixed to 5 ms. **B** FFT power spectra of the Ramsey measurement shown in A. Inset shows the chemical structure of polybutadiene. Its two subgroups (CH and CH_2) are color coded and highlighted in the spectra. The FWHM of the two NMR resonance peaks are 1.3 ppm and 1.4 ppm. Zero-padding is applied.

have been performed. One is the NV nano NMR measurement (bold green) and the other is the conventional NMR measurement with a 400 MHz NMR spectrometer (dark green). In the NV nano NMR measurements the time period of the storage period is fixed. This means that the spin magnetization decay is filtered out and should not effect the decay of the Ramsey experiment. The time period of 5 ms (in 5.15 C) translates to a linewidth of 0.5 ppm. However the FWHM of the peak is 1.3 ppm corresponding to a decay time of 2.5 ms. This deviation can be explained by the high viscosity of the sample. The sample spins are not diffusing fast enough and consequently the averaging out of the dipole-dipole coupling is not complete. The enlarged view in 5.15 C reveals that the conventional NMR spectrometer shows a more than one order of magnitude narrower line.

The achieved linewidth of ≈ 1 ppm in the case of ^{19}F NMR motivated the detection of ^{1}H chemical shifts (range of ≈ 13 ppm). The ^{1}H diffusion measurement of the polybutadiene oil in section 5.9.1 promises a linewidth of less than 1 ppm for the typical sensor depths of this work (figure 5.14). The molecular formula of polybutadiene is $(CH_2CH{=}CHCH_2)_n$ with about $n = 90$ subunits per polymer strand. The ^{1}H spins in the CH_2 and the CH subgroups are expected to show chemical shifts differing by 3.34 ppm. The results of the Ramsey experiment are shown in figure 5.16. As expected two resonance lines can be distinguished in the spectrum that originate from the different chemical shift groups. The FWHM of the peaks are 1.3 ppm and 1.4 ppm. For this particular measurement

the sensor depth is 35.5 nm. According to the discussion of figure 5.14 a three times narrower linewidth is expected. As in the case of the PFPE oil, the high viscosity of the polybutadiene oil circumvent the full motional narrowing effect of a liquid. Hence the measured FWHM is limited by the dipole-dipole coupling between the sample spins.

These are proof-of-principle experiments. Here the used samples are restricted to liquids with a high viscosity. What is missing is the universal application to other samples. Two paths can lead to an universal application. The first is to match the detection volume with the sample volume [41]. The diffusion of the sample spins would not lead to a decay of the spin magnetization anymore. The second solution would be to base the detection on thermally polarized or even hyperpolarized spins. The magnetization would in this case be homogeneous and the diffusion would not alter the correlation signal.

5.10. Solid state nano NMR spectroscopy

NMR spectroscopy of solid samples is an indispensable tool for the characterization of the underlying structure. The precise chemical structure of a sample ultimately defines its properties. Hence the knowledge of the structure is important for example for medical but also for industrial applications. The great challenge in solid state NMR is the stationary dipole-dipole coupling (equation 5.20) that broadens the resonance peak. N sample spins are interacting with each other by dipolar coupling which results in 2^N different NMR lines with different strengths. In conventional NMR there are two ways of counteracting the dipolar broadening. The first is the rotation of the sample around the magic angle (θ=54.7°) with respect to the applied magnetic field. The second method is the application of homo- or heteronuclear decoupling sequences. During these sequences RF pulses rotate the spins and create an additional Hamiltonian term contrary to the dipole Hamiltonian. In this section the NMR spectroscopy of solid-state samples is brought to the nanoscale regime. Especially for the goal of the community to detect single molecules and investigate their dynamics the shown results mark an important step.

5.10.1. Spin diffusion in solids on the nanoscale

In the case of solid state nano NMR the diffusion limit does not apply anymore. Yet the spin magnetization will decay due to by spin diffusion mediated by dipole-dipole coupling among the nuclear spins. This decay is expected to occur on a longer time scale. Spin diffusion of polymers has been investigated by conventional NMR [48]. The measured diffusion coefficient is $\approx$ 1 nm^{2}ms^{-1}, which is approximately two orders of magnitude slower than in the case of spatial diffusion in polybutadiene. Analogue to

the ^{1}H diffusion measurement in polybutadiene, the spin diffusion of ^{1}H spins can be determined by measuring the spin magnetization decay.

The sample is poly(ethyl 2-cyanoacrylate) (superglue) in its solid form. Figure 5.17 shows the results of the sample spins magnetization decay. The exponential fit reveals a decay time of 94 ± 11 ms, a factor 17 larger than in the case of polybutadiene. The sensor depth is 43.7 nm. With equation 5.35 the diffusion coefficient c·D of poly(ethyl 2-cyanoacrylate) can be determined: 10 nm^{2}ms^{-1}.

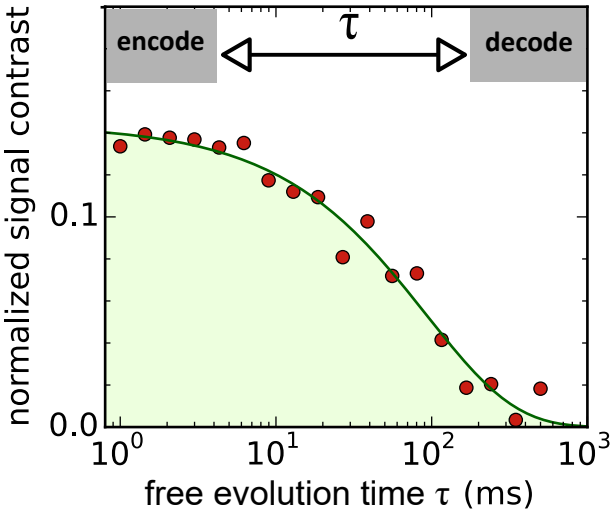

Figure 5.17.: Nanoscale ^{1}H spin diffusion measurement. Magnetization decay measured of ^{1}H spins in solid poly(ethyl 2-cyanoacrylate) (same pulse sequence used as in fig. 5.13). An exponential fit yields a decay time of 94 ± 11 ms. The sensor spin is located 43.7 nm deep in the diamond lattice.

5.10.2. Ramsey experiments on nuclear spins in solids

The next step is the Ramsey measurement of ^{1}H spins in poly(ethyl 2-cyanoacrylate). The results are depicted in figure 5.18 A (top). The corresponding FFT reveals a linewidth of 26 kHz or in relative parameters 206 ppm (figure 5.18 B light orange curve). Strong dipolar coupling between the stationary sample spins leads to the observed broadening. This broad NMR peak hides all individual lines related to e.g. the chemical shift or J coupling.

5.10.3. Homonuclear decoupling: WAHUHA and MREV-8

There are two strategies in the NMR community for counteracting the dipolar broadening. The magic angle spinning as one of them can be ruled out as it is technically too difficult

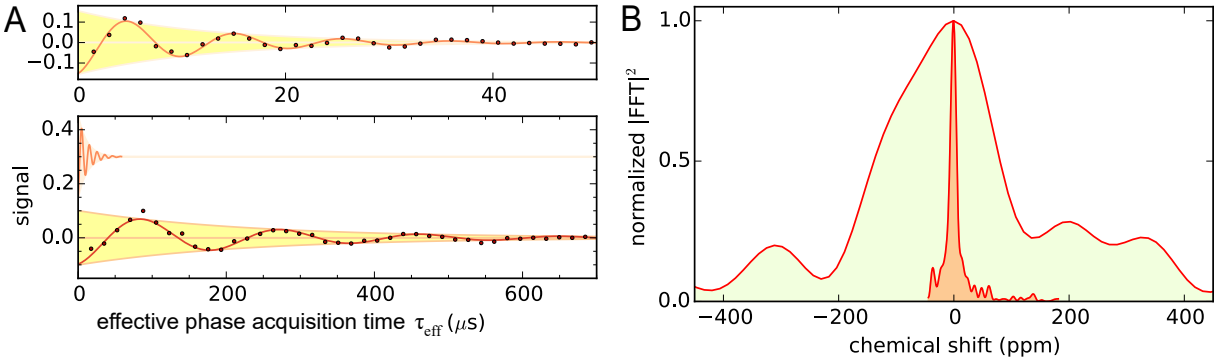

Figure 5.18.: High-resolution solid-state ^{1}H NMR spectroscopy. **A** In the top graph the results of a Ramsey measurement of ^{1}H spins in solid poly(ethyl 2-cyanoacrylate) are shown. The bottom graph shows again the results, but on a longer time scale. In addition to it a Ramsey measurement with homonuclear decoupling (MREV-8) is plotted. The decoupling sequence makes the sample spins less susceptible to the magnetic field which is considered in the effective phase acquisition time τ_{eff}. All results are fitted with an exponentially decaying cosine function. **B** The corresponding FFT power spectra of both measurements is shown. The homonuclear decoupling increases the spectral resolution by a factor of 17, from 26 kHz (206 ppm) to 1.5 kHz (12 ppm).

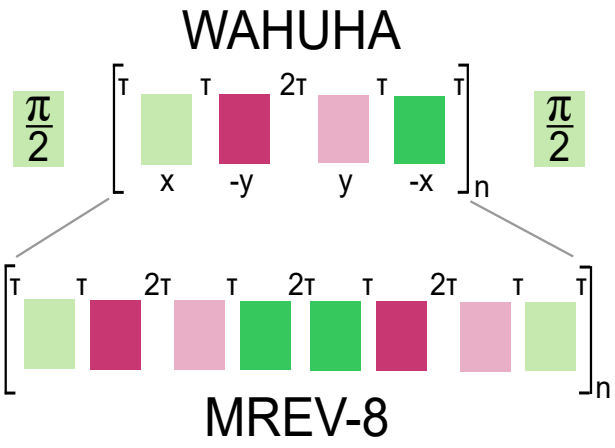

Figure 5.19.: Homonuclear decoupling sequences: WAHUHA and MREV-8. The pulse sequence of WAHUHA (top) and MREV-8 (bottom), incorpated in a Ramsey measurement, is shown. A train of $\pi/2$ pulses with varying phases and free evolution period counteracts the dipole-dipole interaction between the sample spins. Four pulses are applied in the case of WAHUHA and eight pulses in the case of MREV-8. The phase of the pulses (X,-X, Y and -Y) is illustrated in different colours.

to rotate the sample at high magnetic field without deteriorating the properties of the sensor and of the memory [211]. However the implementation of homonuclear decoupling sequences is possible. The sample manipulation part allows the application of any desired

sequence on the sample spins. The utilized decoupling sequences are: WAHUHA [212] and MREV-8 [213, 214]. In both cases $\pi/2$ pulses with different phases are applied.

The $\pi/2$ pulses can be represented by pulse propagators: $R_{X,Y,Z} = e^{-i\frac{\pi}{2}I_{X,Y,Z}}$. The unitary operators are defined as: $X = e^{-iH_X\tau}$, $Y = e^{-iH_Y\tau}$, $Z = e^{-iH_Z\tau}$. The sequences can be described by a train of pulse propagators and waiting times τ. For WAHUHA the sequence is as follows (see also figure 5.19): $-\tau - R_X - \tau - R_{\overline{Y}} - 2\tau - R_Y - \tau - R_{\overline{X}} - \tau -$. It is assumed that the only interaction acting on the sample spins is the dipolar coupling. In the absence of pulses, the Z operator would act through out the evolution time. The pulse propagators on the other hand induce varying effective operators during the evolution time. For WAHUHA the order of acting operators is: $\mathrm{Z} - \mathrm{Y} - \mathrm{X} - \mathrm{X} - \mathrm{Y} - \mathrm{Z}$. The average Hamiltonian of this sequence of operators can be formed. It vanishes in the first order and thus cancels out the dipole interaction. The sequence can be repeated every $6 \cdot \tau$. The susceptibility to the sample spins magnetization is reduced by the homonuclear decoupling sequence. In the case of the WAHUHA sequence, the chemical shift splitting for example would be reduced by a factor of $c_{\mathrm{dec,WAHUHA}} = 1/\sqrt{3}$.

A higher order canceling of the average Hamiltonian can be achieved by the extended version of the WAHUHA sequence which is MREV-8. Expressed by the pulse propagators and waiting time τ the MREV-8 is (figure 5.19): $-\tau - R_X - \tau - R_{\overline{Y}} - 2\tau - R_Y - \tau - R_{\overline{X}} - 2\tau - R_{\overline{X}} - \tau - R_{\overline{Y}} - 2\tau - R_Y - \tau - R_X - \tau -$. Assuming again the presence of dipolar interaction the corresponding order of effective unitary operators is: $\mathrm{Z} - \mathrm{Y} - \mathrm{X} - \mathrm{X} - \mathrm{Y} - \mathrm{Z} - \mathrm{Z} - \overline{\mathrm{Y}} - \mathrm{X} - \mathrm{X} - \overline{\mathrm{Y}} - \mathrm{Z}$. The factor for MREV-8 by which the magnetic susceptibility is reduced is $c_{\mathrm{dec,MREV8}} = \sqrt{2}/3$. The homonuclear decoupling is most effective, the faster the rotation of the spins is performed.

Both homonuclear decoupling sequences are applied during the Ramsey experiments of ^{1}H spins in poly(ethyl 2-cyanoacrylate). They significantly prolong the dephasing time of the spins. In the bottom graph of figure 5.18 A the two measurement with and without MREV-8 are displayed for comparison. For the measurement with MREV-8 the total evolution time is modified with the factor $c_{\mathrm{dec,MREV8}}$. The FFT yields a FWHM of 1.5 kHz (12 ppm). The line is a factor of 17 narrower compared to the case of no homonuclear decoupling.

The aforementioned ratio of total interrogation time and the effective phase accumulation time $c_{\mathrm{dec,WAHUHA}}$ and $c_{\mathrm{dec,MREV8}}$ can be determined for each sequence. For this purpose the $\pi/2$ pulses of the Ramsey sequence are detuned and the corresponding shift in the resulting NMR spectrum is determined. By applying WAHUHA and MREV-8 sequences a mismatch between the detuning frequency and the resulting shift is expected. For various detunings, the shift is measured and is plotted in figure 5.20. Linear fits yield a slope of $c_{\mathrm{dec,WAHUHA}} = 0.57 \pm 0.01$ and $c_{\mathrm{dec,MREV8}} = 0.46 \pm 0.01$. Both values fit with

the scaling factors found in the literature [215].

The length of each pulse is $t_{\pi/2}$=3 μs which needs to be reduced in order to achieve a better homonuclear decoupling. This can be achieved by an amplifier with a higher RF power and by optimizing the RF structure. In principle other homonuclear decoupling sequences besides WAHUHA and MREV-8 can be applied as well. If multiple nuclear spin species are involved then applying heteronuclear decoupling would be necessary [216].

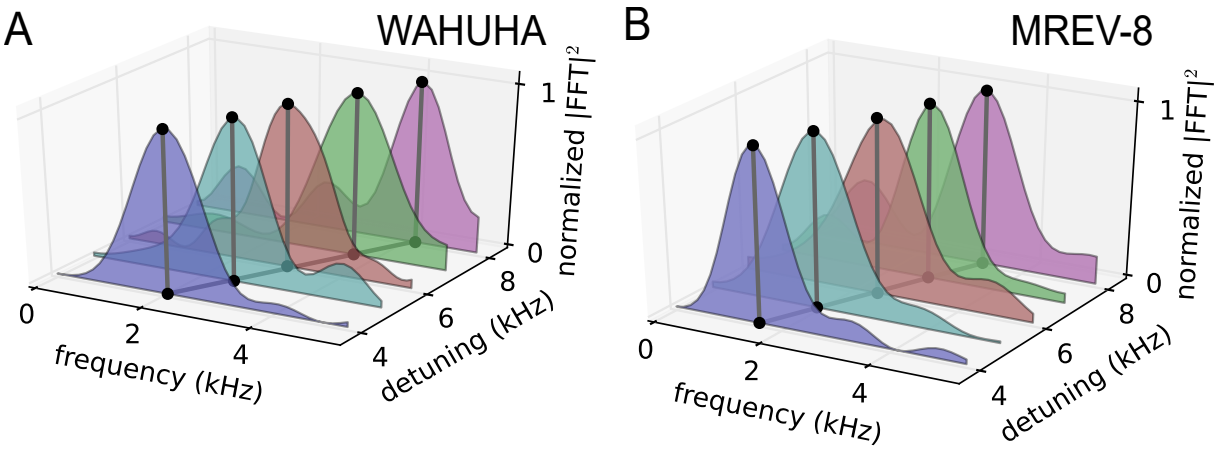

Figure 5.20.: Ratio of effective phase accumulation time τ_{eff} to total interrogation time for WAHUHA and MREV-8. The magnetic field susceptibility in a Ramsey measurement is reduced by applying homonuclear decoupling pulses. The reduction factor is different for WAHUHUA and MREV-8. It can be measured by detuning the $\pi/2$ pulses of the Ramsey measurement and determining the shift in the resulting NMR spectra. For a whole set of detuning frequencies the results can be fitted by a linear function. The fit yields a slope of $c_{\text{WAHUHA}} = 0.57 \pm 0.01$ and $c_{\text{MREV-8}} = 0.46 \pm 0.01$. The intercept of the linear fit reveals the detuning from the resonance frequency of the sample spins.

5.11. Multilayer nano NMR

In this work the ability to precisely determine the depth is shown. It is also possible to discriminate between small differences in the resonance frequency. Furthermore the spin magnetization decay measurement is a tool to characterize the diffusion dynamics of the sample spins. All together opens the possibility to also investigate multiple layers with nanometer resolution [27].

To demonstrate the feasibility of our technique a ^{1}H containing solid poly(ethyl 2-cyanoacrylate) layer is deposited on the diamond surface. On top a fluorinated sample, namely PFPE oil, is placed. Figure 5.21 A shows the described arrangement. The measurement task is to determine the distances to the sensor and to analyze its composition.

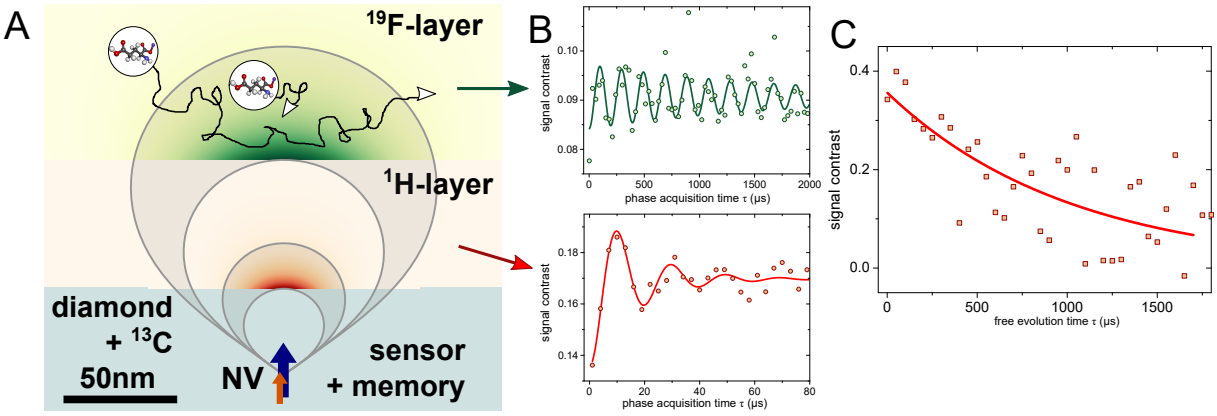

Figure 5.21.: Nanoscale Multilayer NMR. **A** The sensor-memory spin based nanoscale NMR system in diamond is used to characterize a proton and fluorine containing multilayer. Selective detection of ^{1}H spins in solid poly(ethyl 2-cyanoacrylate) and of ^{19}F spins in PFPE oil is possible by their distinct resonance frequencies. The detection volume (containing sample spins that contribute to half of the signal B^2_{rms}) is marked by shaded regions for both layers. The strength of the dipole interaction is indicated by the darkness of the shade. **B** Separate Ramsey measurements are conducted for the ^{19}F containing (upper curve) and the ^{1}H containing layer (lower curve). The diffusing ^{19}F spins in the PFPE oil show a long lasting signal due to the motional averaging effect on the dipole-dipole interaction. Whereas the ^{1}H spin signal in solid poly(ethyl 2-cyanoacrylate) is decaying with 16 ± 3 μs. The fit function in both cases is an exponentially decaying cosine. **C** Spin magnetization decay is measured for the ^{1}H spin layer. The exponential fit yields a decay time of 1.0 ± 0.2 ms. The depth of the sensor spin is 38.1 ± 0.1 nm. The ^{1}H layer is 56.9 nm thick.

The PFPE oil is not containing proton spins and is not miscible with the poly(ethyl 2-cyanoacrylate). Therefore the PFPE oil can be investigated by its ^{19}F-NMR signal. The distance of the sensor to the ^{19}F spins in the oil is determined with the method introduced in section 5.8. The results are plotted in figure 5.11 (light green curve) and the fit yields a distance of ≈ 95 nm. This distance represents an upper boundary for the ^{1}H spins containing layer. The sensor's depth can be determined via the ^{1}H signal: 38.1 ± 0.1 nm (figure 5.11 light red curve). Accordingly the thickness of the proton layer is 56.9 nm.

Next Ramsey experiments are performed separately on both layers in order to examine the mobility of their spins. The measured T_2^* time of ^{19}F spins in PFPE is more than 1 ms (see figure 5.21 B top). This is a sign of a high mobility of the ^{19}F spins indicating a liquid. The ^{1}H signal from poly(ethyl 2-cyanoacrylate) on the other hand decays much faster with T_2^*= 16 ± 3 μs (see figure 5.21 B bottom). This fast decay is expected from solid-state spins. The spin magnetization of spins in solids however is expected to last much longer. Its decay is measured for ^{1}H spins in poly(ethyl 2-cyanoacrylate) and yields a decay time of 1.0 ± 0.2 ms, two orders of magnitude longer than the T_2^* time

(see figure 5.21 C). Therefore it can be concluded that the ^{1}H-spins are not mobile and dipole-dipole coupling is leading to fast dephasing.

5.12. Sensitivity

An important parameter for a sensing technique is its sensitivity. The sensitivity needs to be analyzed in the context of the measurements task. NMR spectroscopy aims for a high spectral resolution which scales with $\delta\nu = 1/\tau$. In the case of the sensor-memory based protocol a spectral resolution of sub Hz can in principle be achieved. During the long storage time (and hence long phase acquisition time τ) the sensor spin is idle which might reduce the sensitivity. However so far the actually achieved spectral resolution, is limited by the sample properties to around 150 Hz (see equation 5.6).

For the discussion of sensitivity of the NV nano NMR it is assumed that all spins exhibit the same resonance frequency (single nuclear spin species and single chemical shift component). Furthermore any other noise source than projection noise is not considered. For the task of precisely determining the frequency of the sample spins the sensitivity is:

$$\eta_\nu = \frac{\sigma_S\sqrt{t_{\mathrm{tot}}}}{dS/d\nu} \tag{5.36}$$

with

$$\sigma_S\sqrt{t_{\mathrm{tot}}} = \sqrt{t+\tau+T_{\mathrm{read}}}/2\,, \tag{5.37}$$

$$dS/d\nu = 2\pi\tau vis\frac{\gamma^2 B_{\mathrm{rms}}^2 t^2}{8}\exp\left(-\frac{\gamma^2 B_{\mathrm{rms}}^2 t^2}{4} - \left(\frac{t}{T_2^{\mathrm{sensor}}}\right)^n\right). \tag{5.38}$$

σ_S stands for the statistical projection noise of the QND readout of the memory spin. The total measurement t_{tot} is the sum of the sensing time t, the phase acquisition time τ and the QND readout time T_{read}. The visibility of the signal is discussed in section 5.7 and is around 0.65. The typically chosen sensing time t in the measurements is around 200 μs which is approximately the average T_2^{sensor}. For t $\approx T_2^{\mathrm{sensor}}$ and t $\ll \tau$, T_{read} the sensitivity is:

$$\eta_\nu \approx \frac{\sqrt{\tau+T_{\mathrm{read}}}}{\tau\gamma^2 B_{\mathrm{rms}}^2 (T_2^{\mathrm{sensor}})^2}\cdot\exp\left(\frac{\gamma^2 B_{\mathrm{rms}}^2 (T_2^{\mathrm{sensor}})^2}{4}+1\right). \tag{5.39}$$

In our case the field of the statistical magnetization is weak with values ranging from 9 to 46 nT. Hence we can assume that $B_{\mathrm{rms}}T_2^{\mathrm{sensor}}$ is much smaller than 1, which leads to the approximation of equation 5.39:

$$\eta_\nu \approx \frac{\sqrt{\tau+T_{\mathrm{read}}}}{\tau\gamma^2 B_{\mathrm{rms}}^2 (T_2^{\mathrm{sensor}})^2}\cdot\exp(1). \tag{5.40}$$

Additionally in this study the phase acquisition time τ is limited by the decay time T, which mainly depends on T_2^* and T_D of the sample spins. It is around 2.5 ms, a factor of 3 smaller than the readout time. In this case η_ν can be written as:

$$\eta_\nu \approx \frac{2}{\sqrt{T}\gamma^2 B_{\mathrm{rms}}^2 (T_2^{\mathrm{sensor}})^2} \cdot \exp(1). \tag{5.41}$$

Once the limit of T is overcome and $\tau \gg T_{\mathrm{read}}$ applies, then the sensitivity η_ν will scale with $1/\sqrt{\tau}$:

$$\eta_\nu \approx \frac{1}{\sqrt{\tau}\gamma^2 B_{\mathrm{rms}}^2 (T_2^{\mathrm{sensor}})^2} \cdot \exp(1). \tag{5.42}$$

The sensitivity can also be defined for the task of detecting the strength of sample spin magnetization B_{rms} with a fixed spectral resolution $\delta\nu$.

$$\eta_{B\mathrm{rms}} = \frac{\sigma_S \sqrt{t_{\mathrm{tot}}}}{dS/dB_{\mathrm{rms}}^2} \tag{5.43}$$

with

$$dS/dB_{\mathrm{rms}}^2 = vis \frac{\gamma^2 t^2}{4} \exp\left(-\frac{\gamma^2 B_{\mathrm{rms}}^2 t^2}{2} - \left(\frac{t}{T_2^{\mathrm{sensor}}}\right)^n\right) \tag{5.44}$$

For a weak field of the sample spin magnetization B_{rms}t is $\ll 1$ and it is necessary to utilize T_2^{sensor} as the sensing time t.

$$\eta_{B\mathrm{rms}} = \frac{2\sqrt{T_2^{\mathrm{sensor}} + \tau + T_{\mathrm{read}}}}{\gamma^2 (T_2^{\mathrm{sensor}})^2} \cdot \exp(1) \tag{5.45}$$

Figure 5.22 shows the scaling of the standard deviation of an exemplary NMR measurement. The scaling for the power spectrum is $\propto 1/\mathrm{N_{avg}}$ and $\propto 1/\sqrt{N_{\mathrm{avg}}}$ for the time series data.

5.13. Comparison between the NV NMR methods

Since the first demonstration of NMR detection with NV centers in diamond the pulse sequences have been enhanced with the goal of achieving a higher spectral resolution. The three main pulse sequences currently used for high spectral resolution nanoscale NV NMR are: correlation spectroscopy [50], continuous sampling [200, 201, 39] and the here presented memory based correlation spectroscopy. In the following a comparison between these three sequences is presented.

The implementation of correlation spectroscopy purely based on the electron spin is simple as it does not require any additional resource like a storage medium or a stable

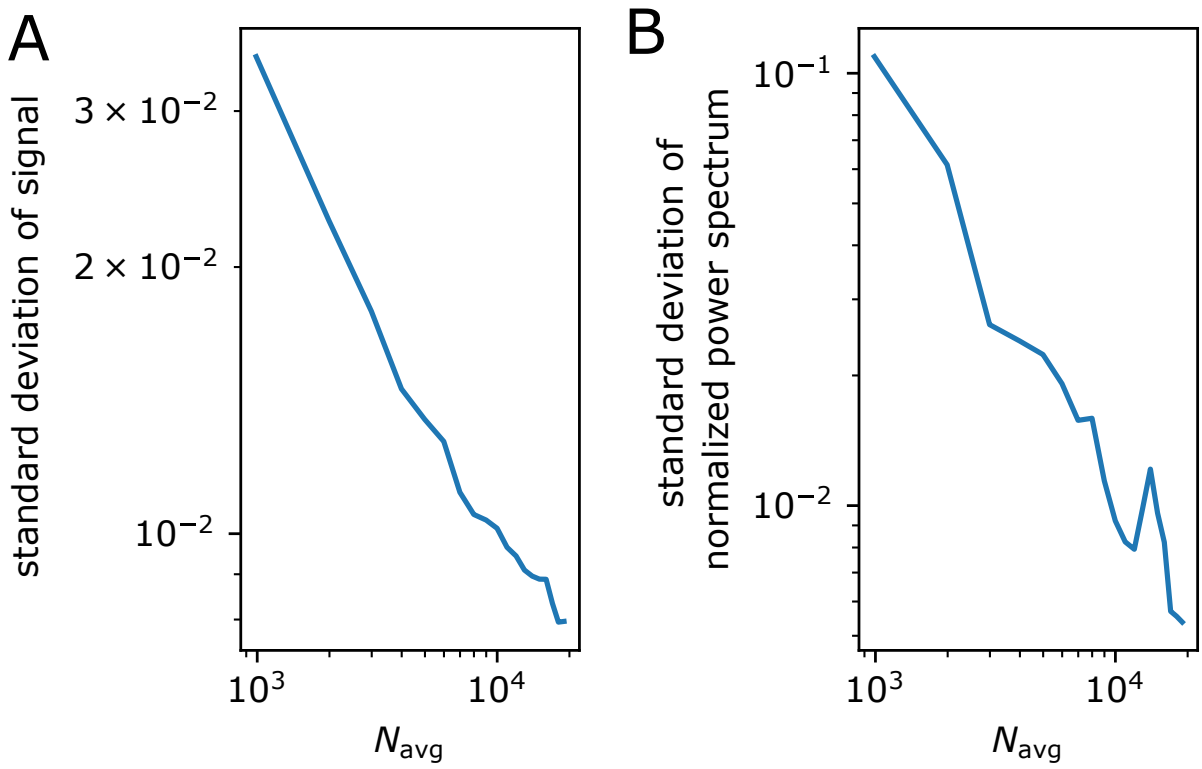

Figure 5.22.: Standard deviation scaling of an exemplary NMR measurement. The standard deviation scaling of the Ramsey measurement of ^{19}F spins in PFPE is plotted (displayed in Figure 5.15 A). The standard deviation of data from the fit is determined and plotted for increasing measurement time (N_{avg}). **A** shows the deviation of the time series from the fit. Here the scaling is $\propto 1/\sqrt{N_{\mathrm{avg}}}$. **B** shows the deviation of the normalized power spectrum data from the fit. The power spectrum scales with $\propto 1/\mathrm{N_{avg}}$. The first standard deviation point is set for $N_{\mathrm{avg}} = 1000$. The total number of 100 data points with $T_{\mathrm{meas}} = 17.8$ ms corresponds to an averaging measurement time of 30 min.

timing source. It can be implemented at any applied magnetic field. The main drawback of the technique is that its resolution is limited by the T_1^{sensor} time which is a few ms. Second if no memory spin is available then the readout is additionally charged with photon-shot noise. The readout is therefore inefficient and makes long averaging times necessary.

The continuous sampling technique, also called quantum heterodyne (Qdyne) or coherently averaged synchronized readout (CASR), is motivated by its sensor unlimited resolution. Furthermore its sensitivity does not scale with the target resolution since the sample signal is continuously sampled. For a test signal produced by a signal generator narrow linewidth with up to mHz FWHM were measured [200, 201, 39]. When it comes to nuclear spins it is difficult to achieve high spectral resolution with this technique. The

reasons are the continuous entangling between the sensor spin and the sample spins and sensor spin projection which induces a back-action on the sample spins. This leads to dephasing. The effect depends on the hyperfine coupling between sensor and sample spins. For samples more than 10 μm away from the sensor spin the back-action induced broadening is only on the order of a few Hz. Indeed with a 13 μm deep ensemble of sensor spins the thermally polarized sample spins could be detected and a linewidth of 3 Hz could be achieved [39]. But a demonstration of high spectral resolution with nanometer scale samples or even single nuclear spins is not unfeasible with continuous sampling. Besides the aforementioned measurement back-action, the laser readout pulses during the evolution time can induce excitation of dark spins on the diamond surface or of radicals in the sample [46]. This accounts for an additional source of noise and leads to relaxation of the sample spins. For (solid) poly(ethyl 2-cyanoacrylate) e.g. the spin magnetization decays after a few hundred laser pulses [217, 218]. The latter can be prevented in the case of a micrometer distance between the sensor and the sample by illuminating with total internal reflection which would only affect the sensor spins [39]. However in the nm-case the diffraction of light will lead to simultaneous sample illumination.

The measurement back-action can be attenuated by performing a weak measurement [218]. In the experiment this means a reduction of the sensing time. Consequently the contrast is reduced and more averaging measurement steps are required. On the other hand more readout pulses can be applied within one total sweep of measurement. Depending on the measurement task a trade-off between spectral resolution and measurement sensitivity needs to be made. The continuous sampling technique relies on single laser pulses that exhibit photon-shot noise. This reduces the sensitivity substantially. Repetitive readout [28] helps and has been applied [201] but single shot readout is not feasible, due to the required ms long measurement time [29].

The memory based NMR detection on the other hand applies readout in a single-shot. More importantly it does not have the measurement back-action limitation. In the sample manipulation part the sensor spin is not excited and there is no entanglement between the sensor and the sample spins. Additionally methods have been introduced to circumvent the dissipation effect of the sensor on the sample spins [15]. However the idle mode of the sensor can be seen as a disadvantage since for a significant part of the total measurement time no signal is acquired. Once the sample manipulation part is much longer than the readout time (a few ms) it will dominate the total measurement time. The sensitivity can be increased by e.g. adding more sensor spins. By deterministically initializing their memory spins a collective application of the sequence is possible. Implementation of compressed sensing would also reduce the required measurement time substantially [219].

It can be concluded that the continuous sampling technique and the memory based

NMR detection have both their advantages and disadvantages. In the end it will depend on the task which sequence will be more suitable. E.g. for the high resolution spectroscopy of strongly coupled small clusters of nuclear spins the measurement back-action and the photon-shot noise dominated readout are two obstacles. Therefore the memory based NMR detection would be favorable. However for very weakly coupled nuclear spins the continuous sampling technique could outplay the memory based one by its predicted shorter measurement time. Interestingly the measurement of micrometer-scale samples [39] had a duration similar to the NMR measurements based on a memory spin (see table A.3) due to the weak sample spins' signal.

The choice of the technique will also be defined by the applied magnetic field strength. If a high magnetic field (B > 1 T) is required to e.g. facilitate chemical shift detection then the continuous sampling technique is not likely to be used since currently the necessary Rabi frequencies Ω cannot be reached ($\Omega = \gamma \cdot B$ are required, for ^{1}H spins at 1 T, Ω is 42.576 MHz). The memory based sensing has also the advantage that any NMR sequence can be applied in a straightforward manner to the sample spins e.g. homonuclear decoupling. In the case of the continuous sampling method an arbitrary NMR sequence other than a simple FID or an echo sequence is difficult to implement. In Qdyne the higher order signal originating from ^{13}C spins might overlap with the ^{1}H spin signal [220] and working with ^{13}C purified diamond sample or adjusting the sequence might be necessary.

5.14. Outlook

The NV Nano NMR experiments have shown great potential for NMR spectroscopy. Now this potential can be converted into an useful application in chemistry, biology or medicine. However still improvements of the NV nano NMR method need to be conducted.

The NV Nano NMR technique has the potential to detect and to image single molecules. For this purpose it will be essential to position the single molecules right above the location of a NV center in diamond. Work to functionalizing the diamond surface is going on [221]. Once the single molecule is successfully attached to the diamond, the hyperfine gradient created by the NV center could be used to map out the nuclear spin locations within the molecule. Besides the stationary operation of NV Nano NMR it can also be used for imaging larger samples. Indeed NMR imaging has been demonstrated for large samples but with low spectral resolution [43, 44]. One possibility has been be to scan the molecule over the sensor or vice versa with an AFM. The other approach is to work with an ensemble of NV centers and image them with a widefield setup. Resolution beyond the diffraction limit can be achieved by the STED technique [31] or STORM [222]. With the high spectral resolution shown in this work it should now be possible to image and

identify molecules on a nanometer scale. Regarding spatial resolution a magnetic field gradient can be helpful. For example a gradient of 10 mT/nm has been produced by a magnetic write head and measured by the NV center [195].

In contrast to conventional NMR spectrometers, NV Nano NMR does not fundamentally need a high magnetic field. The continuous sampling e.g. can work at ultra-low magnetic fields. The memory based sensing however requires at least 0.25 Tesla in order to have a sufficiently long nuclear spin lifetime. But this can be achieved by permanent magnets [29]. This would mean a solely room-temperature operation and would allow a miniaturization of the whole experimental setup. Additionally there is no need to add a reference molecule to the sample like in the case of conventional NMR. The NV center electron spin or the intrinsic ^{13}C spins can act as a reference. All these aspects suggest that it should be possible to develop a low-cost benchtop NMR spectrometer based on the NV Nano NMR technique. The main challenge however is to achieve a high spectral resolution comparable to conventional NMR spectrometers.

For liquid samples the inhomogeneity of the statistical polarization represents a limit to the achievable spectral resolution. This can be solved by trapping the sample inside nanofabricated dimples [41]. In that case the detection volume would match the sample volume and the signal would not get lost because of diffusion. Another approach is to increase the detection volume (and sacrificing spatial resolution) up to the point that thermal polarization dominates over the statistical. The thermal polarization of all nuclear spins is the same. Hence diffusion would not degrade the signal and would consequently not limit the spectral resolution.

In solid samples on the other hand the dipolar broadening requires to be suppressed in order to achieve a high spectral resolution. Therefore homonuclear decoupling needs to be implemented with faster nuclear spin operations. The rotations in the homonuclear decoupling sequences would be more instantaneous and the decoupling would work better [215]. Magnetic write heads e.g. have shown their eligibility to induce fast nuclear spin manipulation [195]. The second decoupling strategy in conventional solid-state NMR is to rotate the sample along the magic angle with respect to the magnetic field orientation. A recent study suggests that magic angle spinning at low fields may be possible in conjunction with NV centers in diamond [211]. These suggested improvements should lead to much higher spectral resolution.

In the case of the memory spin based sensing, more memory spins can be included in order to gain multibit information in each measurement run. This becomes especially important when the targeted spectral resolution is in the Hz range and the corresponding time scale is on the order of seconds. The NV Nano NMR sequence has the advantage of being compatible with arbitrary NMR sequences. So far only 1 dimensional NMR se-

quences have been applied. The application of two or higher dimensional NMR sequences can be imagined in the near future. It can also be pointed out that the sequence can be applied to electron spins as well. The combination of ESR and NMR enables a new set of experiments.

Another promising application of NV centers is as a room-temperature mediator of polarization to sample spins. Despite intensive research so far hyperpolarized nuclear spins outside the diamond lattice have not been detected. The crucial parameters are the density of NV centers and their distance to the surface. Nanostructured diamond [223] or nanodiamonds can substantially increase the surface to molecule contact area and enhance the polarization transfer. Conventional NMR spectroscopy would benefit from hyperpolarized nuclear spins. It would also be possible to combine NV Nano NMR spectroscopy and polarization transfer in one system. This would increase the sensitivity of the NV Nano NMR and reduce the measurement time.

Another application is a quantum simulator with single nuclear spins on the diamond surface [198]. In that regard the surface can be terminated with fluorine atoms or attached to a 2d material containing nuclear spins e.g. hexagonal boron nitride [197]. In this scenario the NV center in diamond would play the role of the sensor qubit.

6. Super-resolution microscopy of sensor spins

Physicists have ever since developed different imaging methods that allowed a better and better insight into matter. Many nobel prizes have been awarded for these inventions. Examples of these imaging methods are e.g. x-ray scattering, transmission electron microscopy (TEM), scanning near-field optical microscopy (SNOM), atomic force microscopy (AFM) and scanning tunneling microscopy (STM). These techniques achieve unprecedented spatial resolution but lack universal application. The methods are restricted to specific samples, e.g. crystals in the case of x-ray scattering or image only the surface topology. Optical microscopy on the other hand offers the possibility to e.g. image cells via fluorescent biomarkers. In that regard nanodiamonds containing NV centers have been proposed as bio-labels due to their non-cytotoxicity [224]. Furthermore optical microscopy of NV centers (sensor spins) has been combined with magnetic resonance to achieve nanometer scale metrology.

In optical microscopes the diffraction of light limits the achievable resolution. The diffraction limit was formulated by Ernst Abbe in 1873:

$$d = \frac{\lambda}{2\ n\ \sin\alpha} \tag{6.1}$$

with λ the excitation wavelength, n the refractive index and α the half of the angular aperture of the objective. This limit means that two objects with a distance less than d will be not be resolvable by an optical microscope. If the object is emitting light, as is the case for fluorescing NV centers, the Rayleigh criteria has to be applied. The light does not appear as a point, but rather as a diffraction pattern which is described by the point spread function (PSF). The minimum distance between two emitters in order to be resolvable according to Rayleigh is:

$$d = \frac{1.22\lambda}{2\ n\ \sin\alpha}. \tag{6.2}$$

In the case of imaging NV centers in diamond using a high NA oil objective, the resolution will be limited to around 267 nm. Sensing with an ensemble of NV centers would therefore not be able with a resolution beyond this limit. Biologists and chemists are however

interested in observing much finer structures in the obtained images. One solution to achieve a sub-diffraction resolution is to scan the sample attached to an AFM on top of a sensor spin [43]. The necessity to attach the sample to the AFM tip is not an easy task and therefore has limited application.

This chapter deals with concepts overcoming the diffraction limit (see section 6.1). Here the STORM method is applied to NV centers in diamond to achieve a resolution beyond the diffraction limit. Section 6.2 describes the photo-ionization mechanism of NV centers that enables the application of STORM. In the main section 6.3 STORM microscopy of NV centers is presented. Section 6.4 shows results of combining STORM microscopy with magnetic resonance techniques. In the end an outlook describes applications of the technique (section 6.5). The results of this chapter are published in [222].

6.1. Super-resolution techniques

A new concept of sub-diffraction limited microscopy was suggested by Stefan Hell. The general idea is to exploit the non-linear optical response of emitters and spatially restrict the region where fluorescence can be emitted. The theoretical work was formulated in 1994 [31] and the experimental verification followed in 1999 [225]. The technique called stimulated emission depletion (STED) achieves the spatial restriction with a donut shaped laser beam. This beam has the task to suppress the fluorescence emission by all emitters within the donut mode. It is overlapped with an excitation laser of gaussian shape. As a result, fluorescence is only emitted in the non-overlapping region of the two laser beams: in the center. The mechanism, suppressing the spontaneous emission is called stimulated emission. It can be achieved by a laser wavelength matching the emission spectrum. In addition to this the laser intensity needs to exceed the saturation intensity of stimulated emission. The high laser intensity then deexcites the emitter before it can relax by spontaneously emitting a photon. The donut mode has a gaussian profile. Therefore the laser intensity next to the zero intensity point does not increase instantaneously to the maximum point. However the response of the emitter becomes sharper when the maximum laser intensity increases. As a consequence the region where the fluorescence of emitters is suppressed becomes larger. The resolution therefore scales as:

$$\sigma = \frac{\lambda}{2\ n\ \mathrm{sin}\alpha\sqrt{1 + I_{max}/I_{sat}}}. \tag{6.3}$$

where the maximum laser intensity of the donut laser beam is I_{max} and the saturation laser intensity is I_{sat}. Typically laser intensities on the order of $\frac{\mathrm{GW}}{\mathrm{cm}^2}$ are used for STED microscopy. Another mechanism to switch off the fluorescence is to transfer the emitters to a long-lived (on the order of ms) dark state e.g. a metastable state or another charge

state. This technique is called ground state depletion (GSD) and typically requires many orders of magnitude lower laser intensity. The STED technique has been implemented with NV centers as well and allowed microscopy well beyond the diffraction limit [35, 226]. Since the NV center is photo-stable high laser intensities can be applied and as a result a resolution of 2.4 nm has been achieved [226]. On the other hand GSD was implemented by exploiting the NV^0 state as a long-lived dark state [131]. The study at that time did not identify the dark state as a different charge state. This was confirmed later [132, 36]. Furthermore the charge state transfer rates were analyzed for a large range of wavelengths and intensities [36] and the optimum wavelength for switching efficiently to the NV^0 state was determined.

Another approach to overcome the diffraction limit relies on the fact that there is a difference between resolution and localization accuracy. While resolution represents the minimum distance two objects need to have in order to be resolvable, the localization accuracy refers to the accuracy with which the position of an emitter can be determined. The optical microscope images an emitter with a characteristic point spread function (PSF) which can be represented by an Airy pattern. The pattern can be approximated by a gaussian function in the center. Its localization accuracy can be expressed by (without considering noise) [227]:

$$\sigma = \frac{0.51 \cdot \lambda}{n \, \sin\alpha \sqrt{N}} \tag{6.4}$$

with the number of detected photons N. Hence if multiple emitters within a diffraction limit can be localized individually, this would break the limit set by the diffraction. This can be achieved by stochastically switching the emitters on and off. Switching off means that the emission of fluorescence is prevented. In fluorophores e.g. intrinsic stochastic processes can be exploited in order to optically activate or deactivate the fluorophores. The on-/off-ratio usually depends on the excitation laser. It can be tuned in order to increase the probability to only have single emitters within a diffraction limited region emitting fluorescence (for a time interval). A CCD camera can record an image, with the single emitters being localized after a post-processing step. One by one every emitter can be localized by this procedure and an image with a resolution beyond the diffraction limit is constructed. Stochastic optical reconstruction microscopy (STORM) and Photo-activated localization microscopy (PALM) are two examples for this stochastic switching based super-resolution microscopy [32, 33, 34]. The difference between the two methods are the used fluorophores. While STORM works with photoswitchable organic dyes, PALM on the other hand exploits photoswitchable fluorescent proteins.

Widefield illumination together with CCD imaging allows a parallel identification of emitter locations. This results in fast processing which is especially interesting for the imaging of living cells. As an application molecules are targeted with fluorophores and im-

aged by STORM microscopy with a resolution of a few ten nanometers [228, 229, 230, 231]. For both, the deterministic and the stochastic approach of super-resolution microscopy, the Nobel prize in chemistry was awarded to Eric Betzig, Stefan Hell and William Moerner in the year 2014.

In this work the STORM technique is implemented for the first time with NV centers in diamond. Ensembles of NV centers are illuminated in a wide-field setup and their fluorescence counts are acquired in a parallel fashion. The method relies on the laser-induced charge state dynamics of the NV center which enables stochastic switching between charge states [36]. This mechanism is explained in the following section 6.2. STORM microscopy is applicable to all NV centers in bulk diamond, due to the observed homogeneous charge state properties. In contrast to fluorophores, the NV center is not solely an emitter, but also possesses an electron spin, which can act as a magnetic field sensor [77, 78].

6.2. NV center photo-ionization

The charge state properties of the NV center have been briefly discussed in the introduction 2.5. For the purpose of this investigation the two charge states NV^- and NV^0 are relevant (see figure 6.1). The fluorescence of both charge states differs in wavelength (see figure 2.5) and can therefore be separated by a suitable optical filter. In addition to this the excitation spectrum of both charge states differs as well [36, 133].

Detailed knowledge has recently been gained about the laser induced charge state dynamics [132, 36]. Ionization from NV^- to NV^0 has been observed as well as the reverse process called recombination. Both processes are induced by two photons and depend on the laser wavelength and its intensity [132, 36]. For ionization, the NV^- charge state first needs to be excited (see fig. 6.1). A second photon can transfer the electron to the conduction band. As a result, the charge state is switched to NV^0. The recombination to the NV^- charge state is analogue to the ionization. First the NV^0 charge state is excited by a photon. Subsequently a second photon can levitate an electron from the valence band into the ground state of the NV^0, thereby switching to the NV^-. Both ionization and recombination occur stochastically. Due to the two-photon involvement the charge state lifetimes, τ_{on} and τ_{off}, are inversely proportional to the square of the laser intensity I_{L}^2 (see figure 6.2 B): $\tau_{\mathrm{on}}, \tau_{\mathrm{off}} \propto I_{\mathrm{L}}^{-2}$. On the other hand, the fluorescence rate Γ is linearly proportional to I_{L} (see figure 6.2 A): $\Gamma \propto I_{\mathrm{L}}$. Consequently the product of charge state lifetime τ_{on} and fluorescence count rate Γ will be proportional to the inverse of laser intensity I_{L} (see figure 6.2 C). This product represents the average number of photons per burst n and will increase for lower I_{L}: $n \propto I_{\mathrm{L}}^{-1}$. Furthermore there is a dependence to the excitation wavelength. For a wavelength of λ_{L}=594 nm the number of photons per burst

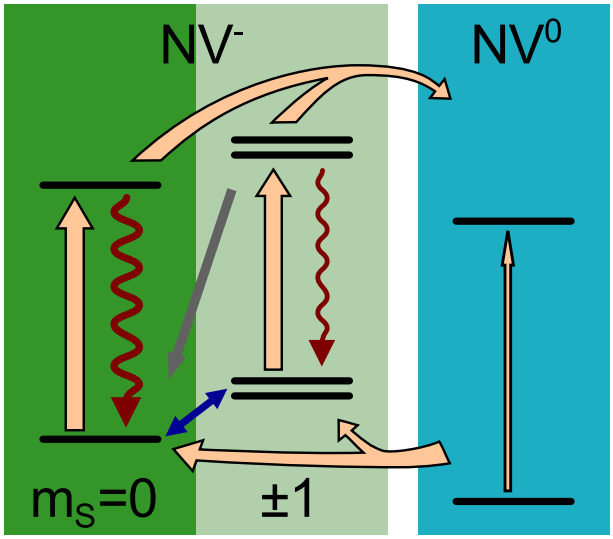

Figure 6.1.: Scheme of charge state energy levels of the NV center in diamond. The two charge states of the NV center are the negatively (NV^-) and the neutrally charged state (NV^0). Both are represented by their energy levels. Additionally NV^- is subdivided into the m_s=0 and m_s=± 1 states. Orange arrows depict the transition into other states induced by the laser. Wavy red arrows stand for the fluorescence and the gray arrow for spin polarization. The MW can induce transitions between the spin states and is represented by a blue double arrow. The strength of the transition is indicated by the width of the arrows.

is found to be increased [132, 36]. Moreover the laser induced charge state ratio depends on the wavelength. For example the ratio between the NV^- and the NV^0 state is around 10 %: 90 % for λ_L=594 nm and around 70 %: 30 % for λ_L=532 nm (see figure 6.2 D). For low power laser illumination with λ_L=594 nm the charge state switching occurs on a timescale of seconds and therefore becomes visible in a NV^- fluorescence time trace (see figure 6.3).

The stochastic charge state switching (see figure 6.3) is similar to the behavior of the STORM fluorophores. Additionally the ionization rates for different bulk NV centers are found out to be the same. Therefore the stochastic charge state switching is suitable for STORM imaging.

6.3. STORM microscopy of NV centers in diamond

The procedure is to illuminate the NV centers in a wide-field configuration with a 594 nm laser of low intensity and record the images with the CCD camera. Depending on the requirements the on-off ratio and the switching rates can be controlled by the selected wavelength λ_L and laser intensity I_L. The wavelength of λ_L = 594 nm is suitable, due to a

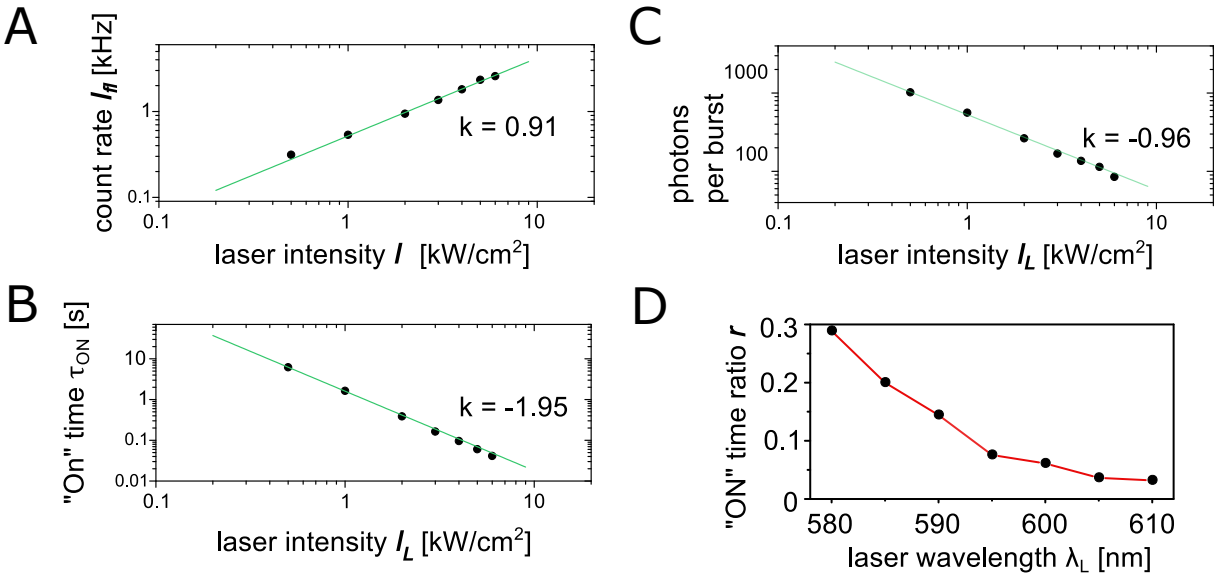

Figure 6.2.: Laser intensity and laser wavelength dependence of photo-ionization. A Linear dependence of the fluorescence counts on the laser intensity. B Inverse quadratic dependence of the NV^- charge state lifetime on the laser intensity. C Inverse linear dependence of the number of photons per burst on the laser intensity. D The NV^- to NV^0 ratio in dependence of the laser wavelength.

higher number of photons per burst compared to other wavelengths. On average $n \sim 600$ photons can be collected within a lifetime of $\tau_{on} \sim 2\,s$ for a intensity of $I_L \sim 1\,kW/cm^2$ (see fig. 6.3). The experimental setup for the STORM measurements on NV centers has been described in chapter 2.6.2. It enables confocal microscopy in combination with an APD on one hand and a widefield illumination combined with CCD imaging on the other hand. The latter can be achieved by electronically flipping the lenses and the mirrors into the illumination and detection path, respectively. The fluorescence timetrace in figure 6.3 is taken with an APD. Here two NV centers are illuminated by a 594 nm laser with a $I_L \approx 1\,kW/cm^2$. Distinct cases are revealed in the timetrace (see figure 6.3). A low count rate refers to the detection of background photons. Hence in this case both NV centers reside in the NV^0 state. Two high fluorescence levels can be distinguished in the timetrace. The lower level corresponds to the case of a single NV center being in the NV^- charge state. The higher level shows approximately doubled fluorescence counts and represents the case of both NV centers residing in the NV^- charge state. With the determined count rate corresponding to a single NV^- center, a fluorescence threshold can be set and all unwanted cases can be discarded.

The STORM measurement protocol is shown in figure 6.3 (top). The 594 nm laser illumination is constantly on. The CCD imaging however is pulsed in frames. Selecting

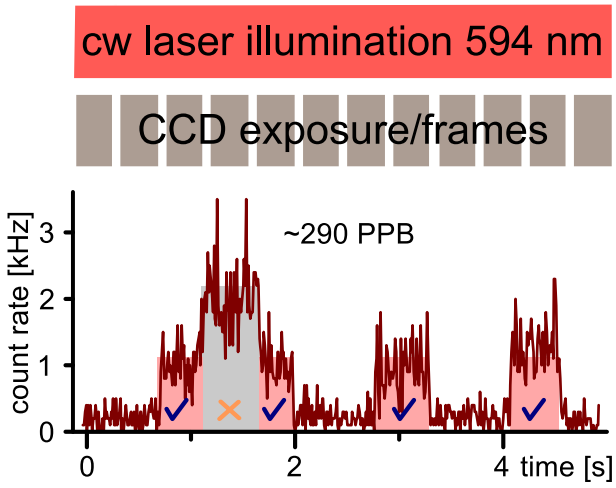

Figure 6.3.: STORM measurement sequence and charge state switching trace. Top shows the sequence applied to obtain STORM images. Laser at a wavelength of 594 nm is continuously applied. Simultaneously a CCD camera records the images. The bottom presents a fluorescence trace recorded by an APD. An optical filter prevents the detection of NV^0 fluorescence and ensures the distinguishability between NV^0 and NV^-. The level of fluorescence determines whether one, two or no NV centers are in the NV^- charge state. For STORM imaging only cases where one NV resides in the NV^- charge state are relevant. The average number of photons per burst is 290.

the exposure time of a single frame is crucial. The reason is the asynchronous switching of charge states. It makes sense to set the exposure time of the CCD camera equal to the previously determined average lifetime of the NV^- charge state τ_{on}. This allows an efficient imaging of the NV centers. Moreover since NV centers in bulk diamond are typically not photo-bleaching, they can be illuminated for an unlimited time.

Postprocessing plays an important role in the STORM imaging method. The goal is to detect a single emitter in a diffraction limited spot in a single CCD frame. The most important indicator are the detected fluorescence counts within a diffraction limited region. A lower fluorescence threshold excludes all the cases in which the emitters are all in the NV^0 charge state. On the other hand an upper fluorescence threshold filters out all cases in which two or more NV centers are in the NV^- charge state. By applying these two thresholds, the unwanted cases can be discarded. There is however still the possibility that two NV centers contribute to the counts. For these cases an additional postprocessing step helps. All frames are checked for an antisymmetrical shape of the PSF. Frames with a significant deviation from the expected shape are discarded.

The remaining frames are all fitted by a 2d gaussian function which approximately describes the PSF of the emitters [232]. The fit yields a position $[x_i, y_i]$ for each frame i. The corresponding position uncertainty $\sigma_{x/y,i}$ depends on the total number of photons

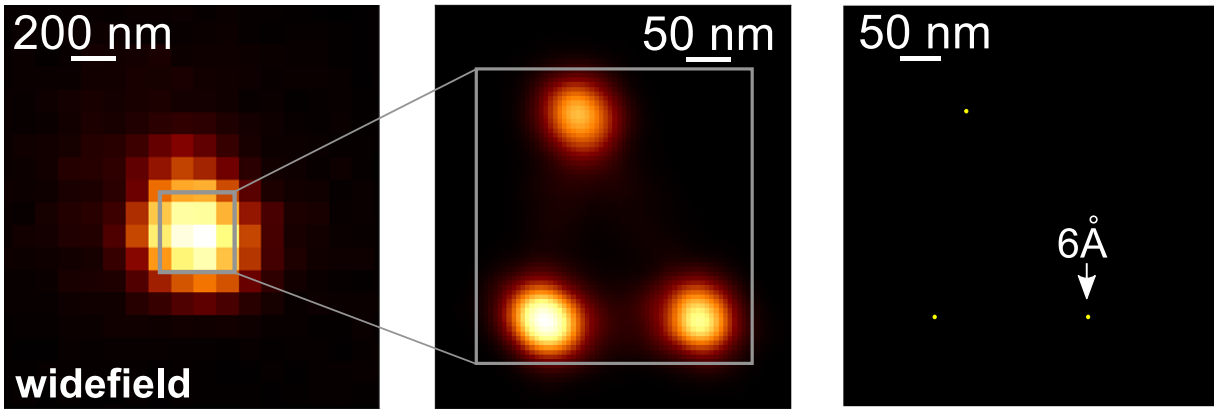

Figure 6.4.: Sub-diffraction-limit imaging of NV centers by the STORM technique. Left: CCD image shows a single blur created by three emitting NV centers that are not resolved due to the diffraction limit. Center: STORM image depicts three different location distributions corresponding to single NV centers. Right: Emitters are localized with an accuracy of 6 Å by fitting the location distribution. The average NV^- charge state lifetime is 1 s and on average 350 photons are emitted per burst.

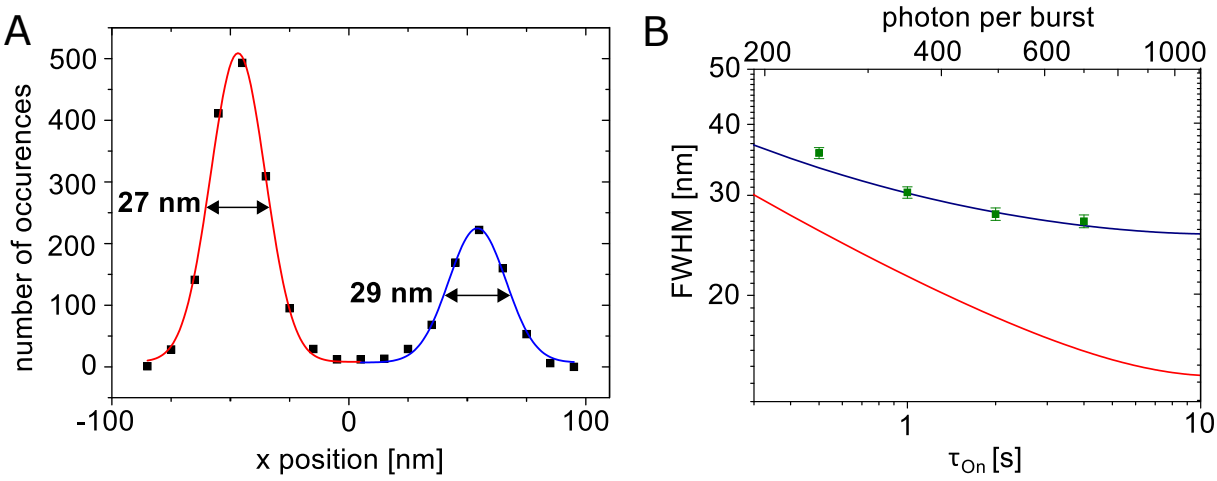

Figure 6.5.: Resolution obtained by the STORM technique. A Line scan of a STORM image exhibits two emitters. The FWHM of the two distributions are 27 nm and 29 nm, respectively. The average NV^- charge state lifetime is 4 s. B Resolution is plotted in dependence of the NV^- charge state lifetime (lower x-axis) and the number of photons per burst (upper x-axis). Green points show the measurement results and are fitted by equation 6.8. The fit is depicted as a blue curve. The fit function considers the drift during the accumulation of the image and the number of signal and background photons. The red plot illustrates the achievable resolution in the case when sample drift is negligible.

contributing to the frame n_i. The uncertainty is expected to be smaller than the diffraction

limit $\sigma_{\lambda,i}$ as it scales with:

$$\sigma_{x/y,i} \propto \sigma_{\lambda,i}/\sqrt{n_i}. \tag{6.5}$$

All 2d Gaussian functions with the obtained positions $[x_i, y_i]$ and standard deviations $\sigma_{x/y,i}$ can be summed up:

$$p(x,y) = \sum_i \frac{1}{2\pi\sigma^2_{x/y,i}} \exp\left(-\frac{(x-x_i)^2+(y-y_i)^2}{2\sigma^2_{x/y,i}}\right) \tag{6.6}$$

As a result, distinguishable distributions corresponding to single NV centers should be resolvable in the map.

STORM is first demonstrated with three NV centers in a diffraction limited area. The left fluorescence image in figure 6.4 is obtained by illuminating the spot with a 532 nm laser and a laser intensity reaching saturation ($I_\mathrm{L} \approx 200\,\mathrm{kW/cm^2}$). The higher fluorescence count rate hints to the existence of multiple NV centers. There is however no possibility of localizing the NV centers individually with the obtained image. On the other hand, the STORM measurement taken with 594 nm laser light and with intensities on the order of $I_\mathrm{L} \approx 1\,\mathrm{kW/cm^2}$ reveals three resolvable location distributions corresponding to three NV centers (see figure 6.4 (center)). On average 350 photons per burst are detected with an average NV^- charge state lifetime of 1 s. The achieved resolution (FWHM) is around 30 nm. The distributions can be fitted in order to localize the NV centers even better (see right side of figure 6.4). The localization accuracy scales with M the number of fits belonging to a particular NV center: $\hat{\sigma}_{x/y} = \sigma_{x/y}/\sqrt{M}$. Here M is on average ≈ 2000 which yields a localization accuracy of $\hat{\sigma}_{x/y}$=6 Å. This additional gain in localization accuracy is only possible if the NV centers are separated more than the location uncertainty $\sigma_{x/y,i}$.

In the equation 6.5 the scaling of the resolution $\sigma_{x/y,i}$ is shown. Here effects like sensor pixelation and background photons are not considered. However in the experiment they do limit the resolution and therefore have to be included into the equation. The standard deviation according to the paper by Thompson et. al [233] is:

$$\sigma^2_{x/y,i} = \frac{\sigma^2_{\lambda,i}}{n_i} + \frac{a^2/12}{n_i} + \frac{8\pi\sigma^4_{\lambda,i}b^2}{a^2 \cdot n_i^2} \tag{6.7}$$

with the pixel size on the CCD camera a=100 nm and the background photons $b(t) \approx 1 + 0.3\,\mathrm{s^{-1}} \cdot t$.

Regarding the resolution a higher number of photons per burst n_i is desirable and can be achieved by further decreasing the laser intensity I_L: $n_i \propto I_\mathrm{L}^{-1}$ (see figure 6.2 C). However the charge state lifetime and consequently the chosen exposure time increases quadratically by reducing I_L: $\tau_\mathrm{on} \propto I_\mathrm{L}^{-2}$ (see figure 6.2 B). This means that n_i increases with the square-root of the exposure time. The number of background photons increases with the exposure time as well and at a critical point can dominate the resolution limit.

Therefore an optimum exposure time for gaining the best possible standard deviation $\sigma^2_{x/y,i}$ can be determined.

Figure 6.5A shows a lineplot of a STORM measurement. The average number of photons is ≈ 700 with an average charge state lifetime of 4 s. The FWHM of the two location distributions is 27 nm and 29 nm, respectively. FWHM for varying charge state lifetimes are measured and plotted in figure 6.5B. On the other hand the theoretical scaling is represented in equation 6.7 and plotted in figure 6.5B (red curve) in dependence of the charge state lifetime/exposure time t. There is a clear deviation between the measured and the theoretical scaling. Theoretically a resolution of ≈ 14 nm is achievable. The reason for the deviation is the occurrence of sample drift. Long term drift can partially be compensated by localizing the emitters with high intensity laser light (532 nm and in saturation power). Additionally different measures, like building a robust sample stage are taken in order to reduce the drift of the sample. The short term drift, in the extreme case, during a CCD exposure time can however not easily be get rid of. The drift in the experimental setup is estimated to be $\sigma_{\text{drift}} \approx 10$ nm. This can be added to the equation 6.7:

$$\sigma^2_{x/y} = \sigma^2_{x/y,i} + \sigma^2_{\text{drift}}. \tag{6.8}$$

The blue curve in figure 6.5B shows the corresponding values and matches well with the measurement data.

This is a proof-of-principle experiment showing that STORM imaging of NV centers with a resolution of 27 nm is possible. This is the first time demonstration of optical sub-diffraction imaging in parallel fashion with NV centers. A higher photon collection efficiency [234] and a reduced sample drift would enable a resolution of less than ≈ 10 nm. Furthermore it can be envisioned to tailor the photo-ionization with the goal of e.g. achieving a higher number of photons per burst. This can potentially be accomplished by locally changing the Fermi level of the diamond [235, 137].

6.4. Sub-diffraction limit magnetic resonance

In contrast to the STORM fluorophores the NV centers in diamond have an electron spin. The idea is to achieve a combination of high spatial resolution via STORM with the high magnetic field sensitivity via ODMR, named STORM-ODMR. This would have two advantages. First it would enable nanoscale sensing by an ensemble of NV centers with a spatial resolution beyond the diffraction limit [74, 156, 45, 236]. And second the localization of NV centers would be enhanced by the STORM-ODMR technique. The latter can be achieved by selectively driving single NV electron spins within an ensemble and thus locally changing the fluorescence response [74, 237, 238, 239].

As a proof-of-principle experiment STORM-ODMR is demonstrated on two NV cen-

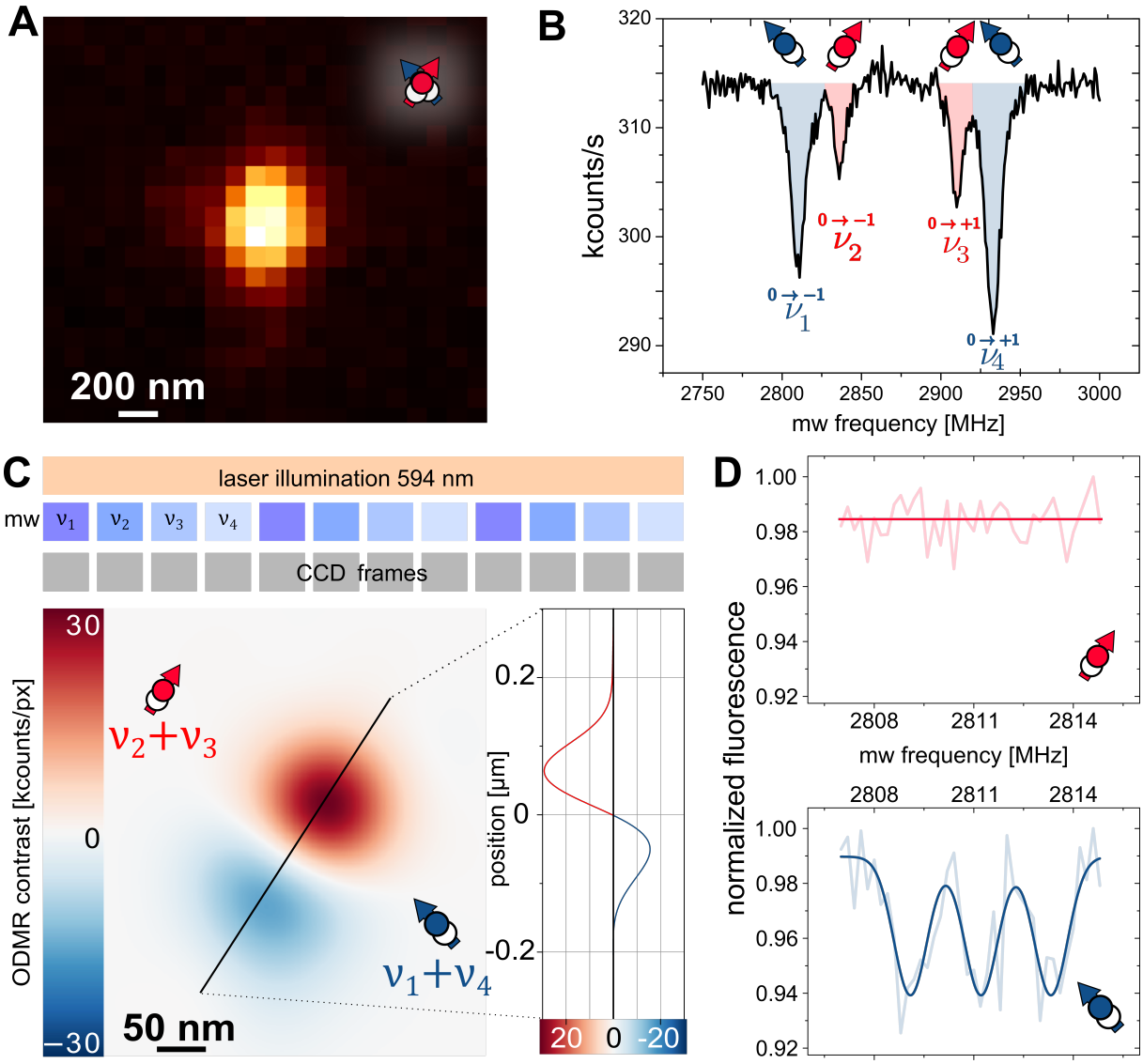

Figure 6.6.: Sub-diffraction limit magnetic field sensing. A CCD image is shown with two unresolvable NV centers. The two defects have different crystallographic orientations as depicted in the inset. B Results of continuous wave ODMR of the two NV centers are shown. Four resonance peaks are detected, corresponding to two different NV orientations. C STORM-ODMR measurement is performed. Upper part shows the corresponding sequence. In addition to the laser illumination at 594 nm, resonant MW radiation is applied. Its frequency alternates between the four resonance frequencies for each CCD frame. The CCD images corresponding to one pair of MW frequencies (ν_1 and ν_4) are subtracted from the other images (ν_2 and ν_3). This results in two distributions of emitter locations which is outlined in the line scan on the right. D STORM-ODMR is obtained with a high spectral resolution. The ODMR spectra can be assigned to individual NV centers. Only one NV reveals a hyperfine resolved resonance in the spectra.

ters within a diffraction limited spot (see figure 6.6A). The requirement is that both NV centers differ in their spin transition frequency. This can be achieved by the application of a magnetic field gradient which leads to different Zeeman shifts. In the context of NV centers a gradient field of 10 mT/nm has been generated by magnetic write heads [195]. In this work however two NV centers are used that have different orientations in the diamond crystal. An applied magnetic field has different angles to the two NV centers' axes which results in separable resonance lines [77]. This is shown by a continuous wave (cw) ODMR measurement (see figure 6.6B). For this purpose laser illumination with a wavelength of 532 nm and at saturation intensities is focused to the NV centers for spin initialization and readout. In addition to this MW radiation is switched on. The MW frequencies are varied in a range of 50 MHz. Four dips in fluorescence are detected which correspond to a successful spin transition to m_s=±1. The outer peaks (ν_1, ν_4) correspond to the first NV and the inner peaks (ν_2, ν_3) to the second NV. Furthermore the four resonances can be divided into the states they are transferred to, starting from the m_s=0 state: the two peaks on the left belong to the transition to m_s=-1 and the right resonances to the transition to m_s=+1 (see figure 6.1). Up to this point it is not possible to say from which NV center position, the distinct resonance frequencies are coming from.

STORM-ODMR is implemented by extending the STORM sequence by MW application (see figure 6.6C (top)). The MW frequency is synchronously switched after each CCD frame between ν_1 through ν_4. The postprocessing explained in the previous section is applied again to the obtained frames. The resulting location distributions that correspond to the frequencies $\nu_{1,4}$ are summed up. On the other hand the location distributions belonging to $\nu_{2,3}$ are subtracted. This procedure results in the image shown in figure 6.6C. A positive (in red) and a negative (in blue) location distribution can be observed which correspond to two individual NV centers. In this case the distance between the NV centers is larger than the STORM resolution $\sigma_{x/y,i}$. STORM-ODMR leads to the observation of a zero-point between the two distributions which is highlighted by a linescan in figure 6.6C. This means that NV centers with a distance smaller than $\sigma_{x/y,i}$ can still be resolved by STORM-ODMR.

Here the used sequence of STORM-ODMR only shows the detection of electron spin states. In principle it can be replaced by other more complex sequences which are sensitive to nearby nuclear spins. This would enable nuclear spin imaging on the nanoscale. Towards this goal a higher magnetic field sensitivity is shown in conjunction with STORM. The achievable spectral resolution in an ODMR experiment can be optimized up to the limit set by the T_2^* time (limited by the ^{13}C nuclear spin bath [240]). This allows to resolve the hyperfine interaction with nuclear spins in the near vicinity. However in the previously shown STORM-ODMR measurement the obtained ODMR peaks are broad-

ened by MW power (see figure 6.6B). Therefore the MW power is decreased and a higher frequency sampling around the resonance peak ν_1 is introduced. As a result, for each NV center in figure 6.6C a separate ODMR spectrum with high spectral resolution can be measured (see figure 6.6D). The frequency range only covers the resonance of one NV center. Consequently only the latter shows three resonance lines corresponding to the hyperfine coupling to the intrinsic ^{14}N nuclear spin. The total contrast of the STORM-ODMR spectrum is 18 % which is close to the achievable contrast in conventional ODMR (i.e. $\approx 30\,\%$). In principle the ODMR sequence can be replaced by a sequence which is sensitive to nuclear spins farther away [21].

The magnetic field sensitivity of the STORM-ODMR technique can be determined from the spectrum in figure 6.6D. The three hyperfine ($m_I = -1, 0, 1$) induced resonance lines all contribute to the sensitivity and can therefore be added up:

$$\delta B = \left(\sum_{m_I=-1,0,1} \left. \frac{d\Gamma}{d\nu} \right|_{\max} \right)^{-1} \sigma_\Gamma \frac{2\pi}{\gamma_e} \sqrt{T} \tag{6.9}$$

with the maximum slope $d\Gamma/d\nu_{\max}$, the standard deviation of the data from the fit σ_Γ, the gyromagnetic ratio of the electron spin γ_e and the total measurement time T. The calculated sensitivity is $\delta B \approx 190\,\mu\mathrm{T}/\sqrt{\mathrm{Hz}}$. Additionally the theoretically achievable magnetic field sensitivity can be predicted if the fluorescence count rate, the ODMR contrast and the linewidth are known. It is limited by photon shot noise and gives a four times lower value. This deviation is explained by the fluctuation in laser power and the postprocessing process.

In the case of a single NV electron spin measured in a confocal microscope the fluorescence count rate is much higher. Therefore in a shot noise limited experiment with a similar T_2^* time, a sensitivity of $\approx 180\,\mathrm{nT}/\sqrt{\mathrm{Hz}}$ can be achieved [241]. This is a $\approx 10^3$ smaller value than for STORM ODMR and means a $\approx 10^6$ shorter measurement time. However STORM ODMR has the advantage that it can be applied in a parallel fashion to an ensemble of NV centers. Scanning high-resolution methods like STED or GSD on the other hand need to scan to each NV, one by one. In an example both methods can be compared to each other. For an assumed spatial resolution of $\approx 30\,\mathrm{nm}$ in a $100 \times 100\,\mu\mathrm{m}^2$ area in diamond a total number of $\approx 10^7$ NV centers should be resolvable. CCD imaging with 1024×1024 pixels would allow to perform sensing with all $\approx 10^7$ NV centers simultaneously. The STED technique should be able to achieve the aforementioned sensitivity of $\delta B \approx 180\,\mathrm{nT}\sqrt{\mathrm{Hz}}$. Parallel sensing with 10^7 NV centers would still outperform scanning based technique. In this example the STORM ODMR technique would be one order of magnitude faster.

6.5. Application

The NV electron spin is motivated as a nanoscale sensor for temperature [80], electric [154] and magnetic fields [77, 78]. In this work NMR spectroscopy on the nanoscale has been demonstrated with NV centers in diamond [184]. For all these applications sensitivity improves with N the number of NV electron spins as $\propto \sqrt{N}$. The first application of STORM with NV centers and its combination with ODMR opens a new avenue to parallel sensing with a high spatial and spectral resolution. An ensemble of NV centers with a high density and a depth of a few nanometer can be used for the aforementioned sensing applications [156, 45, 236, 242, 243, 244, 24, 25].

Furthermore the determined magnetic field sensitivity of $\delta B \approx 190\,\mu\mathrm{T}/\sqrt{\mathrm{Hz}}$ can be further improved. It is limited by the T_2^* time which is approximately the inverse of the achievable linewidth in ODMR. In the experiments shown here, the ODMR linewidth is $\sim 1\,\mathrm{MHz}$. Diamond samples with a reduced $^{13}\mathrm{C}$ concentration can however exhibit a decoherence rate of $\sim 1\,\mathrm{kHz}$ [240]. The current optical excitation rate of the STORM experiments is on the same order. Matching the optical excitation rate with the inverse of the T_2^* time is necessary to yield a minimum ODMR linewidth (in cw ODMR). Reducing the ODMR linewidth to $\sim 1\,\mathrm{kHz}$ would enhance the sensitivity by three orders of magnitude. Combined with the envisioned STORM resolution of 14 nm the parallel STORM ODMR approach could potentially outperform scanning techniques by orders of magnitude. Pulsed MW sequences can also be implemented within the STORM ODMR technique and would allow a better control of the electron spin dynamics. Especially dynamical decoupling sequences would enable sensing based on the longer T_2 rather than the T_2^* time [16, 24, 154, 80]. Furthermore nearby nuclear spins can be included as memory spins to store phase information before readout [29, 73].

The other application of NV centers that would benefit from STORM is the use of nanodiamonds as functionalized bio markers [224]. Fluorescent nanodiamonds have the advantage of being photostable and showing non-cytotoxicity. Besides the use for localization imaging in cells the nanodiamonds can be used e.g. for temperature sensing [80]. STORM would in either case increase the resolution beyond the diffraction limit. It is however important that the charge state switching properties of the NV centers are homogeneous among different nanodiamonds. The relationship between the nanodiamonds size and its NV^- probability has been investigated [245]. The study observed a decrease in NV^- fluorescence for smaller sizes of nanodiamonds. Thermal oxidation helped to recover the NV^- charge state.

In this work the charge switching behavior in nanodiamonds is investigated. The examined nanodiamonds are commercially available MSY diamond with an average size of

50 nm and 100 nm. First of all single NV centers are characterized by their fluorescence response upon illumination with 532 nm. The laser power is set to 50 μW and resulted in a varying fluorescence intensity between 100 and 250 kcount/s. This can be explained by the differing orientation of the NV center's optical dipole which affects the excitation efficiency. Moreover the charge state switching in nanodiamonds is analyzed analogue to the work conducted for single NV centers in bulk diamond [36]. Laser illumination at 594 nm and at 180 nW laser intensity (measured before the objective) should lead to the observation of charge state blinking in the fluorescence timetrace (similar to figure 6.3). Within the 50 nm nanodiamond sample, the NV centers do not show a switching between charge states. In the 100 nm nanodiamond sample, a fraction of all NV centers is showing charge state switching. Out of 479 NV centers, 168 NVs reveal jumps in the fluorescence timetrace and are analyzed with the HMM model [36, 29, 179]. The analysis yields ionization and recombination rates and fluorescence count rates for the NV^- charge state. The NV^- probability can be determined out of it and is plotted in a histogram 6.7A. In bulk diamond the NV^- probability is constantly measured to be around 10 % (at 594 nm). In the nanodiamond case it varies from 0 % to 100 %. Furthermore the number of photons per burst can be calculated which is particularly interesting for STORM microscopy. This value is plotted against the fluorescence counts and shows a large spread as well (see figure 6.7B). The case of a single NV center in bulk diamond is shown with the blue curve in figure 6.7B. While in some cases the values measured in nanodiamonds outperform the bulk case, the inhomogeneity of the properties prevents the implementation of the STORM technique. The inhomogeneity can be explained by the different Fermi levels in nanodiamonds which are highly affected by the surface. Additionally electron tunneling between different defects may play a role. These effects can lead to a blinking behavior of the fluorescence response similar to the photo-ionization. This has actually been exploited for localization based super-resolution microscopy [246].

In the STED or the GSD technique high laser intensities are used which can lead to damages in cells. STORM microscopy on the other hand applies, at least, three orders and six orders of magnitude lower laser intensities compared to GSD and STED, respectively, which makes it much more bio-compatible.

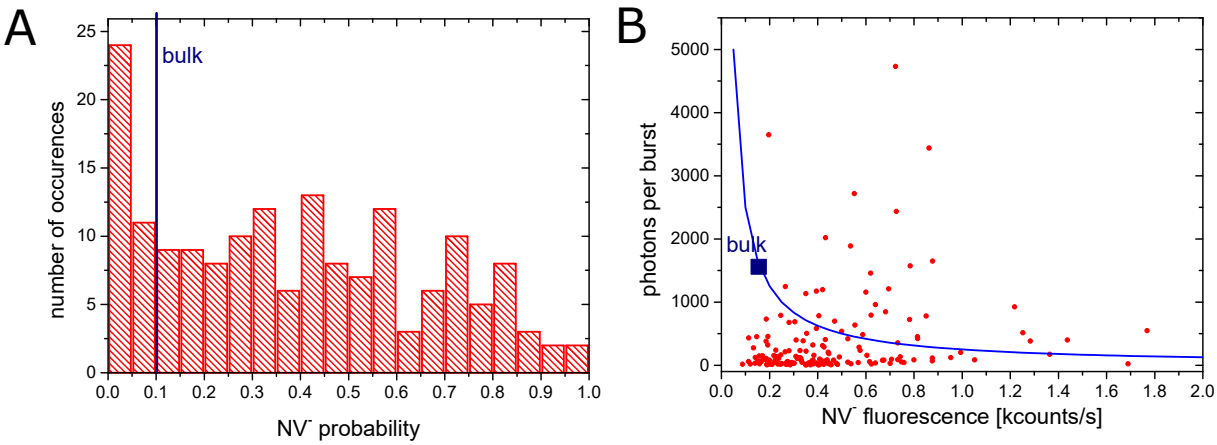

Figure 6.7.: Charge state switching properties in nanodiamonds. A Histogram of NV^- probability obtained by analyzing 168 single NV centers showing a charge state blinking. The NV^- probability in the case of bulk diamond is marked with a blue line. B Number of photons per burst for NV centers in nanodiamonds plotted in dependence of their NV^- fluorescence. The corresponding charge state behavior in bulk diamond is shown as a blue curve. The value for the used intensity is highlighted with a blue square. The applied laser has a wavelength of 594 nm and an intensity of 180 nW.

A. Appendix

symbol	value	description
T_2^{sensor}	$\approx 0.3\,\text{ms}$	coherence time of **sensor** spin, limiting t
T_1^{sensor}	$6\,\text{ms}$	dissipation time of **sensor** spin, limiting T_2^{mem}
T_2^{mem}	$9\,\text{ms}$	coherence time of **memory** spin, limiting quantum storage time [30, 15]
T_1^{mem}	$4\,\text{min}$	dissipation time of **memory** spin, limiting T and classical storage time [15]
T_2^*	$\sim 10\,\mu\text{s} - 3\,\text{ms}$	coherence time of **sample** spins, limiting T
T_D	$\sim 5 - 0.1\,\text{s}$	diffusion time of **sample** spins through detection volume, limiting T
T	$\sim 10\,\mu\text{s} - 3\,\text{ms}$	spin maximum phase acquisition time τ of **sample** spins, limiting NMR spectral resolution
t	$50 - 600\,\mu\text{s}$	phase accumulation time of **sensor** spin, determining signal strength S
τ	$1\,\mu\text{s} - 0.5\,\text{s}$	phase acquisition (free evolution) time of **sample** spins, e.g. in a Ramsey (magnetization decay) experiment

Table A.1.: List of time constants and variables used in chapter 5.

nuclear spin	sensor-sample coupling c ($\text{Hz}\,\text{nm}^3$)
^1H	79,083
^{19}F	74,440
^{13}C	19,890

Table A.2.: Parameter c: $c = \mu_0\hbar\gamma\gamma_s/8\pi^2$ stands for the strength of sensor-sample spin coupling. μ_0 is the magnetic constant, $\hbar$ is the reduced Planck constant, γ is the gyromagnetic ratio of the sensor and γ_s that of the sample spin.

Experiment	T_{meas} [ms]	# n	N_{avg}	T_{tot}	t [μs]	d [nm]
Fig. 5.15A	17.8	100	2e4	9h:53min:20s	300	51.7
Fig. 5.15C	21.4	500	1.6e4	47h:33min:20s	400	51.7
Fig. 5.16A	19.5	100	1.8e4	9h:45min:00s	300	35.5
Fig. 5.13	$14.7 + k \cdot 5$	7	1.9e4	1h:5min:50.1s	300	34.4
Fig. 5.17	$8.4 + 500^{k/17}$	18	4.3e4	21h:17min:0.7s	400	43.7
Fig. 5.18A top	16.1	67	1e4	2h:59min:47s	400	43.7
Fig. 5.18A bottom	$16.1 + k \cdot 1.5/59$	60	1.4e4	3h:55min:54s	400	43.7

Table A.3.: List of data points n, measurement time per data point T_{meas}, number of averaging per data point N_{avg}, total acquisition time T_{tot}, sensing time t and sensor (NV) depth d. Wherever T_{meas} is a variable and not constant, a formula has been given for each data point $0 \leq k \leq n-1$.

Acknowledgements

There are a number of people who supported me during my journey to the phd. I will always be thankful for their support. The journey started many years ago on a snowy day with my first visit to Stuttgart. On that day Prof. Jörg Wrachtrup gave me the opportunity to work in his group, which I happily accepted. He put a lot of trust in my capabilities to achieve the aimed scientific goals. I am very thankful to him for his support and his mentoring. Many thanks also to Philipp Neumann, who was a great supervisor and taught me many aspects of NV center physics and research in general. His passion for our field of research was very motivating and has left a lasting impression on me. My lab and office mate was Matthias Pfender with whom I worked very closely on the high magnetic field setup. It was a very successful collaboration and I am very grateful to him for his support and for all the discussions that we had on scientific and non-scientific topics. I would also like to thank Sebastian Zaiser, who was my other office mate, for all the great conversations and his help.

I would also like to thank Gerald Waldherr who supported me a lot in the beginning of my time in Stuttgart. Thanks also to Prof. Fedor Jelezko who despite being very busy found time to discuss science with me and also agreed on being a referee of my phd thesis. I am very grateful to Ralf Kamella, Markus Neuwirth and the mechanical workshop who helped us setting up our optical table and the superconducting magnet and who constructed many pieces of the setup. I am also grateful to the electronics workshop who fabricated MW waveguides and other electronic parts for us. Furthermore the sensing experiments would not have been possible without the creation of shallow NV centers by Andrej Denisenko and Felipe Favaro de Oliveira. Also the diamonds provided by Prof. Isoya were essential for our work. I would like to thank them all. Moreover the superconducting magnet needed liquid helium delivery twice a week. We were fortunate to have the low temperature department with competent guys like Bernd Schobel, Dario, Frank and Joachim Lefevre who provided us with liquid helium. Thanks to them all. I would like to thank Ingmar Jakobi especially for his help in creating nice graphics for our papers. Special thanks also goes to Mrs. Claudia Unger who was very helpful from the first day until the last day of my appointment. I am also grateful to Prof. Sebastian Loth for being the referee of my phd thesis and to Prof. Maria Daghofer for chairing the exam.

There are many institute members who have contributed to this phd work and who made me feel comfortable in the institute. I would like to name a few of them and thank them for their support: Andrea Zappe, Rolf Reuter, Stephan Hirschmann, Rainer Stöhr, Nikolas Abt, Julia Michl, Ingmar Jakobi, Tomi Oeckinghaus, Thomas Wolf, Florestan Ziem, Thomas Kornher, Roman Kolesov, Matthias Widmann, Petr Siyushev, Florian Dolde, Boris Naydenov, Dominik Schmid-Lorch, Friedemann Reinhard, Boris Yavkin, Marc Scheffler, Farida Shagieva, Mrs. Ivanka Spajic and Torsten Rendler.

Here I would also like to thank his Holiness Hadhrat Mirza Masroor Ahmad who encouraged me to follow my dream of being a scientist. And finally I would like to thank my family. My parents invested a lot of time, effort and money into my education. I am very thankful to them. My wife Hamda is an amazing life partner. Without her support and advice I would not have succeeded. I thank her for everything. My sons Sajeel and Arsalan both came into my life during this journey. I would like to thank them for all the enjoyable time we are spending together.

Eidesstattliche Erklärung

Hiermit erkläre ich an Eides statt, dass ich die vorliegende Arbeit selbst verfasst habe und keine anderen als die angegebenen Quellen und Hilfsmittel benutzt habe.
Nabeel Aslam
Stuttgart, den 4.10.2018

Bibliography

[1] F. Bloch, W. W. Hansen, and M. Packard. *Nuclear Induction.* Phys. Rev. **69**, 127–127 (Feb 1946).
URL http://dx.doi.org/10.1103/PhysRev.69.127

[2] E. M. Purcell, H. C. Torrey, and R. V. Pound. *Resonance Absorption by Nuclear Magnetic Moments in a Solid.* Phys. Rev. **69**, 37–38 (Jan 1946).
URL http://dx.doi.org/10.1103/PhysRev.69.37

[3] M. H. Levitt. *Spin Dynamics: Basics of Nuclear Magnetic Resonance. 2nd ed.* John Wiley & Sons Ltd (2008). ISBN 978-0-470-51117-6.

[4] L. Ciobanu, D. Seeber, and C. Pennington. *3D MR microscopy with resolution 3.7?m by 3.3?m by 3.3?m.* Journal of Magnetic Resonance **158**(1), 178 – 182 (2002). ISSN 1090-7807.
URL http://dx.doi.org/https://doi.org/10.1016/S1090-7807(02)00071-X

[5] A. Blank and J. H. Freed. *ESR Microscopy and Nanoscopy with ?Induction? Detection.* Israel Journal of Chemistry **46**(4), 423–438 (2010).
URL http://dx.doi.org/10.1560/IJC_46_4_423

[6] C. A. Opitz, M. Kulke, M. C. Leake, C. Neagoe, H. Hinssen, R. J. Hajjar, and W. A. Linke. *Damped elastic recoil of the titin spring in myofibrils of human myocardium.* Proceedings of the National Academy of Sciences **100**(22), 12688–12693 (2003). ISSN 0027-8424.
URL http://dx.doi.org/10.1073/pnas.2133733100

[7] T. Maly, G. T. Debelouchina, V. S. Bajaj, K.-N. Hu, C.-G. Joo, M. L. Mak?Jurkauskas, J. R. Sirigiri, P. C. A. van der Wel, J. Herzfeld, R. J. Temkin, and R. G. Griffin. *Dynamic nuclear polarization at high magnetic fields.* The Journal of Chemical Physics **128**(5), 052211 (2008).
URL http://dx.doi.org/10.1063/1.2833582

[8] M. P. Ledbetter, I. M. Savukov, D. Budker, V. Shah, S. Knappe, J. Kitching, D. J. Michalak, S. Xu, and A. Pines. *Zero-Field Remote Detection of NMR with*

a Microfabricated Atomic Magnetometer. Proceedings of the National Academy of Sciences of the United States of America **105**(7), 2286–2290 (2008). ISSN 00278424. URL http://www.jstor.org/stable/25451458

[9] J. C. Allred, R. N. Lyman, T. W. Kornack, and M. V. Romalis. *High-Sensitivity Atomic Magnetometer Unaffected by Spin-Exchange Relaxation*. Phys. Rev. Lett. **89**, 130801 (Sep 2002).
URL http://dx.doi.org/10.1103/PhysRevLett.89.130801

[10] R. A. Webb. *New technique for improved low?temperature SQUID NMR measurements*. Review of Scientific Instruments **48**(12), 1585–1594 (1977).
URL http://dx.doi.org/10.1063/1.1134950

[11] P. G. Meredith, D.J. and O. Symko. *Application of a SQUID magnetometer to NMR at low temperatures*. J Low Temp Phys **13** (1973).
URL https://doi.org/10.1007/BF00656548

[12] J. A. Sidles. *Noninductive detection of single?proton magnetic resonance*. Applied Physics Letters **58**(24), 2854–2856 (1991).
URL http://dx.doi.org/10.1063/1.104757

[13] H. J. Mamin, M. Poggio, C. L. Degen, and D. Rugar. *Nuclear magnetic resonance imaging with 90-nm resolution*. Nature Nanotechnology **2**(5), 301–306 (May 2007). ISSN 1748-3395.
URL http://dx.doi.org/10.1038/nnano.2007.105

[14] A. Gruber, A. Drabenstedt, C. Tietz, L. Fleury, J. Wrachtrup, and C. vonBorczyskowski. *Scanning confocal optical microscopy and magnetic resonance on single defect centers*. Science **276**(5321), 2012–2014 (1997). ISSN 00368075, 10959203.
URL http://dx.doi.org/10.1126/science.276.5321.2012

[15] M. Pfender, N. Aslam, H. Sumiya, S. Onoda, P. Neumann, J. Isoya, C. Meriles, and J. Wrachtrup. *Nonvolatile quantum memory enables sensor unlimited nanoscale spectroscopy of finite quantum systems*. arXiv:1610.05675 [cond-mat, physics:quant-ph] (October 2016). ArXiv: 1610.05675.
URL http://arxiv.org/abs/1610.05675

[16] G. Balasubramanian, P. Neumann, D. Twitchen, M. Markham, R. Kolesov, N. Mizuochi, J. Isoya, J. Achard, J. Beck, J. Tissler, V. Jacques, P. R. Hemmer, F. Jelezko, and J. Wrachtrup. *Ultralong spin coherence time in isotopically engineered diamond*. Nature Materials **8**(5), 383–387 (April 2009). ISSN 1476-1122,

1476-4660.
URL http://dx.doi.org/10.1038/nmat2420

[17] L. Viola, E. Knill, and S. Lloyd. *Dynamical Decoupling of Open Quantum Systems.* Phys. Rev. Lett. **82**, 2417–2421 (Mar 1999).
URL http://dx.doi.org/10.1103/PhysRevLett.82.2417

[18] G. S. Uhrig. *Keeping a Quantum Bit Alive by Optimized π-Pulse Sequences.* Phys. Rev. Lett. **98**, 100504 (Mar 2007).
URL http://dx.doi.org/10.1103/PhysRevLett.98.100504

[19] G. de Lange, Z. H. Wang, D. Ristè, V. V. Dobrovitski, and R. Hanson. *Universal Dynamical Decoupling of a Single Solid-State Spin from a Spin Bath.* Science **330**(6000), 60–63 (2010). ISSN 0036-8075.
URL http://dx.doi.org/10.1126/science.1192739

[20] J. Du, X. Rong, N. Zhao, Y. Wang, J. Yang, and R. B. Liu. *Preserving electron spin coherence in solids by optimal dynamical decoupling.* Nature **461**(7268), 1265–1268 (October 2009). ISSN 1476-4687.
URL http://dx.doi.org/10.1038/nature08470

[21] N. Zhao, J. Honert, B. Schmid, M. Klas, J. Isoya, M. Markham, D. Twitchen, F. Jelezko, R.-B. Liu, H. Fedder, and J. Wrachtrup. *Sensing single remote nuclear spins.* Nature Nanotechnology **7**(10), 657–662 (2012). ISSN 1748-3387.
URL http://dx.doi.org/10.1038/nnano.2012.152

[22] S. Kolkowitz, Q. P. Unterreithmeier, S. D. Bennett, and M. D. Lukin. *Sensing Distant Nuclear Spins with a Single Electron Spin.* Phys. Rev. Lett. **109**, 137601 (Sep 2012).
URL http://dx.doi.org/10.1103/PhysRevLett.109.137601

[23] T. H. Taminiau, J. J. T. Wagenaar, T. van der Sar, F. Jelezko, V. V. Dobrovitski, and R. Hanson. *Detection and Control of Individual Nuclear Spins Using a Weakly Coupled Electron Spin.* Phys. Rev. Lett. **109**, 137602 (Sep 2012).
URL http://dx.doi.org/10.1103/PhysRevLett.109.137602

[24] T. Staudacher, F. Shi, S. Pezzagna, J. Meijer, J. Du, C. A. Meriles, F. Reinhard, and J. Wrachtrup. *Nuclear Magnetic Resonance Spectroscopy on a (5-Nanometer)3 Sample Volume.* Science **339**(6119), 561–563 (February 2013). ISSN 0036-8075, 1095-9203.
URL http://dx.doi.org/10.1126/science.1231675

[25] H. J. Mamin, M. Kim, M. H. Sherwood, C. T. Rettner, K. Ohno, D. D. Awschalom, and D. Rugar. *Nanoscale Nuclear Magnetic Resonance with a Nitrogen-Vacancy Spin Sensor*. Science **339**(6119), 557–560 (February 2013). ISSN 0036-8075, 1095-9203.
URL http://dx.doi.org/10.1126/science.1231540

[26] M. Loretz, S. Pezzagna, J. Meijer, and C. L. Degen. *Nanoscale nuclear magnetic resonance with a 1.9-nm-deep nitrogen-vacancy sensor*. Applied Physics Letters **104**(3), 033102 (2014).
URL http://dx.doi.org/10.1063/1.4862749

[27] S. J. DeVience, L. M. Pham, I. Lovchinsky, A. O. Sushkov, N. Bar-Gill, C. Belthangady, F. Casola, M. Corbett, H. Zhang, M. Lukin, H. Park, A. Yacoby, and R. L. Walsworth. *Nanoscale NMR spectroscopy and imaging of multiple nuclear species*. Nature Nanotechnology **10**(2), 129–134 (February 2015). ISSN 1748-3387.
URL http://dx.doi.org/10.1038/nnano.2014.313

[28] L. Jiang, J. S. Hodges, J. R. Maze, P. Maurer, J. M. Taylor, D. G. Cory, P. R. Hemmer, R. L. Walsworth, A. Yacoby, A. S. Zibrov, and M. D. Lukin. *Repetitive Readout of a Single Electronic Spin via Quantum Logic with Nuclear Spin Ancillae*. Science **326**(5950), 267–272 (2009). ISSN 0036-8075, 1095-9203.
URL http://dx.doi.org/10.1126/science.1176496

[29] P. Neumann, J. Beck, M. Steiner, F. Rempp, H. Fedder, P. R. Hemmer, J. Wrachtrup, and F. Jelezko. *Single-Shot Readout of a Single Nuclear Spin*. Science **329**(5991), 542–544 (2010). ISSN 0036-8075, 1095-9203.
URL http://dx.doi.org/10.1126/science.1189075

[30] S. Zaiser, T. Rendler, I. Jakobi, T. Wolf, S.-Y. Lee, S. Wagner, V. Bergholm, T. Schulte-Herbrüggen, P. Neumann, and J. Wrachtrup. *Enhancing quantum sensing sensitivity by a quantum memory*. Nature Communications **7**, 12279 (August 2016). ISSN 2041-1723.
URL http://dx.doi.org/10.1038/ncomms12279

[31] S. W. Hell and J. Wichmann. *Breaking the diffraction resolution limit by stimulated emission: stimulated-emission-depletion fluorescence microscopy*. Optics letters **19**(11), 780–782 (1994).

[32] E. Betzig, G. H. Patterson, R. Sougrat, O. W. Lindwasser, S. Olenych, J. S. Bonifacino, M. W. Davidson, J. Lippincott-Schwartz, and H. F. Hess. *Imaging Intracellular Fluorescent Proteins at Nanometer Resolution*. Science **313**(5793), 1642–1645

(September 2006). ISSN 0036-8075, 1095-9203.
URL http://dx.doi.org/10.1126/science.1127344

[33] S. T. Hess, T. P. Girirajan, and M. D. Mason. *Ultra-High Resolution Imaging by Fluorescence Photoactivation Localization Microscopy.* Biophysical Journal **91**(11), 4258–4272 (December 2006). ISSN 0006-3495.
URL http://dx.doi.org/10.1529/biophysj.106.091116

[34] M. J. Rust, M. Bates, and X. Zhuang. *Sub-diffraction-limit imaging by stochastic optical reconstruction microscopy (STORM).* Nature Methods **3**(10), 793–796 (October 2006). ISSN 1548-7091.
URL http://dx.doi.org/10.1038/nmeth929

[35] E. Rittweger, K. Y. Han, S. E. Irvine, C. Eggeling, and S. W. Hell. *STED microscopy reveals crystal colour centres with nanometric resolution.* Nature Photonics **3**(3), 144–147 (February 2009). ISSN 1749-4885, 1749-4893.
URL http://dx.doi.org/10.1038/nphoton.2009.2

[36] N. Aslam, G. Waldherr, P. Neumann, F. Jelezko, and J. Wrachtrup. *Photo-induced ionization dynamics of the nitrogen vacancy defect in diamond investigated by single-shot charge state detection.* New Journal of Physics **15**(1), 013064 (January 2013). ISSN 1367-2630.
URL http://dx.doi.org/10.1088/1367-2630/15/1/013064

[37] M. V. G. Dutt, L. Childress, L. Jiang, E. Togan, J. Maze, F. Jelezko, A. S. Zibrov, P. R. Hemmer, and M. D. Lukin. *Quantum register based on individual electronic and nuclear spin qubits in diamond.* Science **316**(5829), 1312–1316 (2007). ISSN 0036-8075, 1095-9203.
URL http://dx.doi.org/10.1126/science.1139831

[38] G. Waldherr, Y. Wang, S. Zaiser, M. Jamali, T. Schulte-Herbrüggen, H. Abe, T. Ohshima, J. Isoya, J. F. Du, P. Neumann, and J. Wrachtrup. *Quantum error correction in a solid-state hybrid spin register.* Nature **506**(7487), 204–207 (February 2014). ISSN 0028-0836.
URL http://dx.doi.org/10.1038/nature12919

[39] D. R. Glenn, D. B. Bucher, J. Lee, M. D. Lukin, H. Park, and R. L. Walsworth. *High-resolution magnetic resonance spectroscopy using a solid-state spin sensor.* Nature **555**(7696), 351–354 (March 2018). ISSN 1476-4687.
URL http://dx.doi.org/10.1038/nature25781

[40] I. Fescenko, A. Laraoui, J. Smits, N. Mosavian, P. Kehayias, J. Seto, L. Bougas, A. Jarmola, and V. M. Acosta. *Diamond magnetic microscopy of malarial hemozoin nanocrystals*. arXiv:1808.03636 [cond-mat, physics:physics] (August 2018). ArXiv: 1808.03636.
URL http://arxiv.org/abs/1808.03636

[41] M. J. Shon and A. E. Cohen. *Mass Action at the Single-Molecule Level*. Journal of the American Chemical Society **134**(35), 14618–14623 (2012). PMID: 22889156.
URL http://dx.doi.org/10.1021/ja3062425

[42] P. London, J. Scheuer, J.-M. Cai, I. Schwarz, A. Retzker, M. B. Plenio, M. Katagiri, T. Teraji, S. Koizumi, J. Isoya, R. Fischer, L. P. McGuinness, B. Naydenov, and F. Jelezko. *Detecting and Polarizing Nuclear Spins with Double Resonance on a Single Electron Spin*. Physical Review Letters **111**(6), 067601 (August 2013).
URL http://dx.doi.org/10.1103/PhysRevLett.111.067601

[43] T. Häberle, D. Schmid-Lorch, F. Reinhard, and J. Wrachtrup. *Nanoscale nuclear magnetic imaging with chemical contrast*. Nature Nanotechnology **10**(2), 125–128 (February 2015). ISSN 1748-3387.
URL http://dx.doi.org/10.1038/nnano.2014.299

[44] D. Rugar, H. J. Mamin, M. H. Sherwood, M. Kim, C. T. Rettner, K. Ohno, and D. D. Awschalom. *Proton magnetic resonance imaging using a nitrogen?vacancy spin sensor*. Nature Nanotechnology **10**(2), 120–124 (February 2015). ISSN 1748-3387.
URL http://dx.doi.org/10.1038/nnano.2014.288

[45] S. Steinert, F. Ziem, L. T. Hall, A. Zappe, M. Schweikert, N. Götz, A. Aird, G. Balasubramanian, L. Hollenberg, and J. Wrachtrup. *Magnetic spin imaging under ambient conditions with sub-cellular resolution*. Nature Communications **4**, 1607 (March 2013).
URL http://dx.doi.org/10.1038/ncomms2588

[46] A. O. Sushkov, I. Lovchinsky, N. Chisholm, R. L. Walsworth, H. Park, and M. D. Lukin. *Magnetic Resonance Detection of Individual Proton Spins Using Quantum Reporters*. Phys. Rev. Lett. **113**, 197601 (Nov 2014).
URL http://dx.doi.org/10.1103/PhysRevLett.113.197601

[47] P. N. J. W. N. Abt, S. Zaiser. Unpublished.

[48] Q. Chen and K. Schmidt-Rohr. *Measurement of the local 1H spin-diffusion coefficient in polymers*. Solid State Nuclear Magnetic Resonance **29**(1?3), 142–152 (February 2006). ISSN 0926-2040.
URL http://dx.doi.org/10.1016/j.ssnmr.2005.09.008

[49] E. Hahn. *Spin Echoes*. Physical Review **80**(4), 580–594 (November 1950).
URL http://dx.doi.org/10.1103/PhysRev.80.580

[50] T. Staudacher, N. Raatz, S. Pezzagna, J. Meijer, F. Reinhard, C. A. Meriles, and J. Wrachtrup. *Probing molecular dynamics at the nanoscale via an individual paramagnetic centre*. Nature Communications **6**, 8527 (2015).
URL http://dx.doi.org/10.1038/ncomms9527

[51] O. Jardetzky and G. Roberts. *NMR in Molecular Biology*. Academic Press (1981). ISBN 978-0-12-380580-5.

[52] W. F. Boron and E. L. Boulpaep. *Medical Physiology: A Cellular And Molecular Approach*. Elsevier/Saunders (2005). ISBN 1-4160-2328-3.

[53] P. Glover and S. P. Mansfield. *Limits to magnetic resonance microscopy*. Reports on Progress in Physics **65**(10), 1489 (2002).
URL http://stacks.iop.org/0034-4885/65/i=10/a=203

[54] *Most powerful superconducting magnet reaching 32 T*.
URL https://nationalmaglab.org/magnet-development/magnet-science-technology/magnet-projects/32-tesla-scm

[55] T. G. Walker and W. Happer. *Spin-exchange optical pumping of noble-gas nuclei*. Rev. Mod. Phys. **69**, 629–642 (Apr 1997).
URL http://dx.doi.org/10.1103/RevModPhys.69.629

[56] C. R. Bowers and D. P. Weitekamp. *Transformation of Symmetrization Order to Nuclear-Spin Magnetization by Chemical Reaction and Nuclear Magnetic Resonance*. Phys. Rev. Lett. **57**, 2645–2648 (Nov 1986).
URL http://dx.doi.org/10.1103/PhysRevLett.57.2645

[57] J. Natterer and J. Bargon. *Parahydrogen induced polarization*. Progress in Nuclear Magnetic Resonance Spectroscopy **31**(4), 293 – 315 (1997). ISSN 0079-6565.
URL http://dx.doi.org/https://doi.org/10.1016/S0079-6565(97)00007-1

[58] R. Kaptein. *Simple rules for chemically induced dynamic nuclear polarization*. J. Chem. Soc. D pages 732–733 (1971).
URL http://dx.doi.org/10.1039/C29710000732

[59] J. Strand, B. D. Schultz, A. F. Isakovic, C. J. Palmstrøm, and P. A. Crowell. *Dynamic Nuclear Polarization by Electrical Spin Injection in Ferromagnet-Semiconductor Heterostructures*. Phys. Rev. Lett. **91**, 036602 (Jul 2003).
URL http://dx.doi.org/10.1103/PhysRevLett.91.036602

[60] G. Lampel. *Nuclear Dynamic Polarization by Optical Electronic Saturation and Optical Pumping in Semiconductors*. Phys. Rev. Lett. **20**, 491–493 (Mar 1968).
URL http://dx.doi.org/10.1103/PhysRevLett.20.491

[61] T. R. Carver and C. P. Slichter. *Polarization of Nuclear Spins in Metals*. Phys. Rev. **92**, 212–213 (Oct 1953).
URL http://dx.doi.org/10.1103/PhysRev.92.212.2

[62] T. R. Carver and C. P. Slichter. *Experimental Verification of the Overhauser Nuclear Polarization Effect*. Phys. Rev. **102**, 975–980 (May 1956).
URL http://dx.doi.org/10.1103/PhysRev.102.975

[63] I. C. R. S. K. I. M. S. D. C. J. D. W. P. D. W. J. K. J. B. A. H. Hersman, F. William and S. Patz. *Large Production System for Hyperpolarized 129Xe for Human Lung Imaging Studies*. Academic radiology **15** (June 2008).
URL https://doi.org/10.1016/j.acra.2007.09.020

[64] T. C. Eisenschmid, R. U. Kirss, P. P. Deutsch, S. I. Hommeltoft, R. Eisenberg, J. Bargon, R. G. Lawler, and A. L. Balch. *Para hydrogen induced polarization in hydrogenation reactions*. Journal of the American Chemical Society **109**(26), 8089–8091 (1987).
URL http://dx.doi.org/10.1021/ja00260a026

[65] R. W. Adams, J. A. Aguilar, K. D. Atkinson, M. J. Cowley, P. I. P. Elliott, S. B. Duckett, G. G. R. Green, I. G. Khazal, J. López-Serrano, and D. C. Williamson. *Reversible Interactions with para-Hydrogen Enhance NMR Sensitivity by Polarization Transfer*. Science **323**(5922), 1708–1711 (2009). ISSN 0036-8075.
URL http://dx.doi.org/10.1126/science.1168877

[66] D. Rugar, R. Budakian, H. J. Mamin, and B. W. Chui. *Single spin detection by magnetic resonance force microscopy*. Nature **430**(6997), 329–332 (July 2004). ISSN 0028-0836.
URL http://dx.doi.org/10.1038/nature02658

[67] D. Budker and M. Romalis. *Optical Magnetometry* **3** (12 2006).

[68] *Gravity Probe B: Exploring Einstein's Universe with Gyroscopes* (2004). URL http://einstein.stanford.edu/content/education/GP-B_T-Guide4-2008.pdf

[69] D. Drung, C. Abmann, J. Beyer, A. Kirste, M. Peters, F. Ruede, and T. Schurig. *Highly Sensitive and Easy-to-Use SQUID Sensors.* IEEE Transactions on Applied Superconductivity **17**(2), 699–704 (June 2007). ISSN 1051-8223. URL http://dx.doi.org/10.1109/TASC.2007.897403

[70] D. Vasyukov, Y. Anahory, L. Embon, D. Halbertal, J. Cuppens, L. Neeman, A. Finkler, Y. Segev, Y. Myasoedov, M. L. Rappaport, M. E. Huber, and E. Zeldov. *A scanning superconducting quantum interference device with single electron spin sensitivity.* Nature Nanotechnology **8**(9), 639–644 (September 2013). ISSN 1748-3395. URL http://dx.doi.org/10.1038/nnano.2013.169

[71] C. L. Degen, M. Poggio, H. J. Mamin, C. T. Rettner, and D. Rugar. *Nanoscale magnetic resonance imaging.* Proceedings of the National Academy of Sciences **106**(5), 1313–1317 (February 2009). ISSN 0027-8424, 1091-6490. URL http://dx.doi.org/10.1073/pnas.0812068106

[72] P. Neumann, R. Kolesov, B. Naydenov, J. Beck, F. Rempp, M. Steiner, V. Jacques, G. Balasubramanian, M. L. Markham, D. J. Twitchen, S. Pezzagna, J. Meijer, J. Twamley, F. Jelezko, and J. Wrachtrup. *Quantum register based on coupled electron spins in a room-temperature solid.* Nature Physics **6**(4), 249–253 (April 2010). ISSN 1745-2473. URL http://dx.doi.org/10.1038/nphys1536

[73] P. C. Maurer, G. Kucsko, C. Latta, L. Jiang, N. Y. Yao, S. D. Bennett, F. Pastawski, D. Hunger, N. Chisholm, M. Markham, D. J. Twitchen, J. I. Cirac, and M. D. Lukin. *Room-Temperature Quantum Bit Memory Exceeding One Second.* Science **336**(6086), 1283–1286 (August 2012). ISSN 0036-8075, 1095-9203. URL http://dx.doi.org/10.1126/science.1220513

[74] F. Dolde, I. Jakobi, B. Naydenov, N. Zhao, S. Pezzagna, C. Trautmann, J. Meijer, P. Neumann, F. Jelezko, and J. Wrachtrup. *Room-temperature entanglement between single defect spins in diamond.* Nature Physics **9**(3), 139–143 (March 2013). ISSN 1745-2473. URL http://dx.doi.org/10.1038/nphys2545

[75] N. Kalb, A. A. Reiserer, P. C. Humphreys, J. J. W. Bakermans, S. J. Kamerling, N. H. Nickerson, S. C. Benjamin, D. J. Twitchen, M. Markham, and R. Han-

son. *Entanglement distillation between solid-state quantum network nodes*. Science **356**(6341), 928–932 (2017). ISSN 0036-8075.
URL http://dx.doi.org/10.1126/science.aan0070

[76] P. C. Humphreys, N. Kalb, J. P. J. Morits, R. N. Schouten, R. F. L. Vermeulen, D. J. Twitchen, M. Markham, and R. Hanson. *Deterministic delivery of remote entanglement on a quantum network*. Nature **558**(7709), 268–273 (June 2018). ISSN 1476-4687.
URL http://dx.doi.org/10.1038/s41586-018-0200-5

[77] G. Balasubramanian, I. Y. Chan, R. Kolesov, M. Al-Hmoud, J. Tisler, C. Shin, C. Kim, A. Wojcik, P. R. Hemmer, A. Krueger, T. Hanke, A. Leitenstorfer, R. Bratschitsch, F. Jelezko, and J. Wrachtrup. *Nanoscale imaging magnetometry with diamond spins under ambient conditions*. Nature **455**(7213), 648–651 (2008).
URL http://dx.doi.org/10.1038/nature07278

[78] J. R. Maze, P. L. Stanwix, J. S. Hodges, S. Hong, J. M. Taylor, P. Cappellaro, L. Jiang, M. V. G. Dutt, E. Togan, A. S. Zibrov, A. Yacoby, R. L. Walsworth, and M. D. Lukin. *Nanoscale magnetic sensing with an individual electronic spin in diamond*. Nature **455**(7213), 644–647 (2008).
URL http://dx.doi.org/10.1038/nature07279

[79] D. L. Sage, K. Arai, D. R. Glenn, S. J. DeVience, L. M. Pham, L. Rahn-Lee, M. D. Lukin, A. Yacoby, A. Komeili, and R. L. Walsworth. *Optical magnetic imaging of living cells*. Nature **496**(7446), 486–489 (April 2013). ISSN 1476-4687.
URL http://dx.doi.org/10.1038/nature12072

[80] P. Neumann, I. Jakobi, F. Dolde, C. Burk, R. Reuter, G. Waldherr, J. Honert, T. Wolf, A. Brunner, J. H. Shim, D. Suter, H. Sumiya, J. Isoya, and J. Wrachtrup. *High-Precision Nanoscale Temperature Sensing Using Single Defects in Diamond*. Nano Letters **13**(6), 2738–2742 (June 2013). ISSN 1530-6984.
URL http://dx.doi.org/10.1021/nl401216y

[81] G. Kucsko, P. C. Maurer, N. Y. Yao, M. Kubo, H. J. Noh, P. K. Lo, H. Park, and M. D. Lukin. *Nanometre-scale thermometry in a living cell*. Nature **500**(7460), 54–58 (August 2013). ISSN 1476-4687.
URL http://dx.doi.org/10.1038/nature12373

[82] J. D. Breeze, E. Salvadori, J. Sathian, N. M. Alford, and C. W. M. Kay. *Continuous-wave room-temperature diamond maser*. Nature **555**(7697), 493–496 (March 2018).

ISSN 1476-4687.
URL http://dx.doi.org/10.1038/nature25970

[83] A. C. Victor. *Heat Capacity of Diamond at High Temperatures.* Journal of Chemical Physics **36**(7), 1903 (1962).
URL http://dx.doi.org/10.1063/1.1701288

[84] G. Davies and M. F. Hamer. *Optical studies of the 1.945 eV Vibronic Band in Diamond.* Proceedings of the Royal Society A: Mathematical, Physical and Engineering Science **348**(1653), 285–298 (February 1976).
URL http://dx.doi.org/10.1098/rspa.1976.0039

[85] N. Reddy, N. Manson, and E. Krausz. *Two-laser spectral hole burning in a colour centre in diamond.* Journal of Luminescence **38**(1-6), 46–47 (1987). ISSN 0022-2313.
URL http://dx.doi.org/10.1016/0022-2313(87)90057-3

[86] J. Martin, R. Wannemacher, J. Teichert, L. Bischoff, and B. Köhler. *Generation and detection of fluorescent color centers in diamond with submicron resolution.* Applied Physics Letters **75**(20), 3096–3098 (1999).
URL http://dx.doi.org/10.1063/1.125242

[87] A. Mainwood. *Nitrogen and nitrogen-vacancy complexes and their formation in diamond.* Phys. Rev. B **49**, 7934–7940 (Mar 1994).
URL http://dx.doi.org/10.1103/PhysRevB.49.7934

[88] F. Waldermann, P. Olivero, J. Nunn, K. Surmacz, Z. Wang, D. Jaksch, R. Taylor, I. Walmsley, M. Draganski, P. Reichart, A. Greentree, D. Jamieson, and S. Prawer. *Creating diamond color centers for quantum optical applications.* Diamond and Related Materials **16**(11), 1887 – 1895 (2007). ISSN 0925-9635.
URL http://dx.doi.org/https://doi.org/10.1016/j.diamond.2007.09.009

[89] V. M. Acosta, E. Bauch, M. P. Ledbetter, C. Santori, K.-M. C. Fu, P. E. Barclay, R. G. Beausoleil, H. Linget, J. F. Roch, F. Treussart, S. Chemerisov, W. Gawlik, and D. Budker. *Diamonds with a high density of nitrogen-vacancy centers for magnetometry applications.* Phys. Rev. B **80**, 115202 (Sep 2009).
URL http://dx.doi.org/10.1103/PhysRevB.80.115202

[90] J. Meijer, B. Burchard, M. Domhan, C. Wittmann, T. Gaebel, I. Popa, F. Jelezko, and J. Wrachtrup. *Generation of single color centers by focused nitrogen implantation.* Applied Physics Letters **87**(26), 261909 (dec 2005). ISSN 0003-6951.
URL http://dx.doi.org/10.1063/1.2103389

[91] J. R. Rabeau, P. Reichart, G. Tamanyan, D. N. Jamieson, S. Prawer, F. Jelezko, T. Gaebel, I. Popa, M. Domhan, and J. Wrachtrup. *Implantation of labelled single nitrogen vacancy centers in diamond using N-15.* Applied Physics Letters **88**(2), 023113 (2006).

[92] *SRIM ® – Stopping and Range of Ions in Matter.* software.
URL `http://www.srim.org`

[93] S. Pezzagna, B. Naydenov, F. Jelezko, J. Wrachtrup, and J. Meijer. *Creation efficiency of nitrogen-vacancy centres in diamond.* New Journal of Physics **12**(6), 065017 (2010).
URL `http://dx.doi.org/10.1088/1367-2630/12/6/065017`

[94] B. K. Ofori-Okai, S. Pezzagna, K. Chang, M. Loretz, R. Schirhagl, Y. Tao, B. A. Moores, K. Groot-Berning, J. Meijer, and C. L. Degen. *Spin properties of very shallow nitrogen vacancy defects in diamond.* Phys. Rev. B **86**, 081406 (Aug 2012).
URL `http://dx.doi.org/10.1103/PhysRevB.86.081406`

[95] K. Ohno, F. Joseph Heremans, L. C. Bassett, B. A. Myers, D. M. Toyli, A. C. Bleszynski Jayich, C. J. Palmstrøm, and D. D. Awschalom. *Engineering shallow spins in diamond with nitrogen delta-doping.* Applied Physics Letters **101**(8), 082413 (2012).
URL `http://dx.doi.org/10.1063/1.4748280`

[96] D. J. Twitchen, M. E. Newton, J. M. Baker, T. R. Anthony, and W. F. Banholzer. *Electron-paramagnetic-resonance measurements on the divacancy defect center $R4/W6$ in diamond.* Phys. Rev. B **59**, 12900–12910 (May 1999).
URL `http://dx.doi.org/10.1103/PhysRevB.59.12900`

[97] A. Lenef and S. C. Rand. *Electronic structure of the N-V center in diamond: Theory.* Physical Review B **53**(20), 13441–13455 (May 1996).
URL `http://dx.doi.org/10.1103/PhysRevB.53.13441`

[98] J. P. Goss, R. Jones, P. R. Briddon, G. Davies, A. T. Collins, A. Mainwood, J. A. van Wyk, J. M. Baker, M. E. Newton, A. M. Stoneham, and S. C. Lawson. *Comment on "Electronic structure of the N-V center in diamond: Theory".* Physical Review B **56**(24), 16031–16032 (Dec 1997).
URL `http://dx.doi.org/10.1103/PhysRevB.56.16031`

[99] A. Lenef and S. C. Rand. *Reply to "Comment on 'Electronic structure of the N-V center in diamond: Theory' ".* Physical Review B **56**(24), 16033–16034 (Dec 1997).
URL `http://dx.doi.org/10.1103/PhysRevB.56.16033`

[100] J. Maze, A. Gali, E. Togan, Y. Chu, A. Trifonov, E. Kaxiras, and M. Lukin. *Properties of nitrogen-vacancy centers in diamond: group theoretic approach.* arXiv:1010.1338v1 [quant-ph] (2010).

[101] J. P. Goss, R. Jones, P. R. Briddon, G. Davies, A. T. Collins, A. Mainwood, J. A. van Wyk, J. M. Baker, M. E. Newton, A. M. Stoneham, and S. C. Lawson. *Comment on "Electronic structure of the N-V center in diamond: Theory"*. Physical Review B **56**(24), 16031–16032 (December 1997).
URL `http://dx.doi.org/10.1103/PhysRevB.56.16031`

[102] G. Davies and M. F. Hamer. *Optical studies of the 1.945 eV Vibronic Band in Diamond*. Proceedings of the Royal Society A: Mathematical, Physical and Engineering Science **348**(1653), 285–298 (February 1976).
URL `http://dx.doi.org/10.1098/rspa.1976.0039`

[103] A. Batalov, V. Jacques, F. Kaiser, P. Siyushev, P. Neumann, L. Rogers, R. McMurtrie, N. Manson, F. Jelezko, and J. Wrachtrup. *Low Temperature Studies of the Excited-State Structure of Negatively Charged Nitrogen-Vacancy Color Centers in Diamond*. Physical Review Letters **102**(19), 195506 (May 2009). ISSN 0031-9007, 1079-7114.
URL `http://dx.doi.org/10.1103/PhysRevLett.102.195506`

[104] P. Neumann, R. Kolesov, V. Jacques, J. Beck, J. Tisler, A. Batalov, L. Rogers, N. B. Manson, G. Balasubramanian, F. Jelezko, and J. Wrachtrup. *Excited-state spectroscopy of single NV defects in diamond using optically detected magnetic resonance*. New Journal of Physics **11**, 013017 (2009).
URL `http://dx.doi.org/10.1088/1367-2630/11/1/013017`

[105] F. Jelezko, I. Popa, A. Gruber, C. Tietz, J. Wrachtrup, A. Nizovtsev, and S. Kilin. *Single spin states in a defect center resolved by optical spectroscopy.* Applied Physics Letters **81**(12), 2160–2162 (2002).
URL `http://dx.doi.org/10.1063/1.1507838`

[106] P. Tamarat, T. Gaebel, J. Rabeau, M. Khan, A. Greentree, H. Wilson, L. Hollenberg, S. Prawer, P. Hemmer, F. Jelezko, and J. Wrachtrup. *Stark Shift Control of Single Optical Centers in Diamond*. Physical Review Letters **97**(8), 083002 (August 2006). ISSN 0031-9007, 1079-7114.
URL `http://dx.doi.org/10.1103/PhysRevLett.97.083002`

[107] P. Tamarat, N. B. Manson, J. P. Harrison, R. L. McMurtrie, A. Nizovtsev, C. Santori, R. G. Beausoleil, P. Neumann, T. Gaebel, F. Jelezko, P. Hemmer, and

J. Wrachtrup. *Spin-flip and spin-conserving optical transitions of the nitrogen-vacancy centre in diamond.* New Journal of Physics **10**(4), 045004 (2008).
URL http://dx.doi.org/10.1088/1367-2630/10/4/045004

[108] C. Santori, P. Tamarat, P. Neumann, J. Wrachtrup, D. Fattal, R. Beausoleil, J. Rabeau, P. Olivero, A. Greentree, S. Prawer, F. Jelezko, and P. Hemmer. *Coherent Population Trapping of Single Spins in Diamond under Optical Excitation.* Physical Review Letters **97**(24), 247401 (December 2006). ISSN 0031-9007, 1079-7114.
URL http://dx.doi.org/10.1103/PhysRevLett.97.247401

[109] A. Gali, M. Fyta, and E. Kaxiras. *Ab initio supercell calculations on nitrogen-vacancy center in diamond: Electronic structure and hyperfine tensors.* Physical Review B **77**(15), 155206 (Apr 2008).
URL http://dx.doi.org/10.1103/PhysRevB.77.155206

[110] A. Gali. *Identification of individual ^{13}C isotopes of nitrogen-vacancy center in diamond by combining the polarization studies of nuclear spins and first-principles calculations.* Phys. Rev. B **80**, 241204 (Dec 2009).
URL http://dx.doi.org/10.1103/PhysRevB.80.241204

[111] S. Felton, A. M. Edmonds, M. E. Newton, P. M. Martineau, D. Fisher, D. J. Twitchen, and J. M. Baker. *Hyperfine interaction in the ground state of the negatively charged nitrogen vacancy center in diamond.* Physical Review B **79**(7), 075203 (February 2009). ISSN 1098-0121, 1550-235X.
URL http://dx.doi.org/10.1103/PhysRevB.79.075203

[112] A. Gali. *Identification of individual C 13 isotopes of nitrogen-vacancy center in diamond by combining the polarization studies of nuclear spins and first-principles calculations.* Physical Review B **80**(24), 241204 (2009).
URL http://dx.doi.org/10.1103/PhysRevB.80.241204

[113] A. Gali, T. Simon, and J. E. Lowther. *An ab initio study of local vibration modes of the nitrogen-vacancy center in diamond.* New Journal of Physics **13**(2), 025016 (2011).
URL http://dx.doi.org/10.1088/1367-2630/13/2/025016

[114] C. Kurtsiefer, S. Mayer, P. Zarda, and H. Weinfurter. *Stable solid-state source of single photons.* Physical Review Letters **85**(2), 290–293 (2000).
URL http://dx.doi.org/10.1103/PhysRevLett.85.290

[115] A. M. Zaitsev. *Vibronic spectra of impurity-related optical centers in diamond*. Physical Review B **61**, 12909–12922 (May 2000).
URL http://dx.doi.org/10.1103/PhysRevB.61.12909

[116] T. Gaebel, I. Popa, A. Gruber, M. Domhan, F. Jelezko, and J. Wrachtrup. *Stable single-photon source in the near infrared*. New Journal of Physics **6**(1), 98 (2004).
URL http://dx.doi.org/10.1088/1367-2630/6/1/098

[117] L. J. Rogers, S. Armstrong, M. J. Sellars, and N. B. Manson. *Infrared emission of the NV centre in diamond: Zeeman and uniaxial stress studies*. New Journal of Physics **10**(10), 103024 (2008).
URL http://dx.doi.org/10.1088/1367-2630/10/10/103024

[118] V. M. Acosta, A. Jarmola, E. Bauch, and D. Budker. *Optical properties of the nitrogen-vacancy singlet levels in diamond*. Phys. Rev. B **82**, 201202 (Nov 2010).
URL http://dx.doi.org/10.1103/PhysRevB.82.201202

[119] J. H. N. Loubser and J. A. van Wyk. *Optical spin-polarization in a triplet state in irradiated and annealed Typ Ib diamonds*. Diamond Research **11**, 4–8 (1977).

[120] J. Harrison, M. J. Sellars, and N. B. Manson. *Measurement of the optically induced spin polarisation of N-V centres in diamond*. Diamond and Related Materials **15**(4-8), 586–588 (2006).
URL http://dx.doi.org/10.1016/j.diamond.2005.12.027

[121] J. Harrison, M. J. Sellars, and N. B. Manson. *Optical spin polarisation of the N-V centre in diamond*. Journal of Luminescence **107**(1-4), 245–248 (2004).

[122] A. Batalov, C. Zierl, T. Gaebel, P. Neumann, I.-Y. Chan, G. Balasubramanian, P. R. Hemmer, F. Jelezko, and J. Wrachtrup. *Temporal Coherence of Photons Emitted by Single Nitrogen-Vacancy Defect Centers in Diamond Using Optical Rabi-Oscillations*. Physical Review Letters **100**(7), 077401 (February 2008). ISSN 0031-9007, 1079-7114.
URL http://dx.doi.org/10.1103/PhysRevLett.100.077401

[123] N. Manson, J. Harrison, and M. Sellars. *Nitrogen-vacancy center in diamond: Model of the electronic structure and associated dynamics*. Physical Review B **74**(10) (September 2006). ISSN 1098-0121, 1550-235X.
URL http://dx.doi.org/10.1103/PhysRevB.74.104303

[124] G. Chatzidrosos, A. Wickenbrock, L. Bougas, N. Leefer, T. Wu, K. Jensen, Y. Dumeige, and D. Budker. *Miniature Cavity-Enhanced Diamond Magnetometer.* Phys. Rev. Applied **8**, 044019 (Oct 2017).
URL http://dx.doi.org/10.1103/PhysRevApplied.8.044019

[125] J. P. Goss, R. Jones, S. J. Breuer, P. R. Briddon, and S. Öberg. *The Twelve-Line 1.682 eV Luminescence Center in Diamond and the Vacancy-Silicon Complex.* Physical Review Letters **77**(14), 3041–3044 (Sep 1996).
URL http://dx.doi.org/10.1103/PhysRevLett.77.3041

[126] J. H. N. Loubser and J. A. v. Wyk. *Electron spin resonance in the study of diamond.* Reports on Progress in Physics **41**(8), 1201 (1978).
URL http://dx.doi.org/10.1088/0034-4885/41/8/002

[127] J. A. Weil, J. R. Bolton, and J. E. Wertz. *Electron paramagnetic resonance: elementary theory and practical applications.* John Wiley & Sons, Inc. (1994). ISBN 0-471-57234-9.

[128] J. H. N. Loubser. *ESR Studies of Diamond Powders.* Solid State Communications **22**(12), 767–770 (1977).
URL http://dx.doi.org/10.1016/0038-1098(77)90064-3

[129] A. Gali. *Theory of the neutral nitrogen-vacancy center in diamond and its application to the realization of a qubit.* Physical Review B **79**(23), 235210 (June 2009). ISSN 1098-0121, 1550-235X.
URL http://dx.doi.org/10.1103/PhysRevB.79.235210

[130] S. Felton, A. Edmonds, M. Newton, P. Martineau, D. Fisher, and D. Twitchen. *Electron paramagnetic resonance studies of the neutral nitrogen vacancy in diamond.* Physical Review B **77**(8), 081201 (February 2008). ISSN 1098-0121, 1550-235X.
URL http://dx.doi.org/10.1103/PhysRevB.77.081201

[131] K. Y. Han, S. K. Kim, C. Eggeling, and S. W. Hell. *Metastable Dark States Enable Ground State Depletion Microscopy of Nitrogen Vacancy Centers in Diamond with Diffraction-Unlimited Resolution.* Nano Letters **10**(8), 3199–3203 (2010).
URL http://dx.doi.org/10.1021/nl102156m

[132] G. Waldherr, J. Beck, M. Steiner, P. Neumann, A. Gali, T. Frauenheim, F. Jelezko, and J. Wrachtrup. *Dark States of Single Nitrogen-Vacancy Centers in Diamond Unraveled by Single Shot NMR.* Physical Review Letters **106**(15), 157601 (April

2011). ISSN 0031-9007, 1079-7114.
URL http://dx.doi.org/10.1103/PhysRevLett.106.157601

[133] K. Beha, A. Batalov, N. B. Manson, R. Bratschitsch, and A. Leitenstorfer. *Optimum Photoluminescence Excitation and Recharging Cycle of Single Nitrogen-Vacancy Centers in Ultrapure Diamond*. Physical Review Letters **109**(9), 097404 (August 2012).
URL http://dx.doi.org/10.1103/PhysRevLett.109.097404

[134] E. Abe, A. M. Tyryshkin, S. Tojo, J. J. L. Morton, W. M. Witzel, A. Fujimoto, J. W. Ager, E. E. Haller, J. Isoya, S. A. Lyon, M. L. W. Thewalt, and K. M. Itoh. *Electron spin coherence of phosphorus donors in silicon: Effect of environmental nuclei*. Physical Review B **82**(12), 121201 (Sep 2010).
URL http://dx.doi.org/10.1103/PhysRevB.82.121201

[135] P. Siyushev, H. Pinto, M. Vörös, A. Gali, F. Jelezko, and J. Wrachtrup. *Optically Controlled Switching of the Charge State of a Single Nitrogen-Vacancy Center in Diamond at Cryogenic Temperatures*. Physical Review Letters **110**(16), 167402 (April 2013).
URL http://dx.doi.org/10.1103/PhysRevLett.110.167402

[136] M. V. Hauf, B. Grotz, B. Naydenov, M. Dankerl, S. Pezzagna, J. Meijer, F. Jelezko, J. Wrachtrup, M. Stutzmann, F. Reinhard, and J. A. Garrido. *Chemical control of the charge state of nitrogen-vacancy centers in diamond*. Physical Review B **83**(8), 081304 (Feb 2011).
URL http://dx.doi.org/10.1103/PhysRevB.83.081304

[137] B. Grotz, M. V. Hauf, M. Dankerl, B. Naydenov, S. Pezzagna, J. Meijer, F. Jelezko, J. Wrachtrup, M. Stutzmann, F. Reinhard, and J. A. Garrido. *Charge state manipulation of qubits in diamond*. Nature Communications **3**, 729 (March 2012). ISSN 2041-1723.
URL http://dx.doi.org/10.1038/ncomms1729

[138] M. V. Hauf, P. Simon, N. Aslam, M. Pfender, P. Neumann, S. Pezzagna, J. Meijer, J. Wrachtrup, M. Stutzmann, F. Reinhard, and J. A. Garrido. *Addressing Single Nitrogen-Vacancy Centers in Diamond with Transparent in-Plane Gate Structures*. Nano Letters **14**(5), 2359–2364 (2014). PMID: 24716609.
URL http://dx.doi.org/10.1021/nl4047619

[139] M. Pfender, N. Aslam, P. Simon, D. Antonov, G. Thiering, S. Burk, F. Fávaro de Oliveira, A. Denisenko, H. Fedder, J. Meijer, J. A. Garrido, A. Gali, T. Teraji,

J. Isoya, M. W. Doherty, A. Alkauskas, A. Gallo, A. Grüneis, P. Neumann, and J. Wrachtrup. *Protecting a Diamond Quantum Memory by Charge State Control*. Nano Letters **17**(10), 5931–5937 (2017). PMID: 28872881.
URL http://dx.doi.org/10.1021/acs.nanolett.7b01796

[140] L. Robledo, H. Bernien, T. van der Sar, and R. Hanson. *Spin dynamics in the optical cycle of single nitrogen-vacancy centres in diamond*. New Journal of Physics **13**(2), 025013 (2011).
URL http://stacks.iop.org/1367-2630/13/i=2/a=025013

[141] N. B. Manson, L. Rogers, M. Doherty, and L. Hollenberg. *Optically induced spin polarisation of the NV- centre in diamond: role of electron-vibration interaction*. arXiv:1011.2840v1 (2010).
URL http://arxiv.org/abs/1011.2840v1

[142] M. L. Goldman, A. Sipahigil, M. W. Doherty, N. Y. Yao, S. D. Bennett, M. Markham, D. J. Twitchen, N. B. Manson, A. Kubanek, and M. D. Lukin. *Phonon-Induced Population Dynamics and Intersystem Crossing in Nitrogen-Vacancy Centers*. Phys. Rev. Lett. **114**, 145502 (Apr 2015).
URL http://dx.doi.org/10.1103/PhysRevLett.114.145502

[143] M. L. Goldman, M. W. Doherty, A. Sipahigil, N. Y. Yao, S. D. Bennett, N. B. Manson, A. Kubanek, and M. D. Lukin. *State-selective intersystem crossing in nitrogen-vacancy centers*. Phys. Rev. B **91**, 165201 (Apr 2015).
URL http://dx.doi.org/10.1103/PhysRevB.91.165201

[144] M. Steiner, P. Neumann, J. Beck, F. Jelezko, and J. Wrachtrup. *Universal enhancement of the optical readout fidelity of single electron spins at nitrogen-vacancy centers in diamond*. Physical Review B **81**(3), 035205 (January 2010). ISSN 1098-0121, 1550-235X.
URL http://dx.doi.org/10.1103/PhysRevB.81.035205

[145] P. Neumann, J. Beck, M. Steiner, F. Rempp, H. Fedder, P. R. Hemmer, J. Wrachtrup, and F. Jelezko. *Single-Shot Readout of a Single Nuclear Spin*. Science **329**(5991), 542–544 (2010).
URL http://dx.doi.org/10.1126/science.1189075

[146] A. Dréau, P. Spinicelli, J. R. Maze, J.-F. Roch, and V. Jacques. *Single-Shot Readout of Multiple Nuclear Spin Qubits in Diamond under Ambient Conditions*. Physical Review Letters **110**(6), 060502 (February 2013).
URL http://dx.doi.org/10.1103/PhysRevLett.110.060502

[147] G. Waldherr, Y. Wang, S. Zaiser, M. Jamali, T. Schulte-Herbrüggen, H. Abe, T. Ohshima, J. Isoya, J. F. Du, P. Neumann, and J. Wrachtrup. *Quantum error correction in a solid-state hybrid spin register.* Nature **advance online publication** (January 2014). ISSN 0028-0836.
URL `http://dx.doi.org/10.1038/nature12919`

[148] T. H. Taminiau, J. Cramer, T. v. d. Sar, V. V. Dobrovitski, and R. Hanson. *Universal control and error correction in multi-qubit spin registers in diamond.* Nature Nanotechnology **9**(3), 171–176 (March 2014). ISSN 1748-3395.
URL `http://dx.doi.org/10.1038/nnano.2014.2`

[149] J. Meijer, S. Pezzagna, T. Vogel, B. Burchard, H. Bukow, I. Rangelow, Y. Sarov, H. Wiggers, I. Plümel, F. Jelezko, J. Wrachtrup, F. Schmidt-Kaler, W. Schnitzler, and K. Singer. *Towards the implanting of ions and positioning of nanoparticles with nm spatial resolution.* Applied Physics A: Materials Science & Processing **91**, 567–571 (2008). ISSN 0947-8396. 10.1007/s00339-008-4515-1.
URL `http://dx.doi.org/10.1007/s00339-008-4515-1`

[150] I. Jakobi, S. A. Momenzadeh, F. F. de Oliveira, J. Michl, F. Ziem, M. Schreck, P. Neumann, A. Denisenko, and J. Wrachtrup. *Efficient creation of dipolar coupled nitrogen-vacancy spin qubits in diamond.* Journal of Physics: Conference Series **752**(1), 012001 (2016).
URL `http://stacks.iop.org/1742-6596/752/i=1/a=012001`

[151] H. Bernien, B. Hensen, W. Pfaff, G. Koolstra, M. S. Blok, L. Robledo, T. H. Taminiau, M. Markham, D. J. Twitchen, L. Childress, and R. Hanson. *Heralded entanglement between solid-state qubits separated by three metres.* Nature **497**(7447), 86–90 (May 2013). ISSN 0028-0836.
URL `http://dx.doi.org/10.1038/nature12016`

[152] S. Bogdanovi?, S. B. van Dam, C. Bonato, L. C. Coenen, A.-M. J. Zwerver, B. Hensen, M. S. Z. Liddy, T. Fink, A. Reiserer, M. Lon?ar, and R. Hanson. *Design and low-temperature characterization of a tunable microcavity for diamond-based quantum networks.* Applied Physics Letters **110**(17), 171103 (2017).
URL `http://dx.doi.org/10.1063/1.4982168`

[153] B. Hensen, H. Bernien, A. E. Dréau, A. Reiserer, N. Kalb, M. S. Blok, J. Ruitenberg, R. F. L. Vermeulen, R. N. Schouten, C. Abellán, W. Amaya, V. Pruneri, M. W. Mitchell, M. Markham, D. J. Twitchen, D. Elkouss, S. Wehner, T. H. Taminiau, and R. Hanson. *Loophole-free Bell inequality violation using electron spins separated*

by 1.3 kilometres. Nature **526**(7575), 682–686 (October 2015). ISSN 1476-4687.
URL http://dx.doi.org/10.1038/nature15759

[154] F. Dolde, H. Fedder, M. W. Doherty, T. Nobauer, F. Rempp, G. Balasubramanian, T. Wolf, F. Reinhard, L. C. L. Hollenberg, F. Jelezko, and J. Wrachtrup. *Electric-field sensing using single diamond spins*. Nature Physics **7**(6), 459–463 (June 2011). ISSN 1745-2473.
URL http://dx.doi.org/10.1038/nphys1969

[155] B. Grotz, J. Beck, P. Neumann, B. Naydenov, R. Reuter, F. Reinhard, F. Jelezko, J. Wrachtrup, D. Schweinfurth, B. Sarkar, and P. Hemmer. *Sensing external spins with nitrogen-vacancy diamond*. New Journal of Physics **13**(5), 055004 (2011).
URL http://dx.doi.org/10.1088/1367-2630/13/5/055004

[156] S. Steinert, F. Dolde, P. Neumann, A. Aird, B. Naydenov, G. Balasubramanian, F. Jelezko, and J. Wrachtrup. *High sensitivity magnetic imaging using an array of spins in diamond*. Review of Scientific Instruments **81**(4), 043705 (April 2010). ISSN 0034-6748.
URL http://dx.doi.org/10.1063/1.3385689

[157] J. Wrachtrup, C. von Borczyskowski, J. Bernard, M. Orritt, and R. Brown. *Optical detection of magnetic resonance in a single molecule*. Nature **363**(6426), 244–245 (May 1993).
URL http://dx.doi.org/10.1038/363244a0

[158] J. Wrachtrup, C. von Borczyskowski, J. Bernard, M. Orrit, and R. Brown. *Optically detected spin coherence of single molecules*. Physical Review Letters **71**(21), 3565–3568 (November 1993).
URL http://dx.doi.org/10.1103/PhysRevLett.71.3565

[159] F. Jelezko, T. Gaebel, I. Popa, M. Domhan, A. Gruber, and J. Wrachtrup. *Observation of coherent oscillation of a single nuclear spin and realization of a two-qubit conditional quantum gate*. Physical Review Letters **93**(13), 130501 (2004).
URL http://dx.doi.org/10.1103/PhysRevLett.93.130501

[160] J. R. Weber, W. F. Koehl, J. B. Varley, A. Janotti, B. B. Buckley, C. G. V. d. Walle, and D. D. Awschalom. *Defects in SiC for quantum computing*. Applied Physics Letters **109**(10), 102417 (2011). ISSN 00218979.
URL http://dx.doi.org/10.1063/1.3578264

[161] J. J. Pla, K. Y. Tan, J. P. Dehollain, W. H. Lim, J. J. L. Morton, F. A. Zwanenburg, D. N. Jamieson, A. S. Dzurak, and A. Morello. *High-fidelity readout and control of a nuclear spin qubit in silicon.* Nature **496**(7445), 334–338 (April 2013). ISSN 0028-0836.
URL `http://dx.doi.org/10.1038/nature12011`

[162] P. Siyushev, K. Xia, R. Reuter, M. Jamali, N. Zhao, N. Yang, C. Duan, N. Kukharchyk, A. D. Wieck, R. Kolesov, and J. Wrachtrup. *Coherent properties of single rare-earth spin qubits.* Nature Communications **5** (May 2014).
URL `http://dx.doi.org/10.1038/ncomms4895`

[163] D. M. Toyli, C. D. Weis, G. D. Fuchs, T. Schenkel, and D. D. Awschalom. *Chip-scale nanofabrication of single spins and spin arrays in diamond.* Nano Letters **10**(8), 3168–3172 (August 2010).
URL `http://dx.doi.org/10.1021/nl102066q`

[164] D. R. McCamey, J. V. Tol, G. W. Morley, and C. Boehme. *Electronic Spin Storage in an Electrically Readable Nuclear Spin Memory with a Lifetime >100 Seconds.* Science **330**(6011), 1652–1656 (December 2010). ISSN 0036-8075, 1095-9203.
URL `http://dx.doi.org/10.1126/science.1197931`

[165] A. Morello, J. J. Pla, F. A. Zwanenburg, K. W. Chan, K. Y. Tan, H. Huebl, M. Mottonen, C. D. Nugroho, C. Yang, J. A. van Donkelaar, A. D. C. Alves, D. N. Jamieson, C. C. Escott, L. C. L. Hollenberg, R. G. Clark, and A. S. Dzurak. *Single-shot readout of an electron spin in silicon.* Nature **467**(7316), 687–691 (October 2010). ISSN 0028-0836.
URL `http://dx.doi.org/10.1038/nature09392`

[166] R. Kolesov, K. Xia, R. Reuter, M. Jamali, R. Stöhr, T. Inal, P. Siyushev, and J. Wrachtrup. *Mapping Spin Coherence of a Single Rare-Earth Ion in a Crystal onto a Single Photon Polarization State.* Physical Review Letters **111**(12), 120502 (September 2013).
URL `http://dx.doi.org/10.1103/PhysRevLett.111.120502`

[167] R. Kolesov, K. Xia, R. Reuter, R. Stöhr, A. Zappe, J. Meijer, P. R. Hemmer, and J. Wrachtrup. *Optical detection of a single rare-earth ion in a crystal.* Nature Communications **3**, 1029 (August 2012).
URL `http://dx.doi.org/10.1038/ncomms2034`

[168] C. Yin, M. Rancic, G. G. de Boo, N. Stavrias, J. C. McCallum, M. J. Sellars, and S. Rogge. *Optical addressing of an individual erbium ion in silicon.* Nature

497(7447), 91–94 (May 2013). ISSN 0028-0836.
URL http://dx.doi.org/10.1038/nature12081

[169] N. Aslam, M. Pfender, R. Stöhr, P. Neumann, M. Scheffler, H. Sumiya, H. Abe, S. Onoda, T. Ohshima, J. Isoya, and J. Wrachtrup. *Single spin optically detected magnetic resonance with 60?90 GHz (E-band) microwave resonators*. Review of Scientific Instruments **86**(6), 064704 (June 2015).
URL http://dx.doi.org/10.1063/1.4922664

[170] H. Iizuka, T. Watanabe, K. Sato, and K. Nishikawa. *Millimeter-Wave Microstrip Line to Waveguide Transition Fabricated on a Single Layer Dielectric Substrate*. IEICE TRANSACTIONS on Communications **E85-B**(6), 1169–1177 (June 2002). ISSN , 0916-8516.
URL http://search.ieice.org/bin/summary.php?id=e85-b_6_1169&category=B&year=2002&lang=E&abst=

[171] D. Pozar. *Microwave Engineering*. Wiley (2004). ISBN 9780471448785.
URL http://books.google.co.uk/books?id=4wzpQwAACAAJ

[172] G. Fuchs, V. Dobrovitski, R. Hanson, A. Batra, C. Weis, T. Schenkel, and D. Awschalom. *Excited-State Spectroscopy Using Single Spin Manipulation in Diamond*. Physical Review Letters **101**(11), 117601 (September 2008). ISSN 0031-9007, 1079-7114.
URL http://dx.doi.org/10.1103/PhysRevLett.101.117601

[173] A. Gali. *Identification of individual C 13 isotopes of nitrogen-vacancy center in diamond by combining the polarization studies of nuclear spins and first-principles calculations*. Physical Review B **80**(24), 241204 (December 2009). ISSN 1098-0121, 1550-235X.
URL http://dx.doi.org/10.1103/PhysRevB.80.241204

[174] P. Neumann. *Towards a room temperature solid state quantum processor - the nitrogen-vacancy center in diamond*. Ph.D. thesis (2012).
URL http://elib.uni-stuttgart.de/opus/frontdoor.php?source_opus=7505&la=de

[175] L. Childress, M. V. Gurudev Dutt, J. M. Taylor, A. S. Zibrov, F. Jelezko, J. Wrachtrup, P. R. Hemmer, and M. D. Lukin. *Coherent Dynamics of Coupled Electron and Nuclear Spin Qubits in Diamond*. Science **314**(5797), 281–285 (October 2006). ISSN 0036-8075, 1095-9203.
URL http://dx.doi.org/10.1126/science.1131871

[176] V. Jacques, P. Neumann, J. Beck, M. Markham, D. Twitchen, J. Meijer, F. Kaiser, G. Balasubramanian, F. Jelezko, and J. Wrachtrup. *Dynamic Polarization of Single Nuclear Spins by Optical Pumping of Nitrogen-Vacancy Color Centers in Diamond at Room Temperature*. Physical Review Letters **102**(5), 057403 (2009).
URL `http://dx.doi.org/10.1103/PhysRevLett.102.057403`

[177] A. V. Gorshkov, A. M. Rey, A. J. Daley, M. M. Boyd, J. Ye, P. Zoller, and M. D. Lukin. *Alkaline-Earth-Metal Atoms as Few-Qubit Quantum Registers*. Physical Review Letters **102**(11), 110503 (2009).
URL `http://dx.doi.org/10.1103/PhysRevLett.102.110503`

[178] V. B. Braginsky and F. Y. Khalili. *Quantum nondemolition measurements: The route from toys to tools*. Reviews of Modern Physics **68**(1), 1–11 (1996).
URL `http://dx.doi.org/10.1103/RevModPhys.68.1`

[179] N. Zarrabi. *Hidden Markov Modelle für Einzelmolekül̈daten*. Ph.D. thesis, Universität Stuttgart, 3. Phsikalisches Institut (2010). Language = German.
URL `http://nbn-resolving.de/urn:nbn:de:bsz:93-opus-56913`

[180] T. Häberle, T. Oeckinghaus, D. Schmid-Lorch, M. Pfender, F. F. de Oliveira, S. A. Momenzadeh, A. Finkler, and J. Wrachtrup. *Nuclear quantum-assisted magnetometer*. Review of Scientific Instruments **88**(1), 013702 (2017).
URL `http://dx.doi.org/10.1063/1.4973449`

[181] M. Poggio, C. L. Degen, C. T. Rettner, H. J. Mamin, and D. Rugar. *Nuclear magnetic resonance force microscopy with a microwire rf source*. Applied Physics Letters **90**(26), 263111 (2007).
URL `http://dx.doi.org/10.1063/1.2752536`

[182] C. L. Degen, M. Poggio, H. J. Mamin, and D. Rugar. *Role of Spin Noise in the Detection of Nanoscale Ensembles of Nuclear Spins*. Phys. Rev. Lett. **99**, 250601 (Dec 2007).
URL `http://dx.doi.org/10.1103/PhysRevLett.99.250601`

[183] B. E. Herzog, D. Cadeddu, F. Xue, P. Peddibhotla, and M. Poggio. *Boundary between the thermal and statistical polarization regimes in a nuclear spin ensemble*. Applied Physics Letters **105**(4), 043112 (2014).
URL `http://dx.doi.org/10.1063/1.4892361`

[184] N. Aslam, M. Pfender, P. Neumann, R. Reuter, A. Zappe, F. Fávaro de Oliveira, A. Denisenko, H. Sumiya, S. Onoda, J. Isoya, and J. Wrachtrup. *Nanoscale nuclear*

magnetic resonance with chemical resolution. Science **357**(6346), 67–71 (2017). ISSN 0036-8075.
URL http://dx.doi.org/10.1126/science.aam8697

[185] B. Naydenov, V. Richter, J. Beck, M. Steiner, P. Neumann, G. Balasubramanian, J. Achard, F. Jelezko, J. Wrachtrup, and R. Kalish. *Enhanced generation of single optically active spins in diamond by ion implantation.* Applied Physics Letters **96**(16), 163108 (2010). ISSN 00036951.
URL http://dx.doi.org/10.1063/1.3409221

[186] B. Naydenov, F. Reinhard, A. Lämmle, V. Richter, R. Kalish, U. F. S. D'Haenens-Johansson, M. Newton, F. Jelezko, and J. Wrachtrup. *Increasing the coherence time of single electron spins in diamond by high temperature annealing.* Applied Physics Letters **97**(24), 242511 (2010). ISSN 00036951.
URL http://dx.doi.org/10.1063/1.3527975

[187] F. Fávaro de Oliveira, D. Antonov, Y. Wang, P. Neumann, S. A. Momenzadeh, T. Häußermann, A. Pasquarelli, A. Denisenko, and J. Wrachtrup. *Tailoring spin defects in diamond by lattice charging.* Nature Communications **8**, 15409 (May 2017). ISSN 2041-1723.
URL http://dx.doi.org/10.1038/ncomms15409

[188] T. Rosskopf, A. Dussaux, K. Ohashi, M. Loretz, R. Schirhagl, H. Watanabe, S. Shikata, K. M. Itoh, and C. L. Degen. *Investigation of Surface Magnetic Noise by Shallow Spins in Diamond.* Phys. Rev. Lett. **112**, 147602 (Apr 2014).
URL http://dx.doi.org/10.1103/PhysRevLett.112.147602

[189] B. A. Myers, A. Das, M. C. Dartiailh, K. Ohno, D. D. Awschalom, and A. C. Bleszynski Jayich. *Probing Surface Noise with Depth-Calibrated Spins in Diamond.* Phys. Rev. Lett. **113**, 027602 (Jul 2014).
URL http://dx.doi.org/10.1103/PhysRevLett.113.027602

[190] Y. Romach, C. Müller, T. Unden, L. J. Rogers, T. Isoda, K. M. Itoh, M. Markham, A. Stacey, J. Meijer, S. Pezzagna, B. Naydenov, L. P. McGuinness, N. Bar-Gill, and F. Jelezko. *Spectroscopy of Surface-Induced Noise Using Shallow Spins in Diamond.* Phys. Rev. Lett. **114**, 017601 (Jan 2015).
URL http://dx.doi.org/10.1103/PhysRevLett.114.017601

[191] B. Naydenov, F. Dolde, L. T. Hall, C. Shin, H. Fedder, L. C. L. Hollenberg, F. Jelezko, and J. Wrachtrup. *Dynamical decoupling of a single-electron spin at*

room temperature. Physical Review B **83**(8), 081201 (Feb 2011).
URL http://dx.doi.org/10.1103/PhysRevB.83.081201

[192] P. Maletinsky, S. Hong, M. S. Grinolds, B. Hausmann, M. D. Lukin, R. L. Walsworth, M. Loncar, and A. Yacoby. *A robust scanning diamond sensor for nanoscale imaging with single nitrogen-vacancy centres*. Nature Nanotechnology **7**(5), 320–324 (2012). ISSN 1748-3387.
URL http://dx.doi.org/10.1038/nnano.2012.50

[193] F. Ziem, M. Garsi, H. Fedder, and J. Wrachtrup. *Quantitative nanoscale MRI with a wide field of view*. arXiv:1807.08343 [cond-mat] (July 2018). ArXiv: 1807.08343.
URL http://arxiv.org/abs/1807.08343

[194] C. Müller, X. Kong, J.-M. Cai, K. Melentijevi?, A. Stacey, M. Markham, D. Twitchen, J. Isoya, S. Pezzagna, J. Meijer, J. F. Du, M. B. Plenio, B. Naydenov, L. P. McGuinness, and F. Jelezko. *Nuclear magnetic resonance spectroscopy with single spin sensitivity*. Nature Communications **5** (August 2014).
URL http://dx.doi.org/10.1038/ncomms5703

[195] I. Jakobi, P. Neumann, Y. Wang, D. B. R. Dasari, F. El Hallak, M. A. Bashir, M. Markham, A. Edmonds, D. Twitchen, and J. Wrachtrup. *Measuring broadband magnetic fields on the nanoscale using a hybrid quantum register*. Nature Nanotechnology **12**(1), 67–72 (September 2016). ISSN 1748-3387, 1748-3395.
URL http://dx.doi.org/10.1038/nnano.2016.163

[196] I. Lovchinsky, A. O. Sushkov, E. Urbach, N. P. de Leon, S. Choi, K. De Greve, R. Evans, R. Gertner, E. Bersin, C. Müller, L. McGuinness, F. Jelezko, R. L. Walsworth, H. Park, and M. D. Lukin. *Nuclear magnetic resonance detection and spectroscopy of single proteins using quantum logic*. Science (2016). ISSN 0036-8075.
URL http://dx.doi.org/10.1126/science.aad8022

[197] I. Lovchinsky, J. D. Sanchez-Yamagishi, E. K. Urbach, S. Choi, S. Fang, T. I. Andersen, K. Watanabe, T. Taniguchi, A. Bylinskii, E. Kaxiras, P. Kim, H. Park, and M. D. Lukin. *Magnetic resonance spectroscopy of an atomically thin material using a single-spin qubit*. Science **355**(6324), 503–507 (February 2017). ISSN 0036-8075, 1095-9203.
URL http://dx.doi.org/10.1126/science.aal2538

[198] J. Cai, A. Retzker, F. Jelezko, and M. B. Plenio. *A large-scale quantum simulator on a diamond surface at room temperature*. Nature Physics **9**(3), 168–173 (March

2013). ISSN 1745-2473.
URL http://dx.doi.org/10.1038/nphys2519

[199] X. Kong, A. Stark, J. Du, L. P. McGuinness, and F. Jelezko. *Towards Chemical Structure Resolution with Nanoscale Nuclear Magnetic Resonance Spectroscopy.* Physical Review Applied **4**(2), 024004 (August 2015).
URL http://dx.doi.org/10.1103/PhysRevApplied.4.024004

[200] S. Schmitt, T. Gefen, F. M. Stürner, T. Unden, G. Wolff, C. Müller, J. Scheuer, B. Naydenov, M. Markham, S. Pezzagna, J. Meijer, I. Schwarz, M. Plenio, A. Retzker, L. P. McGuinness, and F. Jelezko. *Submillihertz magnetic spectroscopy performed with a nanoscale quantum sensor.* Science **356**(6340), 832–837 (2017). ISSN 0036-8075.
URL http://dx.doi.org/10.1126/science.aam5532

[201] J. M. Boss, K. S. Cujia, J. Zopes, and C. L. Degen. *Quantum sensing with arbitrary frequency resolution.* Science **356**(6340), 837–840 (2017). ISSN 0036-8075.
URL http://dx.doi.org/10.1126/science.aam7009

[202] S. R. Hartmann and E. L. Hahn. *Nuclear Double Resonance in the Rotating Frame.* Physical Review **128**(5), 2042–2053 (December 1962).
URL http://dx.doi.org/10.1103/PhysRev.128.2042

[203] H. J. Mamin, M. H. Sherwood, M. Kim, C. T. Rettner, K. Ohno, D. D. Awschalom, and D. Rugar. *Multipulse Double-Quantum Magnetometry with Near-Surface Nitrogen-Vacancy Centers.* Phys. Rev. Lett. **113**, 030803 (Jul 2014).
URL http://dx.doi.org/10.1103/PhysRevLett.113.030803

[204] J. Scheuer, I. Schwartz, S. Müller, Q. Chen, I. Dhand, M. B. Plenio, B. Naydenov, and F. Jelezko. *Robust techniques for polarization and detection of nuclear spin ensembles.* Phys. Rev. B **96**, 174436 (Nov 2017).
URL http://dx.doi.org/10.1103/PhysRevB.96.174436

[205] F. Shagieva, S. Zaiser, P. Neumann, D. Bhaktavatsala Rao Dasari, R. J. Stöhr, A. Denisenko, R. Reuter, C. Andres Meriles, and J. Wrachtrup. *Microwave-Assisted Cross-Polarization of Nuclear Spin Ensembles from Optically Pumped Nitrogen-Vacancy Centers in Diamond* **18** (03 2018).

[206] D. A. Broadway, J.-P. Tetienne, A. Stacey, J. D. A. Wood, D. A. Simpson, L. T. Hall, and L. C. L. Hollenberg. *Quantum probe hyperpolarisation of molecular nuclear*

spins. Nature Communications **9**(1) (December 2018). ISSN 2041-1723.
URL http://dx.doi.org/10.1038/s41467-018-03578-1

[207] L. M. Pham, S. J. DeVience, F. Casola, I. Lovchinsky, A. O. Sushkov, E. Bersin, J. Lee, E. Urbach, P. Cappellaro, H. Park, A. Yacoby, M. Lukin, and R. L. Walsworth. *NMR technique for determining the depth of shallow nitrogen-vacancy centers in diamond*. Phys. Rev. B **93**, 045425 (Jan 2016).
URL http://dx.doi.org/10.1103/PhysRevB.93.045425

[208] R. Budakian, H. J. Mamin, and D. Rugar. *Suppression of Spin Diffusion near a Micron-Size Ferromagnet*. Physical Review Letters **92**(3), 037205 (January 2004).
URL http://dx.doi.org/10.1103/PhysRevLett.92.037205

[209] S. Kaufmann, D. A. Simpson, L. T. Hall, V. Perunicic, P. Senn, S. Steinert, L. P. McGuinness, B. C. Johnson, T. Ohshima, F. Caruso, J. Wrachtrup, R. E. Scholten, P. Mulvaney, and L. Hollenberg. *Detection of atomic spin labels in a lipid bilayer using a single-spin nanodiamond probe*. Proceedings of the National Academy of Sciences **110**(27), 10894–10898 (July 2013). ISSN 0027-8424, 1091-6490.
URL http://dx.doi.org/10.1073/pnas.1300640110

[210] L. M. Pham, S. J. DeVience, F. Casola, I. Lovchinsky, A. O. Sushkov, E. Bersin, J. Lee, E. Urbach, P. Cappellaro, H. Park, A. Yacoby, M. Lukin, and R. L. Walsworth. *NMR technique for determining the depth of shallow nitrogen-vacancy centers in diamond*. Physical Review B **93**(4), 045425 (January 2016).
URL http://dx.doi.org/10.1103/PhysRevB.93.045425

[211] A. A. Wood, E. Lilette, Y. Y. Fein, N. Tomek, L. P. McGuinness, L. C. L. Hollenberg, R. E. Scholten, and A. M. Martin. *Quantum measurement of a rapidly rotating spin qubit in diamond*. Science Advances **4**(5) (2018).
URL http://dx.doi.org/10.1126/sciadv.aar7691

[212] J. S. Waugh, L. M. Huber, and U. Haeberlen. *Approach to High-Resolution nmr in Solids*. Physical Review Letters **20**(5), 180–182 (January 1968).
URL http://dx.doi.org/10.1103/PhysRevLett.20.180

[213] P. Mansfield, M. J. Orchard, D. C. Stalker, and K. H. B. Richards. *Symmetrized Multipulse Nuclear-Magnetic-Resonance Experiments in Solids: Measurement of the Chemical-Shift Shielding Tensor in Some Compounds*. Physical Review B **7**(1), 90–105 (January 1973).
URL http://dx.doi.org/10.1103/PhysRevB.7.90

[214] W. Rhim, D. D. Elleman, L. B. Schreiber, and R. W. Vaughan. *Analysis of multiple pulse NMR in solids. II.* The Journal of Chemical Physics **60**(11), 4595–4604 (June 1974). ISSN 0021-9606.
URL http://dx.doi.org/10.1063/1.1680944

[215] A. Abragam and M. Goldman. *Nuclear Magnetism: Order and Disorder*. Oxford University Press (1982). ISBN 0-19-851294-5.

[216] M. H. Levitt, R. Freeman, and T. Frenkiel. *Broadband heteronuclear decoupling.* Journal of Magnetic Resonance (1969) **47**(2), 328 – 330 (1982). ISSN 0022-2364.
URL http://dx.doi.org/https://doi.org/10.1016/0022-2364(82)90124-X

[217] M. Pfender. Private communication.

[218] M. Pfender, P. Wang, H. Sumiya, S. Onoda, W. Yang, D. B. R. Dasari, P. Neumann, X.-Y. Pan, J. Isoya, R.-B. Liu, and J. Wrachtrup. *High-resolution spectroscopy of single nuclear spins via sequential weak measurements* page 60 (2018).
URL https://arxiv.org/abs/1806.02181

[219] G. Puentes, G. Waldherr, P. Neumann, G. Balasubramanian, and J. Wrachtrup. *Efficient route to high-bandwidth nanoscale magnetometry using single spins in diamond.* Scientific Reports **4** (April 2014).
URL http://dx.doi.org/10.1038/srep04677

[220] M. Loretz, J. M. Boss, T. Rosskopf, H. J. Mamin, D. Rugar, and C. L. Degen. *Spurious Harmonic Response of Multipulse Quantum Sensing Sequences.* Phys. Rev. X **5**, 021009 (Apr 2015).
URL http://dx.doi.org/10.1103/PhysRevX.5.021009

[221] S. Szunerits and R. Boukherroub. *Different strategies for functionalization of diamond surfaces.* Journal of Solid State Electrochemistry **12**(10), 1205–1218 (October 2008). ISSN 1433-0768.
URL http://dx.doi.org/10.1007/s10008-007-0473-3

[222] M. Pfender, N. Aslam, G. Waldherr, P. Neumann, and J. Wrachtrup. *Single-spin stochastic optical reconstruction microscopy.* Proceedings of the National Academy of Sciences **111**(41), 14669–14674 (October 2014). ISSN 0027-8424, 1091-6490.
URL http://dx.doi.org/10.1073/pnas.1404907111

[223] P. Kehayias, A. Jarmola, N. Mosavian, I. Fescenko, F. M. Benito, A. Laraoui, J. Smits, L. Bougas, D. Budker, A. Neumann, S. R. J. Brueck, and V. M. Acosta. *Solution nuclear magnetic resonance spectroscopy on a nanostructured diamond chip.*

Nature Communications **8**(1) (December 2017). ISSN 2041-1723.
URL http://dx.doi.org/10.1038/s41467-017-00266-4

[224] C.-C. Fu, H.-Y. Lee, K. Chen, T.-S. Lim, H.-Y. Wu, P.-K. Lin, P.-K. Wei, P.-H. Tsao, H.-C. Chang, and W. Fann. *Characterization and application of single fluorescent nanodiamonds as cellular biomarkers.* Proceedings of the National Academy of Sciences **104**(3), 727–732 (2007). ISSN 0027-8424.
URL http://dx.doi.org/10.1073/pnas.0605409104

[225] T. A. Klar and S. W. Hell. *Subdiffraction resolution in far-field fluorescence microscopy.* Opt. Lett. **24**(14), 954–956 (Jul 1999).
URL http://dx.doi.org/10.1364/OL.24.000954

[226] D. Wildanger, B. R. Patton, H. Schill, L. Marseglia, J. P. Hadden, S. Knauer, A. Schönle, J. G. Rarity, J. L. O'Brien, S. W. Hell, and J. M. Smith. *Solid Immersion Facilitates Fluorescence Microscopy with Nanometer Resolution and Sub-Ångström Emitter Localization.* Advanced Materials **24**(44), OP309–OP313 (2012). ISSN 1521-4095.
URL http://dx.doi.org/10.1002/adma.201203033

[227] N. Bobroff. *Position measurement with a resolution and noise-limited instrument.* Review of Scientific Instruments **57**(6), 1152 (1986). ISSN 00346748.
URL http://dx.doi.org/10.1063/1.1138619

[228] W. Hild, M. Breunig, and A. Goepferich. *Quantum dots – Nano-sized probes for the exploration of cellular and intracellular targeting.* European Journal of Pharmaceutics and Biopharmaceutics **68**(2), 153–168 (February 2008). ISSN 0939-6411.
URL http://dx.doi.org/10.1016/j.ejpb.2007.06.009

[229] B. Huang, W. Wang, M. Bates, and X. Zhuang. *Three-Dimensional Super-Resolution Imaging by Stochastic Optical Reconstruction Microscopy.* Science **319**(5864), 810–813 (August 2008). ISSN 0036-8075, 1095-9203. PMID: 18174397.
URL http://dx.doi.org/10.1126/science.1153529

[230] B. Huang, S. A. Jones, B. Brandenburg, and X. Zhuang. *Whole-cell 3D STORM reveals interactions between cellular structures with nanometer-scale resolution.* Nature Methods **5**(12), 1047–1052 (December 2008). ISSN 1548-7091.
URL http://dx.doi.org/10.1038/nmeth.1274

[231] A. Egner, C. Geisler, C. von Middendorff, H. Bock, D. Wenzel, R. Medda, M. Andresen, A. C. Stiel, S. Jakobs, C. Eggeling, A. Schönle, and S. W. Hell. *Fluorescence*

Nanoscopy in Whole Cells by Asynchronous Localization of Photoswitching Emitters. Biophysical Journal **93**(9), 3285–3290 (November 2007). ISSN 0006-3495.
URL http://dx.doi.org/10.1529/biophysj.107.112201

[232] R. H. Webb. *Confocal optical microscopy*. Reports on Progress in Physics **59**(3), 427 (1996).
URL http://dx.doi.org/10.1088/0034-4885/59/3/003

[233] R. E. Thompson, D. R. Larson, and W. W. Webb. *Precise nanometer localization analysis for individual fluorescent probes*. Biophysical journal **82**(5), 2775–2783 (2002).

[234] S. A. Momenzadeh, R. J. Stöhr, F. F. de Oliveira, A. Brunner, A. Denisenko, S. Yang, F. Reinhard, and J. Wrachtrup. *Nano-engineered Diamond Waveguide as a Robust Bright Platform for Nanomagnetometry Using Shallow Nitrogen Vacancy Centers*. arXiv:1409.0027 [cond-mat] (August 2014). ArXiv: 1409.0027.
URL http://arxiv.org/abs/1409.0027

[235] M. V. Hauf, B. Grotz, B. Naydenov, M. Dankerl, S. Pezzagna, J. Meijer, F. Jelezko, J. Wrachtrup, M. Stutzmann, F. Reinhard, and J. A. Garrido. *Chemical control of the charge state of nitrogen-vacancy centers in diamond*. Physical Review B **83**(8), 081304 (February 2011).
URL http://dx.doi.org/10.1103/PhysRevB.83.081304

[236] D. Le Sage, K. Arai, D. R. Glenn, S. J. DeVience, L. M. Pham, L. Rahn-Lee, M. D. Lukin, A. Yacoby, A. Komeili, and R. L. Walsworth. *Optical magnetic imaging of living cells*. Nature **496**(7446), 486–489 (April 2013). ISSN 0028-0836.
URL http://dx.doi.org/10.1038/nature12072

[237] P. C. Maurer, J. R. Maze, P. L. Stanwix, L. Jiang, A. V. Gorshkov, A. A. Zibrov, B. Harke, J. S. Hodges, A. S. Zibrov, A. Yacoby, D. Twitchen, S. W. Hell, R. L. Walsworth, and M. D. Lukin. *Far-field optical imaging and manipulation of individual spins with nanoscale resolution*. Nature Physics **6**(11), 912–918 (November 2010). ISSN 1745-2473.
URL http://dx.doi.org/10.1038/nphys1774

[238] M. S. Grinolds, S. Hong, P. Maletinsky, L. Luan, M. D. Lukin, R. L. Walsworth, and A. Yacoby. *Nanoscale magnetic imaging of a single electron spin under ambient conditions*. Nature Physics **9**(4), 215–219 (April 2013). ISSN 1745-2473.
URL http://dx.doi.org/10.1038/nphys2543

[239] E. H. Chen, O. Gaathon, M. E. Trusheim, and D. Englund. *Wide-Field Multispectral Super-Resolution Imaging Using Spin-Dependent Fluorescence in Nanodiamonds*. Nano Letters **13**(5), 2073–2077 (May 2013). ISSN 1530-6984.
URL http://dx.doi.org/10.1021/nl400346k

[240] N. Mizuochi, P. Neumann, F. Rempp, J. Beck, V. Jacques, P. Siyushev, K. Nakamura, D. Twitchen, H. Watanabe, S. Yamasaki, F. Jelezko, and J. Wrachtrup. *Coherence of single spins coupled to a nuclear spin bath of varying density*. Physical Review B **80**(4), 041201 (July 2009). ISSN 1098-0121, 1550-235X.
URL http://dx.doi.org/10.1103/PhysRevB.80.041201

[241] J. M. Taylor, P. Cappellaro, L. Childress, L. Jiang, D. Budker, P. R. Hemmer, A. Yacoby, R. Walsworth, and M. D. Lukin. *High-sensitivity diamond magnetometer with nanoscale resolution*. Nature Physics **4**(10), 810–816 (October 2008). ISSN 1745-2473.
URL http://dx.doi.org/10.1038/nphys1075

[242] B. J. Maertz, A. P. Wijnheijmer, G. D. Fuchs, M. E. Nowakowski, and D. D. Awschalom. *Vector magnetic field microscopy using nitrogen vacancy centers in diamond*. Applied Physics Letters **96**(9), 092504–092504–3 (March 2010).
URL http://dx.doi.org/doi:10.1063/1.3337096

[243] L. M. Pham, D. L. Sage, P. L. Stanwix, T. K. Yeung, D. Glenn, A. Trifonov, P. Cappellaro, P. R. Hemmer, M. D. Lukin, H. Park, A. Yacoby, and R. L. Walsworth. *Magnetic field imaging with nitrogen-vacancy ensembles*. New Journal of Physics **13**(4), 045021 (April 2011). ISSN 1367-2630.
URL http://dx.doi.org/10.1088/1367-2630/13/4/045021

[244] L. T. Hall, G. C. G. Beart, E. A. Thomas, D. A. Simpson, L. P. McGuinness, J. H. Cole, J. H. Manton, R. E. Scholten, F. Jelezko, J. Wrachtrup, S. Petrou, and L. C. L. Hollenberg. *High spatial and temporal resolution wide-field imaging of neuron activity using quantum NV-diamond*. Scientific Reports **2**, 401 (May 2012). ISSN 2045-2322.
URL http://dx.doi.org/10.1038/srep00401

[245] L. Rondin, G. Dantelle, A. Slablab, F. Grosshans, F. Treussart, P. Bergonzo, S. Perruchas, T. Gacoin, M. Chaigneau, H.-C. Chang, V. Jacques, and J.-F. Roch. *Surface-induced charge state conversion of nitrogen-vacancy defects in nanodiamonds*. Physical Review B **82**(11), 115449 (September 2010). ISSN 1098-0121,

1550-235X.
URL http://dx.doi.org/10.1103/PhysRevB.82.115449

[246] M. Gu, Y. Cao, S. Castelletto, B. Kouskousis, and X. Li. *Super-resolving single nitrogen vacancy centers within single nanodiamonds using a localization microscope*. Optics Express **21**(15), 17639–17646 (July 2013).
URL http://dx.doi.org/10.1364/OE.21.017639